JOINING OF DISSIMILAR METALS: SHAPE MEMORY NITI AND STAINLESS STEELS

CHENG KA PO

PhD

The Hong Kong Polytechnic University

2020

The Hong Kong Polytechnic University

Department of Industrial and Systems Engineering

Joining of Dissimilar Metals: Shape Memory NiTi and Stainless Steels

Cheng Ka Po

A Thesis submitted in partial fulfilment of the requirements for the Degree of Doctor of Philosophy

Jan 2020

Certificate of Originality

I hereby declare that this thesis is my own work and that, to the best of my knowledge and belief, it reproduces no material previously published or written, nor material that has been accepted for the award of any other degree or diploma, except where due acknowledgement has been made in the text.

____

Cheng Ka Po

Acknowledgements

I would like to express my deepest thanks and appreciation to my Academic Supervisors, Professor H.C. Man, Chair Professor of Materials Engineering in the Department of Industrial and Systems Engineering and Dean of Faculty of Engineering of The Hong Kong Polytechnic University, for his most stimulating advice on the execution of my research work. His invaluable guidance, understanding and countless discussions have made my study possible and broadened my intellectual ability in the field of laser materials processing. I am extremely grateful for what he has offered me. I would like to thank Professor H.C. Man once again for giving understanding and support during my illness. Besides, I would like to show my greatest appreciation to my co-supervisor, Dr. Stephen O'Brien, the Director of Operations in the Aviation Services Research Centre of the Hong Kong Polytechnic University, for his support to the research.

I would like to take this opportunity to give my sincere thankfulness to the financial supports from the Department of Industrial and Systems Engineering and the Industrial Centre. Without their support to the research, my completion of this study could not have been accomplished. I would also like to thank all people whose assistance were a milestone in the completion of my study. Advice and comments given by all the professors and technical staff have been a great help in my study and dissertation.

Last, but not least, I would like to thank my family, especially my lovable children, Paco and Samuel, for their forgiveness, caring and encouragement during my study period.

Table of Contents

Abstract

Many researchers have proposed the possibility of welding nickel-titanium (NiTi) to other metal for different applications. The joining of NiTi is relatively well understood with a number of studies presented regarding the joining of two Nitinol (NiTi) specimens. However, it is very difficult to obtain an acceptable weld joint connecting NiTi and stainless steel. The formation of brittle intermetallic compounds is one of the biggest challenges faced during the welding of dissimilar materials. The presence of $TiFe_2$ are thought to be the most common brittle intermetallic compounds formed during the welding of NiTi and stainless steel. As the formation of intermetallic compounds cannot be avoided during the direct welding of NiTi and stainless steel, the addition of a third body, positioned between the two, might be a possible solution to the above. The successful joining of NiTi to other metal has the possibility of extending the NiTi application range. Thus, a strong interest exists in the outcomes of this study.

During this research, laser welding, one of the reliable techniques for the joining of NiTi, was used with an interlayer of either Co or Ni to join NiTi and stainless steel. By altering the laser power, welding speed, the position of the focal plane of the laser beam, with respect to the surface of the specimens and the amounts/shapes of different filler metals, the chemical composition of the weld bead can be varied to minimize deterioration of mechanical properties of the joint. The main effects and the interaction effects of the process parameters on tensile strength are discussed to determine the best combinations of input process parameters for the production of good weld quality of NiTi-Ni-SS joint.

The microstructure of the welded joint was studied using an optical microscope and a scanning electron microscope (SEM). X-ray diffraction analysis (XRD) was used to identify

intermetallic compounds (i.e. $TiFe_2$, $TiCr_2$, $NiTi_2$) in the area of the weld pool. The stress-strain behaviour was evaluated with a tensile test and the hardness studied by the micro-indentation method. The shape memory effect was evaluated by the guided bend method. The corrosion behaviour in Hanks' solution of 37.5°C was studied using the potentiodynamic polarization test.

The results of this research show that the mechanical and functional properties as well as the corrosion resistance in Hank's solution of the laser welded joint can be effectively improved by using nickel as the interlayer between NiTi and stainless steel. The combination of input process parameters with appropriate amounts/shapes of Ni interlayer, could possibly improve the tensile strength of the welded joint from 54% to a maximum of 108%, compared to that of the tensile strength of a directly welded NiTi and a stainless steel joint in this study. A comparison of the corresponding values of corrosion potential and corrosion current density for the joint with rectangular shape and circular shape Ni interlayer indicated that, as expected, welding reduced the corrosion resistance of NiTi. However, an appropriate combination welding process parameters and interlayer quantity could make a better passivation and a lower corrosion current, close to the base material of NiTi. Transmission electron microscopy (TEM) with energy dispersive X-ray spectrometry (EDX) was used in the analysis of fusion zone of welded NiTi-Ni of NiTi-Ni-SS joints and chemical characterization of compounds. A significant difference between the compositions of NiTi-Ni fusion zone with different widths of Ni interlayers was observed. Although monoclinic B19', hexagonal R phase, hexagonal Ni_2Ti and Ni_3Ti, rhombohedral Ni_4Ti_3, cubic $NiTi_2$ and Ni were identified, their amounts were different in different welded samples. The amount of B19' increased to 43% in the fusion zone of the joint, which was welded by the power density of 6.37×10^6 W/cm^2 with interaction time of 1.82ms. Due to this high amount of B19’, the welded joint allowed a recoverable bending distance of 5.00 mm enabling the original position of the welded specimen to be completely recovered after 18s. Diffraction intensity distribution in Debye-Scherrer ring patterns, which were generated from different welding conditions, indicated lattice parameters varied. Microanalysis revealed that Ni_4Ti_3 were presented in different welding conditions and contributed to the shape memory characteristics and strengthened the matrix to increase the yield strength of the welded joint. However, the increase of Ni_4Ti_3 to over 20% of the matrix would be likely to increase the Ms, Mf and Af. At the same time, two-stage phase transformation occurred during heating arising when the amount of Ni_4Ti_3 increased to 26%. When the amount of Ni_4Ti_3 was below about 10%, only a one-stage phase transformation occurred as the heating arising. According to XRD and TEM analysis, the B19’ with a strong preferred orientation of (111) planes and Ni_4Ti_3 with a preferred orientation of (3-1-2) and (2 1-1) planes were found in the fusion zone, which contributed to the improvement of the tensile strength and recoverable bending deflection.

In summary, in the study reported in this thesis, the microstructural evolution in the welding of NiTi and stainless steel has been explored. This study has revealed a variety of phenomena which occur during laser welding, and the relationship between the possible amount of different phases, welding process parameters and amount of Ni interlayer were investigated on the contribution of joint strength, corrosion properties and recoverable bending deflection improvement. The addition of rectangular shape Ni interlayer between NiTi and stainless steel has been demonstrated as a feasible alternative for controlling the chemical composition of fusion zone. Also, the decrease of $NiTi_2$ and increase of B19’ were identified as the crucial phases that affect the joint performance.

List of Figures

List of Tables

List of Abbreviation

ANOVA	Analysis of Variance
CW	Continuous Laser Welding
COD	Crystallography Open Database
DSC	Differential Scanning Calorimetry
EBSD	Electron Backscatter Diffraction
WEDM	Wire electro-discharge machining
EDX	Energy Dispersive X-ray
FZ	Fusion Zone
HAADF	High Angle Annular Dark Field
HAZ	Heat Affected Zone
NiTi	Nickel-titanium
OFAT	One-factor-at-a-time
PW	Pulse Laser Welding
SADP	Selected Area Diffraction Pattern
SEM	Scanning Electron Microscope
SMA	Shape Memory Alloy
SS	Stainless Steel
TEM	Transmission Electron Microscopy
WZ	Weld Zone
XRD	X-ray Diffraction Analysis

1 Introduction

1.1 Background

Nickel-titanium (NiTi) shape memory alloy (SMA) has generated extensive attention and interests throughout a wide range of industries. NiTi alloy is the most popular SMA due to its unique properties such as its pseudoelasticity, shape memory and biocompatibility (Duerig *et al*., 1999; Dilibal *et al*., 2004; Patoor *et al*., 2006). Applications of NiTi, however, are still restricted to niche markets such as aerospace, aviation, biomedical and civil engineering sectors (Morgan, 2004; Song *et al*., 2006; Calkins *et al*., 2006). Currently, the successful application of NiTi appears to be dominated by the biomedical sector (Predki *et al*., 2006) due to the availability of suitable techniques for developing a particular range of NiTi materials.

To extend the use of NiTi to other industries, such as in electrical appliances, aircraft and automobile components, new fabrication techniques especially joining NiTi with other metals to form more complex shapes are needed. Although the subject of joining NiTi has gained more focus, publications regarding the potential of dealing with systematic joining of NiTi to other metals are sparse.

The unique properties and good corrosion resistance of NiTi which make it suitable for medical and aircraft applications. The joining of NiTi has been well studied and good biocompatibility of welded NiTi-NiTi were reported (Chan *et al*., 2012; Caplan, 1991). Limited research, however, has been carried out regarding the joining of NiTi with different metals, maybe because of the potential detrimental microstructures effect of the cumbersome conventional, mechanical NiTi joining method. It is possible that successful achievement of a satisfactory joint is challenging, possibly, because of its limited strength reduction, but more likely because intermetallic compounds inclusions alter the pseudoelasticity (PE) and shape memory effects (SME).

With the above in mind, the seamless integration of intermetallic compounds into products containing other metals is a particularly critical criterion regarding the widespread use of NiTi. Regardless of the above, it is necessary, however, to be able to join NiTi to other metals and further fully understand the relationship between the micro-structural, mechanical and shape memory effects of heterogeneous welding. Steegmuller *et al*. (2004) and Siekmeyer *et al*. (2005) reported the successfully joining of NiTi with Au/Pt, however, the resultant corrosion resistance properties of those joints were poor in the human body. Stainless steel is likewise a commonly used material in medical and aircraft applications due to its strength and good corrosion resistance. However, NiTi is a more expensive material and more difficult to be put into industrial practice when compared to stainless steel. The increasing use of NiTi and stainless steel in different industries is an obvious option due to its more acceptable cost and excellent corrosion resistance, as indicated above. Hence, high strength, toughness and corrosion resistance behaviour resulting from the joining of NiTi and stainless steel is of high importance. Components made by pure NiTi is normally confined to simple and less complex structures and forms. However, currently joining of NiTi and other metals has increasingly attracted more attention in industry because NiTi in combination with different materials can facilitate the improvement of design flexibilities/shape complexity and the reduction of material component costs. The successful joining of NiTi and other metals has the possibility of extending the application range of NiTi.

Many researchers have proposed different applications of NiTi. Brandal *et al*. (2013) stated that NiTi is an ideal material for implantable medical devices. However, problems in its usage in this area, exist, as implantable medical devises, primarily are not made of a single material.

Hence, as with most new products, large expense is usually necessary before universal acceptance. To achieve a cheaper reliable product, intense exploration is necessary. Stainless steel is one of the dominant materials widely used in different applications especially in the biomedical industry, owing to the mechanical properties, workability, low cost and corrosion resistance (Uenishik *et al*., 2002). Etsuko *et al*. (2012) reported that a successful joining of NiTi-SS with 3mm deflection could benefit the orthodontic area. Brandal *et al*. (2013) realised that NiTi could be joined with stainless steel allowing stainless steel to replace part of the NiTi in the component where the unique property of NiTi are not required, and hence reduce cost. In addition, joining NiTi and other metal with different mechanical characteristic could produce hybrid properties of part to improve the implantable biomedical applications. Therefore, a strong interest has arisen regarding the enablement of the joining of NiTi with other biocompatible alloys, such as stainless steel.

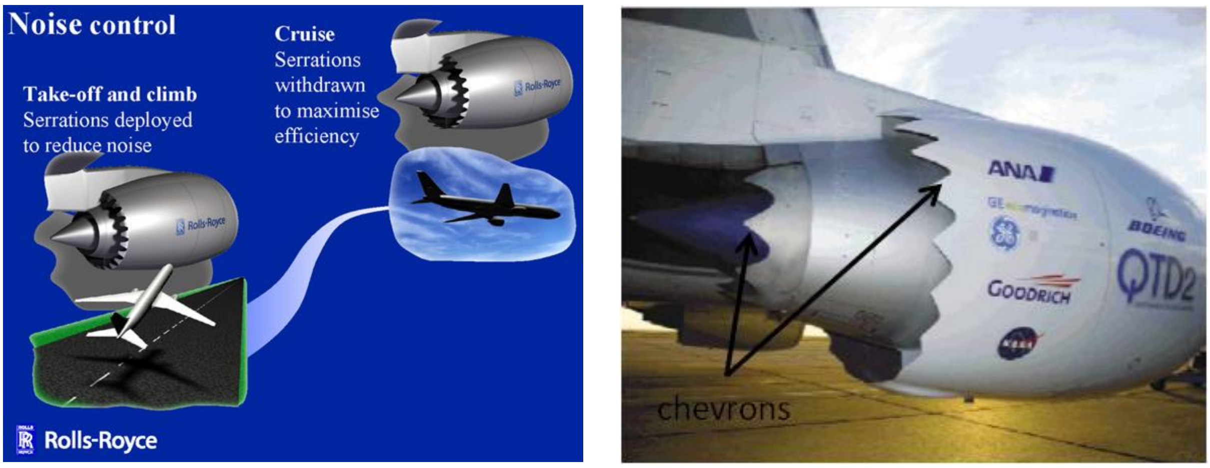

Fig. 1.1 Proposed chevrons design for noise control (Howse, 2001)

Howse (2001) discussed the use of shape memory alloy as a method of controlling noise pollution from aero-engines. Darren *et al*. (2008) reported that a 3-5 db reduction of noise produced by jet engines could be achieved if chevrons could be inserted into the engine exhaust stream but removed from the stream during cruising flight as shown in Fig. 1-1.

Supporting techniques regarding the joining of NiTi and other metals to form complex shapes/components could enable the realization of the proposed applications also shown below in Fig. 1.2 to 1.4.

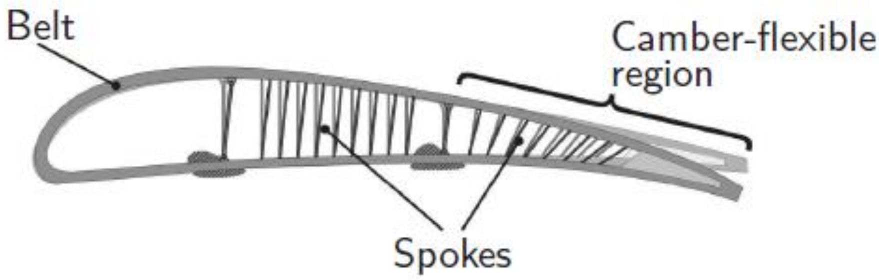

Fig. 1.2 Proposed design of morphing aircraft structures (Campaniel and Sachau., 2000)

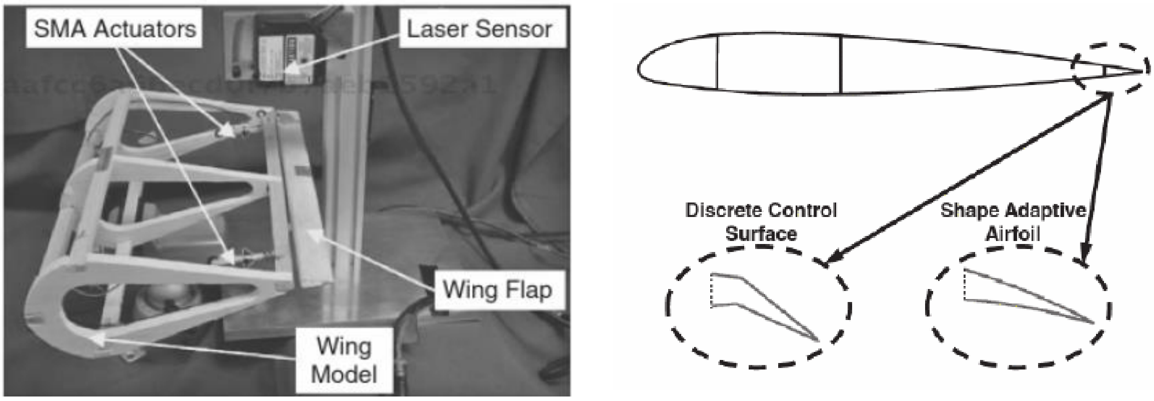

Fig. 1.3 Proposed design for controlling wing flap with the use of SMA (Roh*et al.*, 2009)

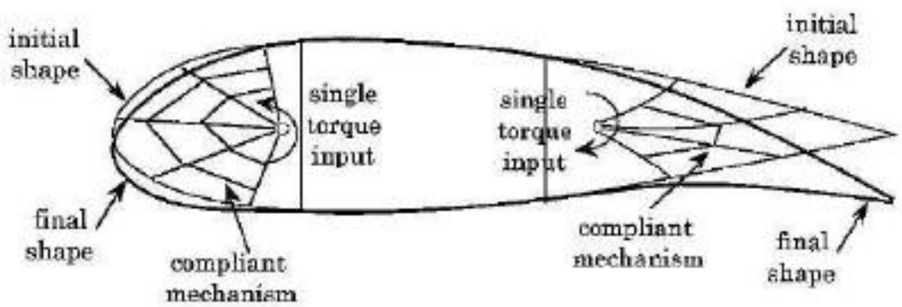

Fig. 1.4 Schematics mechanisms of morphing aircraft structures (Saggere and Kota, 1999)

Valasek (2012) stated that the creation of robust morphing aircraft structures was feasible due to the advances in materials such as NiTi, and many aerodynamic configurations could be developed for aircraft wings by better enabling the control of morphing via heating and cooling the opposing shape memory components. Other researchers proposed design concepts using shape memory effect to likewise achieve the morphing aircraft structures as shown in Fig. 1.2 to 1.4. Roh*et al*. (2009) proposed the use of shape memory effect to control the wing flap angle while Campanile and Sachau (2000) presented a concept of belt-rib design for camber control by lengthen the pressure and shorten the suction side or vice versa depending on the direction of defection. Saggere and Kota (1999) elaborated the concept for a deformable leading edge while Trease (2003) presented a similar concept aimed at deforming the trailing edge. However, no detailed elaboration on the actuation and the joining method between the spokes/ribs and the skin sheet/belt was discussed at the time.

To enable hovering and cruising of the helicopter, different mechanical parts to control the movement of the blades are needed. If the movement of the blades could be controlled by shape memory effect, the need of different mechanical parts could be reduced to improve the carrying capacity and cruise range. Therefore, James *et al*. (2004) proposed a design to mount NiTi inside helicopter blades to enable the deformation of the blades to achieve different geometries in direct relationship to hovering and cruising. The proposed design stated that it could increase the carrying capacity and cruise range by 10 -20%. However, the above proposed mounting method still need the use of fasteners that could increase the total weight of the helicopter. This increase of weight could subsequently reduce the effectiveness of blade deformation. Therefore, if a small piece of NiTi could be joined with stainless steel by welding, additional weight could be minimized.

Although welding of NiTi-NiTi has problems such as formation of brittle intermetallic and variation of composition in the fusion zone, joining a NiTi sheet with stainless steel, when appropriate, can effectively reduce material costs and extend this benefit to biomedical sector and other industries, in which the joint is applied. Examples are, such as aircrafts, automotive component industries, electrical appliances. (Morgan, 2004; Song *et al*., 2006; Calkins *et al*., 2006) and implant (Lu *et al*., 2013). Therefore, joining NiTi to stainless steel could satisfactorily extend the application range and possibly achieve those mentioned applications proposed by different researchers as above, but only to a part that needs shape deformation of a region with 1-5mm (Zhang and Sun, 2013) and different mechanical characteristics as shown in Fig. 1.5.

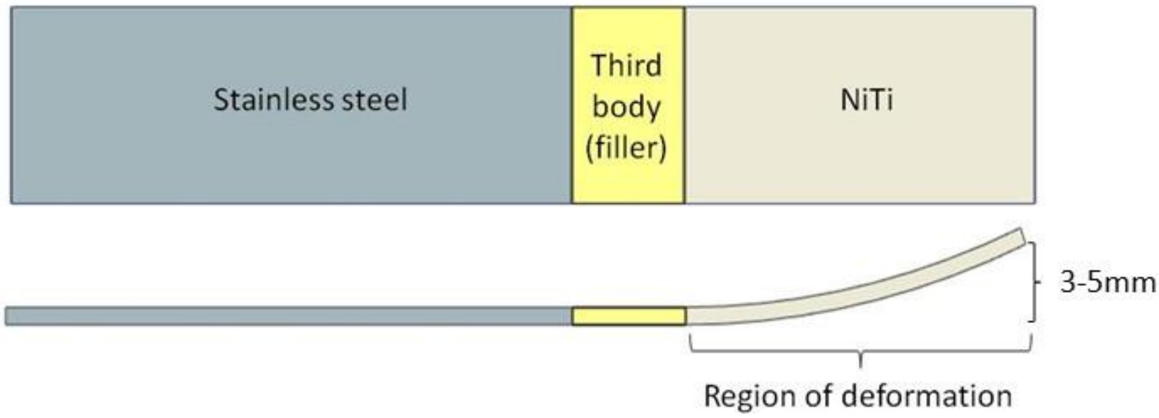

Fig. 1.5 Schematic of deformation structure

Several joining techniques exist, and include adhesive bonding, mechanical fastening and welding. Adhesive bonding is sensitive to temperature and the strength is largely affected by the amount of absorbed moisture (Mubashar *et al*., 2011; Hand *et al*., 1991) while mechanical fastening needs bolting or riveting for joining. Welding may be difficult to implement on components made from pure NiTi. Different kind of arc welding processes such as submerged arc welding, shielded metal arc welding, gas metal arc welding and gas tungsten arc welding have been used for dissimilar metal welding. However, material metallurgical mismatch is caused by the high energy inputs of this welding process (Sun and Karppi, 1996). Promising welding techniques for joining dissimilar materials, however, have been developed to provide high bond strength and a small heat affected zone due to the shorter interaction time. Spot welding, friction stir welding, ultrasonic welding and laser welding are the examples of those techniques. Ultrasonic welding is applicable to the joining of non-metallic materials or the joining of a non-metallic material and metallic material. This process is not applied to the joining of NiTi and stainless steel. Although friction welding/friction stir welding could produce a small heat affected zone, a similar geometrical shape such as round bar is needed. The latter which is not applicable to welding materials in sheet form. Laser welding and spot welding are suitable for joining sheet metals.

Relevant literature reveals that the process parameters can greatly influence the welding behavior of NiTi (Hodgson and Russell, 2000). The welding of shape memory alloys to other metals however, is qualitatively different from welding shape memory alloys together as the physical and thermal properties of the base metals are different, hence greatly affecting the heat transfer during welding. Brittle intermetallic compounds (e.g. $NiTi_2$, Fe_2Ti, or Cr_2Ti when joining NiTi to stainless steel) may be formed in joints. Hora (2004) conducted a preliminary assessment to investigate the laser welding of thin sections of NiTi shape memory alloys. The finding indicated that interfacial cracking was observed, and optimization of the welding parameters was needed to achieve a properly formed weld pool and joint strength. Although welding of NiTi to NiTi is relatively well understood with respect to the fundamentals of the solidification theory, the effect of different weld bead compositions as a result of welding NiTi to other metals upon the properties of the joint has received limited attention. Thus, the accomplishment of an acceptable join is challenged as it is not only limited to strength reduction, but also the inclusions of intermetallic compounds that would alter the pseudoelasticity (PE), shape memory effects (SME), corrosion, fatigue. Insufficient information is available in the literature regarding the effect of process parameters on the welding behavior of welding NiTi and stainless steel sheet, and the subsequent mechanical strength and other properties in the welded pair. Therefore, the joining of NiTi to other metals has been identified as the major obstacle in the development of high integrity applications. Several factors, however, could affect the quality of a weld joint, such as the microstructure of the weld bead, for instance, its grain size and shape, the existence of various phases, porosity, residual stresses and weld bead geometry. Some of these factors can be controlled by controlling the amount and rate of heat input and rate of cooling. Hence, research on various welding methods and optimization of the weld parameters is important to further the understanding of methods of weld bead control. The existence of different desirable or undesirable phases can be controlled by the cooling rates, post weld heat treatment, filler material and further knowledge regarding the unnecessary amount of melting of parent metals. By altering the welding parameters and/or the amount of different filler metals, the composition of the weld can be modified to meet the ultimate requirement of the composition. In dissimilar joints, the need to understand material behavior is even more challenging since two different parent materials have different physical properties leading to differential heat flows, melt convection flow and residual stress distribution. The new chemical composition in the weld pool can lead to the formation of intermetallic compounds. The aim of the study described herein project will look into these approaches in joining NiTi to dissimilar metals. The study will focus on laser welding of NiTi and stainless steel (SS304). NiTi and SS304 sheets were welded in butt joint at different energy inputs by varying the power and moving speed of the laser source. The effects of welding parameters, interlayer (different interlayer materials) and shape/size of the interlayer on the microstructure, chemical composition and mechanical properties of dissimilar welded joints were also investigated.

1.2 Objectives

The aim of this study is to systematically study the weldability of NiTi to stainless steel sheet metal of 1mm thick will be used in this project. The following six key objectives are designed to achieve this aim:

(i) To study the effects of pure Co and Ni as interlayer upon the tensile strength of laser welded joint of NiTi-SS304 with a fixed size of interlayer;

(ii) Using Taguchi method to study the effects of laser welding process parameters upon the tensile strength of laser welded joints of NiTi-SS304 with Ni as interlayer in different size and shape;

(iii) To study the effects of Ni as interlayer, its size, shape and process parameters and their possible interaction with the corrosion behavior of laser welded joints immersed in Hanks' solution at 37.5°C;

(iv) To examine the effect of the welding process parameters and amount of interlayer upon the chemical composition, microstructure and phases formation of the fusion zone of a weld;

(v) To examine the relationship between the amount of different phases, phase orientation and phase distribution in the fusion zone and the resultant mechanical performance;

(vi) To understand the types of intermetallic phases via TEM studies and the transformation characteristics to add new knowledge in NiTi-SS304 welding and potential application for biomedical and aeronautical.

2 Literature Review

2.1 Joining of Nickel-titanium (NiTi)

2.1.1 Material Characteristics of Nickel-titanium (NiTi)

NiTi shape memory alloy is an intermetallic compound consisting mainly of titanium and nickel. The two important NiTi properties are the shape memory effect and pseudo-elasticity, both first observed in the 1960s (Kauffman and Mayo, 1997). The shape memory effect caused by heating is classified as a one-way shape memory while the shape memory effect caused by heating and cooling is classified as a two-way shape memory. Phase transformation induces internal structure changes, such as those in shape and damping, while stress-induced transformation induces pseudo-elasticity.

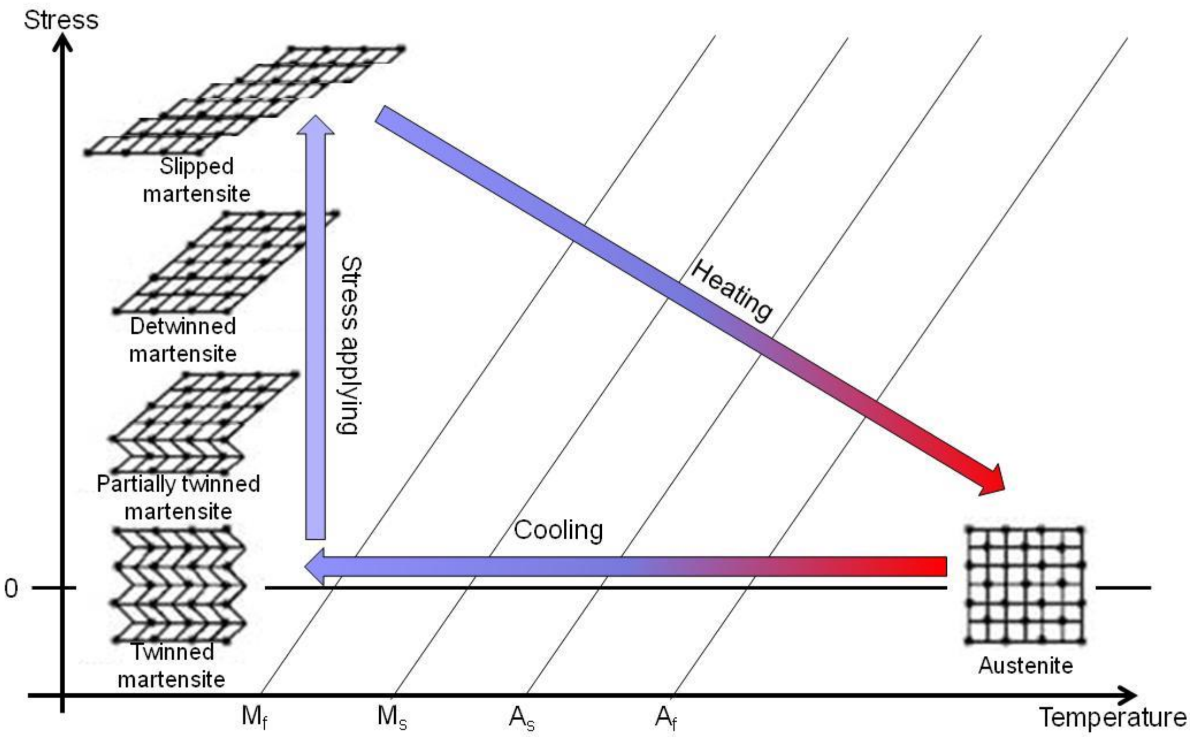

Fig. 2.1 Phase transformation diagram of NiTi (Lagoudas, 2010)

Fig. 2.1 shows the phase transformation of NiTi during the stress and temperature changes. This kind of phase transformation is associated with the following four characteristic temperatures: (i) Austenitic finish temperature, A_f; (ii) Austenitic start temperature, A_s; (iii) Martensitic start temperature, M_s, and (iv) Martensitic finish temperature, M_f. When the temperature is greater than A_f, the structure of NiTi is initially austenite. When the temperature is decreased to below M_s, a martensitic structure starts to form and causes the phase transformation from austenite to twinned martensite at M_f. The occurrence of phase transformation from austenite to martensite depends only on temperature change under zero stress.

The martensite boundaries can be rotated to form a set of variants. The term variant is the designation given to the orientation direction of each martensite crystal formed during the martensitic transformation. If stress is applied, the martensite crystal orientation changes to the most effective variants, to accommodate the direction of the resulting strain. When the stress increases, the twinned martensite initially changes its structure to a partially twinned martensite, later changing its structure to de-twinned martensite. Its corresponding strain from twinned martensite to de-twinned martensite, is approximately several percent and the strain disappears after the stress is removed (unloading). The loading and unloading cycle shows a hysteresis loop: pseudo-elasticity: (Song *et al*., 2006). When the stress level is higher than the stress of the detwinned martensite formed, the NiTi structure becomes slipped martensite and the original shape of the martensite is not preserved. At this stage, if the temperature rises and is greater than A_s, austenite begins to form and ends at a temperature of A_f or above. The initial macroscopic shape is then, preserved.

The process described above is known as the shape memory effect. Martensitic transformation plays a crucial role in the shape memory effect and pseudoelasticity of NiTi. The occurrence of phase transformation from austenite to martensite depends on the composition and thermal/thermo-mechanical treatment (Otsuka and Ren, 2005; Miyazaki and Otsuka, 1986). This change is because of the precipitation of the important secondary Ni_4Ti_3 particles during the thermo-mechanical processing (Li *et al*., 1997; Yeung *et al*., 2004).

2.1.1.1 Overview of Nucleation and Crystal Structure

The structure of a crystalline solid is best described by its unit cell. The unit cell consists of lattice points that represent the locations of atoms. In general, a unit cell is defined by the lengths of three axes (a, b, and c) and the angles (α, β and γ) between them. There are seven different lattice systems for a total of fourteen different unit cell as some of which have more than one type of lattice. Those lattice systems are (i) cubic, (ii) tetragonal, (iii) orthorhombic, (iv) monoclinic, (v) triclinic, (vi) hexagonal and (vii) rhombohedral. The lattice structure of material affects the mechanical and thermal properties (Ashby, 2006). To help differentiate the lattice structure mechanical properties, two different deformation categories can be categorized into bending dominated and stretching dominated structures. Stretching dominated structure (i.e. cubic) is useful to produce high stiffness and low weight parts while bending dominated structure (i.e. tetrakaidecahedron) is useful to produce parts suitable for energy absorption (Evans *et al*., 2001). Therefore, to maximize stiffness and strength, more stretching-dominated structure is needed to obtained (Zhang *et al*., 2015).

Nucleation is an important event in crystal growth. A comprehensive study on growth of crystals should start from an understanding of nucleation process (Sangwal, 1987). Nucleation is the physical reaction which occurs when components in a solution start to precipitate out forming nuclei which attracts more precipitate. When a few atoms join together in a supersaturated system, a change in energy takes place in the process of formation of the cluster. The cluster of such atoms is called embryo. If the embryo grows to a particular size, then greater size of nucleus grow into a crystal. Santhanaraghavan and Ramasamy (2002) defined that four stages are involved in the formation of stable nucleus. There are (i) development of supersaturation; (ii) generation of embryo; (iii) growth of the embryo from the unstable critical state to stable state; and (iv) relaxation process.

The homogeneous nucleation is a spontaneous formation of crystalline nuclei within the interior of parent phase while heterogeneous nucleation is the nuclei form heterogeneously around ions (Claude, 2006). The formation of the crystal nuclei is a complex and difficult process, because the constituent molecules in the system have to be oriented into a fixed lattice. In practice, a number of atoms may come together to form an ordinary cluster known as embryo. This embryo is likely to dissolve again unless it reaches a certain critical size based on the consideration of energy. If the embryo is stable under the prevailing condition, it does not dissolve.

The rate of nucleation is calculated by the nucleation theory and rate of nucleation is nothing but the number of critical nuclei formed per unit time per unit volume. Nucleation is treated as the chain reaction of monomolecular addition to the cluster and ultimately reaching macroscopic dimensions in kinetic theory. The size distribution in the embryo changes and larger ones increases in size when the time increases. When the size attains a critical size (S_c), further growth into macroscopic size is guaranteed. There is also a possibility for the reverse reaction.

The reaction is represented as follows:

$S_k + S_{c-1} = S_c$

Where S_k , S_{c-1} are size of kth cluster and size of cluster before attains a critical size respectively.

Energy is quite essential for the creation of a new phase. When a nucleus forms due to supersaturation of vapour, certain quantity of energy is spent in the creation of a new phase. The free energy change associated with the formation of a nucleus can be written as

$\Delta G = \Delta G_s + \Delta G_v$

ΔG is a combination of surface excess free energy ΔG_s (the product of area of ith face and surface energy per unit area) and volume excess free energy ΔG_v (the product of volume of ith nucleus and energy change per unit volume).

Precipitation of second phases could take place during thermal treatments (Chan *et al*., 2010), alloy manufacturing and thermo-mechanical cycling (Chan *et al*., 2012) in any given shape memory alloy during its service life. They are known to play a critical role in the functionality stability of shape memory allows (Wagner *et al*., 2010). Crystal structures of some of the most commonly observed precipitates in binary Ni - Ti system are reviewed.

The spacegroup of $NiTi_2$ is reported to be F d 3 m and a cubic crystal structure with a lattice parameters of 1:132Å (Mueller and Knott, 1963). An investigation of the precipitation behavior in a Ti rich NiTi alloy concluded that the matrix-precipitate interface remains semi coherent at peak growth and the orientation of Ti_2Ni precipitates in a given NiTi grain even always remains unchanged (Ishida *et al*., 1997). Ni_3Ti precipitates have hexagonal DO24 type ordered structure with a = 5.101 Å and c = 8.307 Å (Taylor and Floyd, 1950).

The spacegroup of Ni_3Ti_2 is reported to be I4/mmm and a tetragonal crystal structure at high temperature with lattice parameter a = 3.095 Å, c = 13.595 Å while a low temperature orthorhombic Ni_3Ti_2 phase with Bbmm space group and lattice parameters a = 4.398 Å, b = 4.370 Å and c = 13.544 Å is reported (Hara *et al*., 1997).

The crystal structure of Ni_4Ti_3 precipitates are reported to have a rhombohedral structure with 6:7 Å and 113:9 Å lattice parameters (Zou *et al*., 1996). The morphology of Ni_4Ti_3 precipitates likes oval disk with tendency to precipitate with its habit plane parallel to the f111g plane of B2 austenite (Tadaki *et al*., 1986).

2.1.2 Problem of NiTi-NiTi Joining and Effect of Post-weld Heat Treatment

During the molten weld pool cooling, hot cracking may occur. NiTi first solidifies and then begins to form grains, while Ni_2Ti remains liquid. The liquid Ni_2Ti moves between the NiTi grain boundaries and finally solidifies into a brittle compound. The cooling creates cracks in the Ni_2Ti phase. Such cracks can propagate through the entire weld and create either a very weak joint can cause joint failure even before the weld has finally cooled (Cieslak, 1993; Wang, 1997). In addition to hot cracking, cold cracking may occur. This occurs when a brittle intermetallic compound of low strength at room temperature, forms in the weld pool (Casper *et al*., 2003; Wu, 2001). The cooling can create cracks at this point, similar to Ni_2Ti in hot cracking, and results in the same poor weld strength. Fox *et al*. (2012) reported that the wide heat affected zones generated during welding may destroy the shape memory effect of the NiTi. If the NiTi is annealed, the shape memory effect is null and void. NiTi loses its previous training in cold working if it is heated above 500°C, but it must be heated above 1300°C to melt in fusion welding processes (Civjan, 1975). Chan *et al*. (2012) reported that the transformation temperatures welded NiTi-NiTi joints affected by the change of microstructure after laser welding. The presence of Ni_3Ti (Chan *et al*., 2011) causes the increase of transformation temperature, however, observation of transformation temperature decreases was also happen that involved a need to further research.

Researchers (Chan *et al*., 2012; Yan and Ge, 2014) reported the presence of Ni_4Ti_3 caused by post-weld heat treatment improve the mechanical properties of NiTi-NiTi joint. Chan *et al*. (2012) also reported that the elongation at fracture was improved after post-weld heat treatment due to the effective removal of dislocation motion. The appropriate post-weld heat treatment contributes significantly on join performance (Yan *et al*., 2007) but optimum post-weld heat treatment condition is needed.

2.2 Joining of NiTi and Other Metal

2.2.1 Selection of Joining Process for Joining NiTi with Stainless Steel

Different joining techniques including adhesive, brazing and welding are well known methods for joining dissimilar materials. Limited available information reported the adhesive bonding of NiTi and the use of epoxy as the NiTi adhesive. Some studies stated the requirement of surface pre-treatment to enhance the adhesion between polymer matrix and NiTi (Paine *et al*., 1992; Rossi *et al*., 2008). Both studies focused only on the joining of the same material. In addition, the strength of the adhesive bonding is largely affected by the amount of absorbed moisture. The latter is difficult to control. Resistance welding has been used to join NiTi and was tested in the early SMA development stages (Nishikawa *et al*., 1982; Beyer *et al*., 1989).

Resistance welding is based on the use of electrical current and mechanical pressure to produce a weld between two parts, the method however, to date, has not been fully explored. Another research study used laser brazing to join NiTi and stainless steel, however, the welding process became unsatisfactorily complex, causing the corrosion resistance to become incompatible with the base materials (Li *et al*., 2006). During the brazing process, the base materials failed to melt thus avoiding certain high temperature metallurgical phenomena. However, brazing process consists of high temperature oxidation elemental segregation and grain growth, both of which affect the initial Shape memory properties. The formation of TiO may occur when joining NiTi and stainless steel using the brazing process.

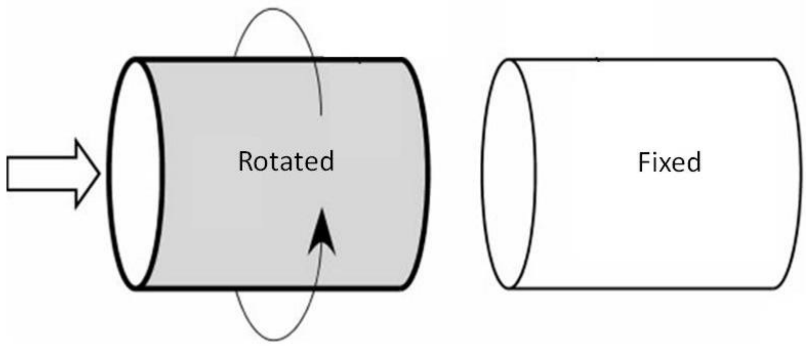

Fig. 2.2 Schematic illustrations of friction welding

Friction welding as shown in Fig. 2.2 was first conducted to weld NiTi in the 1990's (Shinoda *et al*, 1991). Although the NiTi did not melt phase transformation changes in the temperature and loss of strength were found. Fukumoto *et al*. (2010) reported the use of friction welding to join NiTi and stainless steel round bars. A large amount of the brittle Fe_2Ti intermetallic compound was formed at the fusion interface. Friction welding is also suitable for symmetrical geometry (e.g. round bars) only and machining process is needed to remove the upset collar produced after friction welding.

Friction stir welding is a special variant of friction welding (Thomas *et al*, 1991). It consists of a tool with a profile of the threaded/unthreaded pin, which is rotated at a constant speed, to feed into the joint line of two pieces of material, such as NiTi and stainless steel. The welding quality and performance are greatly affected by the tool design and material while the tool wear is a threat against the industrial application of this process. London *et al*. (2005) reported the use of friction stir welding to join NiTi by using polycrystalline cubic boron nitride and tungsten-rhenium tool materials. The result reported a change in the phase transformation temperature after welding, which was similar to the result achieved by arc welding. However, arc welding tends to produce brittle joints possible due to the coarse microstructure and higher thermal stresses and strains left from the welding cycle. Large heat affected zones caused the increase of residual stresses and strains as the larger volume of material expands during heating and contracts during cooling. Qiu *et al*. (2004) reported that NiTi and stainless steel joints welded by the plasma arc welding process resulted in poor joint strength. That poor joint strength was caused by the formation of a brittle weld structure and wide heat affected zone.

Promising welding techniques for joining dissimilar materials have been developed to provide high bond strength and a small heat affected zone due to the shorter interaction time. Laser welding is one of these techniques that transfers much energy to the metal in order to reach a molten state, a cooling state and a solidification state in a very short time. This welding process permits the welding without excessive heating being generated in the remainder of the sheet. Laser welding evolved in automobile, aircraft and aerospace industries. Thus, the preferable welding process would be laser welding which producing narrow welds and less thermal stresses and strains.

2.2.2 Introduction of Laser Welding

Laser welding has two different ways of transferring energy from a laser beam to the welding area: conduction and keyhole modes. A conduction mode welding is characterized by a weld spot cross section in a bowl shape. It has a relatively low penetration depth when compared to the weld diameter. Keyhole mode welding vaporizes the molten material to form a plasma to absorb more energy. The entrance hole remains open to eject the material by the vapor pressure as shown in Fig. 2.3. Its final bead width is usually smaller than in the conduction mode of welding, as the heat is driven deeper into the material. Lee *et al*. (2002) reported that the transition between conduction and keyhole mode of welding is a key aspect of laser welding. The stable melt pools and defect-free welds easily obtained with the conduction weld mode makes it a suitable method for welding thin materials. These are commonly used in the aerospace, automotive and electronic industries as well as in the manufacture of medical devices (Martukanitz, 2005).

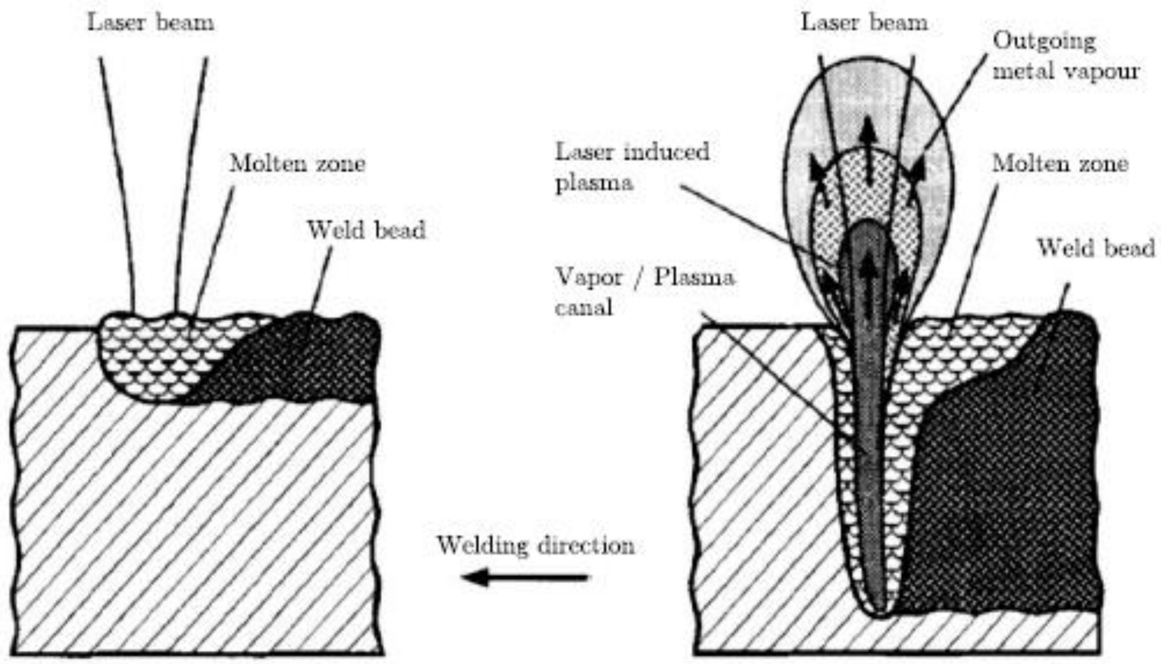

(a) (b)

Fig. 2.3 Principle of laser melting (a) conduction mode, and (b) keyhole mode (Beyer, 1995)

The surface tension of the free liquid surface has a strong effect on liquid motion in the molten pool during laser welding. The energy distribution of the laser beam leading to a higher temperature near the center of the laser spot, a thermal gradient appears at the surface of the molten zone. The surface tension depending on temperature leading to its displacement as shown in Fig. 2.4. If the driving force will lead the center and warmer liquid to flow in the direction to the weld perimeter, this produces a broaden molten area. If a material has a smaller surface tension, it will be pulled toward the higher surface tension material part of the pool. Favez (2009) reported a perfect illustration where the gold is driven to the side of stainless steel and leaded to a huge convection during solidification when welding gold and stainless steel together. In the case of joining NiTi and SS together, similar values of surface tension near their respective melting point cause the NiTi to have the lowest value at the same temperature.

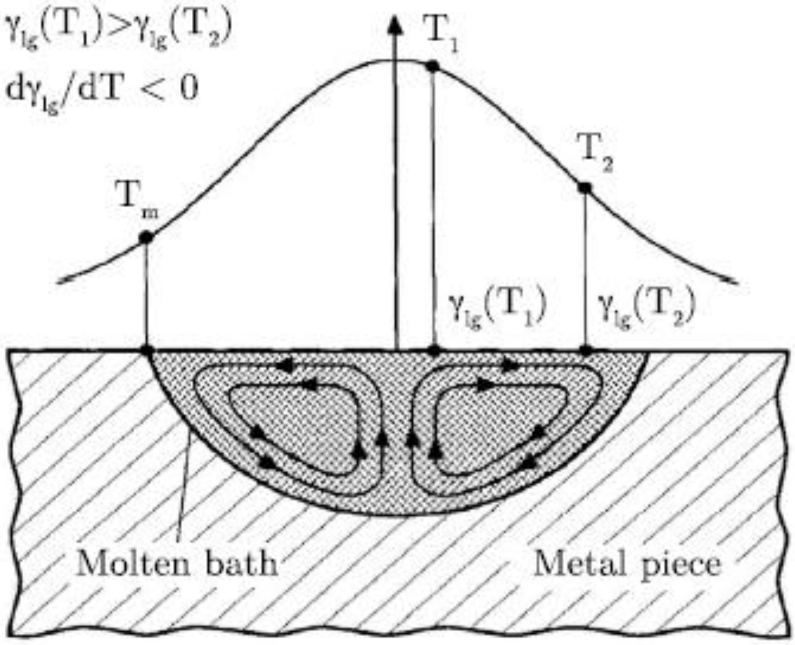

Fig. 2.4 Convection induced by surface tension (Beyer, 1995)

Cooling and solidification occurred when the laser welding is conducted in pulsed mode or when the laser beam moves along the weld pool in continuous mode. Laser welding typically implies very fast solidification speed (Allmen and Blatter, 1995). However, Dantzig and Rappaz (2009) stated that fast solidification rates usually encountered in welding can lead to several non-equilibrium effects such as solute gradient in both solid and liquid, very fine structures.

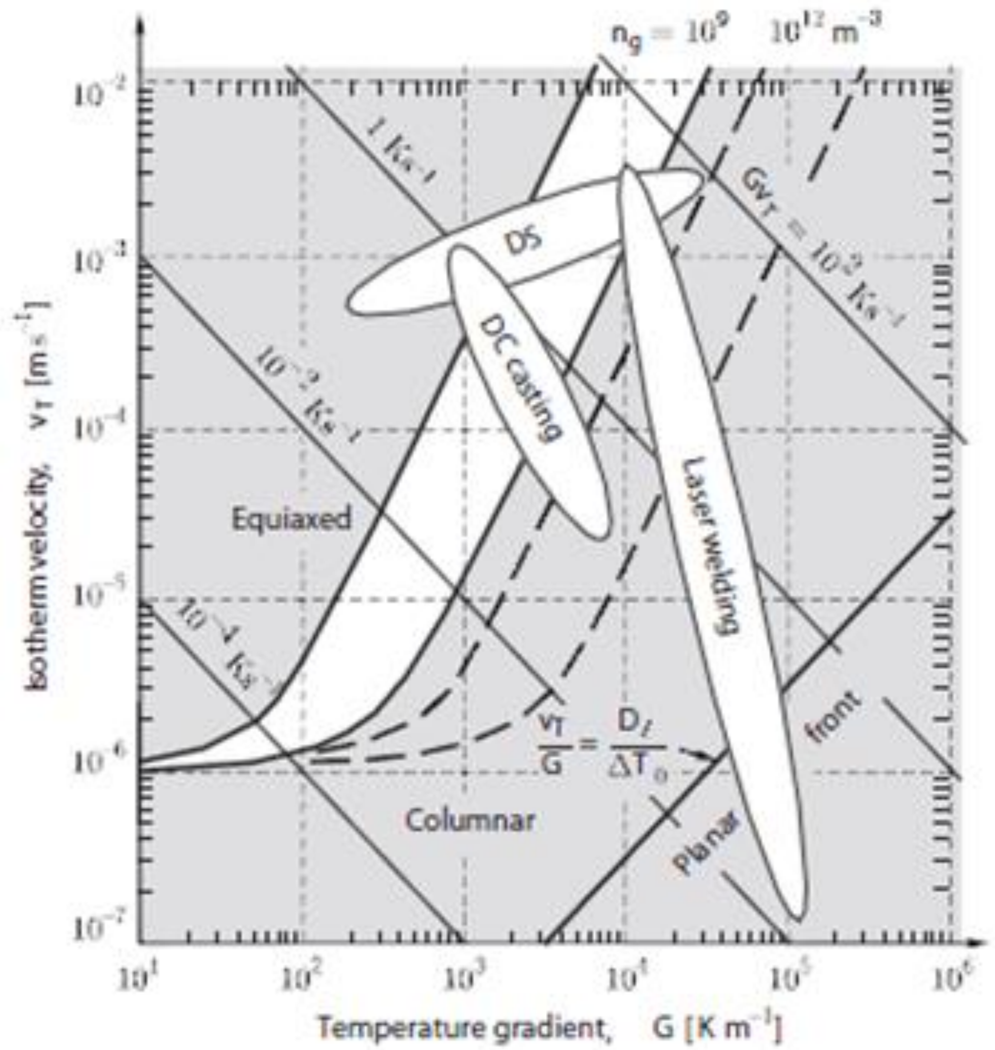

Fig. 2.5 Changes of microstructure on different temperature gradient and isotherm velocity (Dantzig and Rappaz, 2009)

Several factors cause the formation of quite complex microstructures during solidification of multiphase alloys, after welding. Firstly, microsegregation occurs, resulting in a non - uniform distribution of a small amount of the element in the dendrite arms. Secondly, solute elements, trapped in the solidified structure in the short interaction time during solidification leads to composition inhomogeneities and non-equilibrium compositions in the solid phase. Dantzig and Rappaz (2009) reported that laser welding produced almost zero isotherm velocity at the start of solidification and sharply increased to a high value at the end of the solidification.

Such changes caused the transition of microstructure. The change of cooling conditions along the weld pool causes the isotherm speed to increase rapidly as solidification starts, and may lead to different microstructures being formed as shown in Fig. 2.5.

2.2.2.1 Applications of Laser in Welding NiTi

The laser power delivery method has two modes: continuous wave (CW) mode and pulsed wave (PW) mode. Different results can be obtained between these two delivery methods. In the CW laser welding process, high energy density could be achieved by adjusting the laser power and the welding speed. A high welding speed can be achieved by operating with a high laser power especially for a laser system with high energy density (Quintino *et al*., 2007). The pulsed laser welding is characterised by the application of intermittent laser beam powers. The latter would cause melting and solidification at the same time during the welding process by adjusting the pulse duration (Ghaini *et al*., 2007). Due to the benefit of precisely controlling the heating and cooling rates, the pulsed laser welding is commonly used in welding heat-sensitive materials, where a precise heat input are required with low welding speed (Berretta *et al*., 2007). Laser power and welding speed including its depth and width are the main parameters which affect the weld geometry. A weld with drop out is usually produced at a slower welding speed while an undercut weld can be produced when welding speed is higher. NiTi has been successfully welded using pulsed laser technique (Gugel *et al*., 2008; Sevilla *et al*., 2008) and continuous laser welding was also used to join NiTi (Hirose *et al*., 1990; Hsu *et al*., 2001). Sun and Ion (1995) reviewed the laser welding on joining different materials together and reported that joining of Ti and Fe alloys together was possible. Many researchers extensively studied the use of laser welding on NiTi and concluded that laser parameters influenced the microstructure of the fusion zone (Uenishi *et al*., 2002). Hsu *et al.* (2001) also stated that satisfactory performance in both shape memory character and corrosion properties, when immersed in 1.5M H_2SO_4 and 1.5M HNO_3 solutions could be obtained by CO_2 laser welding process. The inhomogeneous of weld metal after welding however, indicated an increase of stress needed to from stress-induced martensite and residual strain.

2.2.2.2 Types of Laser in NiTi Welding Application

Table 2.1 Summary of process parameters used for laser welding (Nd:YAG)

Material	**Thickness**	**Laser type**	**Spot diameter**	**Welding rate**	**Average power**	**Reference**
Ni -51%Ti Ni-51%Ti	1 mm	Continuous laser	0.6mm	1.6 m/min	850W	Falvo*et al.* (2008)
SUS 304L Ti	0.4mm 0.3mm	Continuous laser	0.6 & 1.0 mm	2.5, 10mm/s	600W	Hiraga *et al.* (2002)
SUS 304 NiTi	0.48mm 0.48mm	Pulsed laser	0.3mm	10 m/s	Not mentioned in the paper	Li (2013)
SUS 304L NiTi	0.36mm 0.36mm	Pulsed laser	0.8mm	3 m/s	1000W	Mirshekari (2013)

Both CO_2 and Nd:YAG lasers have been used to join NiTi. Although both lasers can weld NiTi, CO_2 laser welded joints produce more significant effects of mechanical resistance and functional properties while Nd:YAG laser welded joints maintain good functional properties and tensile strength (Luisa and Rosa, 2012). Padmanaban (2010) reported the YAG laser could produce precise and low heat input. It is more effective for micro welding to produce joints with low residual stress, weld distortion and residual stress with high welding speed. Uenishi *et al*. (2002) reported a satisfactory welding of stainless steel and NiTi wires together and

Gugel *et al*. (2008) reported faultless joints between stainless steel and NiTi by Nd:YAG laser welding was achieved. The process parameters used by other researchers as shown in Table 2.1 act as the reference point of this research project.

2.2.2.3 Advancement of Laser and Comparison of Different Lasers in Welding Application

The advances now being made in optical fiber fabrication enable making both fiber for laser resonators and fiber for laser delivery. Fiber laser modes are fast becoming an alternative to many other laser sources such as pulsed lamp pumped Nd:YAG lasers for micro application, and CO_2 laser in many industrial applications. Fiber lasers have been receiving more attention due to their unique advantages of such high beam quality, high power and high efficiency to produce deep penetration welds at high welding speeds (Krishen, 2008). Another important issue will be in the manufacturing industry. By increasing welding speed, the high-power fiber laser may eventually be an investment with low maintenance and operating costs (P'ng and Molian, 2008).

Fiber laser is a laser that is constructed within an optical fiber and is similar in concept to gas lasers and laser diodes. The fiber laser is excited by a diode laser source as a pump, and mirrors aspect: the pump wavelength on one side and the transmittance of the excited wavelength on the other. These lasers, with diffraction limited beam quality offer many futures such as high power density, small spot size, enhances processing speeds and reduced heat affected zones for both cutting and welding applications. The fiber laser has key advantages and receives more attention over other laser technologies such as a unique combination of high energy, beam quality and laser power stability, given a greater breadth of control with. As well as its low total ownership cost, fiber lasers have the ability to produce deep penetration at high welding speeds (Ujjwal, 2017).

The fiber laser is a solid-state laser in which the active gain medium is an optical fiber, doped with rare earth elements such as dysprosium, erbium, neodymium, praseodymium, thulium and ytterbium. Its ability to deliver the laser beam to any area of application and the high quality of the beam mean that it can be focused on a very small dot. Lasers at around 1 Watt of power eventually can harm skin. This is not very much power compared to a small electrical appliances, but fiber lasers are continually becoming more powerful, and have been made with over 1kW of power. This powerful tool, which has a huge variety of different applications is being exploited in a range of applications from imaging molecules to high precision cutting and welding of metals (Quintino *et al*., 2007).

The fiber laser uses the same physics principles as any other laser. However and of important interest is that here are a number of properties that make it special and extremely useful. The most common type of fiber laser is the erbium-doped fiber laser. It is normally operated in Nd-doped glass fiber (doped core), the main element of the fiber laser with a double clad fiber (pump core) and an outer cladding. The fiber is transversely pumped by around a flashlamp and the high beam quality enables the beam to be focused to a small spot with a correspondingly high energy density. The active medium of a fiber is a core of the fiber doped with a rare element.

There are two types of fiber lasers; single mode fiber laser and multi mode fiber laser. Today, the fiber laser of current interest is the erbium-doped fiber amplifier. 1.53 µm is the operating wavelength and for communication wavelength is 1.55 µm, where there are the lowest transmission losses. Single mode fiber lasers are currently available with beam powers up to around 1kW with the wavelength of typically 1070 nm. The power of the multi mode fiber laser is more than 17 kW and the efficiency of both fiber lasers (up to 30%) greatly exceeds the efficiency nowadays achievable with other types of lasers such as lap- or diode-pumped Nd:YAG lasers. The unique characteristics of the fiber laser such as beam quality, focal spot, and high energy density, energy density (E) can be calculated from the following equation:

$$E = \frac{P}{VD}$$

Where P is Laser Power, V is traverse velocity (ms^{-1}) and D is bean diameter (m). The fiber laser produces deep penetration welds with low laser power. Compared with other type of laser, significantly lower heat input can be generated by the fiber laser to produce welds with less distortion. Besides, consistent penetration and profile with extremely low amounts of porosity is given by the high energy stability in the fiber laser. The fiber laser offers a solution that welds faster with higher quality at a lower operational running cost (Kell *et al*., 2006).

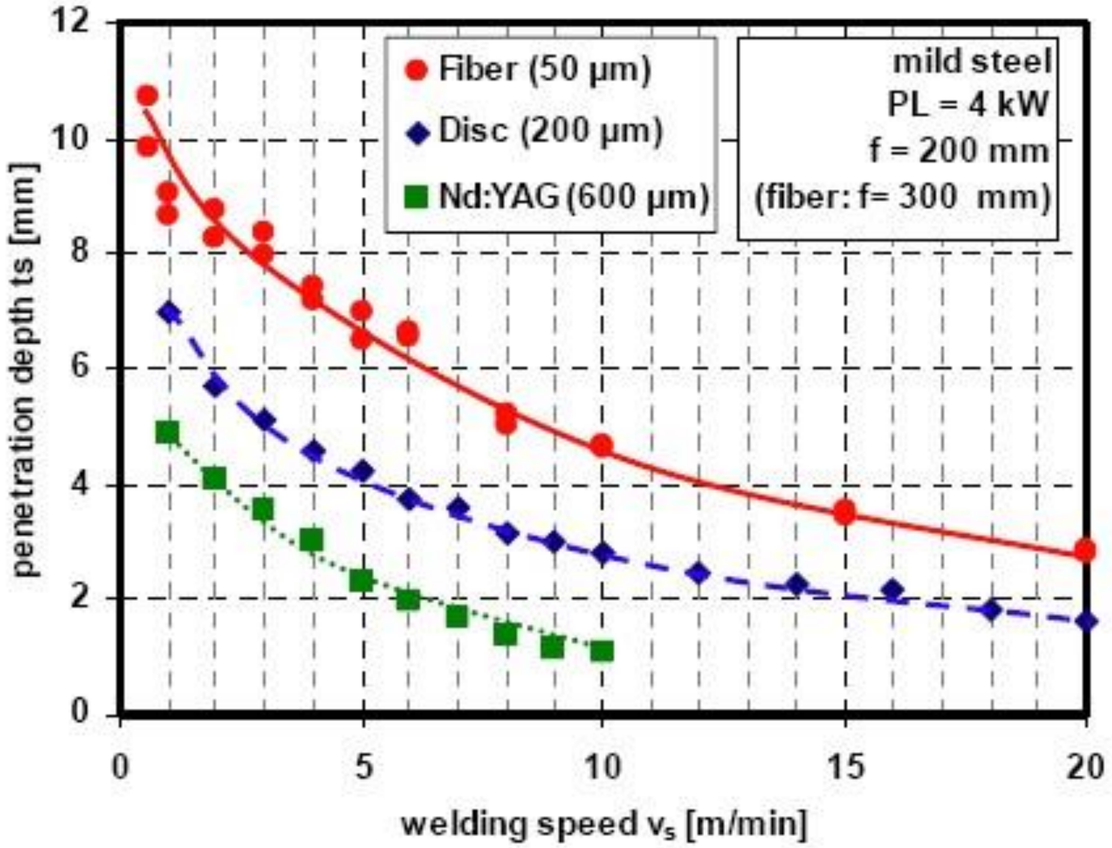

Fig. 2.6 Comparison between three different sources of lasers (Gobel *et al*., 2007)

Gobel *et al.* (2007) compared weld penetration in mild steel materials between different laser sources with different fiber core diameters to see the weld penetration depth as illustrated on Fig. 2.6. The comparison was between fiber laser (50 µm), disc laser (200 µm), and Nd:YAG (600 µm).

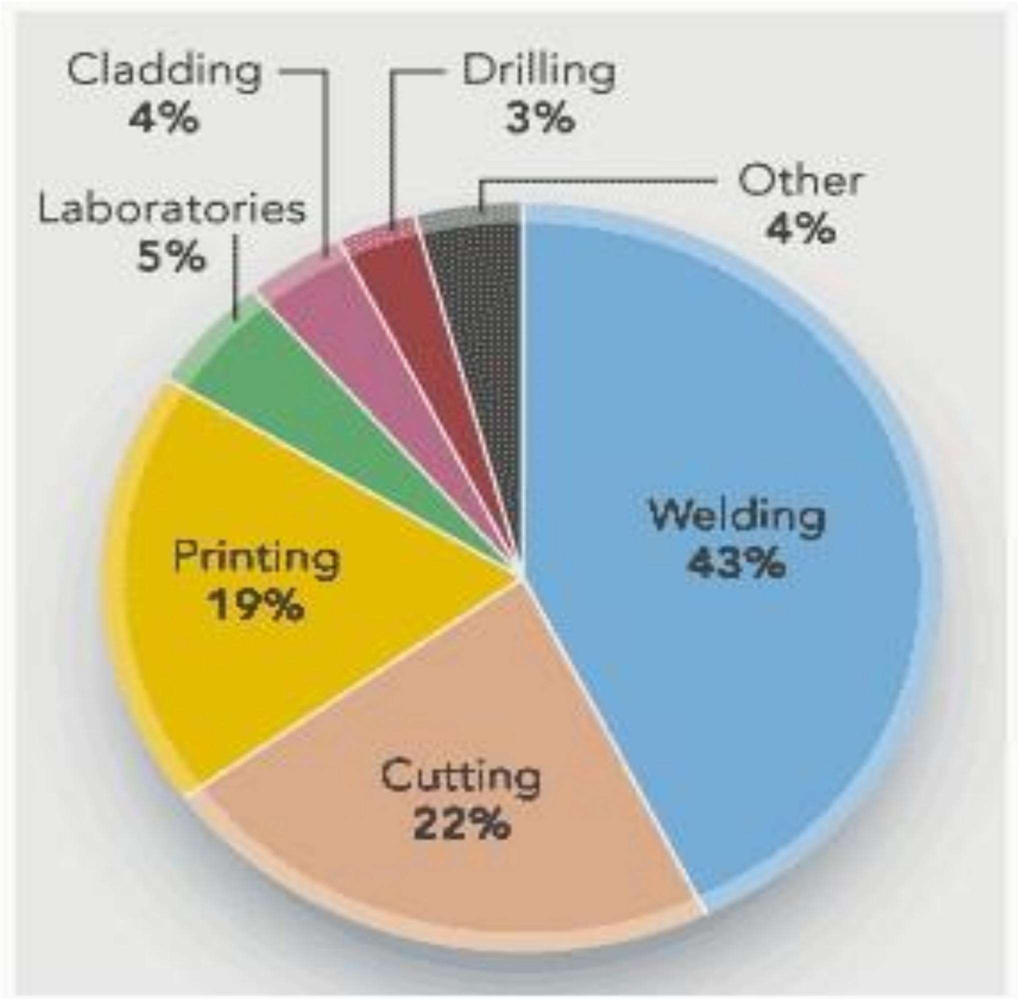

Fig. 2.7 A summary of IPG Photonics high-power laser sales by application (Zhu *et al*., 2005)

The resulting smaller spot size on the work piece is not the only reason for the deeper penetration. The divergence of the focused beam must also be considered. Rudolf (2006) concluded that the laser source will become smaller, there will be increase in power of diode laser and the replacement of solid-state lasers will be produced by a diode pump fiber laser.

It has also been suggested that the application spectrum will extend to create the laser as a universal tool.

There are less operation consumables for the fiber laser compared with other laser sources such as CO_2 lasers which need a supply of consumable gases or Nd:YAG lasers that require a periodic flash lamp change. In addition, the fiber laser enables ten times more efficient in electricity than the power consumption of Nd:YAG to achieve a significantly lower running costs. Some other laser sources require more energy consumption to warm-up the system and also fiber lasers can be used for welding after operating. IPG Photonics, a leading global manufacturer of fiber lasers and amplifiers in numerous markets, reported a rapid technology growth opportunity for materials to be processed with fiber lasers. The opportunities are substantial. Fig. 2.7 shows the application segmentation of fiber lasers shipped by IPG Photonics (Zhu *et al*., 2005).

Zhu *et al.* (2005) studied and investigated the process characteristic and mechanisms involved in CO_2 laser and the diode laser welding of AZ31 alloy. They concluded from their studies that the 8000 W/cm^2 achieve a full penetration using CO_2 laser at welding speed of 150 mm/s or using diode laser at welding speed of 50 mm/s, while 1 mm thick AZ31 sheet welding is quite low. They found that the spot size of the diode laser is limited to conduction welding during defocusing, while good quality keyhole produced by CO_2 laser. They also concluded that the CO_2 laser produces more porosity in comparison with a diode laser. Montgomery *et al*. (2007) have also replicated a comparable form of mechanisms and effects of Nd:YAG and CO_2 laser cleaning of titanium alloy. Triantafyllidis *et al*. (2003) reported that the high power diode laser welded 0.2 mm diameter thermocouples performed better than the Nd:YAG laser welded thermocouple at high temperatures (above 150C°). They added that high power diode laser welded thermocouples had a much faster response time (35% faster) than the Nd:YAG laser welded ones (17% faster). High quality welds better improved the performance of high power diode lasers. Vollertsen and Thomy (2005) compared various lasers such as lamp-pumped, solid-state Nd: YAG laser and of the diode-pumped solid-state Nd:YAG laser in AlSiMgMn (as shown in Fig. 2.8) to construct the relationship curve between welding speed and penetration depth to fully determine the penetration depth of quality.

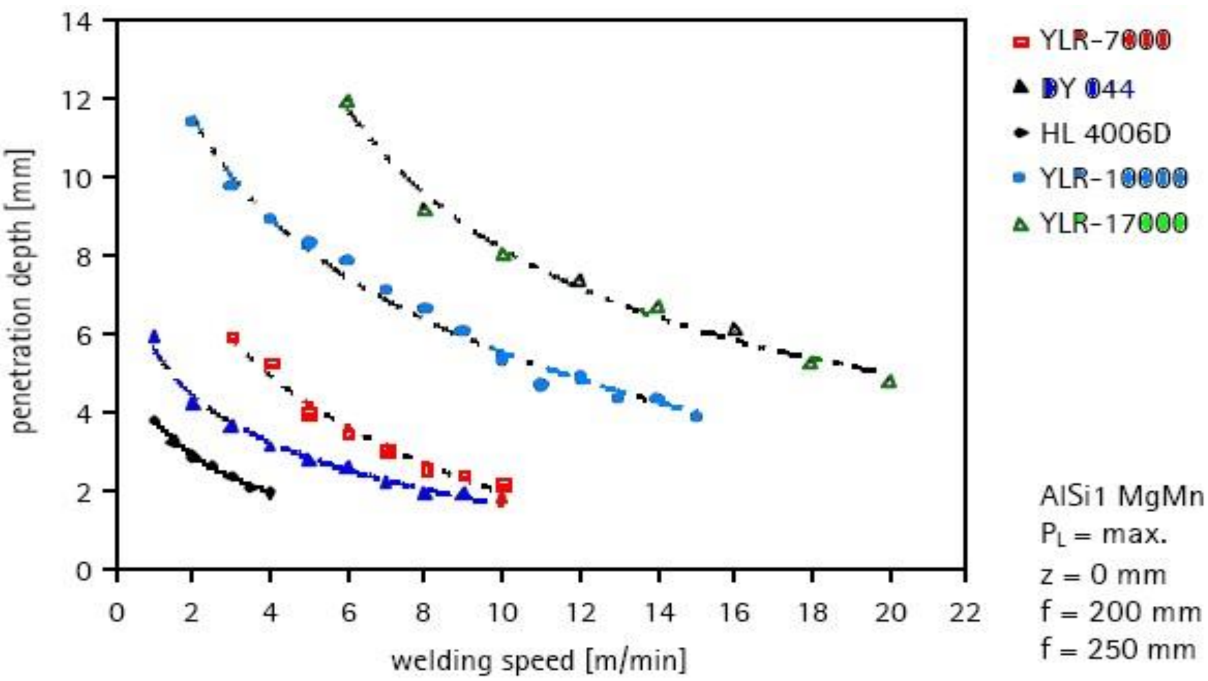

Fig. 2.8 Schematic comparison of penetration for various lasers (Vollertsen and Thomy, 2005)

Tsukamoto (2003) made a comparison between four types of lasers to find the laser characteristics and application as regards welding. The main characteristics are illustrated as regards the interaction with the material, beam quality, oscillator and head size, oscillation efficiency, fiber transmission capability and equipment cost are illustrated in Table 2.2.

It is evident that the fiber lasers, particularly improved beam properties with high power, will become increasingly important in materials processing and their share of the total laser industry will grow substantially (Quintino *et al.*, 2007). The new generation of the high power fiber laser present numerous benefits for industrial purposes, specifically high power with low beam divergence, high efficiency, low maintenance cost and flexible beam delivery (Canning, 2006). Fiber laser was primarily chosen for welding NiTi (Chan *et al*., 2012) due to the above mentioned benefits. Therefore, fiber laser would be the preferable laser welding processing in this study to examine the joining of NiTi and stainless steel.

Table 2.2 between CO_2, YAG-Lamp, YAG - Diode, and Diode Lasers for characteristics and applications (Tsukamoto, 2003)

Characteristics of laser	CO2 Laser	Lamp-pumped YAG	Diode-pumped YAG	Diode
Wavelength (µm)	10.6	1.06	1.06	0.8-0.94
Oscillation efficiency (%)	8-15	1-4	8-15	30-50
Maximum power (kW)	50	10	12	6
Cost per kW (CO_2 = 1)	1	1.4	1.7	≤ 1
Advantages	Easy high power up rating	Fiber transmission capability	Fiber transmission capability high efficiency	High efficiency low cost fiber transmission capability small size
Disadvantages	No fiber transmission capability high plasma absorption	Low efficiency	High cost	Poor beam quality

2.2.3 Consideration of Laser Welding Process for Welding NiTi and Stainless Steel

In comparison with other fusion welding technologies, laser welding is a very promising process as it allows the control of cooling rate and thermal gradient by adjustable energy density and distribution. A better mechanical and metallurgical properties can be obtained due to its high energy density and the high welding speed (Steen, 2003). Shallower molten pool, shorter interaction time and quicker solidification speed can be achieved by the increase of laser power density and the travelling speed of the laser beam. In addition, the phase fractions in the weld pool could be adapted by controlling the position of the laser beam with respect to the weld line (Favez, 2009).

Laser welding can be considered as a metallurgical process and the weld quality is strongly affected by thermal, physical, chemical and mechanical properties of the welding materials (Arthur, 1968). The microstructures in the weld can also be influenced by microsegregation and non-equilibrium phase transformations that occur during solidification. Due to the rapid heating and cooling rates, less microsegregation is expected to occur in laser welding than is induced during other fusion welding methods. The non-equilibrium phase transformation can cause intermetallic brittle phases in the weld.

In laser welding, the peak temperature of the fusion zone (FZ) is usually higher than the melting point of the welding materials. If the welding materials temperature reaches boiling point, the loss of alloy elements occurs leading to variations of mechanical properties and the microstructure of the weld. As the fusion zone will undergo a transformation from the liquid phase to the solid phase, the size and shape of grains and the distribution of inclusions and defects (such as porosity) are then controlled by the solidification rate. The temperature in the heat affected zone (HAZ) is lower than the melting point of materials in laser welding. Although melting cannot occur in the heat affected zone, the heat is sufficient to cause phase transformations. The thermal cycle and temperature gradient in the heat affected zone can influence the phase transformation degree, grain growth, microstructure, composition gradients and residual stresses. A rapid cooling rate can produce finer microstructures, limit grain growth and cause non-equilibrium phases in the weld (Sun and Ion, 1995).

The thermal cycle is composed of rapid heating and cooling phases in laser welding. Metallurgical effects in the fusion zone and heat affected zone are associated with the peak temperature of the melt pool, heating rate and cooling rate in the weld. In addition, the thermal cycle can be affected by the heat transfer and the fluid flow in the melt pool resulting in variations of the temperature gradient, the cooling rate and microstructures in the weld (Ye and Chen, 2002). During the process of solidification, the cooling rate is relatively slower because most the heat is transferred by means of conduction. In laser welding, the heating and cooling phases almost exist consistently (Han *et al*., 2007). For this reason, a weld with the smaller heat affected zone and the larger thermal gradient is expected to be produced in laser welding.

2.2.4 Importance of Laser Welding Process Parameters

Laser welding process parameters also play an important role in determining the optimum quality of the weld zone. Jyotsna, and Indranil (2013) stated that laser welding process parameters include power, speed, defocusing distance and type of shielding gas should be selected based on the thickness of the base metal to produce a complete penetration, minimum size of fusion zone, and acceptable weld profile.

There are huge numbers of laser welding parameters to be considered when performing any welding application. The parameters include laser type, laser power, and laser welding speed, focus position, shielding gas and gas flow rate. The optimization of these parameters is critical to a good quality weld (Chen *et al*., 2008). A critical welding input parameter is the laser beam power followed by welding speed. These parameters significantly influence the resulting weld. Too low power will cause lack of penetration or too high power will cause a drop through of the weld (Balasubramanian *et al*., 2008). The effect of welding speed is clearer in performing continuous butt welds for CO_2 lasers which are operated in the continuous wave mode than for pulsed Nd: YAG lasers. On the other hand pulse frequency and the percentage overlap of each spot might be affected by welding speed. As the thickness increase the penetration depth of the welding decrease as shown in Fig. 2.9. Also by increasing the speed the exposure time for the materials to the laser beam, reduced resulting in reduced absorption of the heat (Dahotre and Harimkar, 2008). Determination of the bead width and the penetration depth as a function of both the incident the welding speed and the laser power, and the effect of the welding speed on the penetration depth is illustrated in Fig. 2.10.

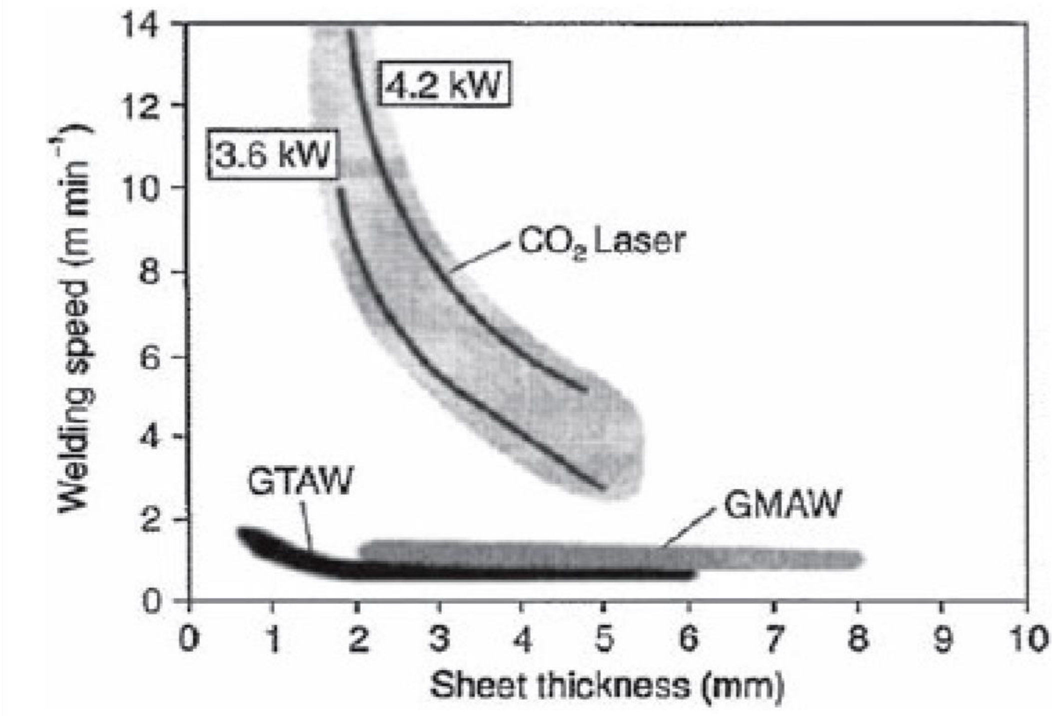

Fig. 2.9 Change of welding speed with respect to sheet thickness (Dahorre and Harimkar, 2008)

To prevent oxidation of the weld surface, shielding gas is normally used. Sibillano (2006) have studied the effect of gas flow rate during welding aluminium alloy using CO_2 laser. It was found that high flow rate created a narrower and deeper keyhole. Kim (1991) investigated the effect of Argon gas flow rate during the welding of AISI316 stainless steel and low carbon steel. They reported that when the flow rate goes to minimum (less than 10 L/min), the penetration depth was reduced and the bead width was increased. It suggested that the low flow rate did not remove the plasma which absorbed the laser power. By increasing the flow rate to 10-30 L/min, a sound bead and deep penetration was achieved. It was also noticed that the increase in the gas pressure caused porosity (Salminen and Fellman, 2007).

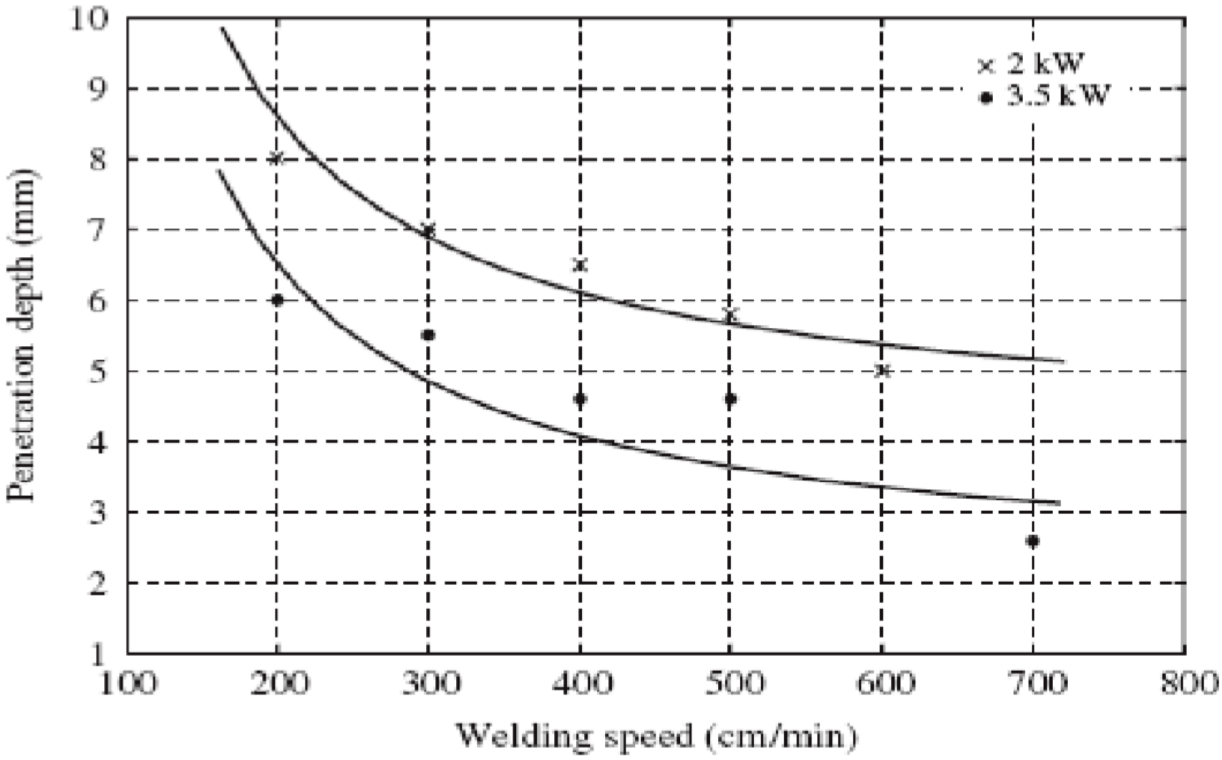

Fig. 2.10 Change of penetration depth with respect to welding speed (Abderrazak *et al.*, 2008)

Good performance of welding depends on the selection of optimum parameters. Typically, the penetration decreases if the laser beam diameter on the surface is too small, and if the focal point in not on the surface to form the keyhole welding. Optimum focusing conditions are very important issues which have a large effect on welding parameters. In welding, focusing the laser beam at the surface of the weld piece is needed to ensure good results. The focus position has a big effect on the weld quality in fiber laser welding (Fellman, 2007).

Most common welding defects include porosity, cracking, residual stress and spatter. Optimum welding parameters can be selected to minimize the welding defects. Porosity is one of the most common defects in welding and is typically caused by shielding gas entrapment before weld solidification. Porosities appear due to various sources in laser welds due to the influence of shielding gas on penetration. Bubbles are normally generated from the keyhole tip and moved along the melt flow inside the molten pool. The bubbles are trapped whilst floating up, resulting in the formation of porosity. Using an SEM test to observe the results of a fractured surface, it was demonstrated that evaporated materials injected in the bubble formed oxides. Various locations of the weld may be characterized by distinct morphologies and distributions. Minor porosity can happen due to trapping of gas bubble during solidification.

Cracking is one of the most serious laser welding defects. Most of the cracks in the welds begin from the restrictions to the free contractions of the material during the cooling cycle. Such restrictions result in the setting up of high tensile stresses causing cracking. Hot cracking problem depends upon cooling rates and polluting elements in weld material. Hot cracking in the weld can be either liquation cracking or solidification cracking. Solidification cracking is cracking in the fusion zone which occurs during solidification. Cracking may be caused due to the differences in strain between weld and materials, or are due to large differences in heating and cooling system. Sometimes heat treatment minimizes the cracking. Wide-ranging studies have been conducted to recognize the mechanism of solidification cracking during laser welding and the effects of the various parameters on the receptiveness to cracking. In one study it was concluded that reducing the speed from 1520 mm/min to 510 mm/min was the main factor for reducing the cracking behaviour by 61% (Dahotre and Harimkar, 2008).

2.3 Difficulties in Joining NiTi and Stainless Steel

2.3.1 Possible Growth of Phases in Welding NiTi and Stainless Steel

Stainless steel being an iron-based metal has at least 12% Cr, hence enabling a passive film. Stainless steel grade 304 (SS304) in most environments is excellent and has a low temperature ductility. Its strain is 40-60% and its yield strength is 200 to 275 MPa. When joining NiTi and stainless steel, the presence of chromium in stainless steel is neglected as it has little impact on the weld composition and compound formation. The Fe-Ni-Ti ternary phase diagram (Cacciamani *et al*., 2006) illustrates a powerful tool to enable the understanding of microstructures of the nominal alloy concentration of each of the three elements. The above has been widely investigated to gather the information of its phase diagram. Chromium can be assimilated with titanium in the quantification process as it has a similar formation, since it is a BCC-stabilizer, compatible with titanium, for iron base alloys (Yen *et al*., 2008).

A phase diagram with N_C elements requires (N_C - 1) + 2 dimensions. In a multicomponent system, the quantity of freedom degrees (N_F) is given by the Gibbs' phase rule. The diffusion path theory is governed by this rule.

$$N_F = N_\varphi - N_C + 2$$

where N_φ is the number of co-existing phases.

The ternary phase diagram (N_C = 3) has three phases (N_ϕ = 3). Two of which N_F are temperature and pressure. Nonetheless, the temperature of the three phases are stable as the pressure is usually fixed.

Kirkaldy ad Brown (1963) established and showed the diffusion behavior basis in multiphase diagrams, the virtual path, the objective of which was to enable the prediction of diffusion paths based on the thermodynamic minimization entropy. Clark (1963) defined conventions to represent ternary diffusion paths and predictions for microstructures at the equilibrium state. This work represented diffusion paths, based on the microstructures of diffusion couples as shown in Fig. 2.11.

As ternary phase diagrams are difficult to represent by using two dimensions ternary phase diagrams are composed of isothermal cuts at selected temperatures and represent equilateral triangle with pure elements at its corners. Dashed lines and arrows of the monovarient lines (as shown in Fig. 2.12) indicates the composition path followed by the liquid among solidification binary crystallization curve (Dantzig and Rappaz, 2009). The isothermal cuts enable the determination of the nucleation and growth of that phase, when different concentrations during the NiTi and stainless steel joining are dealt with. The isothermal cuts, however, are valid only for equilibrium at fixed temperatures.

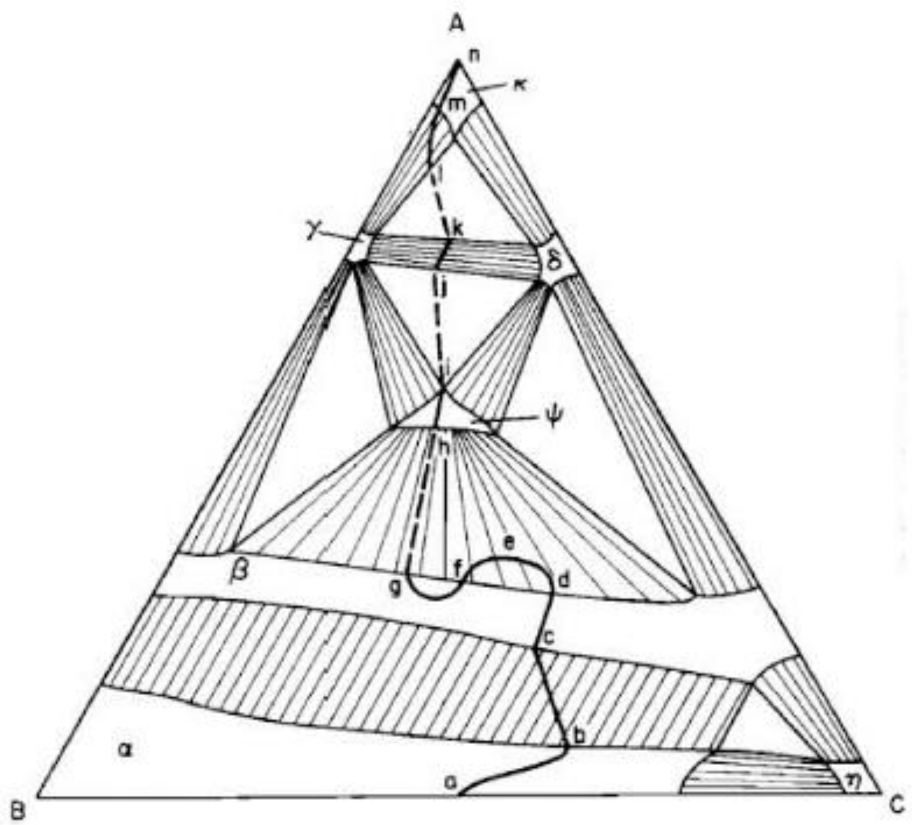

Fig. 2.11 Diffusion paths on the corresponding isothermal cut (Clark, 1963)

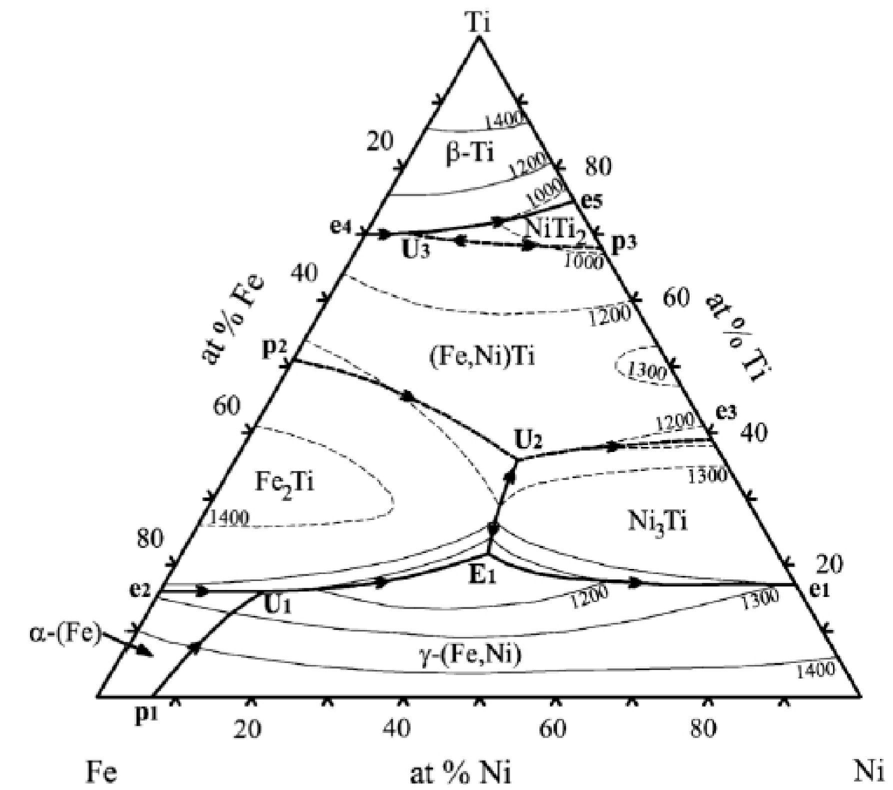

Fig. 2.12 Liquidus projection (Cacciamani *et al*., 2006)

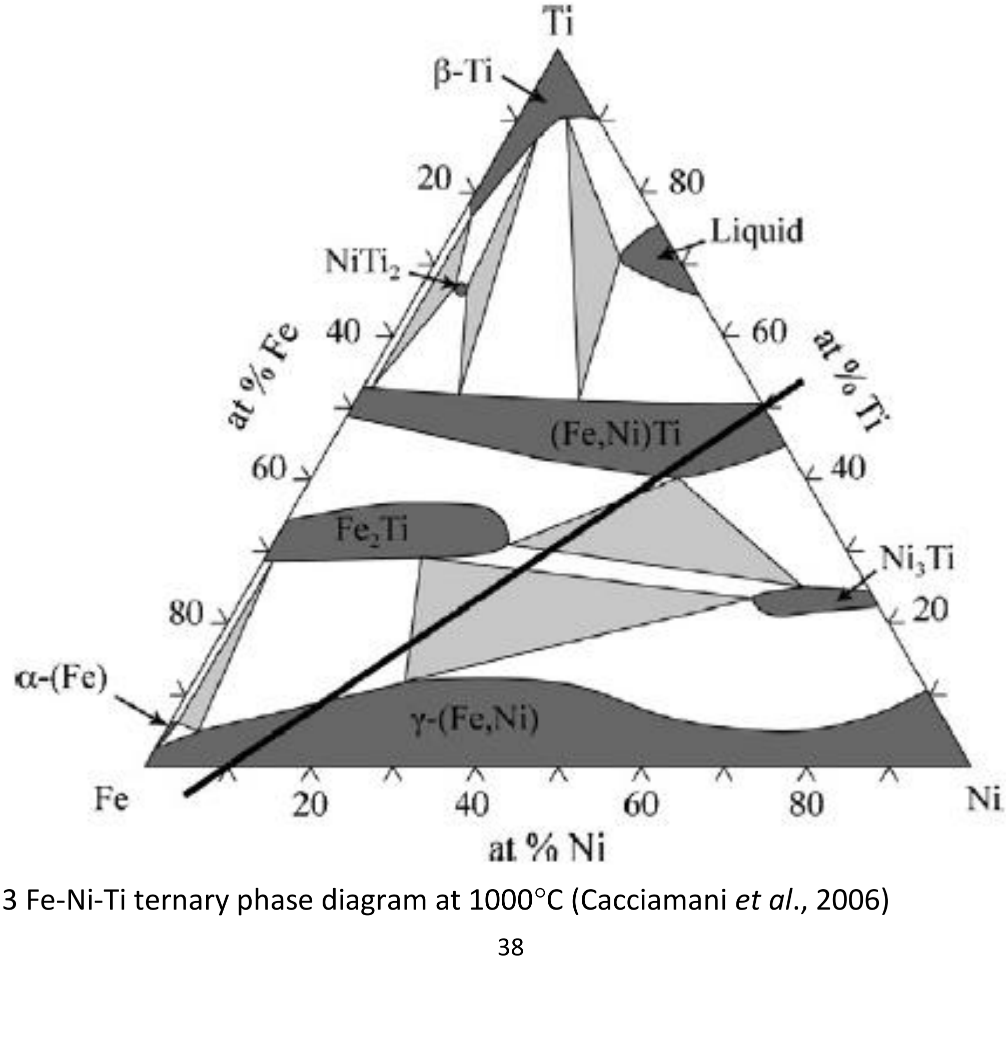

Fig. 2.13 Fe-Ni-Ti ternary phase diagram at 1000°C (Cacciamani *et al*., 2006)

Fig. 2.13 shows that Fe_2Ti and Ni_3Ti can form when welding NiTi and stainless steel. Intermetallic compounds, Fe_2Ti, known to be highly brittle (Uenishi*et al.*, 2002). The formation of brittle intermetallic compounds is a common welding issue containing steel. (Favez *et al.*, 2008). Wang (1997) identified TiFe and $TiFe_2$ as a common problem, which is encountered during either direct fusion welding or solid-state diffusion process (Hinotani, 1990) for joining NiTi and stainless steel.

2.3.2 Problem Encountered in Joining NiTi and Stainless Steel

The joining method consists mainly of soft soldering, brazing and welding. Various welding processes such as transient liquid phase diffusion bonding (Wang, 2008), friction welding (Fulumoto, 2010), brazing (Seki, 2000), micro-beam plasma-arc welding (Qiu, 2004), capacitor discharge welding (Li, 2005), and laser welding (Hall, 2004; Li, 2012; Gugel, 2008), have been widely employed in the investigation of joining NiTi. All these processes involve the melting of materials and hence the introduction of a heat affected zone is obvious during the joining procedure. The welding process involves the melting of the base materials. Although, welding is a promising technique as regard the joining of metal such as direct joining of dissimilar materials is likely to produce irregularities. Examples include damage to the materials themselves because of the material composition change and subsequent formation of intermetallic phases, as the latter are often brittle. Hence, the resulting joints are fragile and have little to no ductility. The difference in mechanical properties of the base materials is caused by the formation of different proportions of intermetallic compounds and crystal structures. Thus, one of the most important challenges when welding dissimilar metals, the formation of intermetallic compounds is one of the greatest.

Because of the specific ratios of the intermetallic forms, it is possible to identify the presence of undesirable phases after joints have been executed. Because of the large Burgers' vectors, the crystal structures of the intermetallic compounds, fracture more easily, as less energy is required for this process. Hence, this disappointing challenge is subject to low crack tolerance (Brandal *et al.*, 2013). The intermetallic compounds such as the Fe_2Ti Laves phase crystal structure, are subject to brittle fracture (Brandal *et al.*, 2013). FeTi is another phase, which can decrease the tensile strength of the joint, formed after welding (Satoh and Yao, 2011), particularly when FeTi regions are sufficiently large. A further research study reported that the difference in the thermal expansion coefficients between NiTi and stainless steel could result in residual stresses and initial cracks in the brittle intermetallic compound regions (Casper *et al.*, 2003). Hence, joining NiTi and stainless steel is a difficult welding process due to the large difference in physical and chemical properties.

2.4 Ways of Minimize Undesirable Intermetallic Compounds in Welding

Intermetallic phases are expected to form in the vast majority of dissimilar metal joining processes where the two base materials are allowed to mix. The formation of brittle intermetallic layers on dissimilar metal fusion interfaces results in reduced joint strength and ductility, greatly reducing the durability of the joined assemblies. Intermetallic compounds often have severely limited homogeneity ranges such as Ni_3Ti, Fe_2Ti. The result of this highly ordered structure is the lack of mobility of the atoms, and long Burgers vectors for slip, especially for those crystals with highly complex structures. These results in minimal deformation accommodated through processes such as creep and plasticity (Satoh, 2013). While the localized inelastic deformation is often observed locally around a crack, the overall ductility is low and intermetallic compound are often called "quasi-brittle" materials. This results in fracture of intermetallic compound through trans-granular cleavage or inter-granular cracking at low temperatures.

To prevent the extensive formation of undesirable intermetallic compounds mentioned above, and which have joint brittleness, it has been found that the amount of intermetallic compounds formed during the joining of steel and aluminium is lowered when a heat sink is placed next to the welded joint (Borrisutthekul *et al*., 2007). Therefore, it is possible that controlling the melting of the base materials period, which when at their melting temperature will help to lessen the formation of undesirable intermetallic compounds. It also should be noted, regarding the above, that if the welded joint over-melts, the austenitic NiTi phase may react by substituting Ni with Fe. Hence this reaction, is likely to lower the martensitic start temperature (M_s) and enable the formation of an R phase, hence leading to the occurrence of a high stress super-elastic plateau (Fernandes *et al*., 2011). When welding NiTi and stainless steel together, a phase change not only occurs in the welded joint, but also in the heat affected zone of the base materials. Researchers have reported that the Ms temperature decreases when the amount of precipitates increase in NiTi (Benat, 2007). Tuissi *et al*. (1999) reported that the chemical composition strongly affected the NiTi martensitic transformation. Therefore, it is necessary to minimize the amount of intermetallic compounds formed and also the region of heat affected zone to increase the strength of the welded joint between NiTi and stainless steel (Brandal *et al*., 2013).

Joining of NiTi and stainless steel together will give complex diffusion across the joint with significant reaction layer formation. The use of interlayer has been used to avoid the formation of brittle intermetallic phases (Wang, 1997) while Mietrach (1987) claimed that successive interlayer avoided the formation of brittle phase on the joining of titanium alloys to ferrous. The excessive diffusion and thermal strains due to mismatch in thermal expansion may be prevented and accommodated by the use of proper ductile interlayer. Of interest is the result of a research study, which reported that an interface between NiTi and stainless steel may help to limit the amount of brittle intermetallic features from forming (Brandal *et al.*, 2013). As a result, the use of filler/interlayer is necessary to prevent or reduce the formation of the above undesirable compounds given above.

2.4.1 Research Study of Different Interlayer for Welding NiTi with Stainless Steel

In order to improve the brittle intermetallic compounds, many researchers produced joints by using various alloys as the filler (Li, 2007; Lee, 2010). Unfortunately, most joints exhibited low strength with fracture due to the presence of brittle intermetallic compounds which were difficult to remove. A feasible way to improve the brittleness of the joint could be a proper filler/interlayer material that is highly soluble with the base materials in order to realize a joint with minimum detrimental brittle phases.

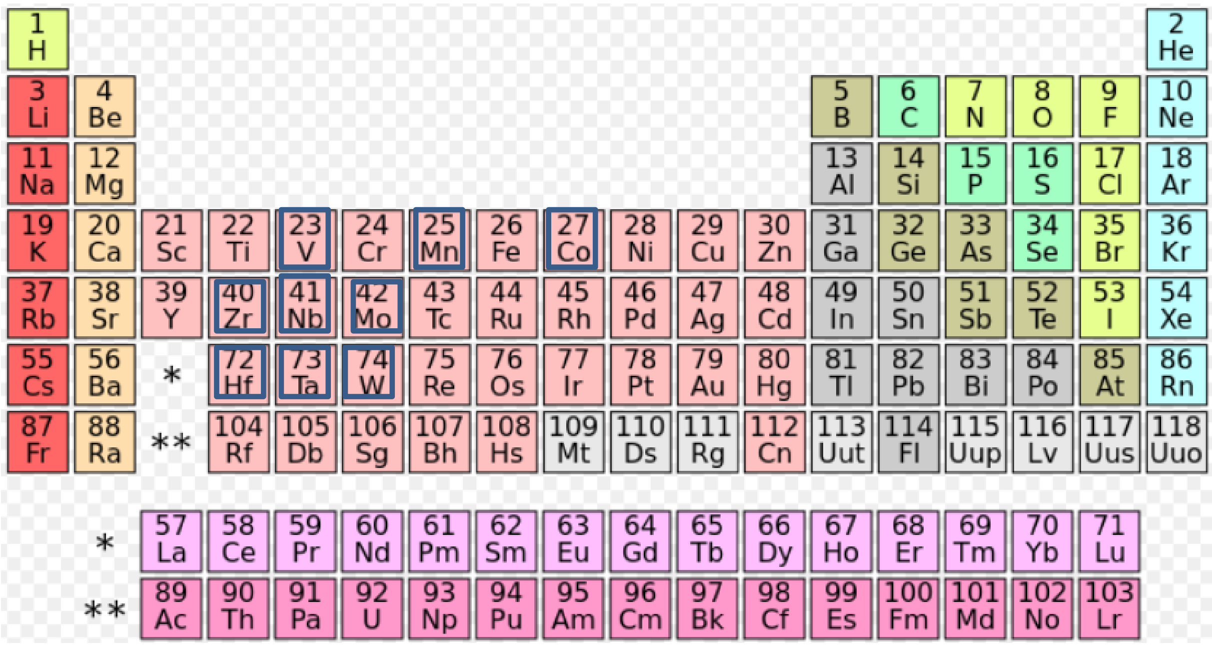

Fig. 2.14 Solubility properties of Ti and Fe with the other elements in the binary alloy periodic system (Massalsak, 1990)

Massalsak (1990) investigated the solubility properties of Fe and Ti with other elements of the periodic table of elements, in temperatures up to 1200°C as shown in Fig. 2.14. It was reported that Ti readily reacts with most of the other elements to form stable and brittle intermetallic compounds, except for a few elements such as Zr, V, Nb, Ta, Hf, Mo and W in the same or adjacent groups of the periodic table of elements.

Hall (2004) and Li *et al*. (2012) added a Ni element that proved to be effective for improving the NiTi sheet joint properties. Hall (2005) reported that both cold and hot cracking could be reduced through the addition of nickel as the filler material and successfully welded NiTi and ferrous alloys by this method. The filler material keeps the NiTi and Fe apart in order to prevent the formation of intermetallic and hot cracking. Kundu (2008) reported the use of Ni as the filler material for joining Ti and stainless steel to improve the bonding strength. Li (2007) reported that three silver based filler materials could join NiTi and stainless steel and the microstructure was improved. Li *et al*. (2013) suggested the use of Co as the filler material for joining NiTi and stainless steel, and reported that the addition of Co as the filler material decreased the amount of brittle intermetallic compounds such as Fe_2Ti and Cr_2Ti in the welded metals, which improved the joint properties. They reported that the joint properties reached a maximum tensile strength of 347MPa and an elongation of 4.2% when 20 mm thick Co filler metal was used. Lee *et al*. (2013) investigated the dissimilar joining between Ti and stainless steel by the addition of an interlayer structure of V–Cr–Ni. It was reported that superior bonding was achieved by the proposed interlayer structure and the bonding strength of the welded joint exceeded the strength of the Ti. This research study further concluded that the addition of a suitable element in the weld pool could modify the mechanical properties and chemical composition of the welded joint. Therefore, a suitable filler material, which has similar thermal expansion properties as the base materials, for dissimilar welding is important. If there is a large difference in thermal expansion properties, larger residual stresses will be formed. Vanadium was first considered as a highly promising interlayer metal for Ti and stainless steel joining, because it has a high compatibility with the Ti base metal. Massalski (1990) introduced β Ti and formed a complete range of solid solutions with the vanadium, whereas the behaviour of α Ti was more limited in this respect. Lison *et al*. (1979) achieved promising properties as the interlayer was further enhanced by a negligible difference in thermal expansion coefficients, with a ratio of Ti:V is 8.5:8.3. Li *et al*. (2013) reported that Cu interlayer could join NiTi and stainless steel and promising mechanical properties was achieved despite the corrosion resistance properties was decreased. However, the application of such joint in biomedical sector still required further study. Therefore, the choice of proper interlayer for the joining of NiTi and stainless steel greatly affects the mechanical properties of the joint.

2.4.2 Selection Criteria of Interlayer

All the research studies indicated that the addition of an appropriate filler material during the welding of NiTi and stainless steel may be a suitable way to control the chemical composition and improve the mechanical properties of the welded joint. There are several criteria for choosing an appropriate filler material. Firstly, it is important that the thermal expansion of the filler material is similar to the base materials to be joined in order to reduce the large residual stress formed. Secondly, the filler should have an unlimited solubility in the liquid phase and limited solubility in the solid phase, while NiTi having a larger solubility in the filler material could bring benefits to the combination and the mechanical properties of the joint. Thirdly, the linear expansion coefficient of the filler material is between that of NiTi and stainless steel, which may help to release the residual stress of the dissimilar welded joint. Fourthly, a high deformation capacity and ductility of the filler material would improve the mechanical properties of the joint. Fifthly, excellent corrosion resistance of the filler material may enhance the corrosion resistance ability of the joint. Lastly, the material cost of the filler material should be considered.

Table 2.3 Summary of properties and cost of different filler materials

	Cobalt	**Molybdenum**	**Nickel**	**Vanadium**	**Silver**	**SS**	**Nitinol**
Thermal Expansion Coefficients (1 ×10-6 °K)	12	5	13	8	19.5	9.6	11
USD Cost per Tonne (USD)	30000	13200	10775	46605	514,986	4733	Nil
Melting point (°C)	1495	2620	1453	1900	961	1500	1300

Research studies showed that a possible filler material for welding NiTi and stainless steel would be Co, Mo, Ni, V and Ag. Although it was reported that a promising joint could be formed by Ag, the thermal expansion coefficients and the cost of the material were too high making it inappropriate for this research. In this research, Co, Mo, Ni and V would be the possible filler materials for welding. Table 2.3 shows a comparison of the thermal expansion coefficients, cost and melting point of different filler materials. Co and Ni would be selected as the filler materials for this study.

2.5 Process Parameters Design Method

The process of adjusting the control variables (parameters) to find the level of parameters that achieve the best outcome is called process parameters design. In the absence of any systematic approach, “trial-and-error” is used. Such method was not efficient in finding the true optimal one. There were several different approaches for the process parameters design included design of experiments, expert system and artificial intelligence such as artificial neural network, expert system, genetic algorithm and etc. (Potente *et al.*, 1993; Blyskal and Meheran, 1994; Vaatainen *et al.*, 1994). There are various techniques (as shown in Fig. 2.15) that have been successfully used in the engineering field.

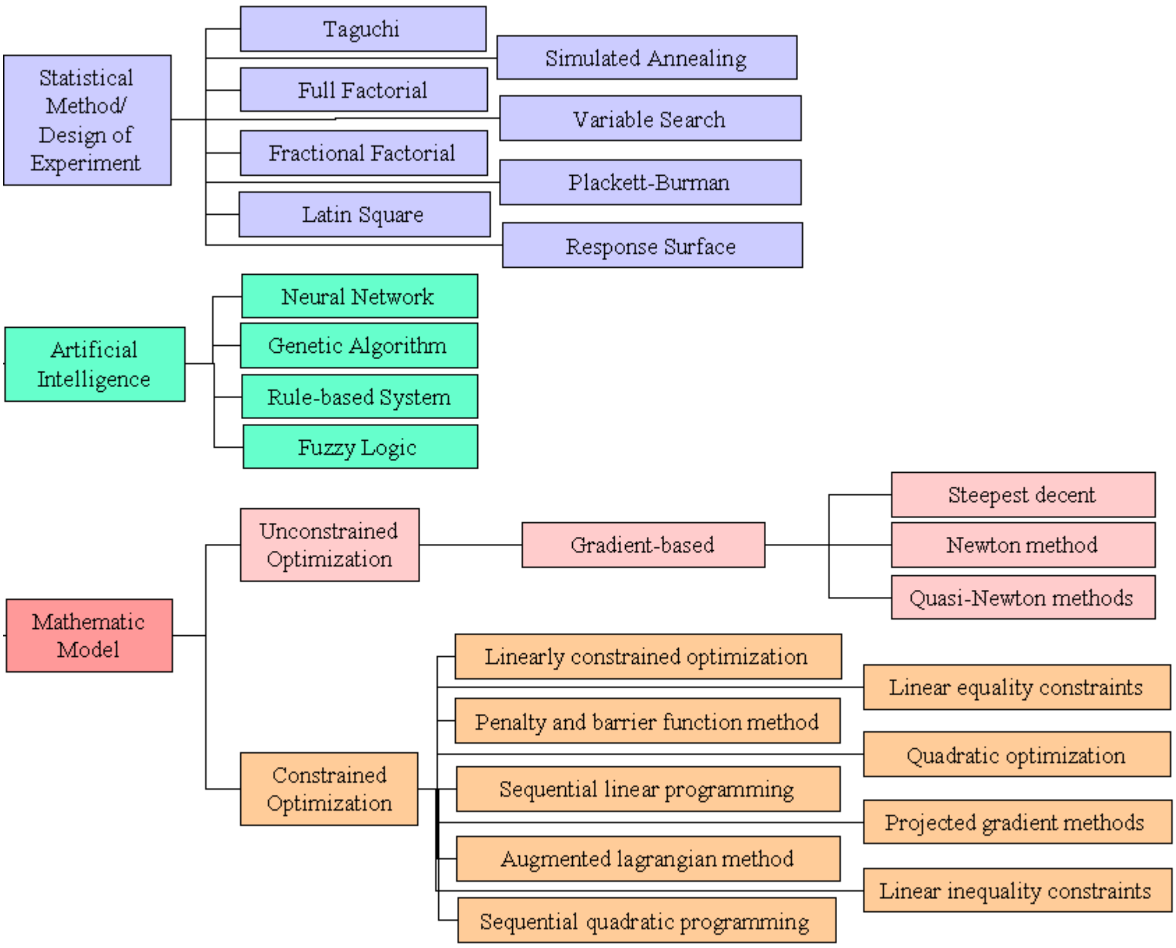

Fig. 2.15 Major categories of process parameters design

2.5.1 Artificial Neural Network

Researchers advocated the use of artificial neural network (ANN) in which the joint performance were typically forecasted from the measured process data. A lot of research took place in the application of ANN to performance prediction (Rewal *et al*., 1998; Petrova and Kazmer, 1999). ANN was a model consisting of many nodes connected from layer to layer. Each node had an output signal that fanned out along the connections to each of the other nodes. Each connection was assigned a relative weight. A node's output depended on the specified threshold and the transfer function. This transfer function specified how the neuron would scale the response to the incoming signal, and produced the output. Once a trained neural network has been created, the joint performance can be predicted from the measured data. As the ANN required significant training, it involved many testing iterations (Garson, 1998).

The quality of the learned network was much depended on the quality of the training data provided. Improvements with respect to learning rates and large sets of training data were still required. Since ANN assumed the process to be a 'black box' with unknown relationships among different parameters, it did not provide insight into the process behavior. Therefore, ANN was not a good choice to solve process parameter design problems because it was unrealistic to supply a sufficiently good training data set covering all possible design cases and parameter combinations due to the complexity and variety of joint design and process parameters settings (Ye and Wang, 1999).

2.5.2 Genetic Algorithm

The Genetic algorithm (GA) is an inherently parallel population-based search method. It was a recent approach to solving problems in rugged solution spaces. The principles of biological evolution, genetic recombination and natural selection were used as the evolutionary search technique while traditional algorithms required excessive computational time to find the global optimum due to the trapping in the local optima. GA simulated the principle of 'survival of the fittest' in a population of potential solutions known as chromosomes, where each chromosome represents one possible solution to the problem to be solved. Because the genetic algorithm explored multiple regions of the solution space simultaneously, it can avoid the local optimization problem and can often find a solution in less time. GA has been widely used in various engineering problems included the development of systems for the optimization of the process parameters based on the results of flow simulation, process planning system to optimize concurrently the operation selections and so on (Kim *et al*., 1996; Lee *et al*., 2001). Probability and statistics governed all of the GA functions. Thus, no two GA runs on the same problem can produce the same results, causing a drawback for the GA, as the finding of an optimum result cannot be guaranteed, during any specific run. This is particularly true if the solution space is rugged, i.e. a case had many local optima or the global optimum was not greatly distinguished. In addition, the statistical nature of the GA can also lead to the problem of determining when to stop the GA population.

2.5.3 Expert System

An alternative to determine a process parameter setting was the use of expert systems where corrective guidelines were presented in the form of "if-then" rules. Rule-based system represented knowledge in terms of a bunch of rules inferred what should be done or, conversely what you could concluded in different situations. A rule-based system consisted of a bunch of IF-THEN rules, a bunch of facts with an interpreter controlling the application of those rules, based on his interpretation of the given facts.

In simper term, the induction approach was the backward chaining rule based systems. People started with some hypothesis (or goal) that were trying both to prove, and keep looking for others that would allow people to conclude the above hypothesis, possibly setting new sub goals for further examination. Induction was a process of reasoning (arguing) which inferred a general conclusion based on individual cases, examples, specific bits of evidence, and other specific types of premises. The deduction approach was a forward chaining rule-based system that the system started based on initial facts, and kept using the rules to draw new conclusions (or take certain actions) given those facts.

A number of rule-based systems were suggested on which to model the process and to reduce dependency on human expertise. The knowledge in such systems was represented by the IF-THEN format. These systems suggested generalized solutions and they were not able to consider the roles and influences of parameters and other conditions that experts brought into account to obtain the process parameters. The main shortcoming of expert systems was that a generalized set of rules might not be applicable across a broad range of part geometries, material properties, and machine dynamics. Another option was the development of an empirical model from data obtained through a set of designed experiments.

2.5.4 Design of Experiment (DOE)

The use of design of experiment (DOE) has grown rapidly and has been adapted for many applications in different areas during the last two decades. Design of experiments (DOE) is a proven method and the most commonly adopted statistical technique used to determine the effects of a number of process variables that affect the response or output of a process. The method was first pioneered by Ronald Fisher in the early 1920s at the Rothamsted Agricultural Field Research Station in London (Bhote and Bhote, 2000). The primary goal was to determine the optimum water, rain, sunshine, fertilizer and soil conditions needed to produce the best crop. Fisher was able to lay out all combinations of the factors which needed to be studied in the experiments to follow by using the DOE technique. After the Second World War, UK practitioners of experimental design brought the method to the United States where the chemical industry was the first to apply it (Montgomery, 1992). The traditional one-factor-at-a-time approach to experimentation was directly replaced by Fisher's approach, providing a heuristic approach to the planning of an experiment enabling an efficient process (Fisher, 1926). With fewer experiments, the collected data could be treated statistically and still result in valid and objective conclusions. With DOE, the data obtained from a set of designed experiments forms an empirical model. Based on the empirical model, the objective function of an optimization problem is defined in terms of quality attributes and the set of inputs. The "optimal" condition obtained is the best set of quality attributes. Textbooks such as Montgomery (1997) and Wu and Hamada (2000) explained the approaches and goals of DOE methods. Full factorial design and Taguchi method are two major approaches to DOE.

2.5.4.1 Full Factorial Experiment

A full factorial experiment is an experiment takes all possible combinations of each factor with all possible levels to study the effect of each factor on the response variable and interactions between factors on the response variable. If an experiment design with 6 input factors set at three level each, it would take 729 experiments. Therefore, the full factorial design requires a large number of experiments to be carried out as stated above if the number of factors increase.

2.5.4.2 Taguchi Method

DOE gained widely used in the world as an essential part for improving process effectiveness and product quality. This recognition was partially due to the work of Prof. Taguchi in Japan who developed Taguchi method based on “orthogonal array”. Experiments concerned with the optimum setting of control parameters using Taguchi method gives a much reduced variance. Taguchi showed how the statistical design of experiments (SDOE or DOE) could help industrial engineers design and manufacture products that were both of high quality and low cost. His approach focused primarily on eliminating the causes of poor quality and on making product performance insensitive to variation. Thus, the blending of the Taguchi method with DOE was found to obtain the best control parameter results. “Orthogonal Array” provides a set of the minimum number of well balanced necessary experiments. If there are k factors, each at 3 levels, only 9 trial runs are needed. Log functions of the desired outputs (Taguchi's Signal-to-Noise ratios) act as optimization objective functions to help in the prediction of optimum results and data analysis.

The S/N ratio for the individual control factors are calculated as given below:

$S_1 1 = (N_1+N_2+N_3)$

$S_1 2 = (N_4+N_5+N_6)$

$S_s 3 = (N_7+N_8+N_9)$

$S_2 1 = (N_1+N_4+N_7)$

$S_2 2 = (N_2+N_5+N_8)$

$S_2 3 = (N_3+N_6+N_9)$

$S_3 1 = (N_1+N_5+N_9)$

$S_3 2 = (N_2+N_6+N_7)$

$S_3 3 = (N_3+N_4+N_8)$

Where N_k is the S/N ratio corresponding to experiment k

Average S/N ratio corresponding to parameter 1 at level 1 = $S_1 1/3$

Average S/N ratio corresponding to parameter 1 at level 2 = $S_1 2/3$

Average S/N ratio corresponding to parameter 1 at level 3 = $S_1 3/3$

Similarly, $S_2 j$ and $S_3 j$ are calculated for parameter 2 and 3 where j is the corresponding level each factor.

The response magnitude in (%) of each parameter in the orthogonal experiment is evaluated by analysis of variance (ANOVA) to identify and quantify the results of different experiment runs (i.e. different laser welding speed). The basic property of ANOVA is that the total sums of the squares (total variation) is equal to the sum of the SS (sums of the squares of the deviations) of all the condition parameters and the error components.

$$SST = SS_1 + SS_2 + SS_3 + \ldots + SS_k.$$

$$SST = \sum_1^n y_i^2 - \frac{G^2}{R}$$

where G is the sum of the resulting data of all trial runs and R is the total number of the experiment runs .

$$SS_k = \sum_{j=1}^{t} \left(\frac{sy_j^2}{t}\right) - \frac{G^2}{R}$$

where k represents one of the tested parameters, j is level number of this parameter, Syj is sum of all trial results involving this parameter k at level j and R is the total number of experiment runs.

2.5.5 Applications of DOE

A number of successful applications of DOE for improving product performance, improving product life and reliability have been reported over the last 15 years (Antony, 1999; Bullington *et al*., 1993; Hamada, 1995). The techniques provided a heuristic approach for planning the experiment so that it could be efficiently performed, but with fewer experiments and so the data collected could be analyzed by statistical methods, resulting in valid and objective conclusions. With DOE, data obtained from a set of experiment formed an empirical model. Based on this model, the objective function of an optimization problem was defined in terms of the joint performance, and the set of inputs that produced the best performance attributes were obtained as the “optimal” point of this optimization problem. Deliz and Caraballo (1995) used a fractional factorial experiment to find the processing conditions that would minimize the deviation of one dimensional measure while Xia and Mallick (1997) and Blyskal (1994) applied DOE techniques to determine optimal settings with respect to one or more dimensional measures. Beard (1999) suggested the use of DOE for process validation. His study was to define a process window such that acceptable parts would be created at anywhere inside that process window. As DOE attempted to increase the information available and reduce the number of required tests for a given number of factors and levels, if the experiment was designed correctly, a large amount of information can be collected with a minimum of experimental effort. As a result, the success of the DOE was depended on the experimental design analysis of collected data and the experimenter’s knowledge of the specific process. It was important to consider and optimize the correct factors at the correct levels.

One of the techniques could be applied to optimize laser welding process parameters is the Taguchi method. It enables the achievement of process parameter optimization, which is insensitive to the variation of environmental conditions and other noise factors, in high quality without increasing the cost (Pan *et al*., 1984). A special orthogonal array is designed in the Taguchi method to study process parameters of different level with a small number of experiments only. It solves the problem induced in classical process parameter design, which is not easy to use with increased number of process parameters, when increased number of experiments needed to be conducted. In contrast to other optimization methods, Taguchi method determines both the optimal results from finite analytical data and the dominant factors involved in the optimization for laser welding from finite analytical data. Chan *et al*. (2010) applied Taguchi method to determine the optimal setting in welding NiTi-NiTi wire and concluded the important factors, laser power and welding speed, that affect the successful joining of NiTi-NiTi. This method has been widely applied in precise manufacture (Chou *et al*., 2001; Miyazawa *et al*., 1993) and also other fields (Tosun, 2006). In this project, both Taguchi method and full factorial method were used.

3 Experimental Details

This chapter describes the framework of the methods applied in the present research work. The second part details the materials, equipment and the experimental procedures that were employed in this project.

3.1 Methodology of Research Study

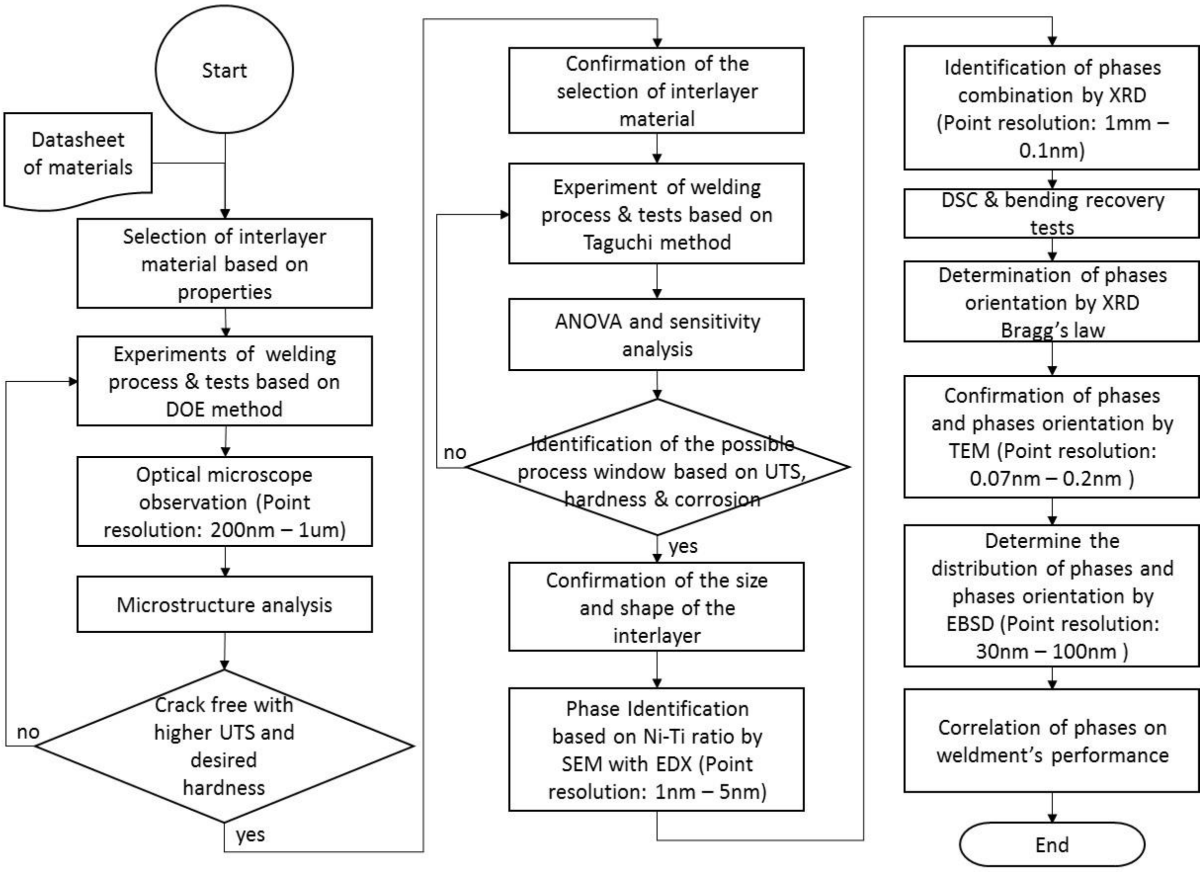

Fig. 3.1 Generic model based methodology of the study

The workflow of the testing and analysis methods used for the evaluation of laser welded joint and the development of the correlation of mechanical properties and chemical composition of the weld pool was proposed and shown in Fig. 3.1. It enables the construction of a structural mechanism to obtain a dedicated process window of laser welding of dissimilar metals to minimize intermetallic compounds (e.g. Ti_2Ni, $TiFe_2$, or $TiCr_2$ in this study). The proposed model is intended to achieve better tensile strength and corrosion behavior with recoverable bending deflection of laser welded NiTi and stainless steel joints.

A preliminary study was conducted to determine a successful welded joint between NiTi and stainless steel, the selection of possible interlayer material was chosen, based on the thermal expansion coefficient, cost, and melting point. Laser welding, tensile test and microhardness test experiments were conducted, followed by microstructure analysis. Crack free weldments with high ultimate tensile strength and the desired hardness were the indicators confirming the appropriate selection of material interlayer for the NiTi and stainless steel weld joint. Once the appropriate interlayer material was identified, the Taguchi method was then used to design a set of minimum number of necessary welding experiments. Tensile tests and microhardness tests were conducted and acted as the performance indicators to identify the prospective process window of joining NiTi and stainless steel together with the interlayer, by means of ANOVA and sensitivity analysis. Welded samples with different filler shape and filler size were selected to perform a corrosion test to identify the appropriate size and shape of interlayer. After that, phase identifications by SEM with EDX and XRD were applied to identify the combination of different phases in the fusion zone of welded samples with acceptable joint strength and corrosion properties. Once the welded samples with minimum unfavorable phases were identified, DSC and recovery bending test were conducted to find out their transformation temperature and recoverable bending deflection. With the preferred welded joint identified, the orientation of phases were calculated by Bragg’s law while TEM analysis was conducted to determine both the phases and the orientation of those phases. Then, the distribution of different phases of the preferred weld joint was determined by EBSD. Finally, the correlation between the amount of different phases and the joint performance included tensile strength, recoverable bending deflection, and phase transformation temperature was made base on the results from XRD, TEM and EBSD.

3.2 Materials and Sample Preparation

In this project, NiTi sheet with 44.5 wt. % of Ti and SS304 stainless steel sheet were used for all the experiments. According to the ISO 6892-1:2009 (E) standard, NiTi and SS304 sheets were cut into the size of 12.5mm (width) x 45mm (length) x 1mm (thickness) by wire electro-discharge machining to ensure the straightness of the edges of both NiTi and SS304 samples. The composition of SS304 provided by the manufacturer is presented in Table 3.1. Before conducting the laser welding, the NiTi samples were annealed at 500°C for 30 minutes in air followed by water quenching to produce pseudoelasticity at room temperature. Then, the oxide layer and contaminants in the NiTi samples were removed by cleaning with 400 grit sand paper and acetone. The surfaces of SS304 samples were cleaned with isopropanol to remove the grease (Pouquet *et al*., 2012).

Table 3.1 Chemical composition of SS304 (wt. %) (UPM, 2019)

	C	Cr	Mn	Ni	S	Si	Ti	P
SS304	0.080	18.000	2.000	8.000	0.030	0.750		0.045

The two main requirements for successful dissimilar welding NiTi and stainless steel should be melted to form a joint and the welded joint should meet the mechanical property criteria imposed by service conditions. The difference in melting point and thermal conductivity usually existing in dissimilar welding makes it difficult to fulfil the first criteria using the laser welding process with not enough energy density. The most important property pertaining to the transport of heat during welding is the thermal conductivity of the materials. Once the first criteria is overcome, most of the effort is spent on achieving the latter goal. It is essential to minimize the brittle intermetallic weld formation. From Table 3.2, it is seen that the thermal conductivity difference between NiTi and stainless steel can lead to asymmetry in weld pool geometry. Additionally, the density difference between NiTi and SS304 can be a driving force for fluid flow in the weld pool, hence affecting the mixing and segregation therein.

Table 3.2 Thermal properties of base metals

	Stainless Steel 304 (SS)	**Nitinol (NiTi)**
Density of liquid (kg/m^3)	8000	6450
Thermal conductivity W/m-K	14.4	10.0
Melting point (°C)	1500	1310

Apart from the difference in thermal properties, differences in the atomic interactions, are reflected in the existence of phases with different crystal structures and mixing. This difference is best expressed in the form of a phase diagram. Fig. 2.8 indicates the relative stability of different phases in the Fe - Ni - Ti system, revealing their composition and temperature functions. Additional to the solid solution of Fe, Ni and Ti, there are several unfavorable intermediate phases (FeTi, Fe_2Ti and $NiTi_2$) in the system which can form from the liquid. Therefore, an addition of interlayer during welding of NiTi and SS304 was used to minimize the mix of NiTi and stainless steel. Based on the discussion in chapter 2.5, 99.99 wt%

Ni and 99.98 wt.% Co were selected as the interlayer between the joining of NiTi and SS304 in all the experiments. Besides, the selected interlayers were cleaned with acetone.

3.3 Welding Parameters and Equipment

The characteristics of fiber lasers are good beam quality, high energy efficiency, low cost of maintenance and compact size. They are suitable for most laser materials process applications. Furthermore, they have been considered to replace other types of laser systems such as Nd:YAG and CO_2 lasers in the industry (Vollertsen and Thomy, 2005). Because of their superior characteristics, fiber lasers are able to produce a deeper penetration weld by using a low laser power (Vollertsen, 2005). A 2000W fiber laser machine with a wavelength of 1.07μm provided by the Industrial and Systems Engineering Department of the Hong Kong Polytechnic University was used for laser welding as shown in Fig. 3.2.

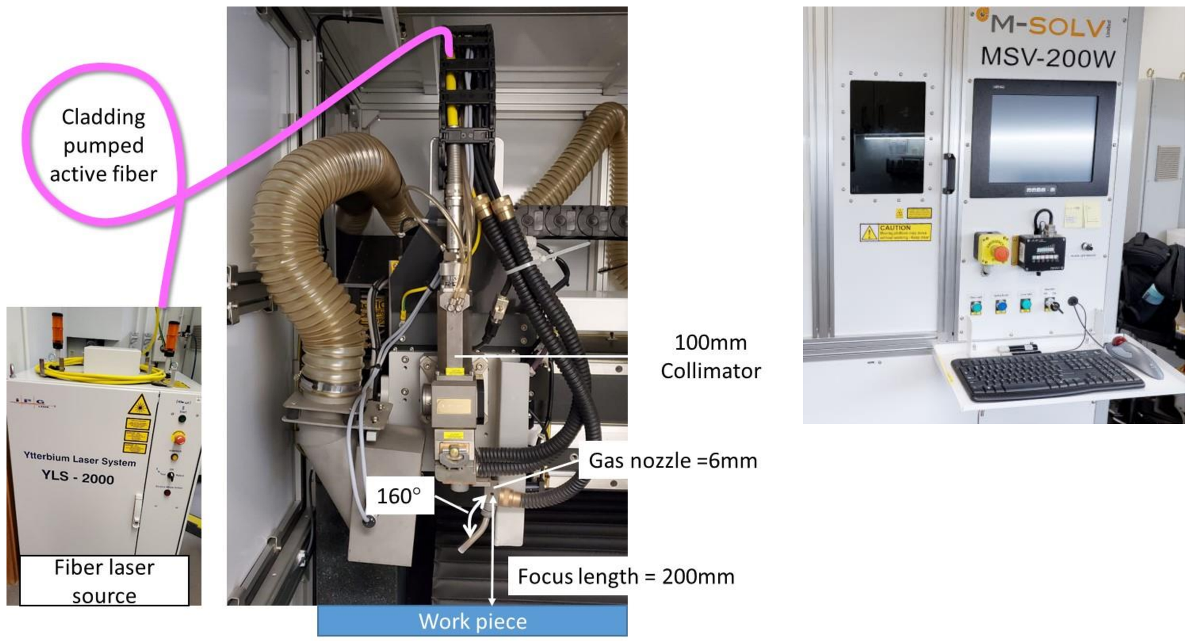

(a) (b)

Fig. 3.2 (a) Experimental setup of laser welding and (b) snapshot of fiber laser machine

Two self-constructed fixture were made to make butt joints with circular shape interlayer and rectangular shape interlayer as shown in Fig. 3.3 to 3.4. The assembly of NiTi and SS304 with or without interlayer was placed in the fixture to make butt joints during laser welding. The fixture, which produces a clamping force, was used to secure the location of the samples to minimize heat distortion during laser welding. The fixture was then mounted on a XY table, the movements of which can be controlled to enable movement relative to the laser beam. The focus position (z direction) was adjusted precisely. Argon gas was used as the shielding gas to prevent or minimize the oxidation during laser welding (Chan *et al.*, 2011). The flow rate of the argon gas was controlled by a flow meter at 3 bar and 20L/min with nozzle size of 6mm.

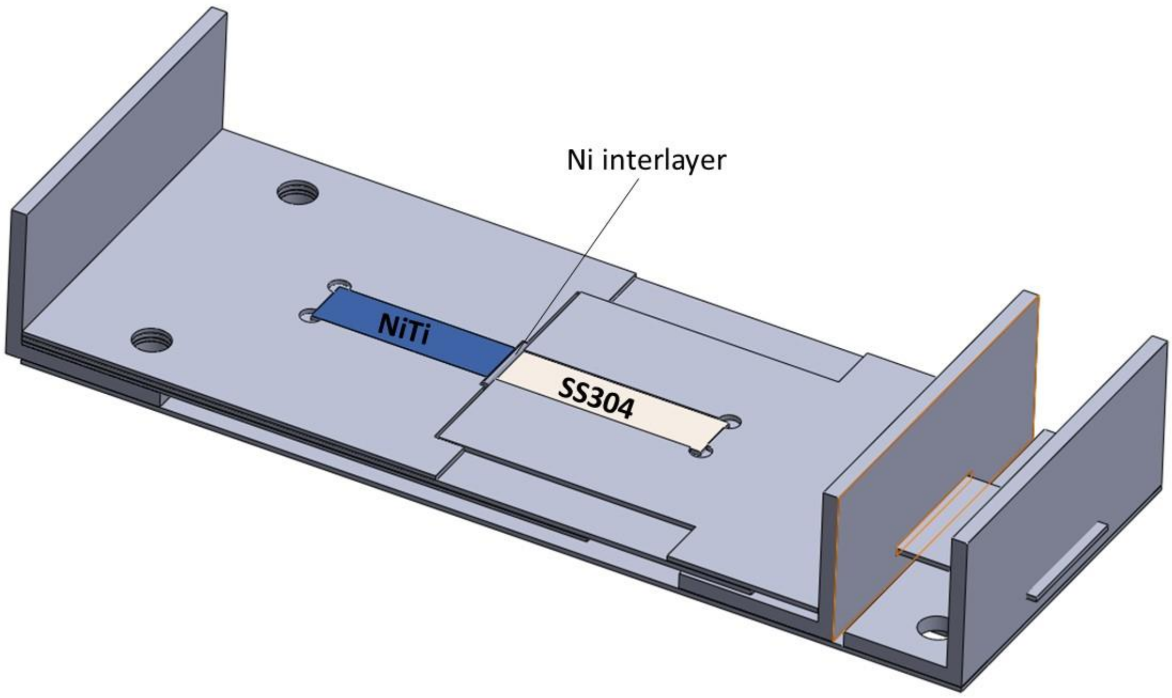

Fig. 3.3 Self-constructed fixture for laser welding with circular shape interlayer

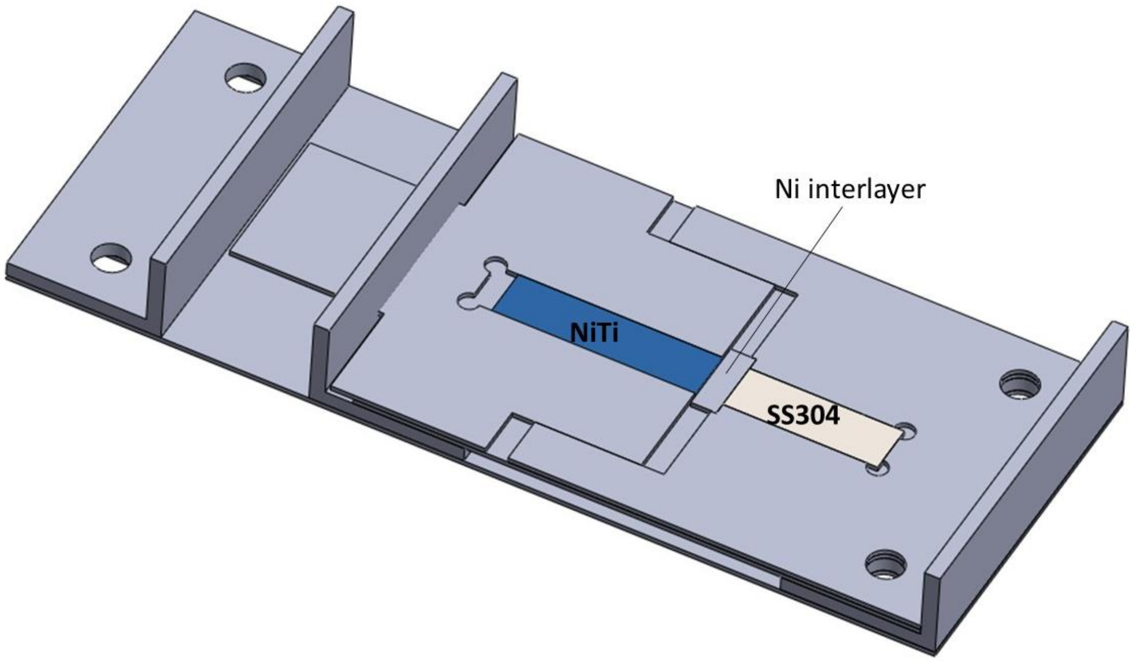

Fig. 3.4 Self-constructed fixture for laser welding with rectangular shape interlayer

3.3.1 Experimental Setup of Preliminary Study

In this preliminary study, at a fixed laser power, the welding speed and the selected interlayer material were studied using the full factorial method to determine the initial process window to produce the full penetrated weld joint. Pulsed wave (PW) mode and continuous wave (CW) mode laser focused at the middle of the sample were conducted to produce a successful welded joint between NiTi and SS304. ∅1mm Co and Ni wires were cut into a length of 14mm and cleaned with acetone before laser welding. These associated welding parameters used in the study are presented in Table 3.3 and 3.4.

The assembly of NiTi and SS304 with Co or Ni interlayer was placed in a self-constructed fixture to make the butt joint as shown in Fig. 3.6 during laser welding. After welding, tensile tests of all samples had been completed to determine the joint strength of the NiTi and stainless steel (NiTi-SS), NiTi and stainless steel with Co (NiTi-Co-SS) and NiTi and stainless steel with Ni (NiTi-Ni-SS) weldments. 3 samples mounted in resin, polished with diamond abrasives to a 6μ surface finish and etched with reagent, were sectioned across the weld, for crack identification by using optical microscopy, as mentioned in chapter 3.5. The phenomena of microsegregation within welds was observed by means of scanning electron microscopy equipped with energy dispersive X-ray spectrometry (EDX). Profiles of microhardness including the base metals and the fusion zone were determined based on the location from base material of NiTi to the fusion zone of the NiTi-interlayer, then, from the Co and Ni interlayer to the fusion interlayer-SS zone and finally to the SS base material.

Table 3.3 Summary of the control factors and settings for pulsed laser

	Factor	Settings		
i	Welding speed (mm/s)	12.5 - 75		
ii	Laser power (W)	1400		
iii	Focus position (mm)	At the middle of the sample		
iv	Shielding gas	Argon at 20L/min with nozzle size of 6mm		
v	Laser wave	Pulsed wave (Freq = 50Hz, pulse duration = 20ms)		
vi	Interlayer material	No (Direct joint)	Co	Ni
vii	Diameter of Interlayer (mm)	No (Direct joint)	∅1mm	

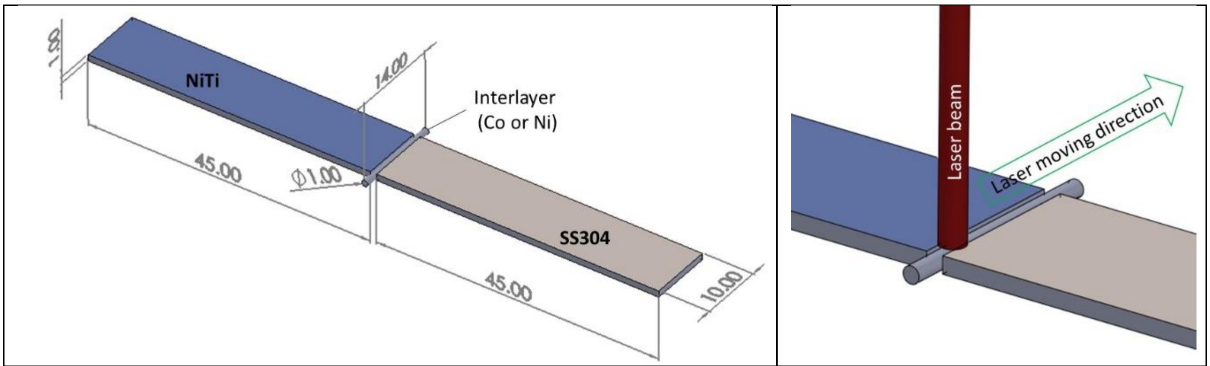

(a) (b)

Fig. 3.5 Schematic diagram of (a) sample assembly with circular shape interlayer and (b) laser welding direction

Table 3.4 Summary of the control factors for welding setup for continuous laser

	Factor	Settings		
i	Welding speed (mm/s)	175 - 300		
ii	Laser power (W)	1400		
iii	Focus position (mm)	At the middle of the sample		
iv	Shielding gas	Argon at 20L/min with nozzle size of 6mm		
v	Laser wave	Continuous wave		
vi	Interlayer material	No (Direct joint)	Co	Ni
vii	Diameter of Interlayer (mm)	No (Direct joint)	∅1mm	

3.3.2 Experimental Setup of Welding with Circular Shape Interlayer

Laser welding parameters have the most effect on the efficiency of the welded joint. Laser power, welding speed and focus position are the most effective parameters in the laser welding process (Glsario *et al*., 2017 and Mehrpouya and Emamiam, 2017). In this experiment, the same fiber laser with higher laser power was used as it showed a higher power intensity compared to the conventional CO_2 and Nd:YAG lasers. Based on the results determined in the preliminary study, a minimum power density to produce the full penetrated weld joint was determined. Therefore, different interaction intervals with the increased energy delivery rate, which consequently reduced the heat affected zone area, was used (Jani *et al*., 2014) for further study.

Investigation of the tensile strength with various degrees of power density from 5.09×10^6 to 6.3×10^6 W/cm^2 with different sizes of interlayer, welding speed, focus position have been conducted to study the functional effect on both pulsed and continuous laser. By analyzing the variance contributed by each factor, the Taguchi method is complemented with the use of statistical analysis to quantify which factors are most significant and dominant. The statistical technique in visualizing variation and the mean were applied in this study to quantify the significant laser welding process parameter in producing a good welded joint. Same size of NiTi and SS304 used in the previous preliminary study were also used in this study while different diameter of Ni interlayers were cut into a length of 14mm. The assembly of NiTi and SS304 with different diameter of Ni interlayer was placed in a self-constructed fixture to make the butt joint as shown in Fig. 3.6 during laser welding.

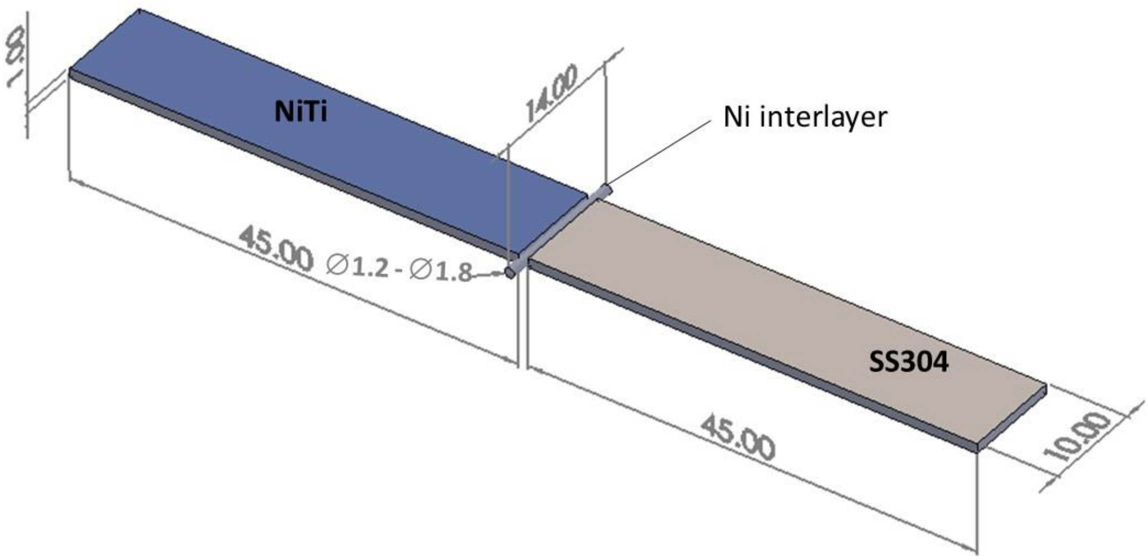

Fig. 3.6 Schematic diagram of sample assembly with circular shape interlayer in different diameters

The Taguchi method was used to study the effects of the laser welding process parameters with the appropriate interlayer shape and their possible interactions with the stress to which a laser welded joint is subjected. Each set of experiments contained 4 control factors and each factor had 3 levels. The control factors of L9 orthogonal arrays were defined as (i) interlayer size, (ii) laser power, (iii) welding speed, and (iv) focus position with respect to the surface of the specimens for both the pulsed and continuous laser. The selected values of each factor are summarized in Table 3.5 and 3.6.

Table 3.5 Summary of the control factors for pulsed laser welding (circular shape interlayer)

Experiment with interlayer		Level 1	Level 2	Level 3	Level 4
Factor i	Interlayer size – circular shape (mm)	∅1.2	∅1.4	∅1.5	∅1.8
Factor iii	Laser power (W)	1600	1800	2000	
Factor iii	Welding speed (mm/s)	25	37.5	50	
Factor iv	Focus position (mm)	-0.5	0	+0.5	

Table 3.6 Summary of the control factors for continuous laser welding (circular shape interlayer)

Experiment with interlayer		Level 1	Level 2	Level 3	Level 4
Factor i	Interlayer size – circular shape (mm)	∅1.2	∅1.4	∅1.5	∅1.8
Factor iii	Laser power (W)	1600	1800	2000	
Factor iii	Welding speed (mm/s)	150	175	200	
Factor iv	Focus position (mm)	-0.5	0	+0.5	

Table 3.7 L36 orthogonal array in the Taguchi experiment (circular shape interlayer)

			Pulsed laser	Continuous laser	
No	Diameter of interlayer (mm)	Laser power (W)	Welding speed (mm/s)		Focus position (mm)
1	1.2	1600	25.0	/	-0.5
2	1.2	1600	37.5	/	0.0
3	1.2	1600	50.0	/	0.5
4	1.2	1800	25.0	/	0.0
5	1.2	1800	37.5	/	0.5
6	1.2	1800	50.0	/	-0.5

7	1.2	2000	25.0	/	0.5
8	1.2	2000	37.5	/	-0.5
9	1.2	2000	50.0	/	0.0
10	1.4	1600	25.0	/	-0.5
11	1.4	1600	37.5	/	0.0
12	1.4	1600	50.0	/	0.5
13	1.4	1800	25.0	/	0.0
14	1.4	1800	37.5	/	0.5
15	1.4	1800	50.0	/	-0.5
16	1.4	2000	25.0	/	0.5
17	1.4	2000	37.5	/	-0.5
18	1.4	2000	50.0	/	0.0
19	1.5	1600	25.0	/	-0.5
20	1.5	1600	37.5	/	0.0
21	1.5	1600	50.0	/	0.5
22	1.5	1800	25.0	/	0.0
23	1.5	1800	37.5	/	0.5
24	1.5	1800	50.0	/	-0.5
25	1.5	2000	25.0	/	0.5
26	1.5	2000	37.5	/	-0.5
27	1.5	2000	50.0	/	0.0
28	1.8	1600	25.0	/	-0.5
29	1.8	1600	37.5	/	0.5
30	1.8	1600	50.0	/	-0.5
31	1.8	1800	25.0	/	0.0
32	1.8	1800	37.5	/	-0.5
33	1.8	1800	50.0	/	0.0
34	1.8	2000	25.0	/	0.5
35	1.8	2000	37.5	/	0.0
36	1.8	2000	50.0	/	0.5
37	1.2	1600	/	150	-0.5
38	1.2	1600	/	175	0.0
39	1.2	1600	/	200	0.5

40	1.2	1800	/	150	0.0
41	1.2	1800	/	175	0.5
42	1.2	1800	/	200	-0.5
43	1.2	2000	/	150	0.5
44	1.2	2000	/	175	-0.5
45	1.2	2000	/	200	0.0
46	1.4	1600	/	150	-0.5
47	1.4	1600	/	175	0.0
48	1.4	1600	/	200	0.5
49	1.4	1800	/	150	0.0
50	1.4	1800	/	175	0.5
51	1.4	1800	/	200	-0.5
52	1.4	2000	/	150	0.5
53	1.4	2000	/	175	-0.5
54	1.4	2000	/	200	0.0
55	1.5	1600	/	150	-0.5
56	1.5	1600	/	175	0.0
57	1.5	1600	/	200	0.5
58	1.5	1800	/	150	0.0
59	1.5	1800	/	175	0.5
60	1.5	1800	/	200	-0.5
61	1.5	2000	/	150	0.5
62	1.5	2000	/	175	-0.5
63	1.5	2000	/	200	0.0
64	1.8	1600	/	150	-0.5
65	1.8	1600	/	175	0.5
66	1.8	1600	/	200	-0.5
67	1.8	1800	/	150	0.0
68	1.8	1800	/	175	-0.5
69	1.8	1800	/	200	0.0
70	1.8	2000	/	150	0.5
71	1.8	2000	/	175	0.0
72	1.8	2000	/	200	0.5

3.3.3 Experimental Setup of Welding with Rectangular Shape Interlayer

Based on the results obtained by Taguchi method, continuous laser welding with laser power of 2000W could achieve better tensile strength. Therefore, further study with a fixed power of 2000W will be conducted to determine the joint performance of laser welded joint with rectangular shape interlayer. Laser welding of NiTi-NiTi, NiTi-Ni, SS304-SS304 and SS304-Ni joint with welding speed of 125 – 200 mm/s were conducted to act as reference of producing NiTi-Ni-SS304 joint with full penetration. Based on the experiment result of NiTi-Ni-SS joint welded with circular shape interlayer, the size of the heat-affected zone is around 2.16mm. To avoid the mixing of Ti with Fe and Cr, the width of the rectangular shape interlayer would be larger than 2.16mm. A 5mm and 8mm size of interlayer were proposed. The selected values of each factor are summarized in Table 3.8 to 3.10.

Table 3.8 Process parameters in laser welding experiments

No	Base metal 1	Based metal 2	Width of Ni interlayer (mm)	Welding speed for NiTi-Ni-SS304 joint (mm/s)		Welding speed (mm/s)
				at SS304-Ni	at NiTi-Ni	
R1	NiTi	NiTi	/	/	/	125
R2	NiTi	NiTi	/	/	/	150
R3	NiTi	NiTi	/	/	/	175
R4	NiTi	NiTi	/	/	/	200
R5	SS304	SS304	/	/	/	125
R6	SS304	SS304	/	/	/	150
R7	SS304	SS304	/	/	/	175
R8	SS304	SS304	/	/	/	200
R9	NiTi	Ni	/	/	/	125
R10	NiTi	Ni	/	/	/	150
R11	NiTi	Ni	/	/	/	175
R12	NiTi	Ni	/	/	/	200
R13	SS304	Ni	/	/	/	125

R14	SS304	Ni	/	/	/	150
R15	SS304	Ni	/	/	/	175
R16	SS304	Ni	/	/	/	200
R5125	NiTi	SS304	5mm	150	125	/
R5150	NiTi	SS304	5mm	150	150	/
R5175	NiTi	SS304	5mm	150	175	/
R5200	NiTi	SS304	5mm	150	200	/
R8125	NiTi	SS304	8mm	150	125	/
R8150	NiTi	SS304	8mm	150	150	/
R8175	NiTi	SS304	8mm	150	175	/
R8200	NiTi	SS304	8mm	150	200	/

Table 3.9 Summary of the control factors for continuous laser welding (rectangular shape)

	Factor	**Settings**
i	Welding speed (mm/s)	110 - 200
ii	Laser power (W)	2000
iii	Focus position (mm)	At the middle of the sample
iv	Shielding gas	Argon at 20L/min with nozzle size of 6mm
v	Laser wave	Continuous wave
vi	Interlayer material	Ni
vii	Width of interlayer	5mm, 8mm

Table 3.10 Process parameters in laser welding experiments with rectangular shape interlayer

No	Laser power (W)	Focus position (mm)	Width of interlayer (mm)	Welding speed at NiTi-Ni (mm/s)	Welding speed at SS304-Ni (mm/s)
R25	2000	0	5	110	200
R26	2000	0	5	100	200

R27	2000	0	5	90	200
R28	2000	0	5	80	200
R29	2000	0	5	70	200
R30	2000	0	5	60	200
R31	2000	0	8	110	200
R32	2000	0	8	100	200
R33	2000	0	8	90	200
R34	2000	0	8	80	200
R35	2000	0	8	70	200
R36	2000	0	8	60	200

Same size of NiTi and SS304 were also used in this study while different width of rectangular shape Ni interlayer was cut into the size of 14mm (width) x 5/8mm (length) x 1mm (thickness) by wire electro-discharge machining to ensure the straightness of the both edges in contact with NiTi and SS304 samples. The assembly of NiTi and SS304 with 5mm/8mm width Ni interlayer was placed in a self-constructed fixture to make the butt joint as shown in Fig. 3.7 during laser welding. The laser beam welded the NiTi-Ni joint and then welded the SS304-Ni joint with the self-constructed fixture.

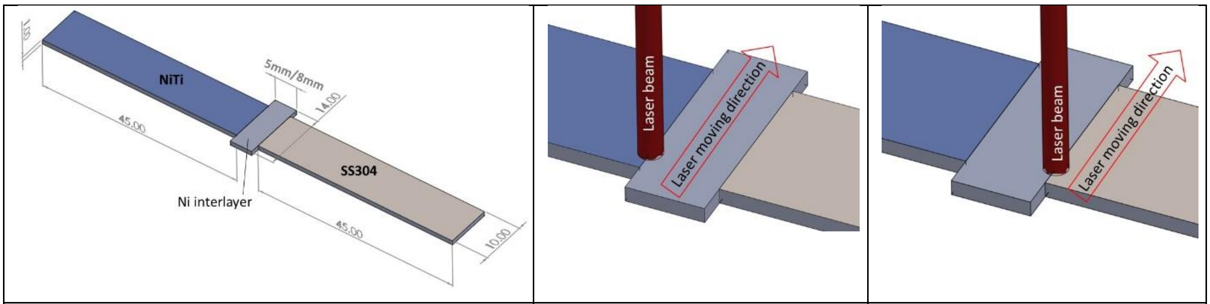

(a)	(b)	(c)

Fig. 3.7 Schematic diagram of (a) sample assembly with rectangular shape interlayer, (b) laser welding on NiTi-Ni joint, and (c) laser welding on SS304-Ni joint

3.4 Mechanical Testing

In this study, three performance indicators were used to represent the performance of the welded joint. One of the performance indicators was expressed as the peak tensile stress of the welded joint. The peak tensile stress was determined by the tensile test. Tensile testing was conducted on a tensile tester with a crosshead speed of 0.2mm/min at room temperature. 3 samples of each welding condition were tested and the averaged values of the maximum stresses were taken.

Fig. 3.8 Guided bend with no die test

The second performance indicators was expressed as the microhardness. The microhardness was conducted on a micro-indentation hardness tester at a load of 0.2kg and a loading time of 15s. A total of 21 indentations were made on the welded joint included both heat affected zone (HAZ) and weld zone (WZ). Each indentation was made by every 125µm and 3 replicas were made to illustrate each measurement. Diagonal lengths of indentations were measured under the magnification of 50X.

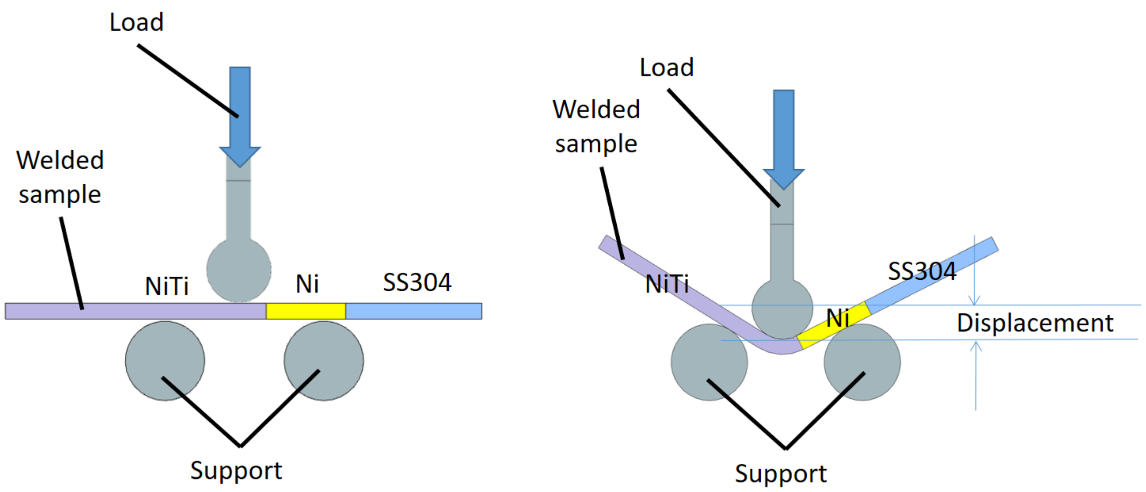

Fig. 3.9 Schematic diagram of the measurement of displacement at break

The last performance indicator was the recoverable bending deflection. Guided bend with no die test according to the standard E290-14 was conducted on a tensile tester (as shown in Fig. 3.8), at room temperature, to bend the welded sample with a crosshead speed of 1mm/min. The rectangular cross-section testing specimen, resting on two supports, was deflected by means of a loading edge, acting on the specimen midway between the supports as shown in Fig. 3.9, until fracture occurred. The test aims to deform the welded sample at a point near the weld line at the NiTi-Ni side causing a bend to form in line with the fracture of this procedure, the force applied to the specimen and the resulting deflection of the specimen at mid span was measured. The displacement at break of three samples with reference to the welding parameters and the performance of shape memory effects will be identified. With the values of the maximum displacement at break, samples were bent to form without the occurrence of fracture (0.1mm reduction of the maximum displacement at break) for shape recovery test. The sample was subjected to 10 cycles of bending to its allowable bending displacement and subsequent recovery to its initial shape at the Austenitic finish temperature, A_f. Then, the maximum allowance bending displacement of the joint was recorded as the recoverable bending deflection of a weld joint.

3.5 Microstructural Analysis

The welded joint, fracture surfaces, width of the weld pool, and the chemical composition were examined using an optical microscope (OM) and scanning electron microscope (SEM) with energy-dispersive X-ray spectroscopy (EDX). X-ray diffraction analysis (XRD), transmission electron microscopy (TEM) and electron backscatter diffraction (EBSD) were used to perform microstructure analysis and phase identification of intermetallic compound in the fusion zone of the welded bead.

In OM and SEM analysis, samples were mounted in epoxy resin and mechanically ground from 220 grit to 1200 grit using sand paper, followed by polishing using 6 micron diamond paste. Finally, the samples were etched with 14 mL HNO_3, 3 mL HF and 82 mL H_2O solution for 25 s to 30 s to reveal the microstructure of NiTi, while a 3 mL HCl and 1 mL HNO_3 solution was used for 25-30s to reveal the microstructure of stainless steel (Gopinath *et al*., 2013). Optical microscopy was carried out using an Olympus BX51M and a Leica DMI5000M optical microscope. Two different scanning electron microscopes were used: a JEOL Model JSM-6490 and Tescan VEGA3 at acceleration voltage of 15kV with backscattered electron and energy dispersive X-ray spectroscopy (EDX) detector. X-ray diffraction using conventional Cu K-alpha radiation was performed using RigakuSmartLab XRD to determine the structural transformations of the NiTi base material at the fusion zone. XRD was performed in the 2θ range of 30° to 80°. The Bragg's law indicates reciprocal relationships between the spacing between the atomic planes (d) and the angle of diffraction (θ), therefore, the diffraction pattern and the crystal lattice can be related by a mathematically constructed reciprocal lattice. In a 3D crystal lattice, multiple sets of equally spaced parallel planes can be identified. The phase identification will be conducted by comparing the measured XRD pattern with the diffraction pattern of phases from the Crystallography Open Database (COD). The intensity of the diffraction signal was plotted against the diffraction angle (2θ). Bragg's law together with plane spacing equations were used for plane orientation identification of different phases.

(a) (b)

Fig. 3.10 Polishing equipment for preparing foil for TEM observation

In TEM analysis, the central area of the welded bead with a diameter of 6mm and a height of 1mm were cut by means of wire electro-discharge machining (WEDM). Foils for TEM observation were then, mechanically ground to 70μm and thinned by twin-jet polishing (as shown in Fig. 3.10) in an electrolyte consisting of 6% $HClO_4$, 34% $C_4H_{10}O$ and 60% CH_3OH (Jiang *et al.*, 2017). TEM observations were conducted on an FEI Talos microscopy (as shown in Fig. 3.11) with angular range of ±40° at an accelerating voltage of 200 keV. Selected area diffraction pattern (SADP) was employed to identify the diffraction pattern, which is the projection of the reciprocal lattice of interest. In SADP, the brightest spot usually appears in the center of the diffraction pattern. The projected SADP could provide two-dimensional crystallographic data by comparing the ratio of ring diameter with the inter planer spacing. Indexing was the process employed to obtain crystallographic data from a material specimen (Xu and Ngan, 2004).

Fig. 3.11 Transmission electron microscope

In EBSD analysis, initial sections were made using a manually operated silicon carbide cut-off saw to enable rapid sectioning. To reduce specimen heating during cutting, a liquid coolant was applied continuously to the specimen and the cutting wheel. In the later stages of sectioning, a 0.5mm thick silicon carbide cutting wheel was used. To prepare the specimen surface, the specimen was ground and polished by a resin bonded diamond disc, followed by water based diamond suspension and the colloidal silica. The prepared surface was chemically etched to reveal the microstructure. EBSD observations were conducted on an AZtec Nordlys Max3 system (as shown in Fig. 3.12) operating at an accelerating voltage of 20kV and a step size of 0.2-2μm (Hosseini *et al.*, 2019). In the results, the raw uncleaned data is always presented in addition to any maps which have been noise reduced.

Fig. 3.12 EBSD system for composition analysis

3.6 Electrochemical Test

The effect of shape and size of the interlayer used for laser welding on the corrosion properties of the welded joint will be obtained by the measurement of corrosion potential and corrosion current density. The corrosion potential and corrosion current density were evaluated by cyclic potentiodynamic polarization test in Hanks' solution to verify the corrosion properties of the welded sample in a simulated body fluid at 37.5 °C based on ASTM F2129 (ASTM, 2004) and G5 (ASTM, 2014). The sample was embedded in epoxy resin with an exposed surface area of 8 mm^2 which consisted of weld zone and heat affected zone of NiTi-Ni side. The sample was then degreased by ultrasonic cleaning for 15 minutes, followed by cleaning in distilled water for 5 minutes.

The sample was immersed in Hanks' solution (a simulated body fluid) for 1 hour before initiating polarization. A saturated calomel electrode (SCE) was used as the reference electrode contacted the solution via the bridge tube and graphite rods were used as the counter electrode to supply the current flowing at the sample during the test. The tests started from 250 mV below the open-circuit potential at a sweep rate of 1 mV/s. Galvanic corrosion potential in the exposed area of weld zone and heat affected zone of NiTi-Ni was captured at both 1 hour and 24 hours. Both NiTi materials as received and welded joint with different welding conditions were selected to perform this test. The measured corrosion potential and corrosion current density of NiTi materials as received would be acted as the reference for results comparison in order to identify the welded joint with acceptable corrosion properties. The results obtained in this test would also enable the identification of unfavorable phases in the welded joint.

3.7 Differential Scanning Calorimetry (DSC)

The different amounts of phases in the fusion zone would affect the transformation behavior of NiTi. Differential scanning calorimetry (DSC) was used to characterize the structural transformation temperatures of the NiTi materials as received and the fusion zone of welds. The DSC plot (as shown in Fig. 3.13) identified the transformation temperatures and described the thermal response of a typical NiTi sample. The transformation temperatures are found from the intercept of the tangents to the transformation peak and base line as per the ASTM F2004-05 standard.

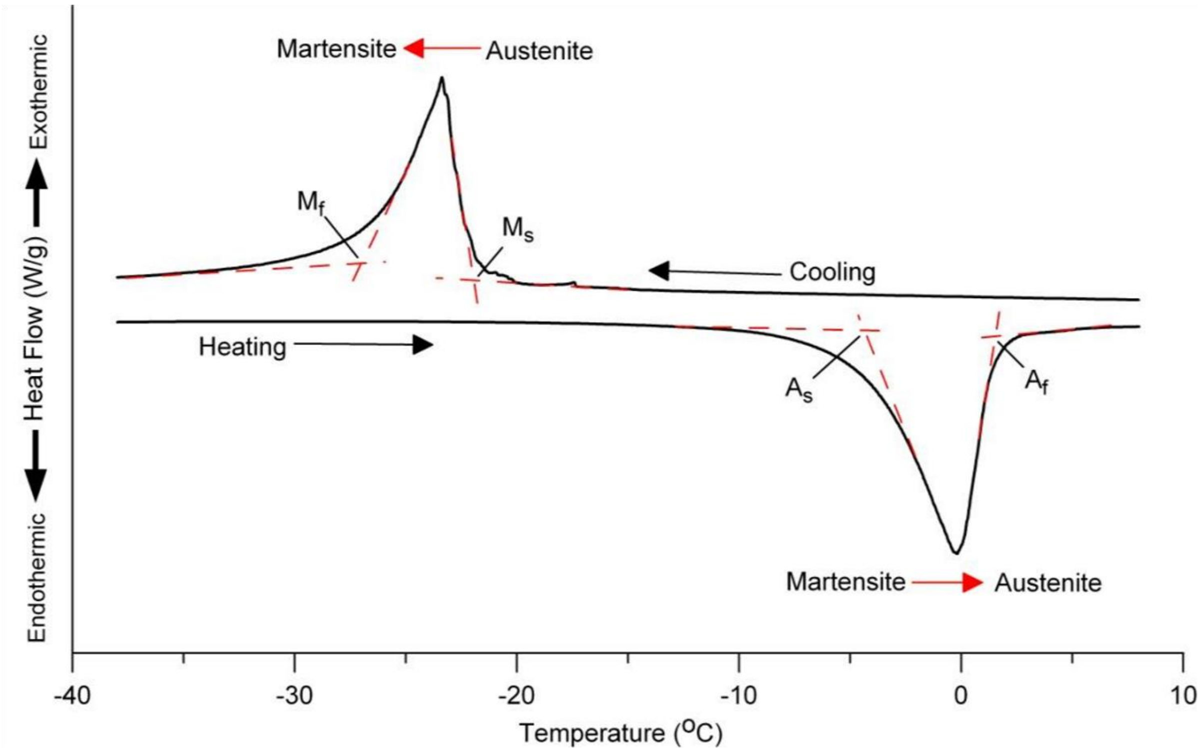

Fig. 3.13 Typical DSC plot for NiTi alloy with identified phase transformation temperature (Hamilton *et al.*, 2004)

A Mettler Toledo DSC3 as shown in Fig. 3.14 was used. The central area of the welded bead with a 3mm square and a height of 1mm were cut by means of wire electro-discharge machining as shown in Fig. 3.15. The specimens were mounted in crimped Al pans. The DSC test was performed at the heating and cooling rates of 10°C/min with nitrogen gas of 10ml/min flow rate to obtain the phase transformation temperatures of the samples (Zotov, *et al.*, 2014). Comparison of results between the NiTi materials as received and welded samples with minimum unfavorable phases were conducted to aid the further correlation between the amount of different phases in the fusion zone and the phase transformation temperature of welded joint, which was done in the later stage. Due to the reduced dimensions of the specimens required for DSC analysis (3 mm square), a precision cutting machine was used to carefully separate the fusion zone from the remaining material. However, as the extension of either the heat affected or fusion zones are within the range of a few millimeters of the welded joint. It is not possible to ensure that the analyzed material comprised only the fusion zone. That is, the DSC sample from the fusion zone could also have some parts of the adjacent heat affected zone.

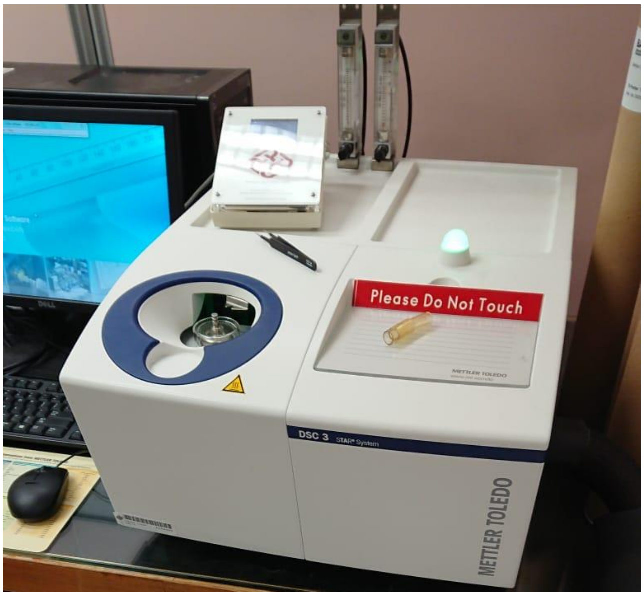

Fig. 3.14 Differential scanning calorimeter

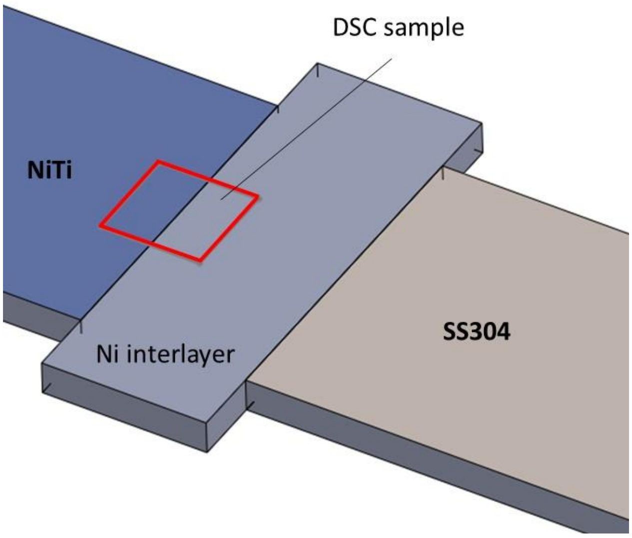

Fig. 3.15 Location of DSC sample for NiTi-Ni-SS joint

4 Results and Discussion I – Preliminary Study

4.1 Introduction

In this chapter, the effect of Co and Ni interlayer for laser welding of NiTi and stainless steel at the same process parameter setting, the tensile strength, hardness, EDX and XRD analysis of NiTi-SS304, NiTi-Co-SS304 and NiTi-Ni-SS304 joints are presented and discussed to find out the possible interlayer for the production of welds with favorable composition across the weld region.

4.2 Effect of Interlayer on Joint Strength

Based on the experiment results by Falvo *et al*. (2013), 850W laser power with beam diameter of 0.6mm welded 1mm NiTi to NiTi and made a good formation of weld bead with power density of 3 x 10^5 Wcm^{-2}. This power density acted as the minimum power density of this preliminary study, 1000W laser power of the fiber laser machine used in this project could achieve this power density. However, full penetration could only achieve when the laser power increased to 1400W at welding speed of 300 mm/s for continuous laser welding and at welding speed of 75 mm/s for pulsed laser welding of NiTi-Ni-SS304. The effect of the laser power at fixed welding speed of 300mm/s on penetration is given in Fig. 4.1.

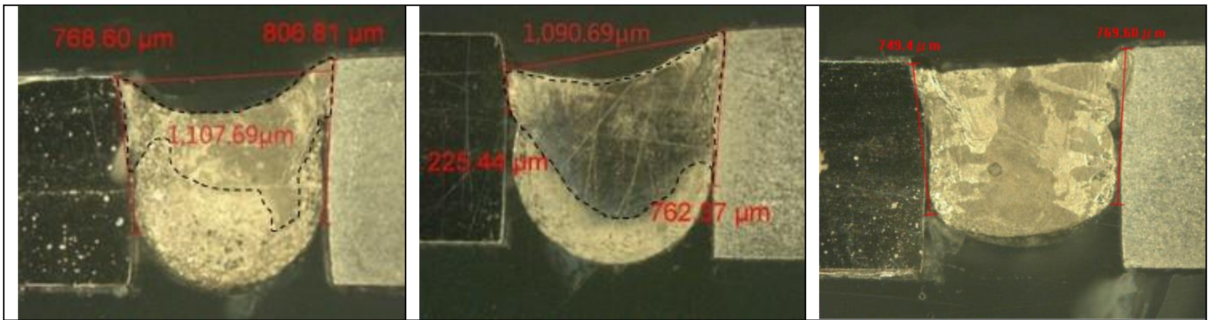

(a)	(b)	(c)

Fig. 4.1 Cross section of NiTi-Ni-SS304 at 300mm/s welding speed with laser power of (a) 1000W, (b) 1200W, and (c) 1400W for continuous laser welding

As 1400W laser power enabled full penetration of NiTi-Ni-SS304 joint, welding NiTi-SS304, NiTi-Co-SS304 and NiTi-Ni-SS304 joint with decreasing welding speed at fixed laser power were conducted.

Based on the stress-strain curves, the results of ultimate tensile strength of the different weld joints were obtained. Fractures of all welded samples were located in the weld zone near NiTi side as shown in Fig. 4.2, no matter whether a pulsed or continuous wave laser and interlayer material was Co or Ni.

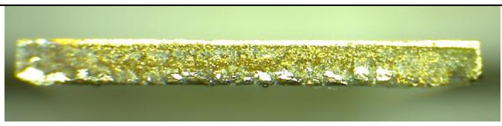	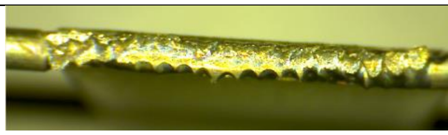
NiTi side	Ni interlayer side
(a) Welding speed = 25mm/s (Sample no: P14)	
	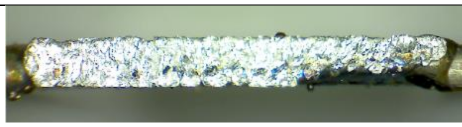
NiTi side	Co interlayer side
(b) Welding speed = 25mm/s (Sample no: P8)	
	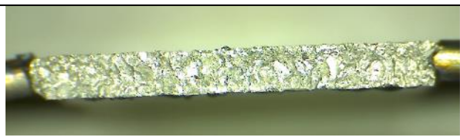
NiTi side	Ni interlayer side
(c) Welding speed = 175mm/s (Sample no:31)	
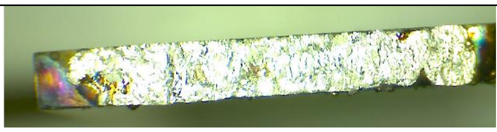	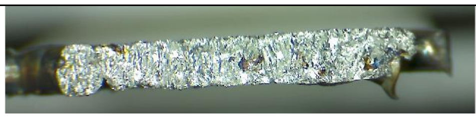
NiTi side	Co interlayer side
(d) Welding speed = 175mm/s (Sample no:25)	

Fig. 4.2 Fracture surface of (a) NiTi-Ni-SS304 (pulsed laser), (b) NiTi-Co-SS304 (pulsed laser), (c) NiTi-Ni-SS304 (continuous laser), and (d) NiTi-Co-SS304 (continuous laser)

The control of the weld joint composition by purely varying welding parameters is not easy, especially if the interlayer is not used. Experiments as shown in Table 4.1 indicated that the cracking occurred (as shown in Fig. 4.3) in NiTi-SS304 joint when welded by both pulsed laser (PW) and continuous laser welding (CW) with different welding speed. The joint strength of the NiTi-SS joint improved with the use of the interlayer of either Co or Ni (as shown in Fig. 4.4) by PW and CW.

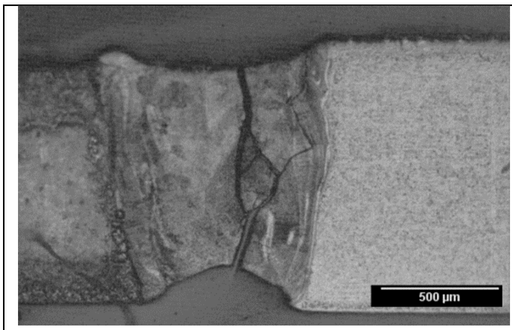

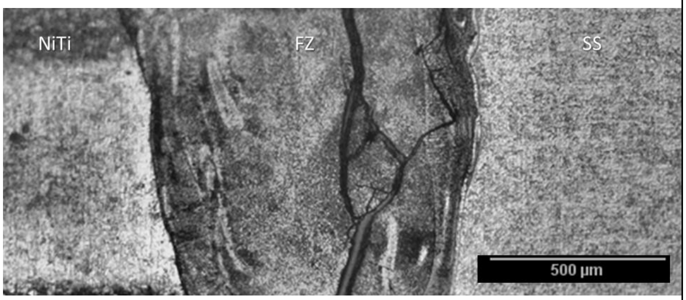

(a) (b)

Fig. 4.3 Macrograph of the cross sectional view of the SS-NiTi weld (Sample no: P19)

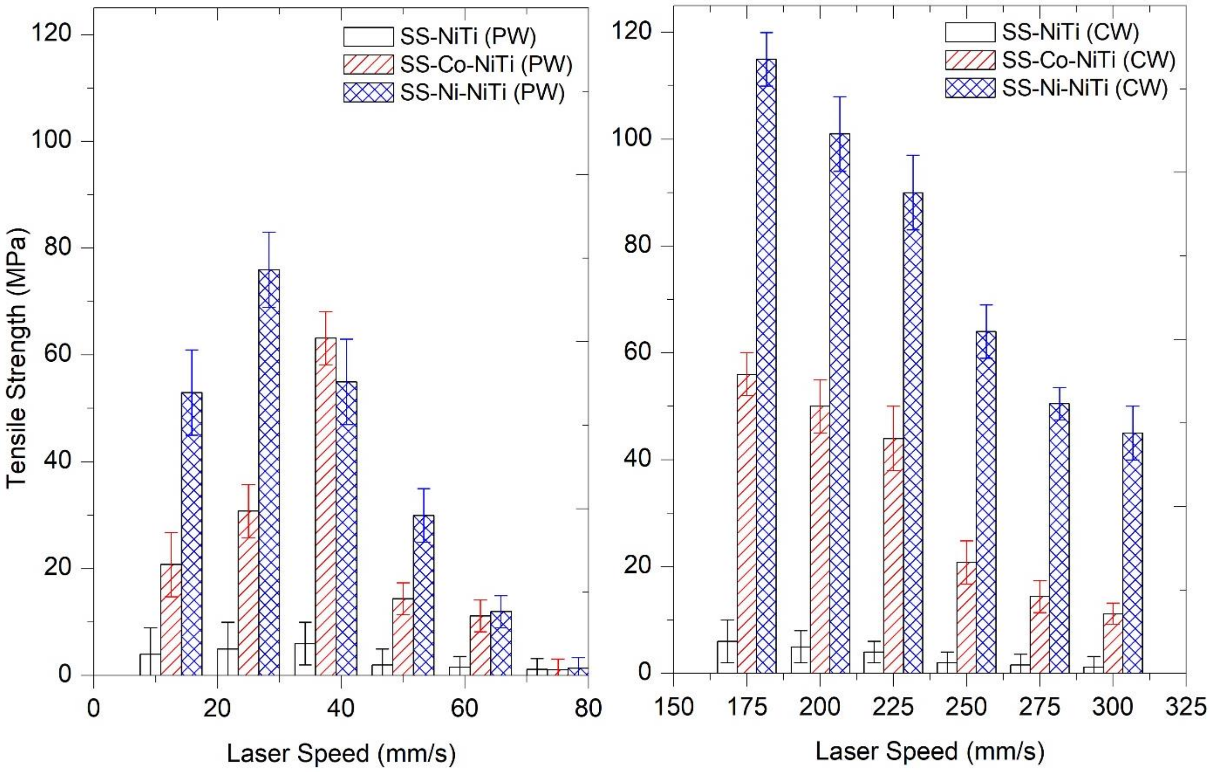

Fig. 4.4 Effect of different interlayer materials on joint strength (laser power = 1400W)

Table 4.1 Observation of joint width with different process parameters

No	Base metal 1	Base metal 2	Interlayer material	Pulsed laser	Continuous laser	Observation
				Welding speed (mm/s)		
P1	NiTi	SS304	/	12.5	/	Full penetration with cracks and undercut
P2	NiTi	SS304	/	25	/	
P3	NiTi	SS304	/	37.5	/	
P4	NiTi	SS304	/	50	/	
P5	NiTi	SS304	/	62.5	/	Partial welded with full penetration and undercut
P6	NiTi	SS304	/	75	/	
P7	NiTi	SS304	Co	12.5	/	Full penetration with undercut
P8	NiTi	SS304	Co	25	/	
P9	NiTi	SS304	Co	37.5	/	
P10	NiTi	SS304	Co	50	/	
P11	NiTi	SS304	Co	62.5	/	Partial welded with full penetration and undercut
P12	NiTi	SS304	Co	75	/	
P13	NiTi	SS304	Ni	12.5	/	Full penetration with undercut
P14	NiTi	SS304	Ni	25	/	
P15	NiTi	SS304	Ni	37.5	/	
P16	NiTi	SS304	Ni	50	/	
P17	NiTi	SS304	Ni	62.5	/	Partial welded with full penetration and undercut
P18	NiTi	SS304	Ni	75	/	
P19	NiTi	SS304	/	/	175	Full penetration with cracks and undercut
P20	NiTi	SS304	/	/	200	
P21	NiTi	SS304	/	/	225	
P22	NiTi	SS304	/	/	250	
P23	NiTi	SS304	/	/	275	
P24	NiTi	SS304	/	/	300	
P25	NiTi	SS304	Co	/	175	Full penetration with undercut
P26	NiTi	SS304	Co	/	200	

P27	NiTi	SS304	Co	/	225	
P28	NiTi	SS304	Co	/	250	
P29	NiTi	SS304	Co	/	275	Partial welded with full penetration and undercut
P30	NiTi	SS304	Co	/	300	
P31	NiTi	SS304	Ni	/	175	Full penetration with undercut
P32	NiTi	SS304	Ni	/	200	
P33	NiTi	SS304	Ni	/	225	
P34	NiTi	SS304	Ni	/	250	
P35	NiTi	SS304	Ni	/	275	Partial welded with full penetration and undercut
P36	NiTi	SS304	Ni	/	300	

4.3 Effect of Interlayer on Chemical Composition

EDX spectrum composition analysis was conducted in the fusion zone of the NiTi-SS304 joint. Results as shown in Fig. 4.5 and Table 4.2 indicated the large amount of Ti, median amount of Fe and a small amount of Ni near the crack region. Base on Ti-Fe ratio, undesirable phases of FeTi or Fe_2Ti or Cr_2Ti appeared to be formed in the fusion zone. Based on the XRD analysis of the welded NiTi and stainless steel joint (as shown in Fig. 4.6), the phase constituting the bulk of the weld consisted of mononclinic B19' NiTi phase, rhombohedral Ni_4Ti_3, hexagonal crystal structure of Fe_2Ti and Cr_2Ti. The monoclinic B19' structure (martensite phase) differs from the cubic B2 structure (austenite phase) by a monoclinic distortion and additions by a shuffling of Ti and Ni atoms on the (110) B2 plane as shown in Fig. 4.7 (Won *et al.*, 2015). The presence of Laves phases (Fe_2Ti and Cr_2Ti) resulted in a greater brittleness and ductility deterioration, making the joint crack under relatively low stress. It is also noted that titanium plays a vital role in the formation of the intermetallic compounds because of the strong chemical affinity of Fe and Cr to Ti.

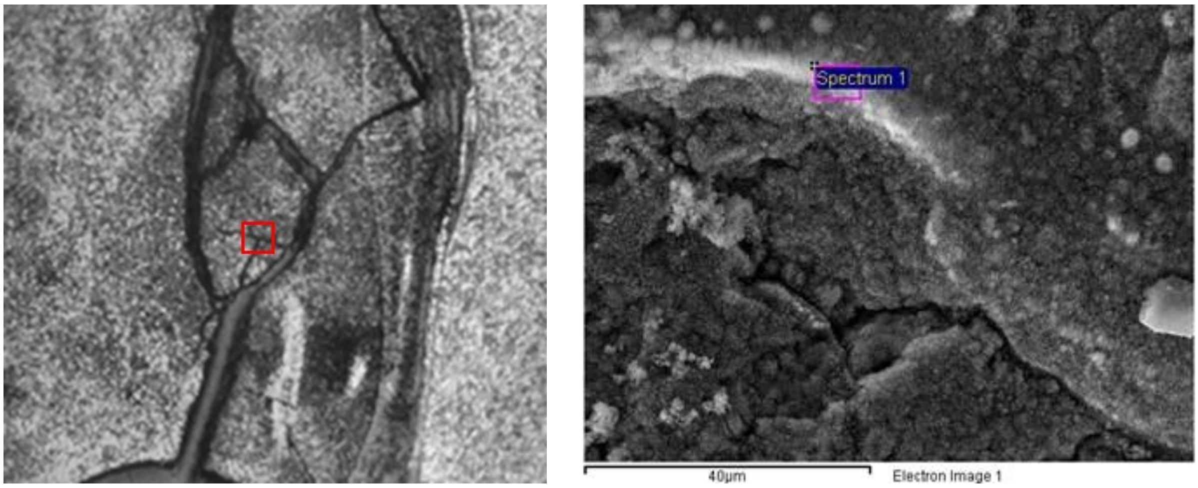

Fig. 4.5 (a) SEM image of NiTi-SS weld (sample no: P19) indicating the EDX line scan along the red line and the region from which the EDX of (b) was taken; (b) EDX spectrum of marked region

Table 4.2 EDX spectrum composition analysis of sample no: P19

Spectrum	Ti	Cr	Fe	Ni	Total
Spectrum 1	48.91	11.04	24.91	12.13	100.00

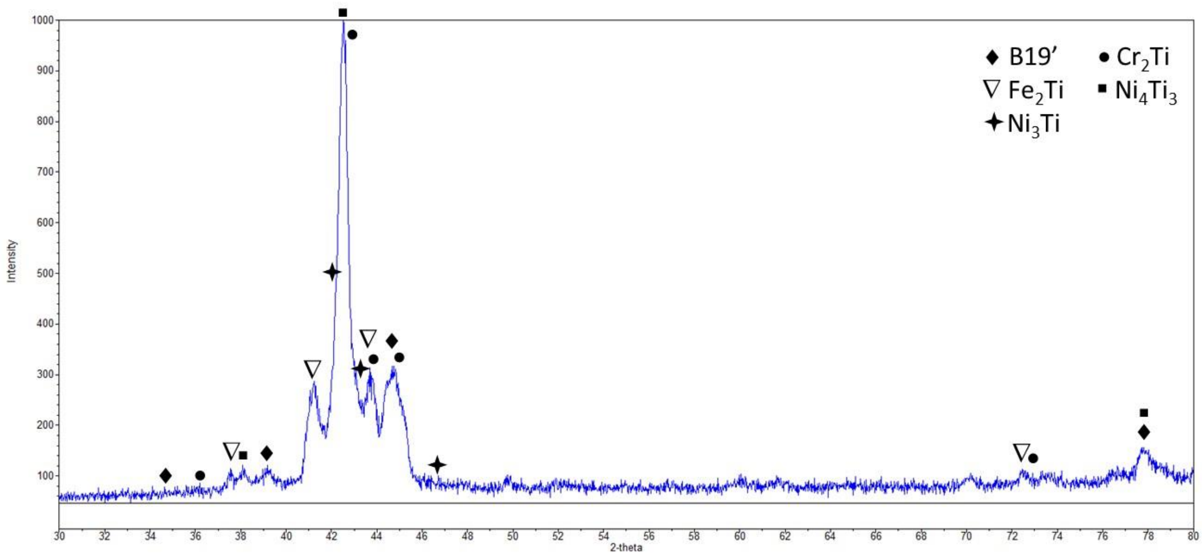

Fig. 4.6 XRD patterns recorded of welded joint of NiTi-SS (sample no: P19)

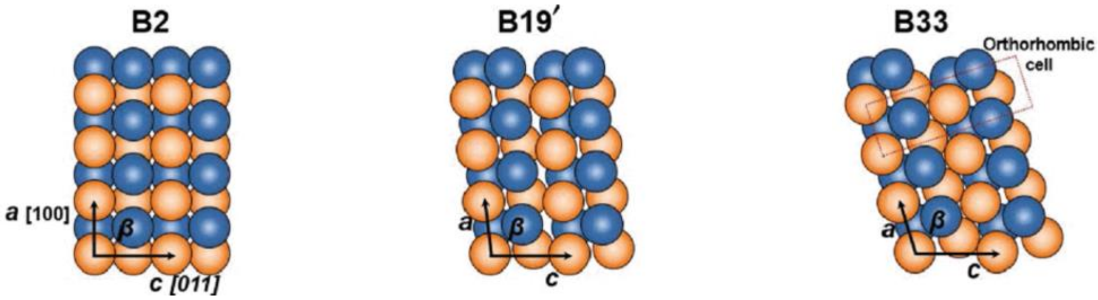

(a) (b) (c)

Fig. 4.7 Atomic Structures of (a) cubic B2 NiTi phase, (b) monoclinic B19’ NiTi phase, (c) orthorhombic B33 NiTi phase with Ni and Ti atoms presented by blue and orange balls respectively (Won *et al.*, 2015)

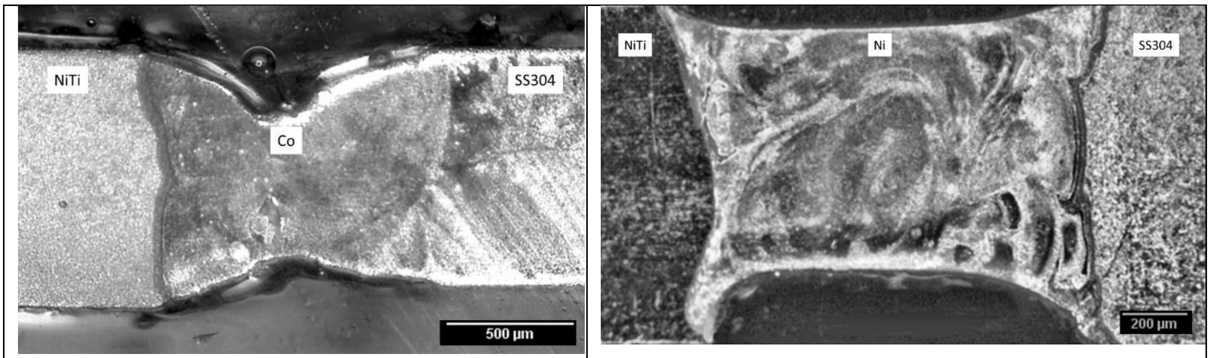

(a) (b)

Fig. 4.8 Macrograph of the cross sectional view of (a) the NiTi-Co-SS weld (Sample no: P25), and (b) the NiTi-Ni-SS weld (Sample no: P31)

Macrograph of the cross section of NiTi-Co-SS (sample no: P25) as shown in Fig. 4.8 indicates a full penetration weld. Co and Fe are close to Ni in the periodic table, thus it is expected that Co and Fe will become a substitute for Ni in the weld pool. Nakata *et al.* (1998) stated that Co has a stronger preference than Fe as a substitute for Ni. As a result, cobalt, as the interlayer also could minimize the formation of Fe_2Ti and Cr_2Ti (as shown in Fig. 4.9) but other intermetallic compounds ($CoTi_2$, Co_2Ti, Co_3Ti) would be formed according to the Ti-Co phase diagram as shown in Fig. 4.10. Many small peaks in the XRD patterns were found and they may be background as most advanced quantitative analysis modules/software are not available for the analysis of smaller peaks in XRD.

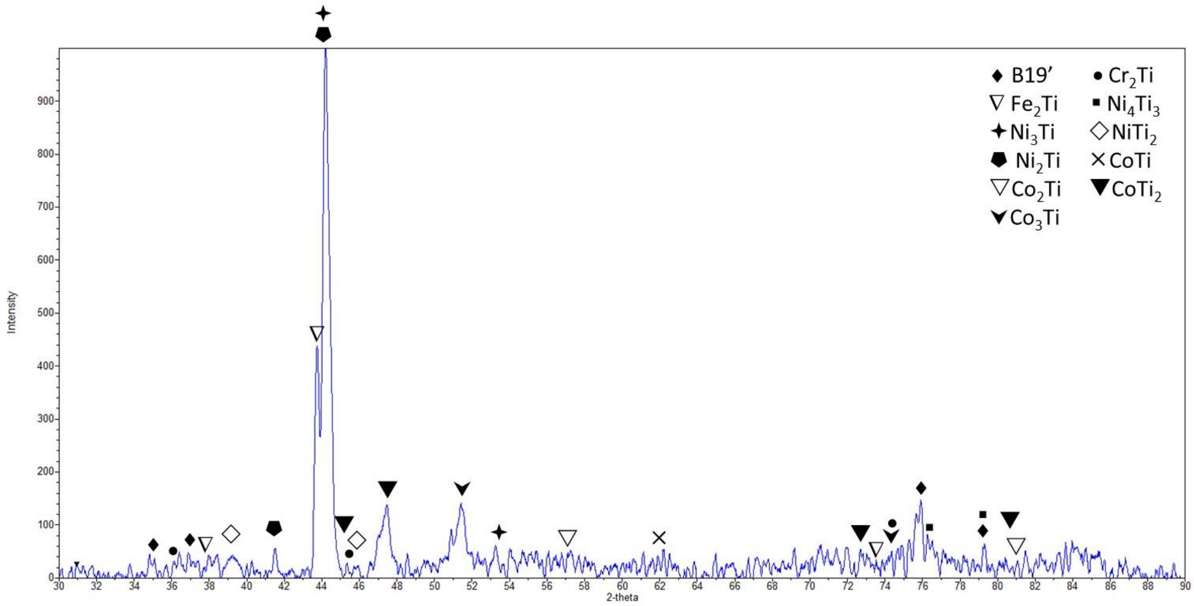

Fig. 4.9 XRD patterns recorded of welded joint of NiTi-Co-SS (sample no: P25)

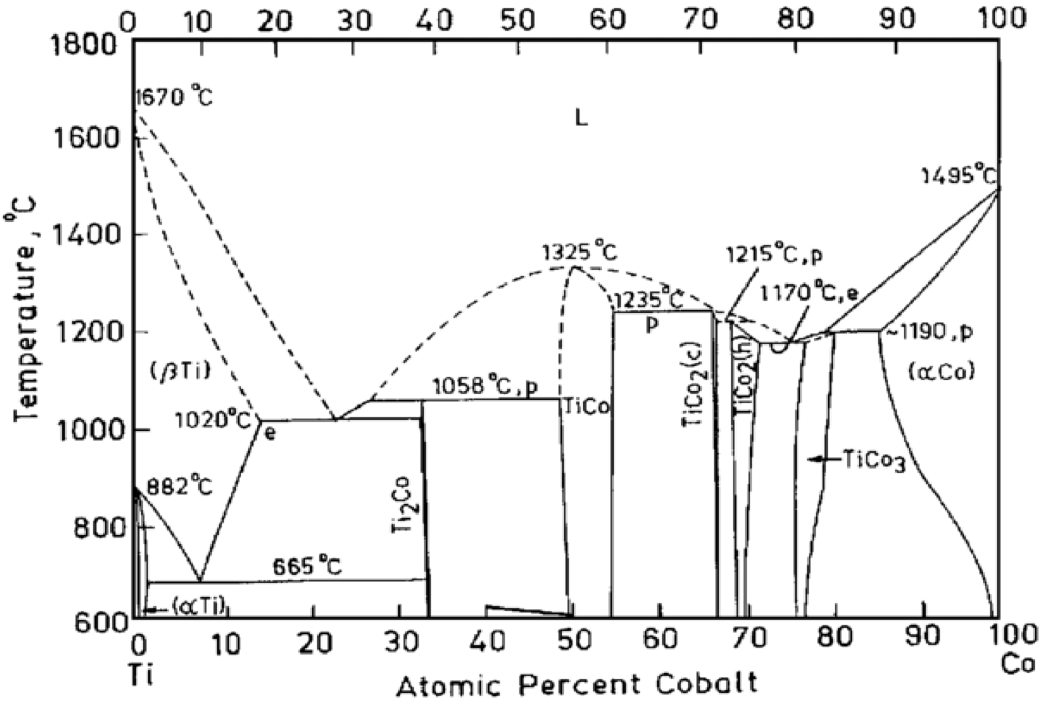

Fig. 4.10 Ti-Co phase diagram (Bandyopadhyay *et al.*, 2000)

A full penetration weld with a fusion zone that is asymmetric was observed in the cross section of NiTi-Ni-SS (sample no: P31) as shown in Fig. 4.8. The increased amount of Ni was expected to minimize the formation of Fe_2Ti and Cr_2Ti in the fusion zone. The microstructural observations made using SEM, together with the composition information, obtained from EDX were used for phase identification. EDX spectrum composition analysis for the cross section of the welded joint of NiTi and stainless steel with Ni interlayer (as shown in Fig. 4.11 and Table 4.3) indicated the presence of a smaller amount of Ti and Fe in the middle of the fusion zone. The increase in the strength of the NiTi-Ni-SS joint is due to the addition of nickel has the characteristic to keep large amounts of Ti and Fe apart in the weld pool, hence minimizing the formation of brittle intermetallics such as Fe_2Ti and Cr_2Ti (Fig. 4.12).

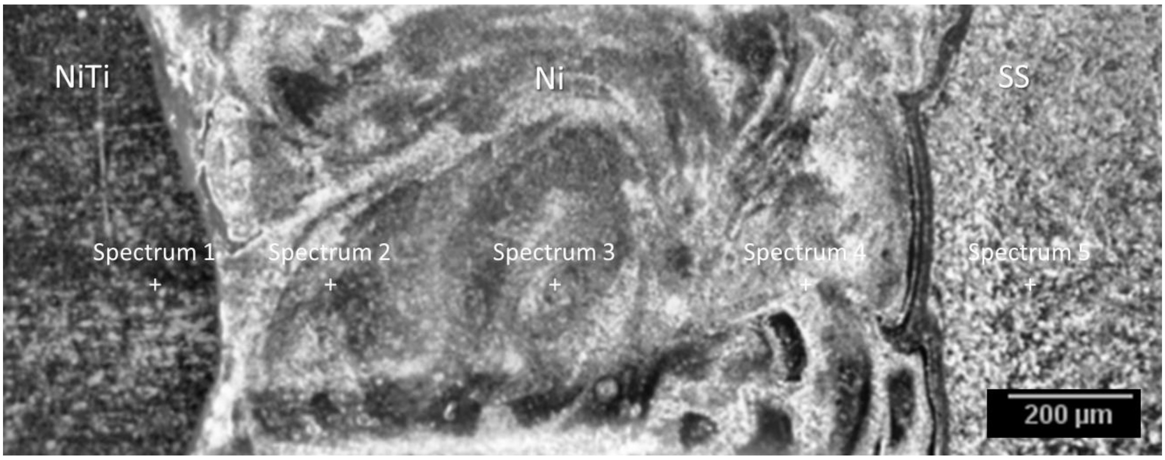

Fig. 4.11 SEM image of NiTi-Ni-SS weld with marked location of EDX spectrum (Sample no: P31)

Table 4.3 EDX spectrum composition analysis of Fig. 4.11.

	Element (wt%)				
Spectrum	**Ti**	**Cr**	**Fe**	**Ni**	**Total**
Spectrum 1	45.43	0.07	0.18	54.32	100.00
Spectrum 2	32.70	0.81	5.68	60.81	100.00
Spectrum 3	17.85	4.06	15.51	62.58	100.00
Spectrum 4	3.79	7.41	28.75	60.05	100.00
Spectrum 5	0.12	11.51	79.86	8.50	100.00

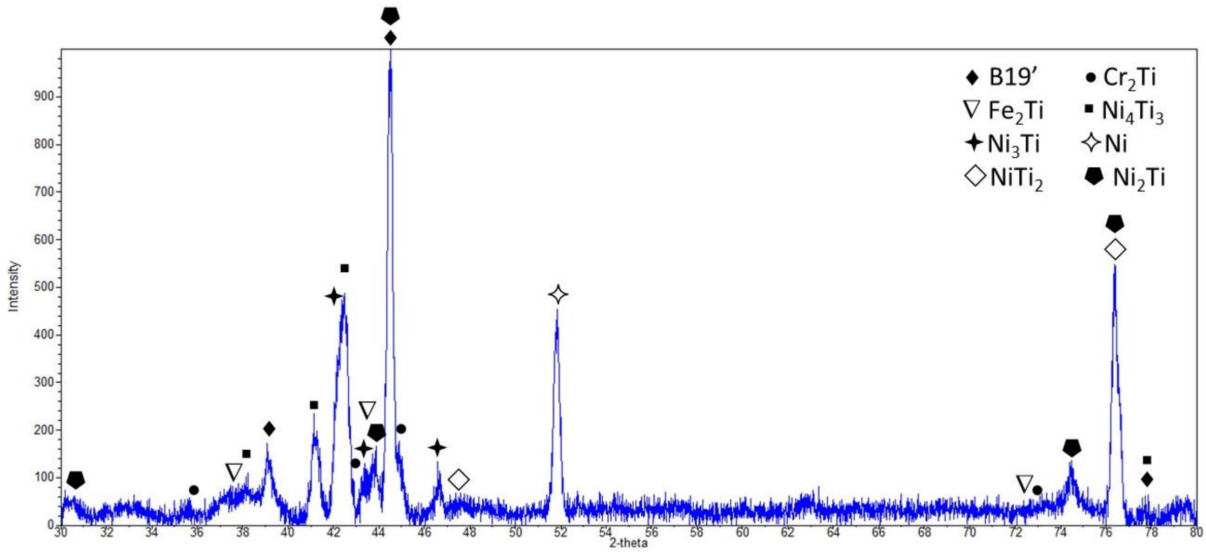

Fig. 4.12 XRD patterns recorded of welded joint of NiTi-Ni-SS (sample no: P31)

4.4 Effect of Interlayer on Hardness

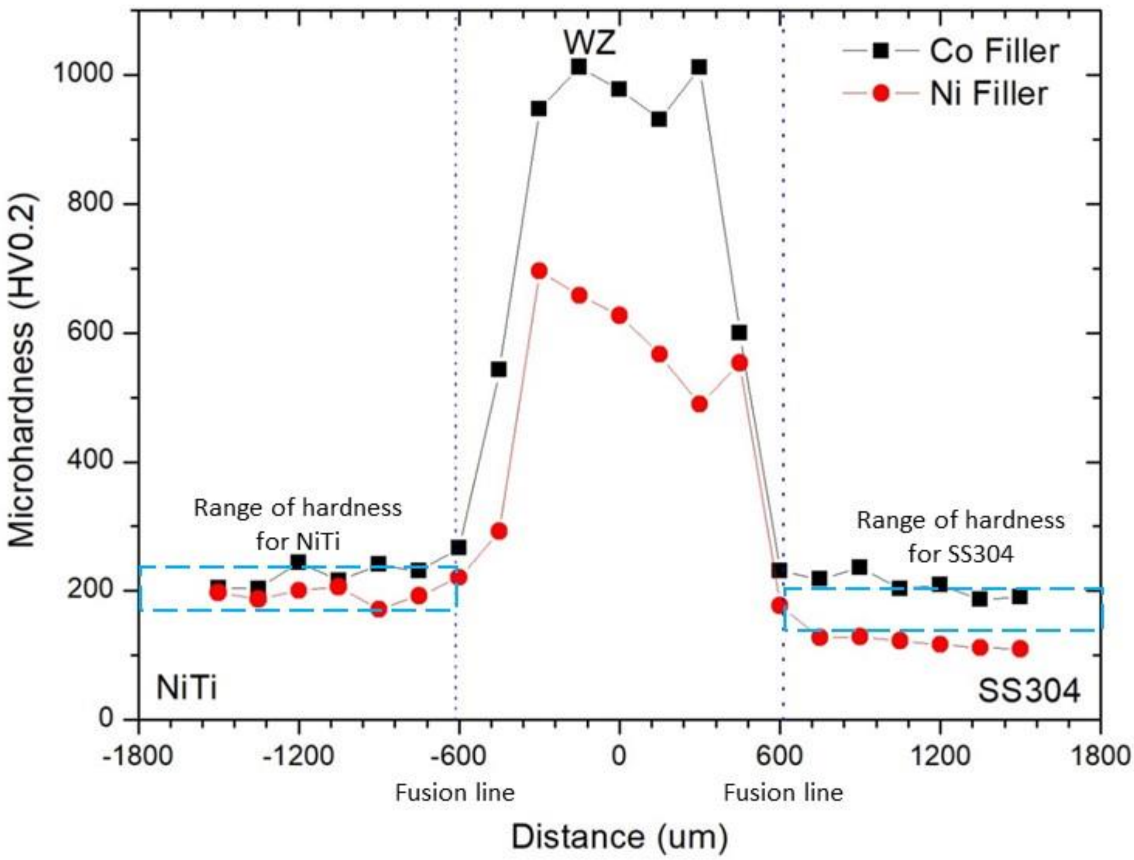

Fig. 4.13 Hardness of the weldment (sample no: P25 and P31)

In investigating the hardness of the joint, it is possible to obtain a considerable hardness increase, related to the intermetallic formation during the welding, in the weld zone of dissimilar joints. Hardness decreases towards the two sides of the base metals reaching expected values of around 200 HV for NiTi and 170 HV for stainless steel 304. Observation of the results of the microhardness test as shown in Fig. 4.13, reveals an increase of hardness (500 - 1000 HV) is noted in the weld zone (WZ) if the interlayer material changes from Ni to Co. Such increase of hardness was caused by the presence of $CoTi_2$, characterized as a high hardness value of about 800Hv (Xue and Wang, 2005), in the weld zone. This hardness increase reduces the toughness or energy to the point of failure because of ductility reduction. Therefore, nickel seems to be the possible interlayer for the production of welds with favorable composition across the weld region.

4.5 Chapter Summary

The effect of Co and Ni interlayer in joining NiTi and stainless steel on microstructure, tensile strength, hardness and chemical composition were investigated. The major observations are summarized as follow:

(i) The present of Co and Ni interlayer could improving the cracking occurred when joining NiTi and SS304 in both pulsed laser and continuous laser welding with same process parameter settings. The undesirable phases of FeTi or Fe_2Ti or Cr_2Ti, play vital role in brittleness, were reduced to enable the achievement of higher joint strength.

(ii) The continuous laser welding, produced the power density of 4.46 x 10^6 W/cm^2, enabled the joint strength of NiTi-Ni-SS joint to achieve the highest value of 115MPa when compared with that of the NiTi-SS and NiTi-Co-SS joint. With the same amount of power density provided, nickel produces favorable composition across the weld region rather than cobalt.

(iii) All welded samples of NiTi-Ni-SS were joined with undercut. The occurrence of undercut caused by the inadequate volume of interlayer material in filling the volume in between the gap of NiTi and SS304 as illustrated in Fig. 4.14. Therefore, in the Taguchi experiment, the effect of diameters of Ni interlayer were studied.

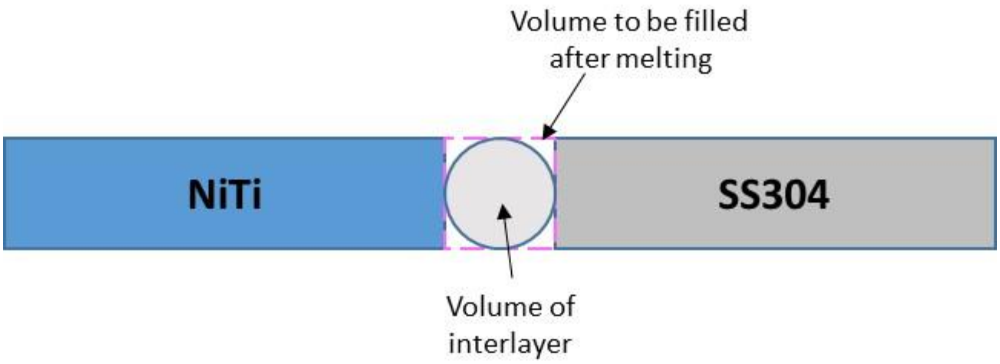

Fig. 4.14 Cross section of NiTi-interlayer-SS304

5 Results and Discussion II – Significant Process Parameters Quantification by Taguchi Method

5.1 Introduction

In this chapter, the quantification of significant laser welding process parameters (laser power, welding speed, diameter of Ni interlayer, focus position) to produce full penetrated NiTi-Ni-SS weldment with desirable tensile strength by Taguchi and statistical analysis is presented and discussed. The effect of rectangular shape Ni interlayer on produce full penetrated NiTi-Ni-SS welded by full factorial method is also presented. The microhardness and corrosion behavior of NiTi-Ni-SS joints welded with both circular shape and rectangular shape interlayer are discussed finally.

Thirty six tests were conducted based on the combinations of control factor defined in the specified orthogonal array table. A response table was completed by preparing specimens for each set of parameters. Taguchi method uses the S/N (signal-to-noise) ratio to determine the most significant factors. For a better result, a larger tensile strength is necessary and hence the larger-the-better criteria was the motivation for the select and used for analysis of this study.

$$\text{S/N ratio} = \log\left[\frac{1}{\mathrm{n}}\sum_{k=1}^{n} Xi^{2}\right] \quad (1)$$

Where X represents the experimental results and n represents the number of tests in one trial. The mean responses of the S/N ratio for tensile strength are calculated for all factors and are tabulated.

Tensile tests of all samples were carried out to determine the joint strength of the NiTi and stainless steel with Ni weldments. Profiles of microhardness including the base metals and the weld zone were determined based on the settings mentioned in previous chapter 3. Phenomena of microsegregation and the weight percentages of elements within welds was observed by means of scanning electron microscopy equipped with energy dispersive X-ray spectrometry (EDX) to identify possible phases in the weld zone. Finally, XRD was used to identify and quantify the chemical composition of the NiTi-Ni-SS weld pool joint.

5.2 L36 Taguchi Experiment on Circular Shape Ni Interlayer

5.2.1 Process Parameters Effects on Tensile Strength (Pulsed Laser Welding)

The effects of the welding speed, laser power, focus position and interlayer size of ∅1.2mm to ∅1.8mm were studied. Based on the circular shape of Ni as the interlayer, no further discussion of experiment 28-36 was performed as no full penetration could be successfully produced with an interlayer of size ∅1.8mm. The maximum tensile strength for interlayer size ∅1.2mm, ∅1.4mm and ∅1.5mm occurs in experiments 8, 17 and 26 as shown in Table 5.1. The preferable process parameters for circular shape interlayer occurs in experiment 8 (interlayer size: ∅1.2mm; laser power: 2000W; welding speed: 37.5mm; focus position: -0.5mm with respect to the surface of the specimens). Further increasing the interlayer size of Ni, however, decreased the strength of the joint. These experimental results as shown in Fig. 5.1 show that interlayer size varies the joint strength while, in this case, a suitable interlayer size of ∅1.2mm is able to improve the tensile strength of the laser welded joint to achieve a maximum of 245MPa.

Since the tensile strength of the weld joint has a “larger-the-better” characteristic, the S/N ratio was, thus, used for the total variation calculation. Fig. 5.2 shows the mean S/N ratio for the experiments.

Table 5.1 Tensile strength of NiTi-Ni-SS joint (pulsed laser welding)

No	Sample no	Diameter of interlayer (mm)	Laser power (W)	Welding speed (mm/s)	Focus position (mm)	Power density (x 10^6 W/mm2)	Tensile strength (MPa)
1	1	1.2	1600	25.0	-0.5	5.09	87
2	2	1.2	1600	37.5	0.0	5.09	97
3	3	1.2	1600	50.0	0.5	5.09	70
4	4	1.2	1800	25.0	0.0	5.73	107
5	5	1.2	1800	37.5	0.5	5.73	121
6	6	1.2	1800	50.0	-0.5	5.73	77
7	7	1.2	2000	25.0	0.5	6.37	195
8	8	1.2	2000	37.5	-0.5	6.37	245
9	9	1.2	2000	50.0	0.0	6.37	230
10	1	1.4	1600	25.0	-0.5	5.09	47
11	2	1.4	1600	37.5	0.0	5.09	72
12	3	1.4	1600	50.0	0.5	5.09	53
13	4	1.4	1800	25.0	0.0	5.73	57
14	5	1.4	1800	37.5	0.5	5.73	73
15	6	1.4	1800	50.0	-0.5	5.73	49
16	7	1.4	2000	25.0	0.5	6.37	90
17	8	1.4	2000	37.5	-0.5	6.37	101
18	9	1.4	2000	50.0	0.0	6.37	63
19	1	1.5	1600	25.0	-0.5	5.09	39
20	2	1.5	1600	37.5	0.0	5.09	54
21	3	1.5	1600	50.0	0.5	5.09	32
22	4	1.5	1800	25.0	0.0	5.73	51
23	5	1.5	1800	37.5	0.5	5.73	61
24	6	1.5	1800	50.0	-0.5	5.73	29
25	7	1.5	2000	25.0	0.5	6.37	20
26	8	1.5	2000	37.5	-0.5	6.37	77
27	9	1.5	2000	50.0	0.0	6.37	44
28	1	1.8	1600	25.0	-0.5	5.09	Fail to join

29	2	1.8	1600	37.5	0.5	5.09	Fail to join
30	3	1.8	1600	50.0	-0.5	5.09	Fail to join
31	4	1.8	1800	25.0	0.0	5.73	Fail to join
32	5	1.8	1800	37.5	-0.5	5.73	Fail to join
33	6	1.8	1800	50.0	0.0	5.73	Fail to join
34	7	1.8	2000	25.0	0.5	6.37	Fail to join
35	8	1.8	2000	37.5	0.0	6.37	Fail to join
36	9	1.8	2000	50.0	0.5	6.37	Fail to join

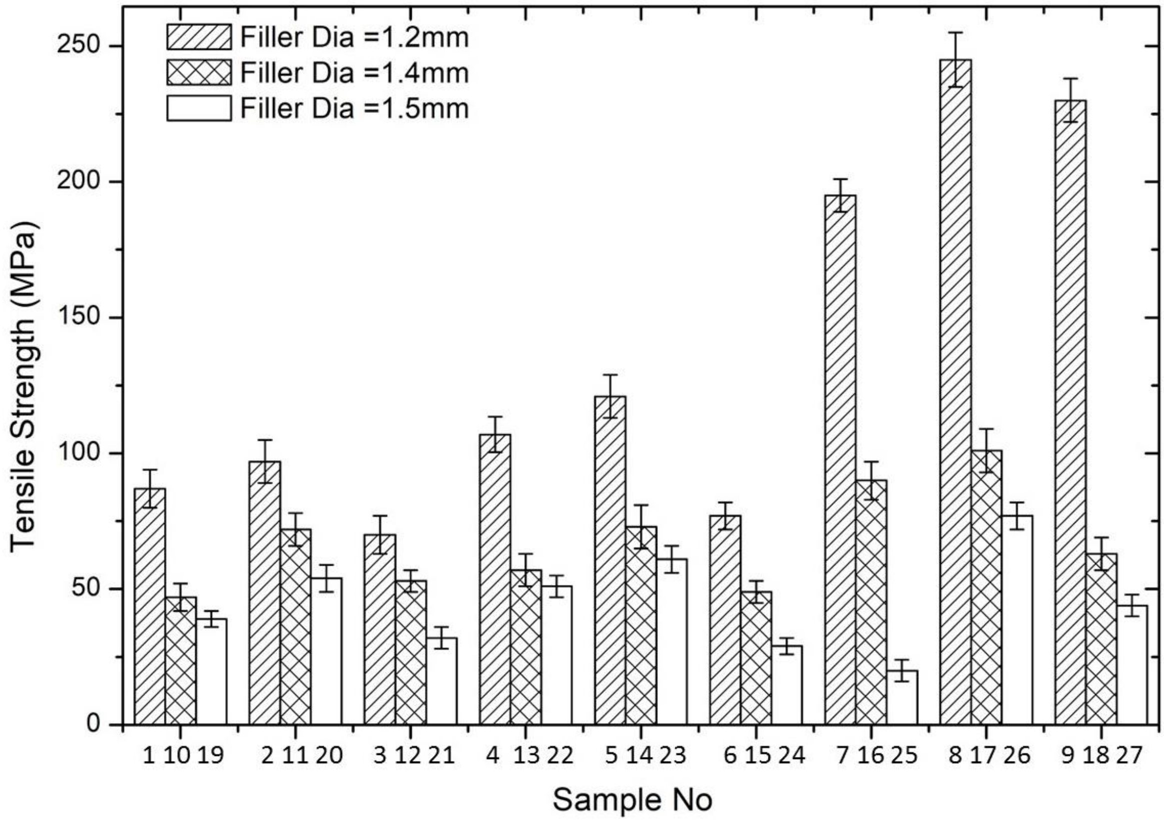

Fig. 5.1 Tensile strength of NiTi-Ni-SS welded joint with different interlayer diameter

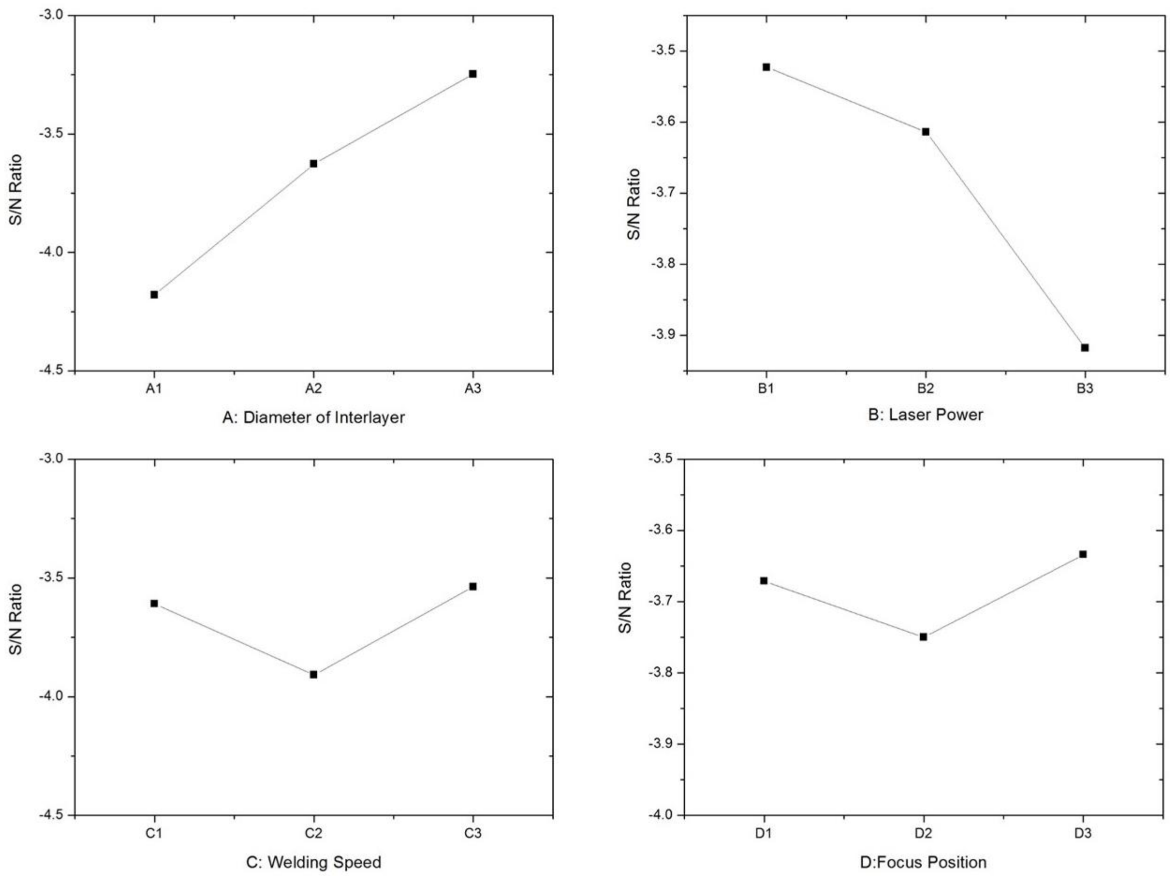

Fig. 5.2 Mean S/N ratio response plots of different factors for pulsed laser welding

Table 5.2 Analysis of Variance (ANOVA) results for tensile strength – PW

	Degree of Freedom	Variation (S)	Variance (V)	F-ratio	Contribution
Diameter of interlayer (mm)	2	3.958	1.979	3.031	72.132
Laser power (W)	2	0.769	0.384	0.589	14.010
Welding speed (mm/s)	2	0.697	0.349	0.534	12.708
Focus position (mm)	2	0.063	0.032	0.048	1.150

Based on the ANOVA results as shown in Table 5.2, it was found that the most significant factor, namely the size of interlayer followed by the welding speed, laser power focus position contributed the greater contribution ratio, to the increased tensile strength. Between the other two, it was observed that highest contribution was the interlayer size (72.132%), while the focus position (1.150%) was the lowest. Both laser power (14.010%) and welding speed (12.708%) had moderate value.

The optimal parameter combination set was found as shown in Fig.5.2. The predicted mean (M) of the response characteristic of tensile strength can be expressed as

M = (A1 – Mc) + (B3 – Mc) + (C2 – Mc) + (D2 – Mc) + Mc

Where A1 is the factor A at level 1, B3 is the factor B at level 3, C2 is the factor C at level 2, D2 is the factor D at level 2, Mc is the current average of S/N ratio.

As the joining of NiTi and stainless steel with interlayer size of ∅1.2mm could achieve better tensile strength than those joints with interlayers sizes ∅1.4mm and ∅1.5mm, ANOVA analysis without the factor of filler diameter was performed once more to determine the contribution ratio.

Table 5.3 Analysis of Variance (ANOVA) results for tensile strength – PW (Interlayer size: ∅1.2mm)

	Degree of Freedom	Variation (S)	Variance (V)	F-ratio	Contribution
Laser power (W)	2	1.222	0.611	89.394	91.576
Welding speed (mm/s)	2	0.089	0.045	6.530	6.690
Focus position (mm)	2	0.023	0.012	1.693	1.734

Table 5.3 shows that laser power contributed the highest ratio (91.576%) to alter the tensile strength while welding speed and focus position contributed 6.690% and 1.734% respectively. The effects of the laser power were the largest and were substantially larger than their interactions. The analyzed results confirmed that the interlayer size is shown to alter the

tensile strength the most while the increase of laser power is shown to increase the tensile strength in the welded joint of NiTi and stainless steel with ∅1.2mm Ni interlayer. Table 5.4 shows that the optimal set of parameter combinations was found to be the same as that determined in Fig. 5.2. The predicted mean of the response characteristic of tensile strength, based on the optimal set of parameter combinations, was calculated. Table 5.5 shows the differences of the actual and the predicted results of the combination optimal set of process parameters.

Table 5.4 Mean S/N Ratio response table for tensile strength – PW (Interlayer size: ∅1.2mm)

	Label	Level 1	Level 2	Level 3	Difference	Rank
Laser power (W)	B	-3.848	-3.999	-4.694	0.846	1
Welding speed (mm/s)	C	-4.173	-4.306	-4.062	0.244	2
Focus position (mm)	D	-4.145	-4.252	-4.143	0.108	3

Table 5.5 Comparison of actual and predicted results of tensile strength

	Predicted result	Experimental result	Difference
Tensile strength	224.2	205	19.2
S/N ratio	-4.694	-4.624	-0.078

5.2.2 Process Parameters Effects on Tensile Strength (Continuous Laser Welding)

In parallel to the pulsed laser welding experiments, the same shape of Ni as the interlayer was used for joining NiTi and stainless steel by means of the use of a continuous wave laser. The effects of the laser power, welding speed, focus position and interlayer size have also been studied. The optimum condition of tensile strength for interlayer size of ∅1.2mm, ∅1.4mm,

∅1.5mm and ∅1.8mm occurs respectfully in, experiment 8, 17, 24 and 28 as shown in Table 5.6. The optimum condition for circular shape interlayer occurs in experiment 17 (interlayer size: ∅1.4mm; laser power: 2000W; welding speed: 150mm; focus position: -0.5mm with respect to the surface of the specimens). These experimental results (as shown in Fig. 5.3), show that the tensile strength of the laser welded joint, with interlayer size ∅1.4mm, could achieve a maximum of 175MPa. Fig. 5.4 shows the S/N ratio for the experiments.

Table 5.6 Levels of the control factors for laser welding (circular shape interlayer)

No	Diameter of interlayer (mm)	Laser power (W)	Welding speed (mm/s)	Focus position (mm)	Power density (x 10^6 W/mm2)	Tensile strength (MPa)
1	1.2	1600	150	-0.5	5.09	46
2	1.2	1600	175	0.0	5.09	9
3	1.2	1600	200	0.5	5.09	23
4	1.2	1800	150	0.0	5.73	41
5	1.2	1800	175	0.5	5.73	36
6	1.2	1800	200	-0.5	5.73	42
7	1.2	2000	150	0.5	6.37	25
8	1.2	2000	175	-0.5	6.37	73
9	1.2	2000	200	0.0	6.37	55
10	1.4	1600	150	-0.5	5.09	114
11	1.4	1600	175	0.0	5.09	82
12	1.4	1600	200	0.5	5.09	120
13	1.4	1800	150	0.0	5.73	127
14	1.4	1800	175	0.5	5.73	105
15	1.4	1800	200	-0.5	5.73	149
16	1.4	2000	150	0.5	6.37	99
17	1.4	2000	175	-0.5	6.37	175
18	1.4	2000	200	0.0	6.37	164
19	1.5	1600	150	-0.5	5.09	66
20	1.5	1600	175	0.0	5.09	25
21	1.5	1600	200	0.5	5.09	41

22	1.5	1800	150	0.0	5.73	120
23	1.5	1800	175	0.5	5.73	42
24	1.5	1800	200	-0.5	5.73	134
25	1.5	2000	150	0.5	6.37	88
26	1.5	2000	175	-0.5	6.37	132
27	1.5	2000	200	0.0	6.37	117
28	1.8	1600	150	-0.5	5.09	151
29	1.8	1600	175	0.5	5.09	120
30	1.8	1600	200	-0.5	5.09	126
31	1.8	1800	150	0.0	5.73	137
32	1.8	1800	175	-0.5	5.73	127
33	1.8	1800	200	0.0	5.73	129
34	1.8	2000	150	0.5	6.37	65
35	1.8	2000	175	0.0	6.37	141
36	1.8	2000	200	0.5	6.37	100

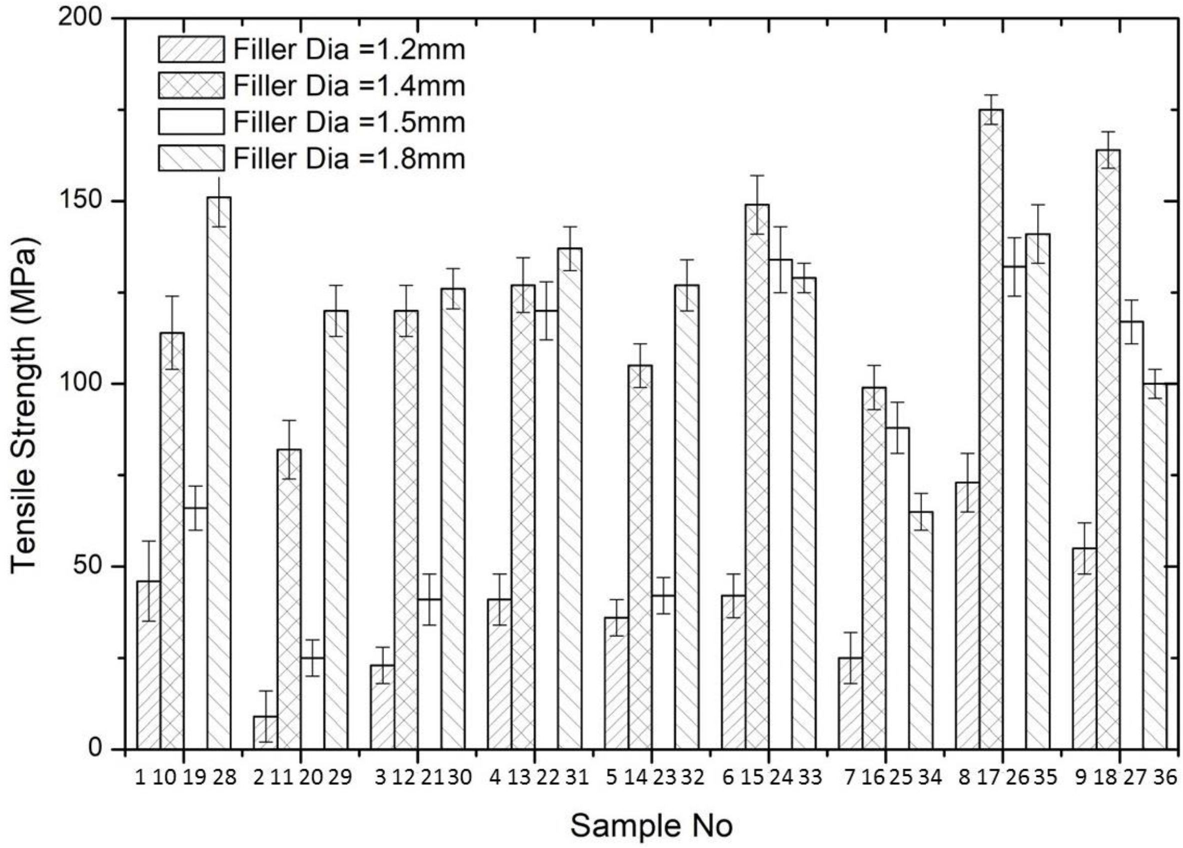

Fig. 5.3 Comparison of tensile strength of welded joint with different filler diameter

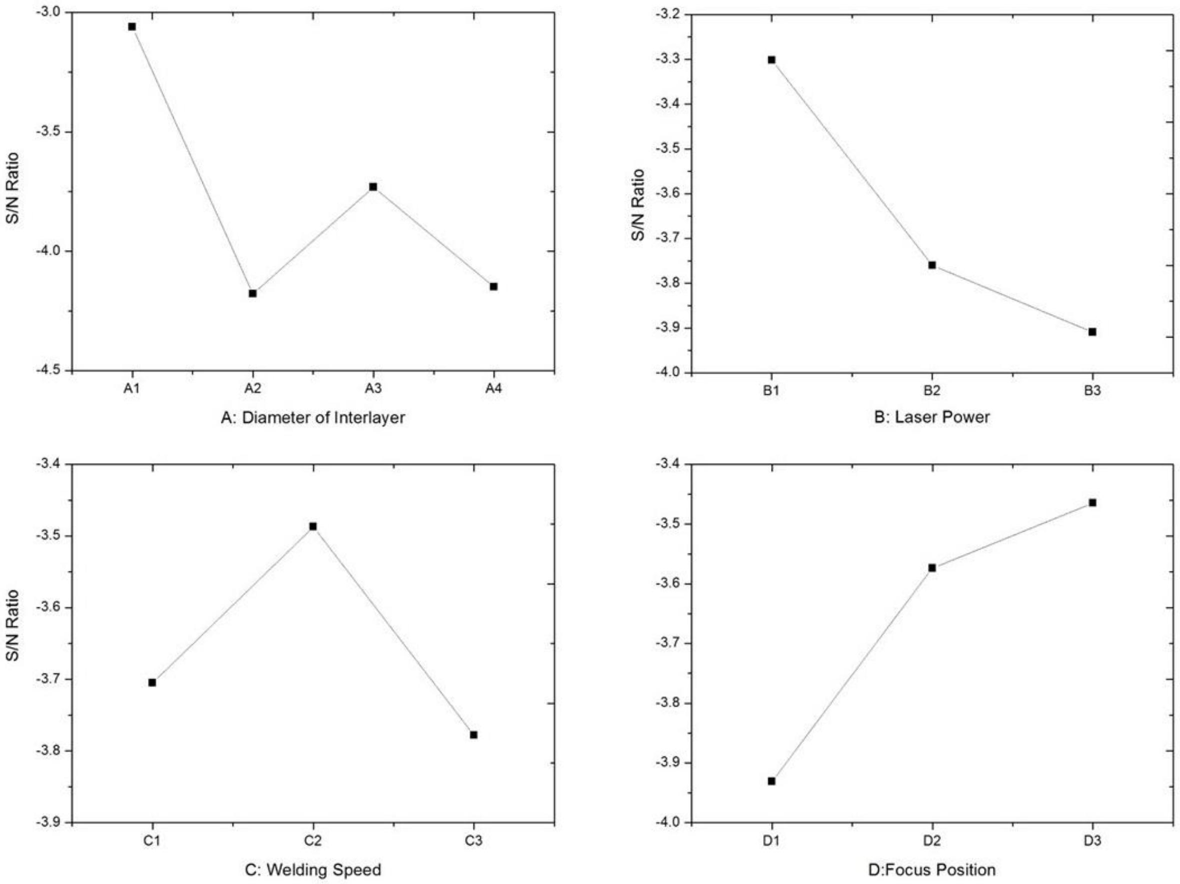

Fig. 5.4 Mean S/N ratio response plots of different factors for continuous laser welding

Table 5.7 Analysis of Variance (ANOVA) results for tensile strength – CW

	Degree of Freedom	Variation (S)	Variance (V)	F-ratio	Contribution
Interlayer size (mm)	3	160.645	53.548	-1.048	98.000
Laser power (W)	2	1.799	0.900	-0.012	1.098
Welding speed (mm/s)	2	0.411	0.206	-0.003	0.249
Focus position (mm)	2	1.069	0.534	-0.007	0.652

Table 5.7, above, gives the results of ANOVA, it is found the most significant factor with a contribution ratio, that increases the tensile strength, is the interlayer size followed by the laser power, focus position and welding speed. It is observed that the contribution ratio of

interlayer size is 98.000, has the higher effect on the joint strength, than the rest of each of the process parameters.

Table 5.8 Mean S/N Ratio response table for tensile strength – CW

	Label	Level 1	Level 2	Level 3	Level 4	Difference	Rank
Interlayer Size (mm)	A	-3.061	-4.178	-3.732	-4.149	1.118	1
Laser Power (W)	B	-3.302	-3.760	-3.909	/	0.607	2
Welding Speed (mm/s)	C	-3.705	-3.487	-3.778	/	0.290	4
Focus Position (mm)	D	-3.931	-3.574	-3.465	/	0.466	3

Table 5.8 shows that the optimal set of combination of parameter is found to be

M = (A2 – Mc) + (B3 – Mc) + (C3 – Mc) + (D1 – Mc) + Mc

As the joining of NiTi and stainless steel with interlayer size of ∅1.4mm could achieve better tensile strength than those joints with interlayer sizes of ∅1.2mm, ∅1.5mm and ∅1.8mm, ANOVA analysis without the interlayer size factor was once more conducted, to determine the contribution ratio.

Table 5.9 Analysis of Variance (ANOVA) results for tensile strength – CW (Interlayer size: ∅1.4mm)

	Degree of freedom	Variation (S)	Variance (V)	F-ratio	Contribution
Laser power (W)	2	0.111	0.055	138.267	38.366
Welding speed (mm/s)	2	0.080	0.040	100.486	27.883
Focus position (mm)	2	0.097	0.049	121.634	33.751

Table 5.10 Mean S/N Ratio response table for tensile strength – CW (Interlayer size: ∅1.4mm)

	Label	Level 1	Level 2	Level 3	Difference	Rank
Laser Power (W)	B	-4.033	-4.104	-4.315	0.269	1
Welding Speed (mm/s)	C	-4.199	-4.119	-4.155	0.207	2
Focus Position (mm)	D	-4.302	-4.311	-4.064	0.251	3

Table 5.11 Comparison of actual and predicted results of tensile strength

	Predicted Result	Experimental Result	Difference
Tensile strength	169	127	42.0
S/N ratio	-4.456	-4.208	-0.248

Table 5.9 shows that the 3 factors contribute similar ratios as regards the tensile strength in the NiTi and stainless steel welded joint with ∅1.4mm Ni interlayer. Table 5.10 shows that the optimal parameter combination was found to be the same as that found in Fig. 5.4. Table 5.11 shows the differences of actual and predicted results of the optimal process set of parameter combinations.

It has been observed that continuous laser welding produces the greatest weld volume, due to its prolonged heating effects, while the pulsed laser welding produces just a full penetration weld with a faster cooling rate, owing to its very slow heat input. As a result, pulsed laser welding could produce joints with lower porosity and less spatter and tends to enhance the mechanical properties of the welded joint. In the above study, it is shown that a higher tensile strength could be achieved by pulsed laser welding, however, such a fast cooling rate causes an increasing in the hardness in the weld zone as shown in Fig. 5.5. Besides, a full weld could be achieved by continuous laser welding. As a result, continuous laser welding has the potential to achieve a better joint of NiTi-Ni-SS.

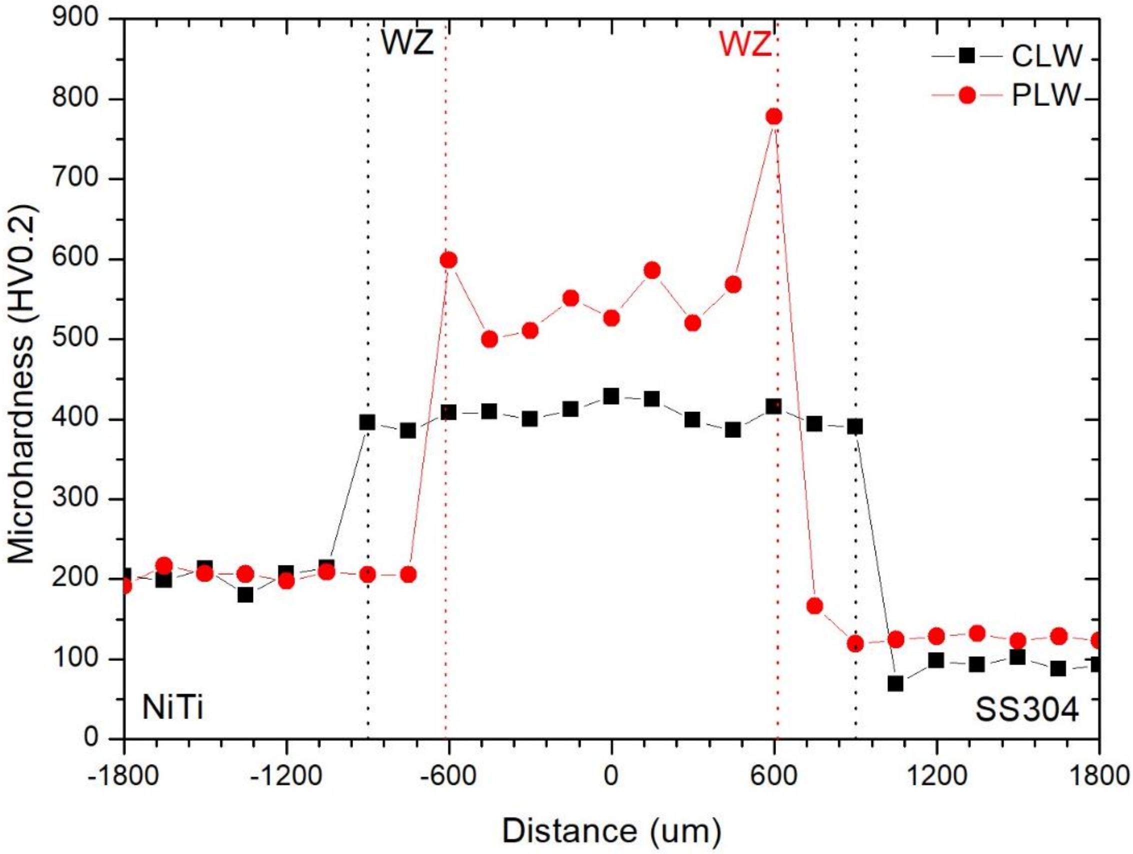

Fig. 5.5 Hardness traces along cross-section of welds made by continuous laser welding (CW – sample no: 17) & pulsed laser welding (PW – sample no: 8)

EDX spectrum composition analysis for the cross section of the NiTi and stainless steel welded joint with Ni interlayer (as shown in Table 5.12) shows that the intensity of Ti sharply drops from the base metal of the NiTi side to the interlayer and then finally to the base meal of the stainless steel side. Both Ti and Fe, however, were still identified in the fusion zone.

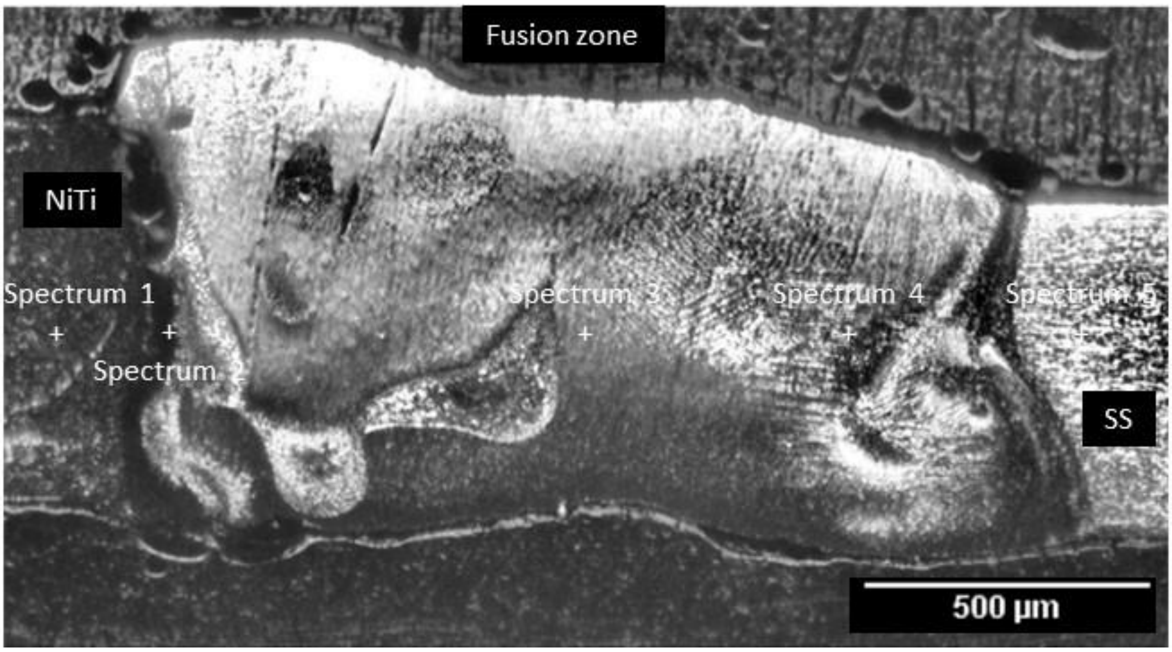

Fig. 5.6 Profiles of Weldments Produced by Continuous Laser Welding (Sample no: 17)

Table 5.12 EDX spectrum composition analysis of NiTi-Ni-SS joint (CW – Sample no: 17)

	Element (wt%)				
Spectrum	**Ti**	**Cr**	**Fe**	**Ni**	**Remarks**
Spectrum 1	45.43	0.07	0.18	54.32	Base Metal (Left side)
Spectrum 2	32.70	0.81	5.68	60.81	
Spectrum 3	17.85	4.06	15.51	62.58	
Spectrum 4	3.79	7.41	28.75	60.05	
Spectrum 5	0.12	11.51	79.86	8.50	Base Metal (Right side)

5.3 Verification of Appropriate Interlayer Shape on Joint Performance

5.3.1 Effect of Interlayer Shape on Tensile Strength (Continuous Laser Welding)

To identify the weldability between NiTi-Ni and SS304-Ni joint, laser welding and tensile test were conducted for the NiTi-Ni and SS304-Ni weldment. Fig. 5.7 shows the tensile strength of the NiTi-Ni and SS-Ni weld joints for various welding speeds at power density of 6.37 X 10^6 W/cm^2. The results also show that a good welded joint can be formed between SS-Ni at interaction time of 1.33ms with a higher tensile strength was obtained while a lower tensile strength of the welded joint was formed between NiTi-Ni at the same welding speed. This indicates that fracture may occur on the NiTi-Ni side of a NiTi-Ni-SS joint. Thus in the following study, the focus should be on the improvement of joint strength on the NiTi-Ni side of NiTi-Ni-SS joint by varying the welding speed at power density of 6.37 X 10^6W/cm^2 while 1.33ms interaction time would be applied for the joining of SS-Ni side of the NiTi-Ni-SS joint.

The same setting as above was used to weld the NiTi-SS304 with and without different rectangular shape interlayer widths to reduce the process window range. Fig. 5.8 shows the tensile strength for the welding of NiTi-SS joint, NiTi-Ni-SS joint with interlayer width of 5mm and NiTi-Ni-SS joint with an interlayer width of 8mm for various welding speeds. The interaction time of joining the SS-Ni side would be 1.33ms as noted in the above experiment. Experiment results reveal that the tensile strength resulting from directly joining NiTi and stainless steel increases to a maximum of 87 MPa, when interaction time decreases to 1.33ms at power density of 6.37x 10^6W/cm^2. With the use of the same welding speed and laser power, the addition of the Ni interlayer increases the tensile strength by 68.97% and 20.69% for an interlayer width of 5mm and 8mm respectively. With the addition of an interlayer, the tensile strength increases with decreasing welding speed in relation to a given power density.

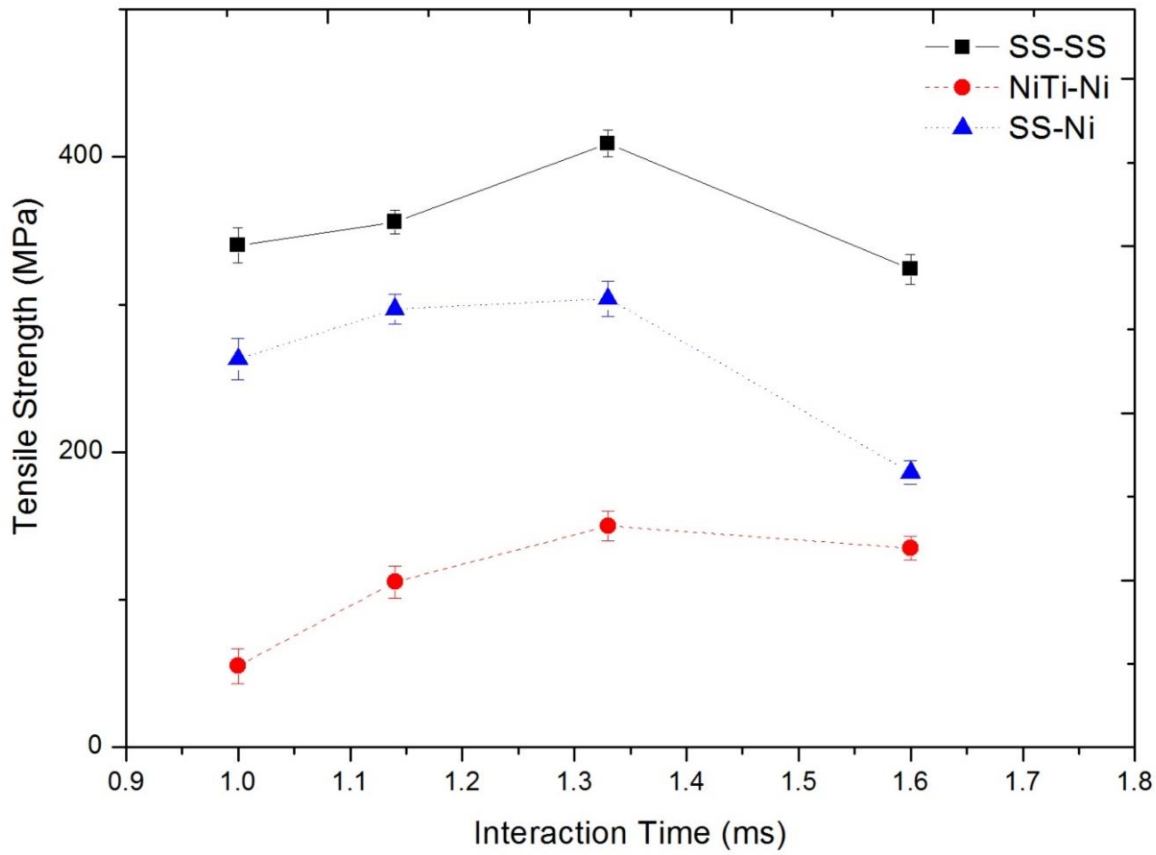

Fig. 5.7 Relationship of tensile strength and interaction time of NiTi-Ni and SS-Ni joints

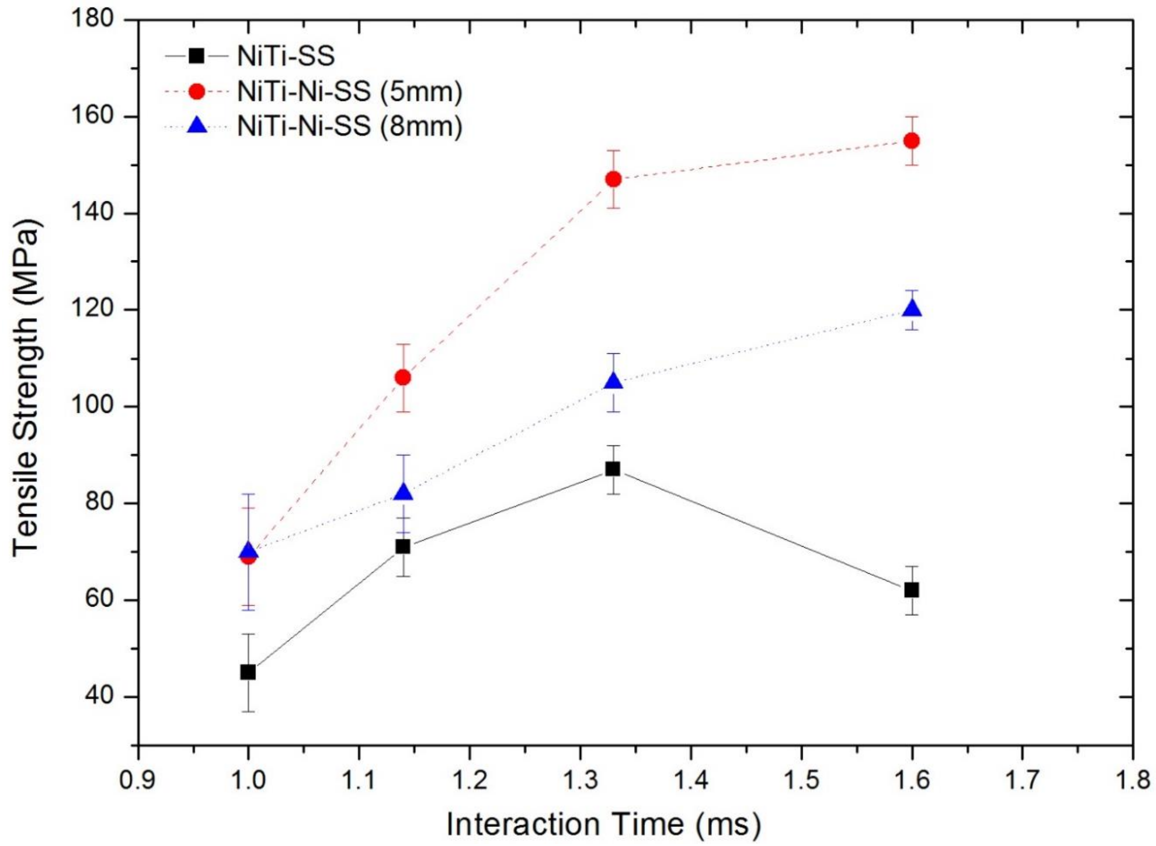

Fig. 5.8 The relationship between tensile strength and interaction time of different joints

The effects of a large range of welding speed regarding the tensile strength of the welded NiTi joint and stainless steel with an interlayer width of 5mm and 8mm is shown in Fig. 5.9. The tensile strength increased gradually until the interaction time attained 1.14ms to produce a full penetration weld and increased sharply at 1.33ms followed by a more gradual increase to a maximum of 1.82ms, when the NiTi and stainless steel was joined by the interlayer width of 5mm. An improvement of tensile strength from 13.79% to a maximum of 104.60% was contributed when compared with the tensile strength of a directly welded NiTi-SS joint. Further welding speed decrease resulted in the degradation of joint strength, due to over welding.

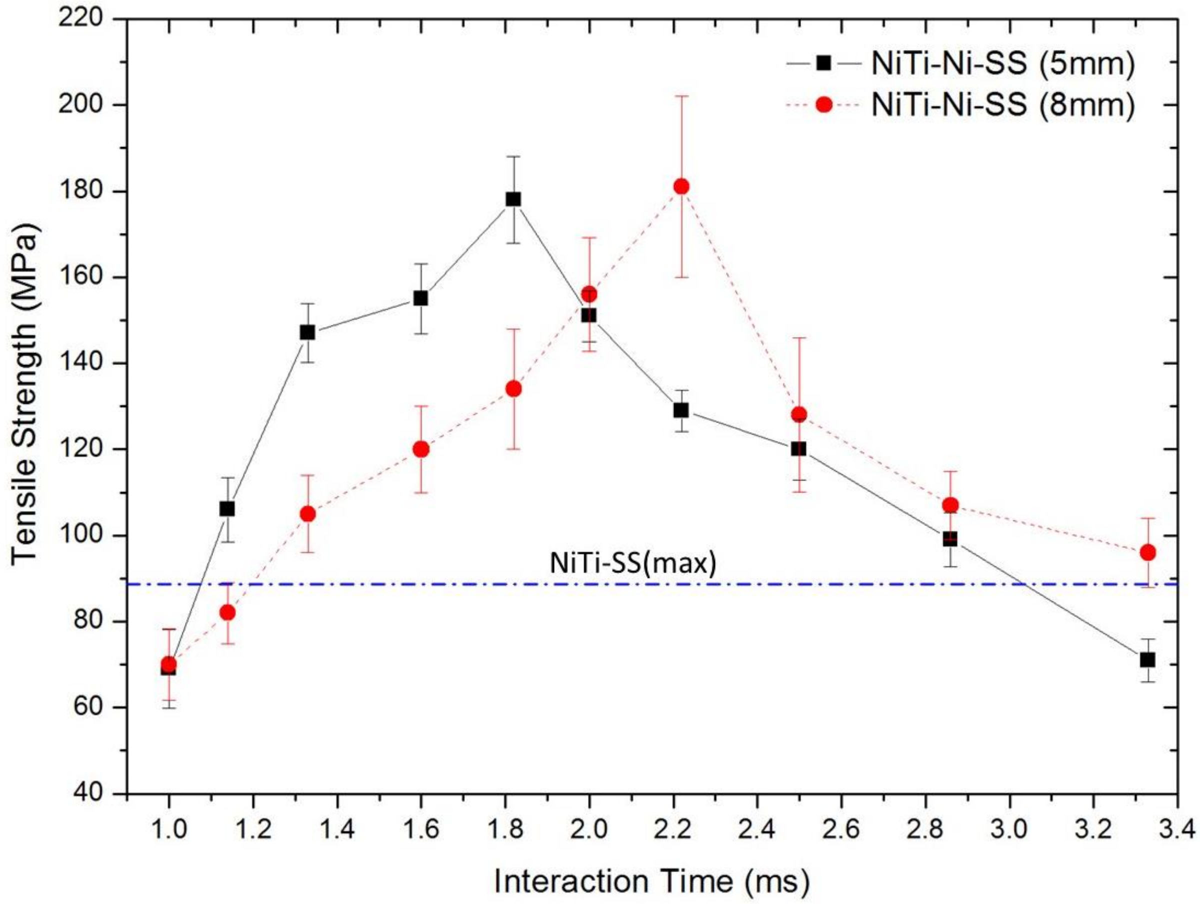

Fig. 5.9 Relationship between tensile strength and interaction time (5mm & 8mm)

When the interlayer width increased from 5mm to 8mm, the increasing tensile strength trend as regards the welding speed followed a similar trend of joint welded with an interlayer width of 5mm. The maximum tensile strength of the joint attained at the interaction time of 2.22ms (a 108.05% improvement), when compared to the results of the tensile strength of a directly welded NiTi and stainless steel joint in this project.

Experimental results as shown in Table 5.13 indicated that the laser welding related to different shapes of the interlayer could achieve similar joint strength when appropriate laser power and welding speed were used. Circular shape interlayers and rectangular shape interlayers could contribute to the improvement of joint strength.

Table 5.13 Joint strength of NiTi-SS and NiTi-Ni-SS at 2000W laser power (samples with highest tensile strength)

Joint	Interlayer shape	Interlayer size	Welding speed (mm/s)	Max. tensile strength (MPa)	Increment of tensile strength when compared with the tensile strength of NiTi-SS
NiTi-SS	/	/	150	87	/
NiTi-Ni-SS	Circular	∅1.4mm	175	175	101.15%
	Rectangular	5mm width	110	178	104.60%
		8mm width	90	181	108.05%

The microstructural observations made, using SEM along with the composition information obtained from EDX, were used for phase identification. The EDX line analysis for the cross section of the fusion NiTi and Ni joint interface (as shown in Fig. 5.10) shows that the intensity of Ti sharply dropped from the base metal side to the interlayer, with only a very small amount of Fe and Cr detected. The experimental results show that the amount of Fe and Cr in the fusion zone of weldment with rectangular shape interlayers could contribute to the elimination of Fe and Cr with the objective of avoid the formation of Cr_2Ti and Fe_2Ti. As a result, rectangular interlayer shapes are determined in line with the appropriate shape of the interlayer when joining NiTi and stainless steel.

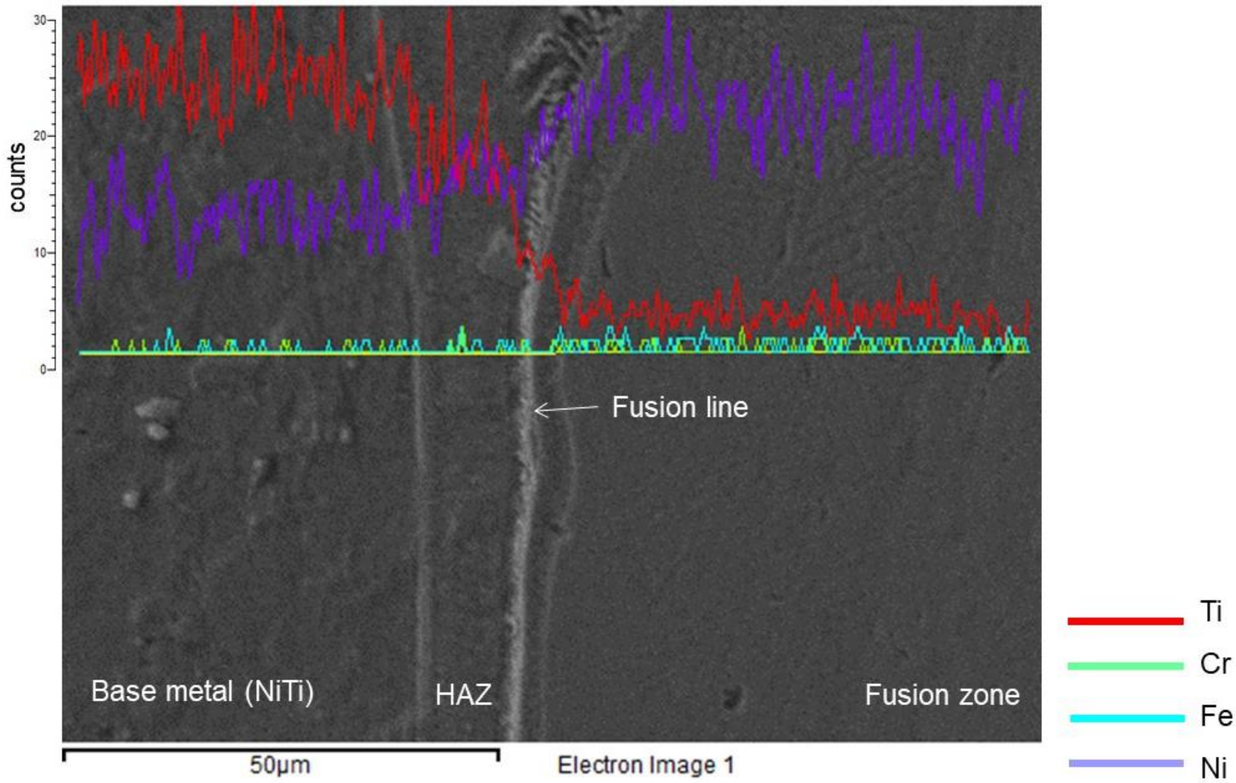

Fig. 5.10 SEM with EDX line analysis in the NiTi fusion interface with Ni

5.3.2 Effect of Interlayer Shape on Hardness (Continuous Laser Welding)

Hardness changes due to the solidification in the fusion regions and change in the grain structure significantly depend on the cooling rate. Fast cooling rate of the base material generates a fine microstructure in the heat affected zones (HAZ) and fusion zones (FZ). In contrast, slow rate in this zones result in coarse microstructure.

Hardness along the longitudinal weld centerline prepared at selected welding speeds for rectangular interlayer widths of 5mm and 8mm were measured as shown in Fig. 5.11. A considerable hardness increased in the weld zone and heat affected zones was noted in dissimilar metal joints. A decreasing hardness towards both base metals reached the expected values of HV hardness for both base metals. The expected hardness value of NiTi was approximately 220HV while that of stainless steel was approximately 170HV. As the width of the rectangular shape interlayer is sufficiently long enough in both cases, the expected hardness value of around 90HV was identified at the middle region of the interlayer as it was noted that the laser heat did not affect that zone as shown in Fig. 5.12.

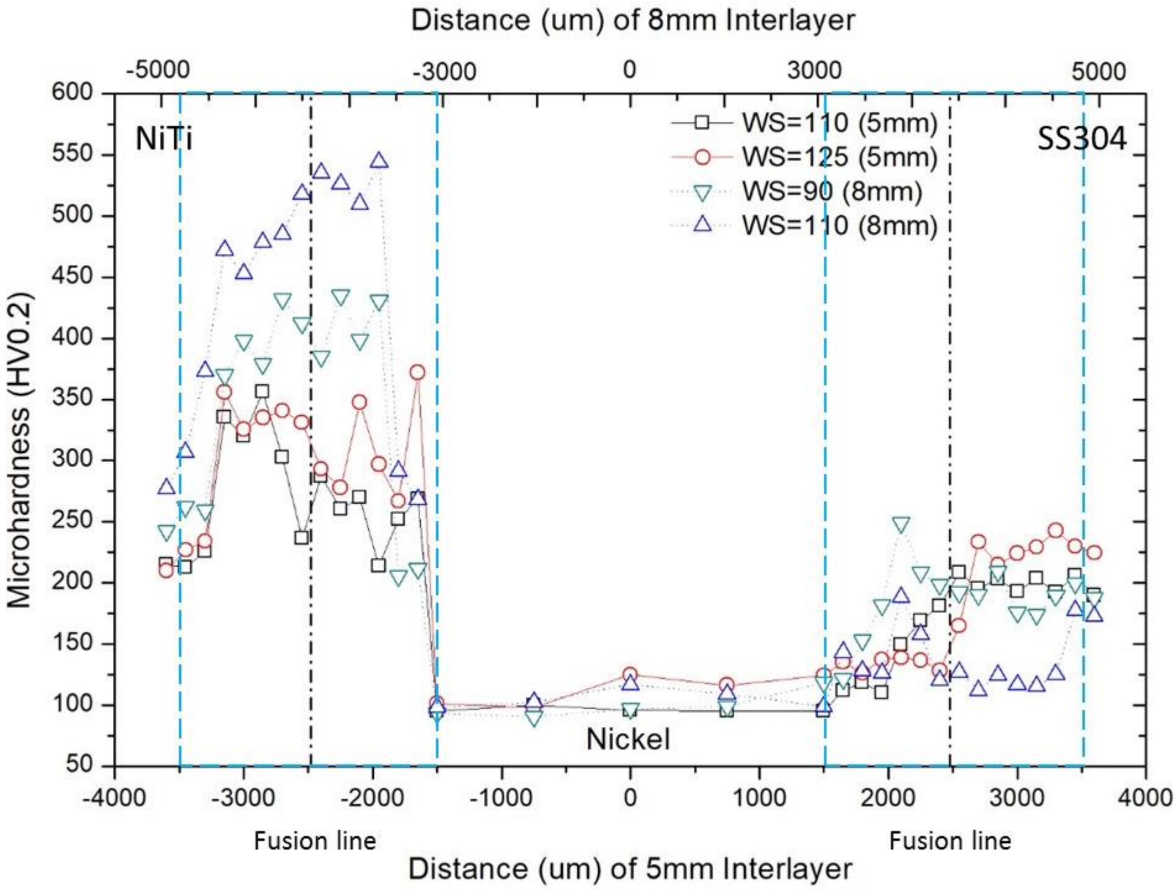

Fig. 5.11 Hardness traces along cross-section of welds (best setting vs worst setting)

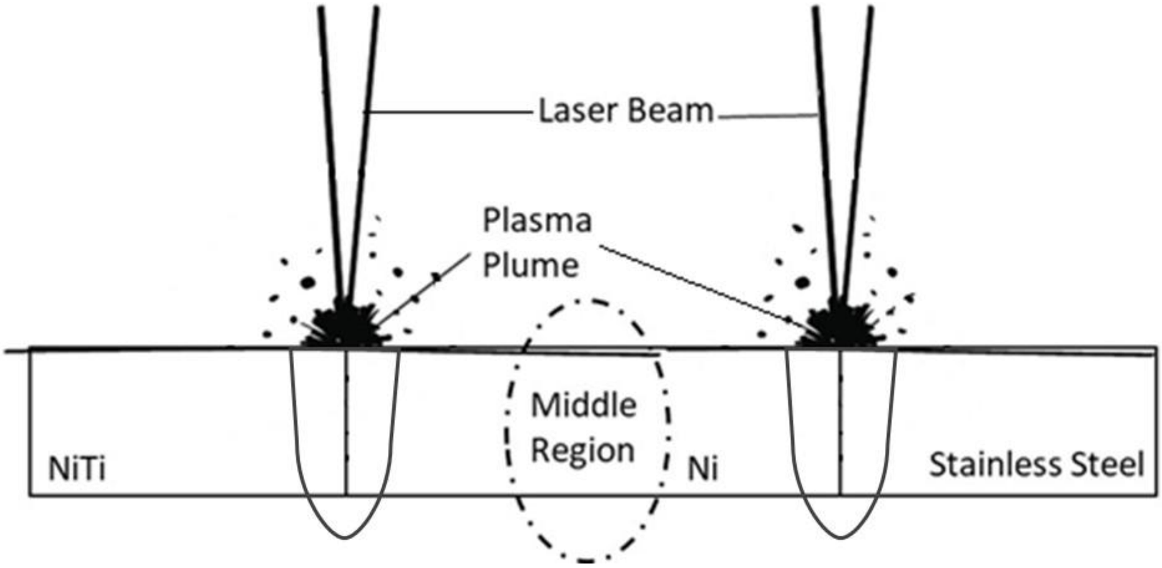

Fig. 5.12 Schematic diagram of the laser welding with rectangular shape interlayer

Titanium has a tendency to form a brittle intermetallic phase with stainless steel to form TiFe and $TiFe_2$. These intermetallic phases make a dramatic increase in the hardness of the welded joint and is accompanied by a decrease of tensile strength if the sufficiency allows an extensive super-elastic bend of the welded joint. An important factor affecting joint properties is the present of the intermetallic compound layer in the fusion zone, while, in contrast, the mechanical properties of the laser welded joints depend on microstructures and weld compositions, both of which are varied by the laser welding process parameters. The addition of the Ni interlayer avoids the formation of FeTi and Fe_2Ti of the welded joint and the increase of Ni content improves the tensile strength and hardness to enable a recoverable bending deflection. With the presence of FeTi and $TiFe_2$, the hardness of the weld joint caused by the direct welding of NiTi and stainless steel was in the range of 740-1324HV (Li, B.F., 2004). By the addition of an interlayer, the elimination of the formation of FeTi and Fe_2Ti resulted in the decrease of the hardness enabling the welded joint to be more ductile. The existence of high hardness peaks, 440-540HV, for welded joint with 8mm wide interlayer were mainly concentrated towards the weld zone of NiTi-Ni side while the existence of high hardness peak for welded joint with 5mm wide interlayer were also concentrated on the same side. However, the welded joint peaks of a width of 5mm interlayer reached 210-380HV, therefore much lower results were achieved from a reduction of intermetallic compounds or higher Ni content in the region. Investigation of phase composition is discussed in the following chapter.

5.3.3 Effect of Interlayer Shape on Corrosion (Continuous Laser Welding)

Corrosion resistance experiments were conducted to measure corrosion properties of the welded samples. The potentiodynamic polarization curve of NiTi materials as received is shown in Fig. 5.13. It was evident that transient behavior was exhibited in NiTi during polarization actively/passively. Also revealed was the corrosion potential of – 251 mV. The corrosion potential of NiTi was found to be nobler than all welded samples.

The polarization curves for the NiTi-Ni-SS joint with the circular shape of Ni and rectangular shape of the Ni interlayer are shown in Fig. 5.14 to 5.17. Tafel curve from which the corrosion current density (i_{corr}) and the corrosion potential (E_{corr}) can be determined while the corrosion current density (I_{Corr}/area) and the corrosion potential (E_{Corr}) are given by the intersection of the Tafel curves. The corrosion parameters derived from the potentiodynamic polarization data by the Tafel method are summarized in Table 5.14.

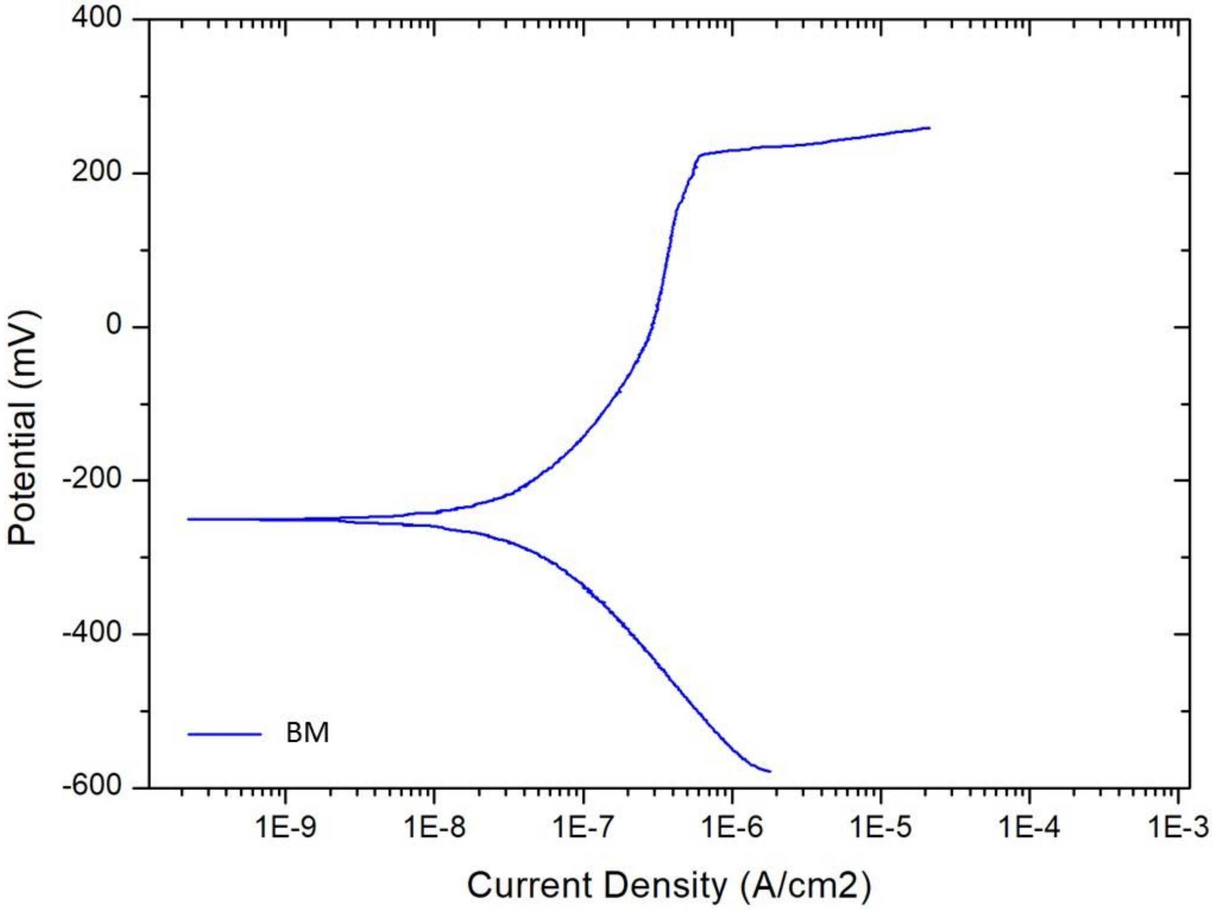

Fig. 5.13 Potentiodynamic polarization curves of NiTi base material recorded after 24 hours exposure to Hank's solution at 37.5°

A metal is said to be passivated if the current flows just above the first plateaus of the open circuit with potential increased before a smooth continuous rise is resumed (likes the curve of NiTi). Such a curve will have a positive slope to represent a passivation region. Corrosion occurs after the breakdown of the passive film and increases steadily with increasing potential when the potential beyond the breakdown potential. Pitting is the form of breakdown and is defined as the pitting potential (Ep).

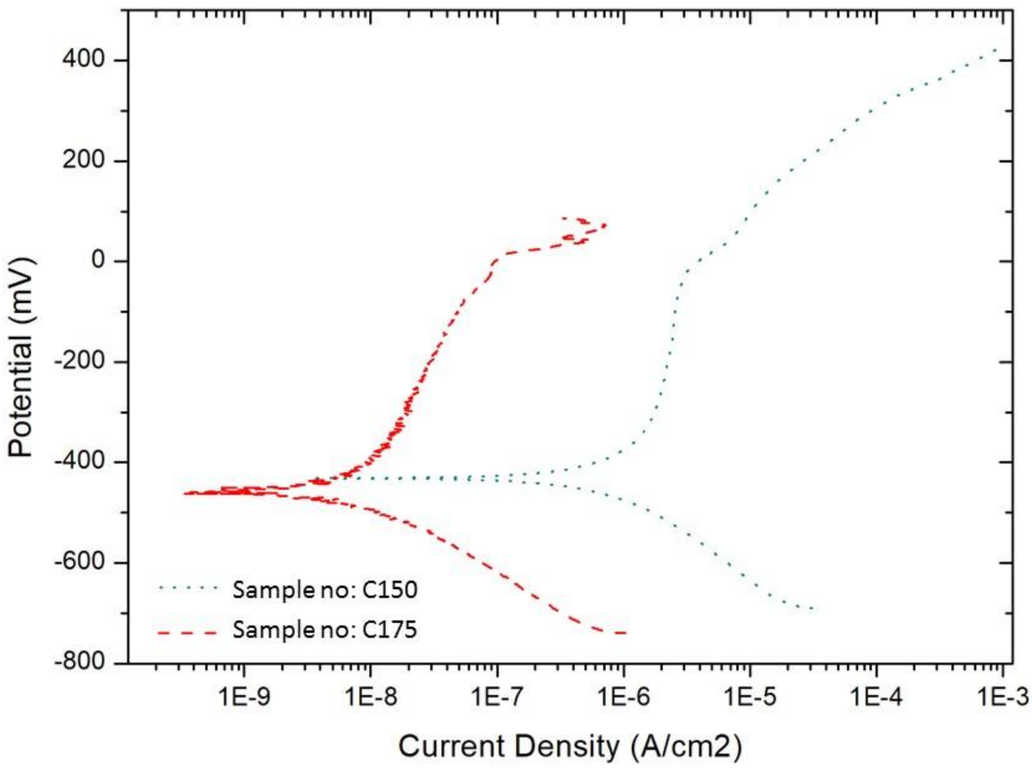

Fig. 5.14 Potentiodynamic polarization curves of welding joint of NiTi-Ni side recorded after 24 hours exposure to Hank's solution at 37.5°(Circular shape interlayer with different welding speed)

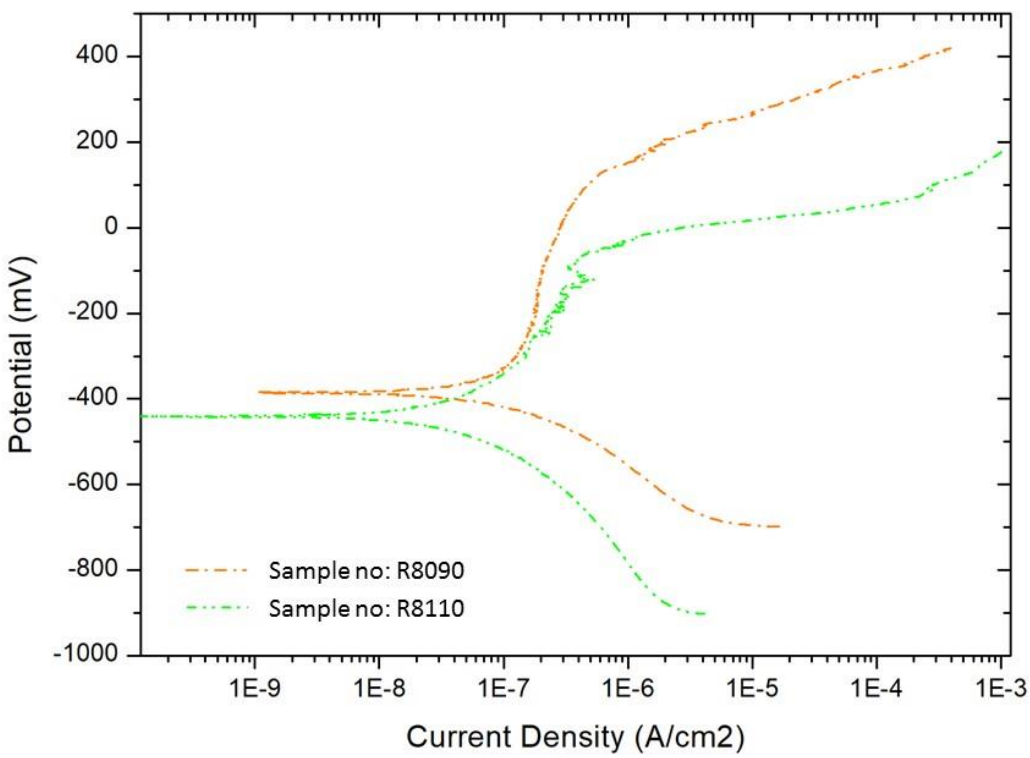

Fig. 5.15 Potentiodynamic polarization curves of welding joint of NiTi-Ni side recorded after 24 hours exposure to Hank's solution at 37.5° (8mm rectangular shape interlayer with different welding speed)

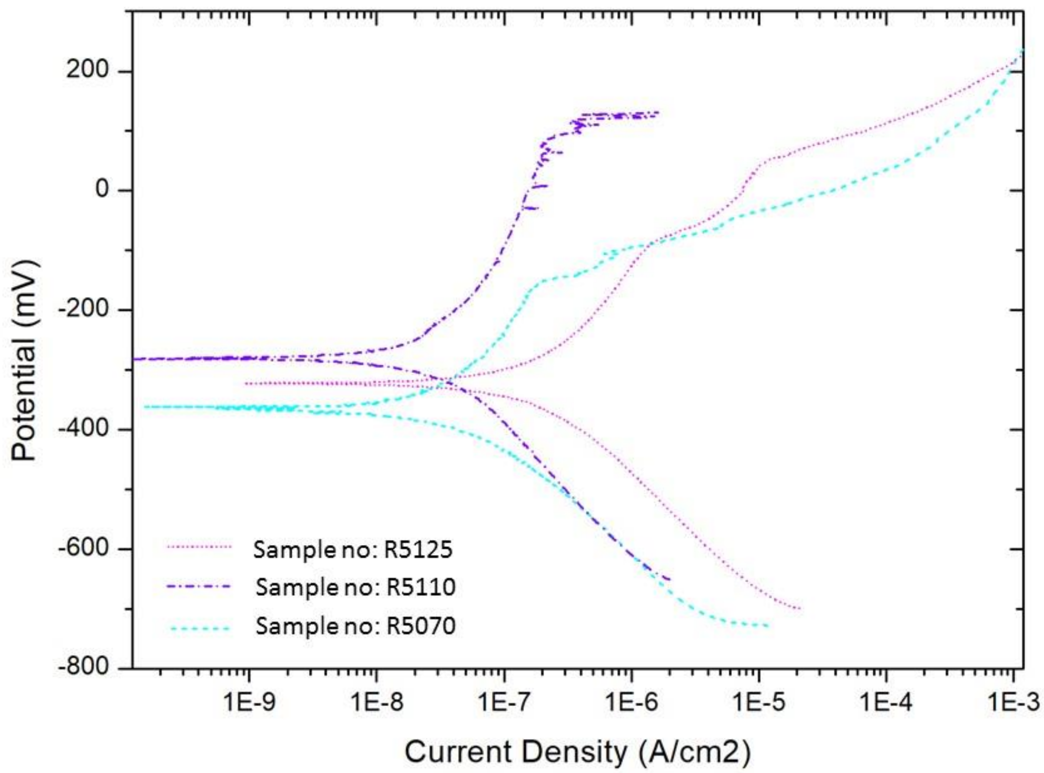

Fig. 5.16 Potentiodynamic polarization curves of welding joint of NiTi-Ni side recorded after 24 hours exposure to Hank's solution at 37.5° (5mm rectangular shape interlayer with different welding speed)

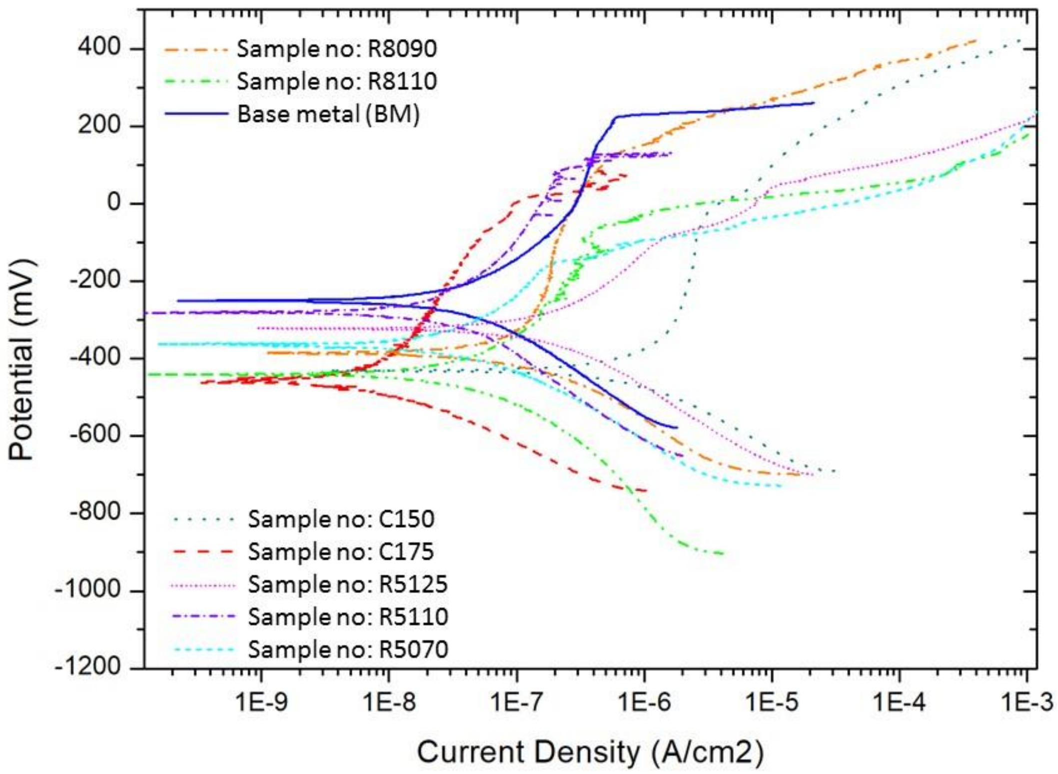

Fig. 5.17 Potentiodynamic polarization curves of all samples recorded after 24 hours exposure to Hank's solution at 37.5°

Table 5.14 Results obtained from Potentiodynamic polarization test

Sample no	Welding speed (mm/s)	Shape of interlayer	Ecorr (mV)	Icorr (nA/cm^2)	Epit (mV)
BM	/	/	-251.026	24.108	219.041
C150	150	Circular	-432.274	501.276	-13.291
C175	175	Circular	-463.219	595.256	11.268
R8090	90	Rectangular (8mm width)	-362.034	47.283	109.015
R8110	110	Rectangular (8mm width)	-385.120	79.447	-67.322
R5070	70	Rectangular (5mm width)	-441.115	46.318	-162.612
R5110	110	Rectangular (5mm width)	-280.497	23.214	81.017
R5125	125	Rectangular (5mm width)	-322.739	108.991	-92.372

By comparing the above parameters for the joints with rectangular shapes and circular shape interlayer, it can be observed, as expected, that welding decreased the corrosion resistance. The $FeTi_2$ and Cr_2Ti cannot be detected by means of XRD in the NiTi welded joint and stainless steel with rectangular shape interlayer while a small amount of $FeTi_2$and Cr_2Ti were detected by means of XRD in the welded joint of NiTi and stainless steel with circular shape interlayer. A non-passivating condition exists in the weld joint of R5070 when the potential and current increases. Fig. 5.14 presents the polarization curves for the fusion zone of NiTi-Ni-SS with a circular shape interlayer at two different welding speeds. The curves illustrates that the corrosion behavior was affected by different welding speed at a fixed laser power. The corrosion tendency was increased by 200% when compared to the base material of NiTi as received. Also, the fusion zone of these welded joint would corrode rapidly and both welded joints gave similar pitting potential. There were one-magnitude increase in corrosion current density which was in the order of 10^{-9} Acm^{-2}. Fig. 5.15 and 5.16 presents the polarization curves for the weld zone and the heat affected of NiTi-Ni side zone, at various welding speeds of fixed laser power with 5mm and 8mm interlayer. The welding speed decreased to 90mm/s for welding NiTi and stainless steel with a 8mm interlayer exhibiting good corrosion resistance. In the case of a 5mm interlayer being used for welding NiTi and stainless steel together, the increase of welding speed to 110mm/s could improve the wear corrosion resistance of the joint due to the reduction of $NiTi_2$ in the fusion zone determined by XRD. Although R5125 has a lower corrosion tendency than that of R5070, its corrosion current is higher than that of R5070, which means that if the passive film is destroyed at the surface and R5125 will begin to rapidly corrode. R5110 has a better passivation than that of other samples and a lower corrosion current due to the reduction of unfavorable phase, which is discussed in the next chapter. The breakdown potential of R8090 and R5110 is 109mV and 81 mV respectively.

The interlayer shape did alter the chemical composition of the NiTi welded and stainless steel joints. The corrosion tendency was increased due to the formation of more $NiTi_2$. Propagation and initiation of localized corrosion occurs at NiTi and Ni joint in the simulated body environment. As a result, the corrosion resistance for welded samples varies depending on the welding speed. The corrosion resistance properties of the weld joint of NiTi and stainless steel is damaged by the presence of $NiTi_2$ as the initiation of pitting occurs in this preferable phase. Therefore, the correlation between the chemical compositions of the fusion zone, the laser welding condition and the changes of mechanical and corrosion properties can be obtained. Besides, the corrosion performance (as shown in Fig. 5.17) was improved effectively due to the variation of the chemical compositions (reduction of the amount of $NiTi_2$) by process parameters. The varying of welding speed and the shape of interlayer improves the corrosion resistance, and the rectangular shape interlayer is more effective than circular shape interlayer. The corrosion potential of sample R5110 was found to be nobler than other samples, however, accuracy of the current density determined by the Tafel slopes should be considered with caution.

The corrosion current density found from the curve may be combined with Faraday's law to determine the mass of the material removed (W) and expressed as:

$$W = \frac{A \; x \; Q}{zF}$$

Where F is Faraday's constant, z is the number of electrons transferred in the reaction, A is atomic weight of the sample and Q is the total charge passed (I_{corr} x time).

As the sample used in this case was not pure metal, the material mass per unit change is equal to the atomic weight of the component divided by different phases/compounds. The equivalent weight expressed as:

$$Equivalent\ weight = \sum_{i=1}^{k} \frac{A_i}{f_i z_i}$$

Where i is the i^{th} phases/compounds in the sample, f_i is the atomic fraction, and z_i is the valence of each phases/compounds.

Once the material weight has been established, the corrosion rate related to exposed surface area (S) and density expressed as:

$$Corrosion\ rate = \frac{\left(\sum_{i=1}^{k} \frac{A_i}{f_i z_i}\right) x \; S}{\rho}$$

If the amount of $NiTi_2$ increased, the increase of atomic fraction of unfavorable phase increases the corrosion rate.

5.4 Chapter Summary

The effect of circular shape and rectangular shape Ni interlayer in joining NiTi and stainless on hardness, corrosion resistance properties and tensile strength were investigated. The major observations are summarized as follow:

(i) Both circular shape and rectangular shape Ni interlayer could improving the tensile strength of NiTi-Ni-SS joint, however, the mixing of Fe, Ti and Ni in the molten pool could not prevented during the welding with circular shape interlayer.

(ii) Elimination of Fe and Cr with the objective of avoid the formation of Cr_2Ti and Fe_2Ti could be achieved by using rectangular shape Ni interlayer with 5mm width.

(iii) The hardness and corrosion resistance of the fusion zone of NiTi-Ni-SS could be improved with decreased amount of unfavorable phase, $NiTi_2$, controlled by varying the welding speed at power density of 6.37 X 10^6 W/cm^2 when using rectangular shape interlayer.

6 Results and Discussion III – Correlation of Chemical Composition on Weldment Performance

6.1 Introduction

In this chapter, the chemical composition of the NiTi-Ni-SS welded samples with 5mm/8mm rectangular shape interlayer were identified by EDX and XRD. The correlation of phases inside the fusion zone on transformation behavior, bending and recovery behavior is presented and discussed. With the preferred welded joint identified, the phase orientation, determined by TEM, and the phases distribution, determined by EBSD, correlated to the mechanical performance are presented and discussed finally.

6.2 Phase Identification on NiTi-Ni-SS joint

6.2.1 Phase Identification by SEM with EDX

To understand the cause of the different joint strengths, microstructural analysis was conducted on both the fusion zone and the heat affected zone. Cross sections of NiTi-Ni-SS with different interlayer width and interaction time (as shown in Fig. 6.1 and 6.7) indicates several different microstructures in the weld. A distinct fusion interface lines between the NiTi and Ni interlayer was observed in all the weldments. When the NiTi and stainless steel was welded with 5mm interlayer width, the lower welding speed as shown in Fig. 6.2 caused a coarse columnar grains formed. The columnar grain size is a welding energy function in that fusion zone, hence impacting the mechanical behavior of the joint. When the interlay width increased to 8mm, the lower welding speed as shown in Fig. 6.5 causes the formation of gas pores, hence leading to a great tensile strength reduction.

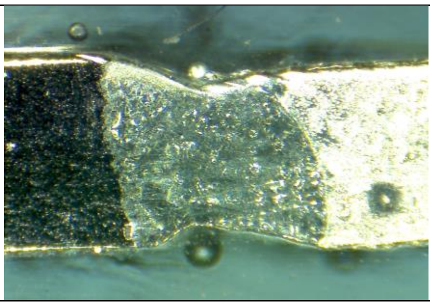

(a) Sample R5070

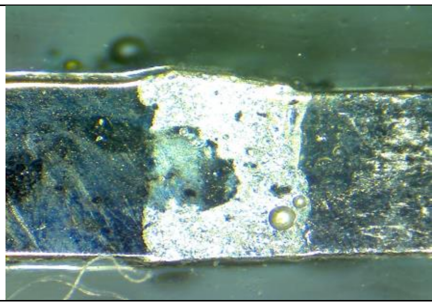

(b) Sample R5090

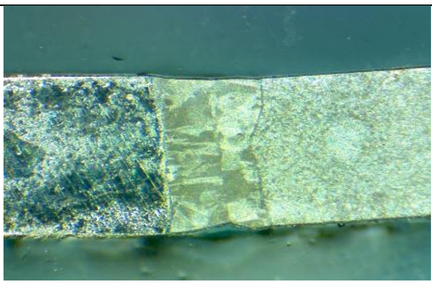

(c) Sample R5110

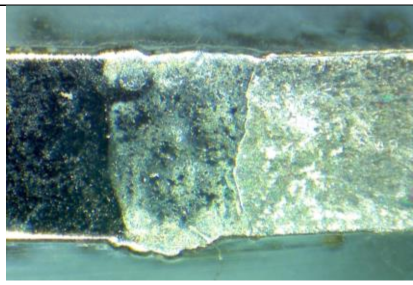

(d) Sample R5125

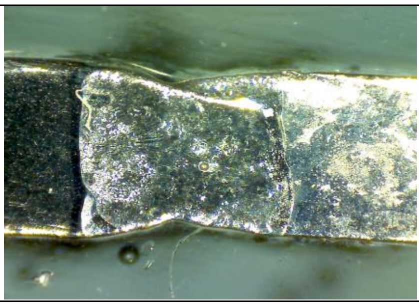

(e) Sample R8070

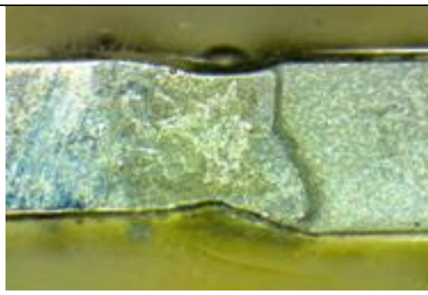

(f) Sample R8090

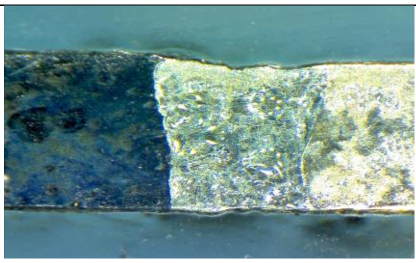

(g) Sample R8110

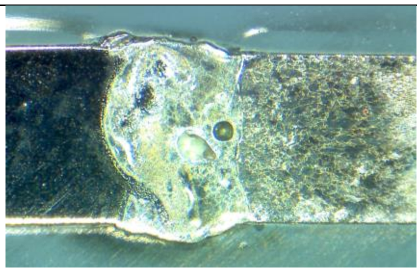

(h) Sample R8125

Fig. 6.1 Snapshot of NiTi-Ni-SS joint with different interaction time and interlayer width

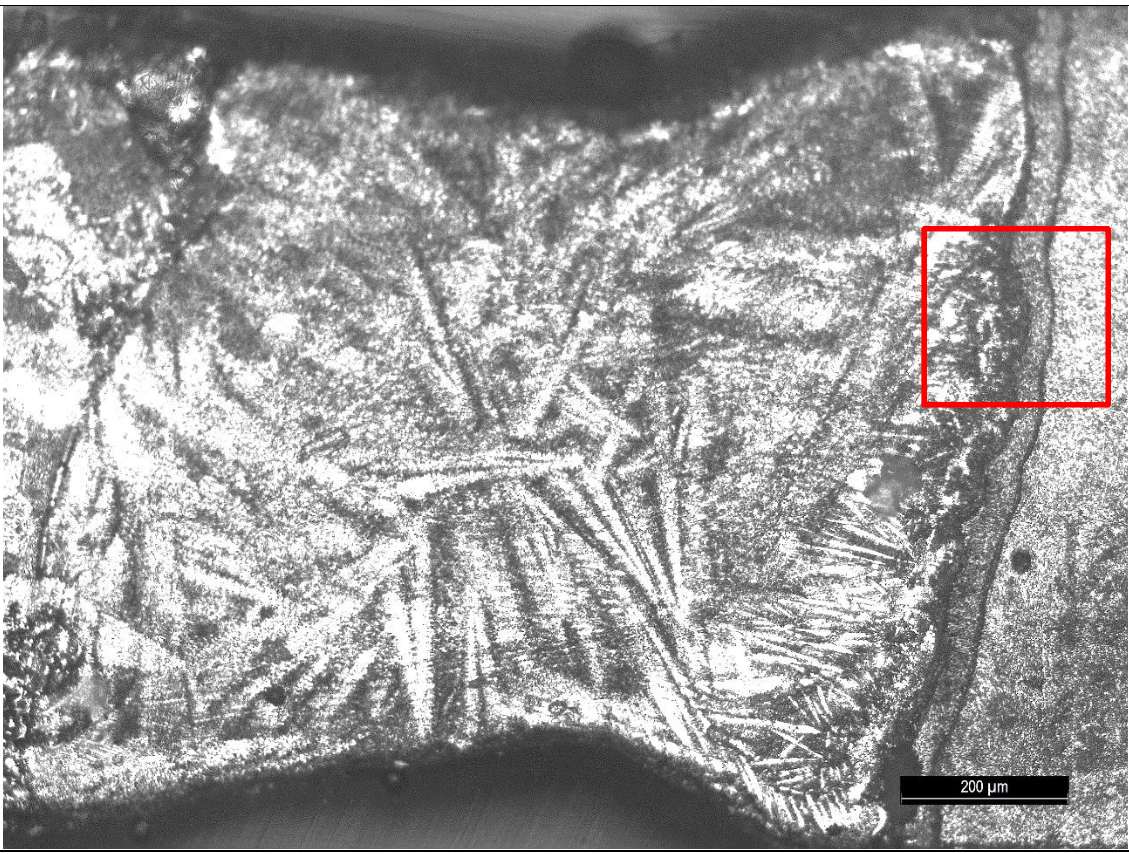

(a) Snapshot of the fusion zone

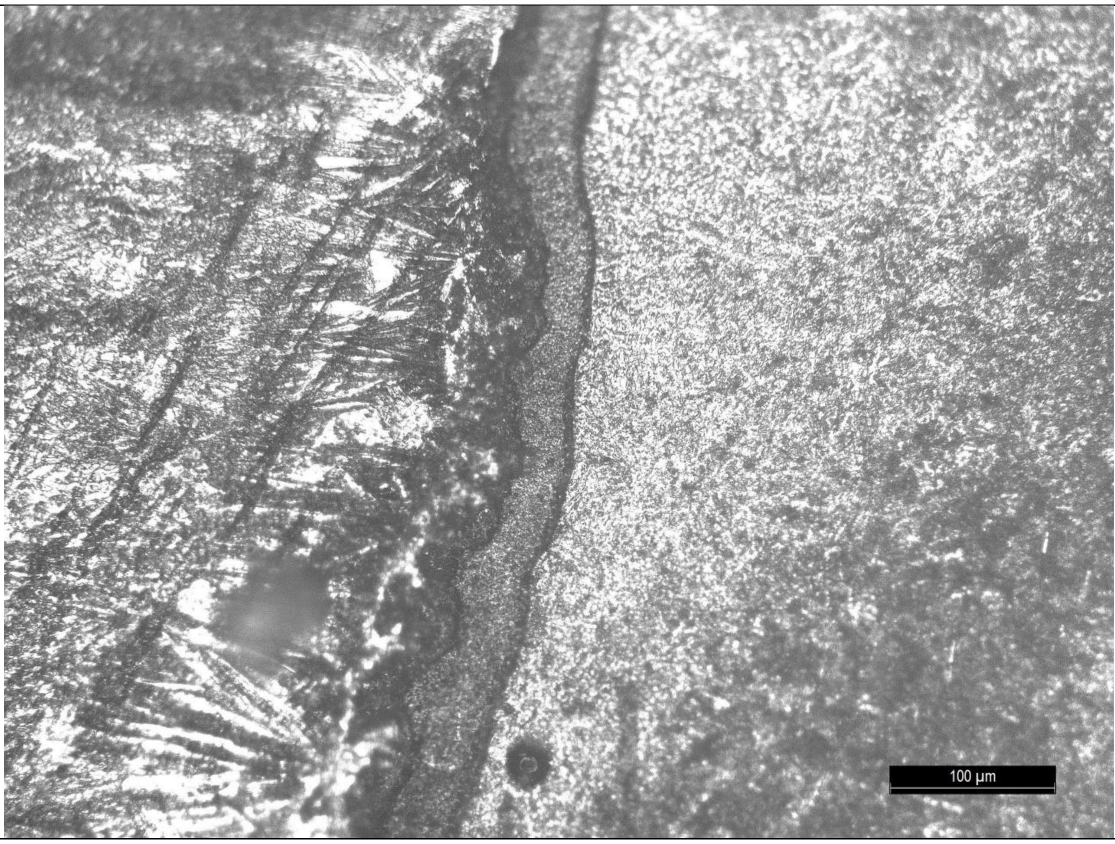

(b) Snapshot of the indicated region in (a)

Fig. 6.2 Cross section of NiTi-Ni-SS joint (sample no: R5070)

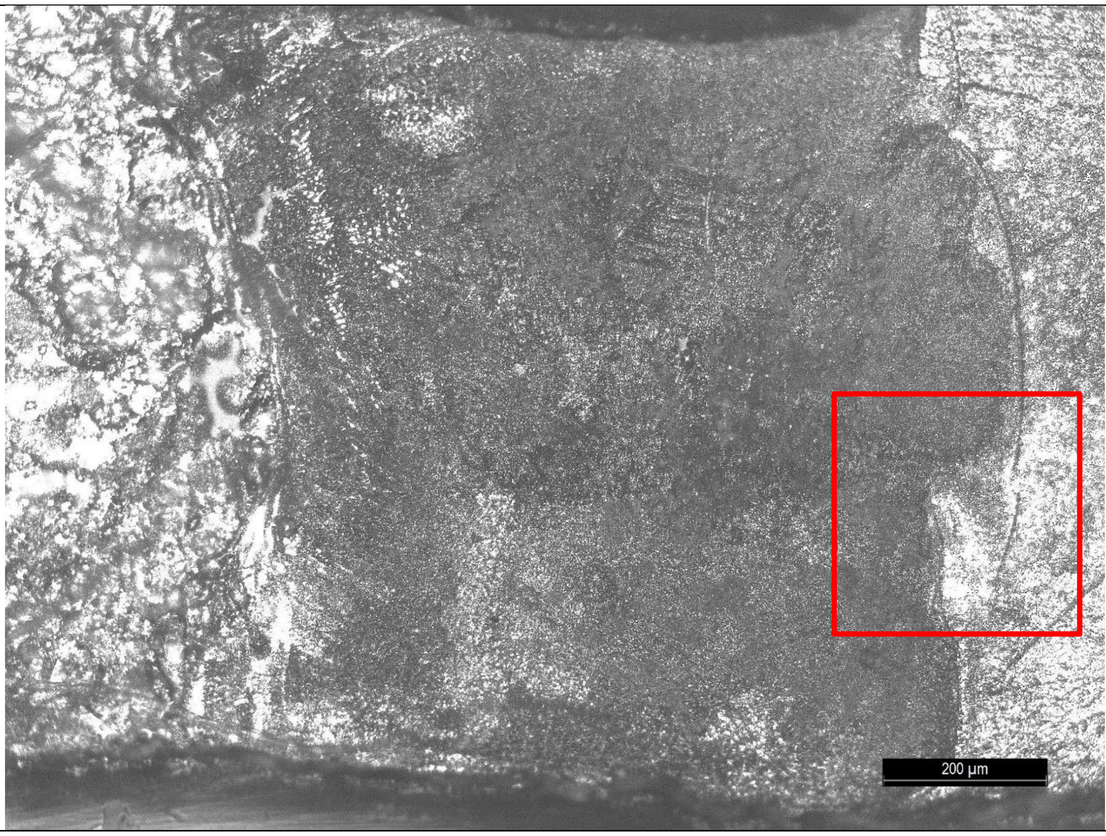

(a) Snapshot of the fusion zone

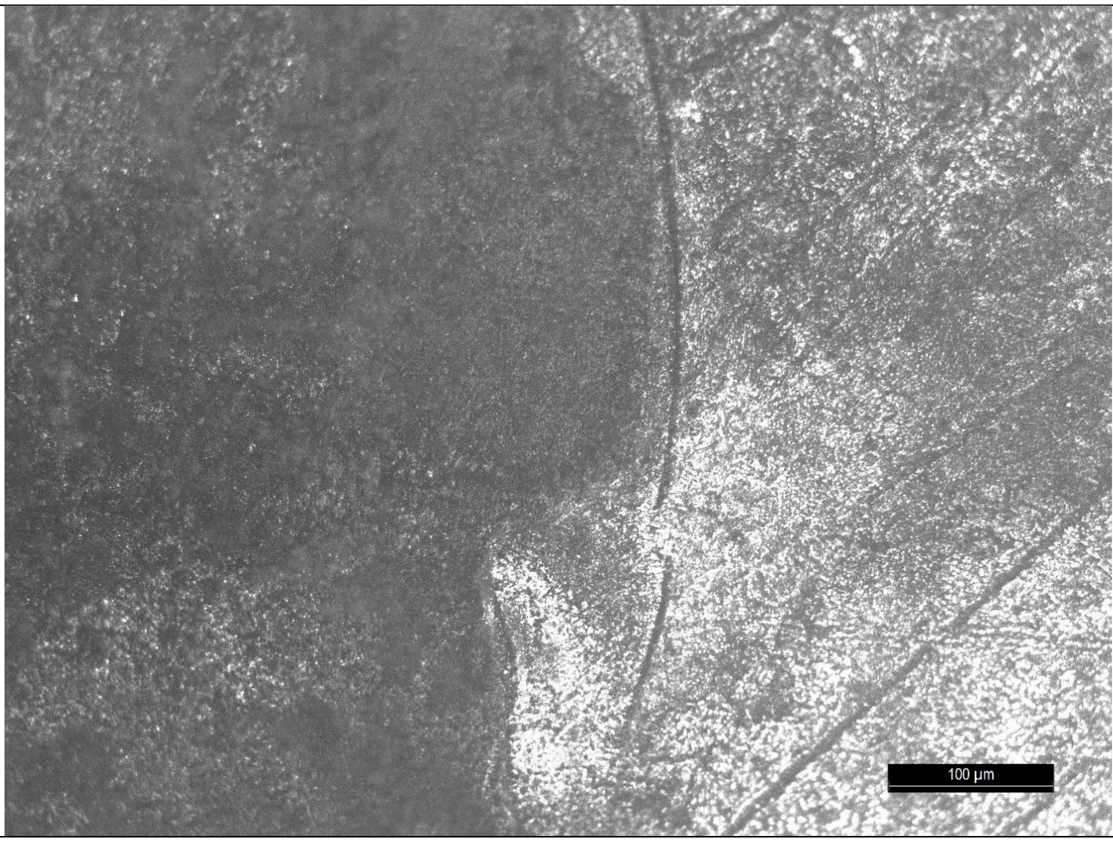

(b) Snapshot of the indicated region in (a)

Fig. 6.3 Cross section of NiTi-Ni-SS joint (sample no: R5110)

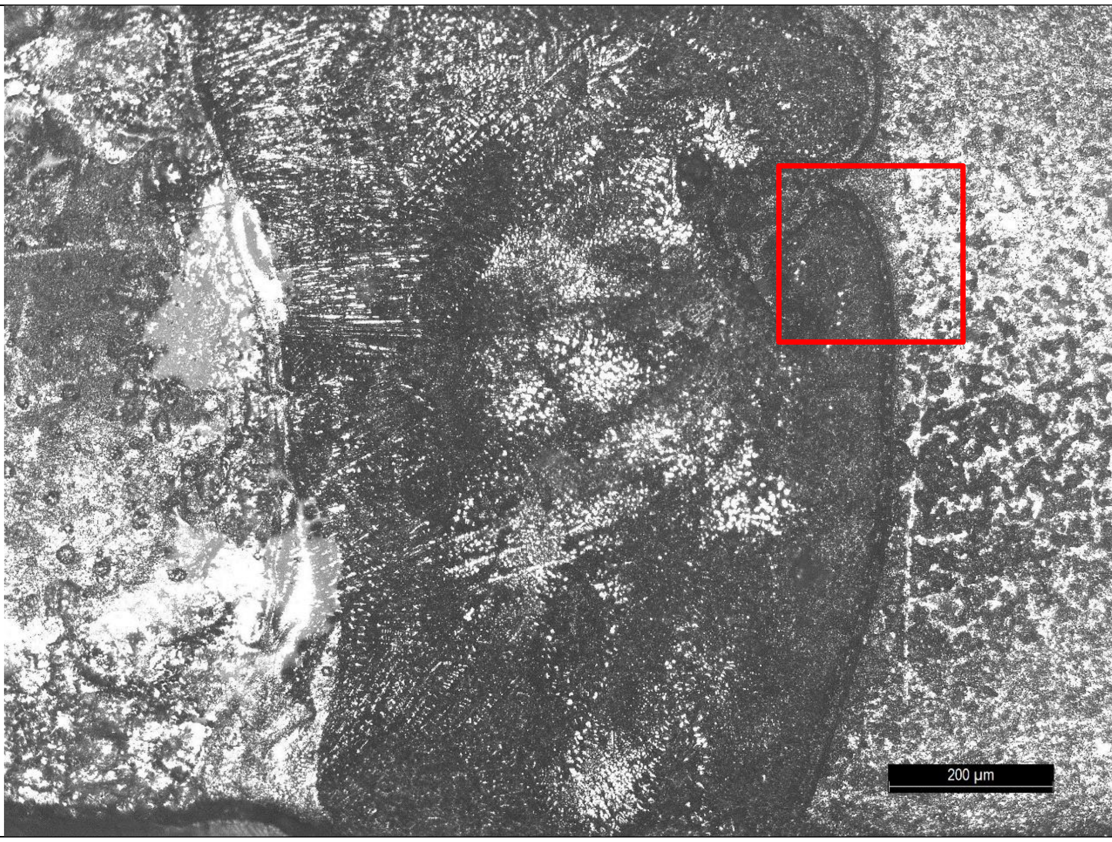

(a) Snapshot of the fusion zone

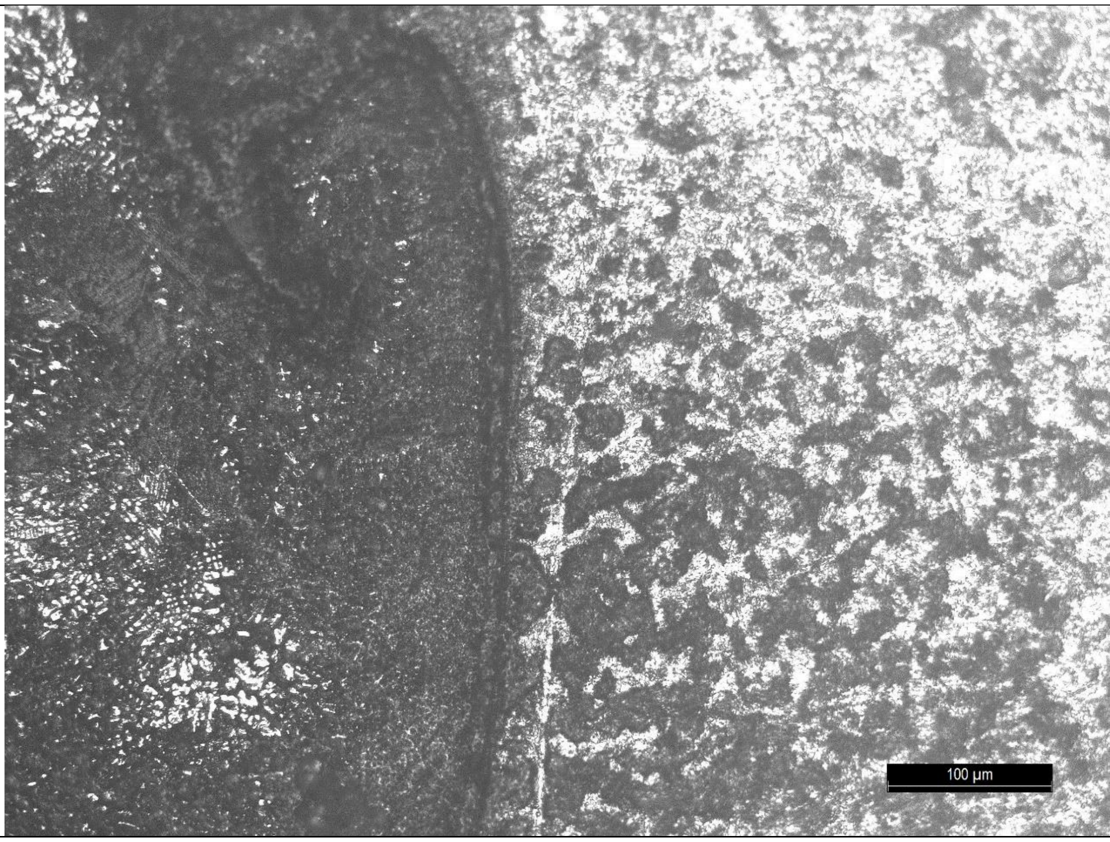

(b) Snapshot of the indicated region in (a)

Fig. 6.4 Cross section of NiTi-Ni-SS joint (sample no: R5125)

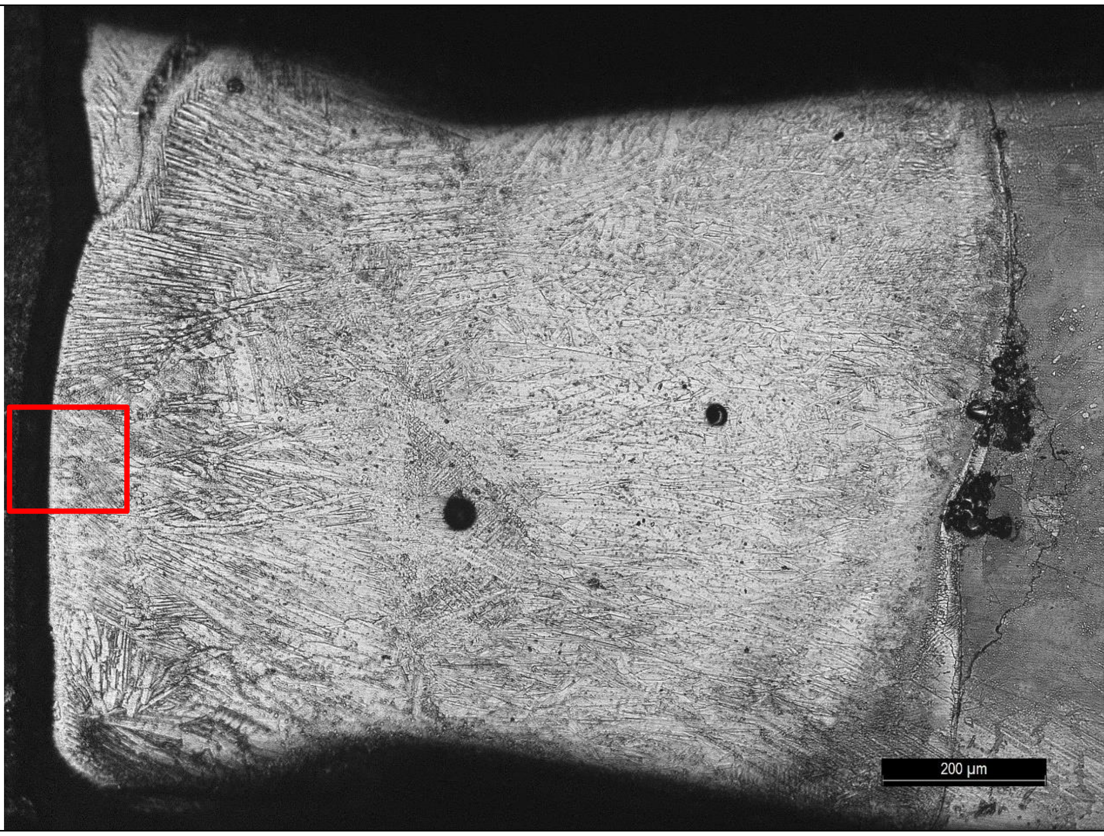

(a) Snapshot of the fusion zone

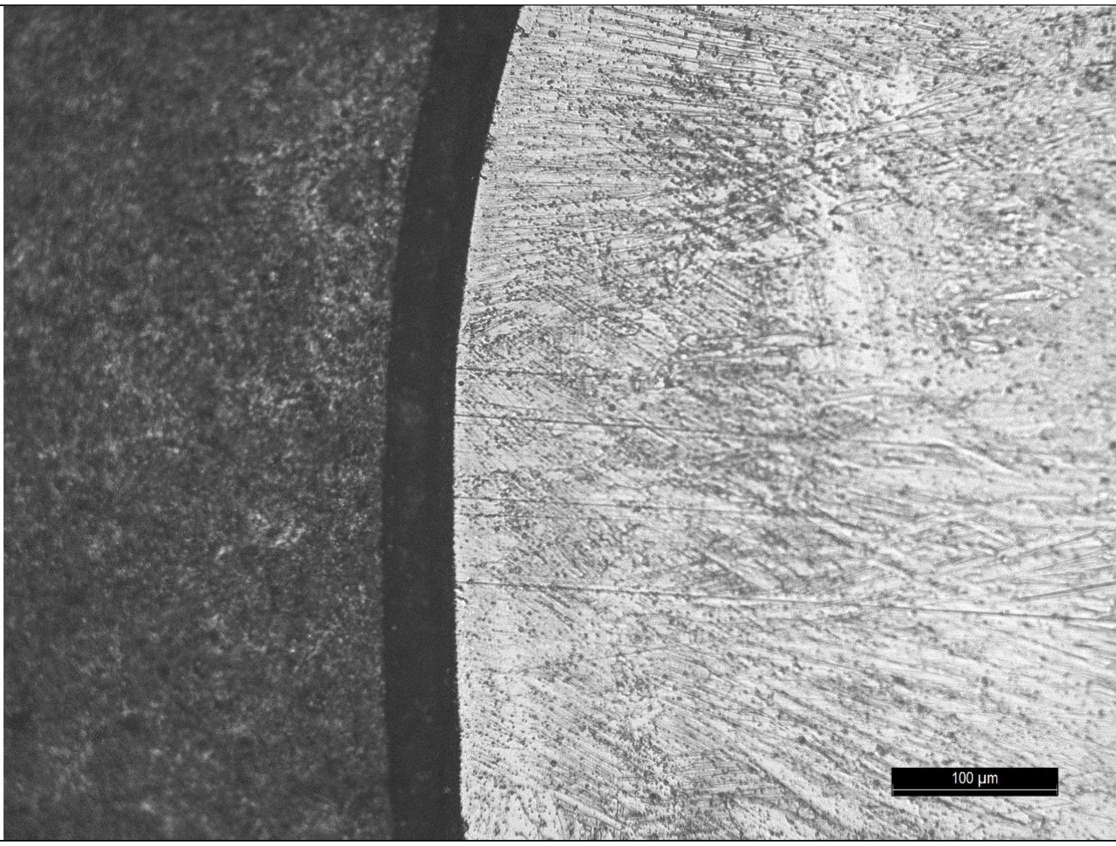

(b) Snapshot of the indicated region in (a)

Fig. 6.5 Cross section of NiTi-Ni-SS joint (sample no: R8070)

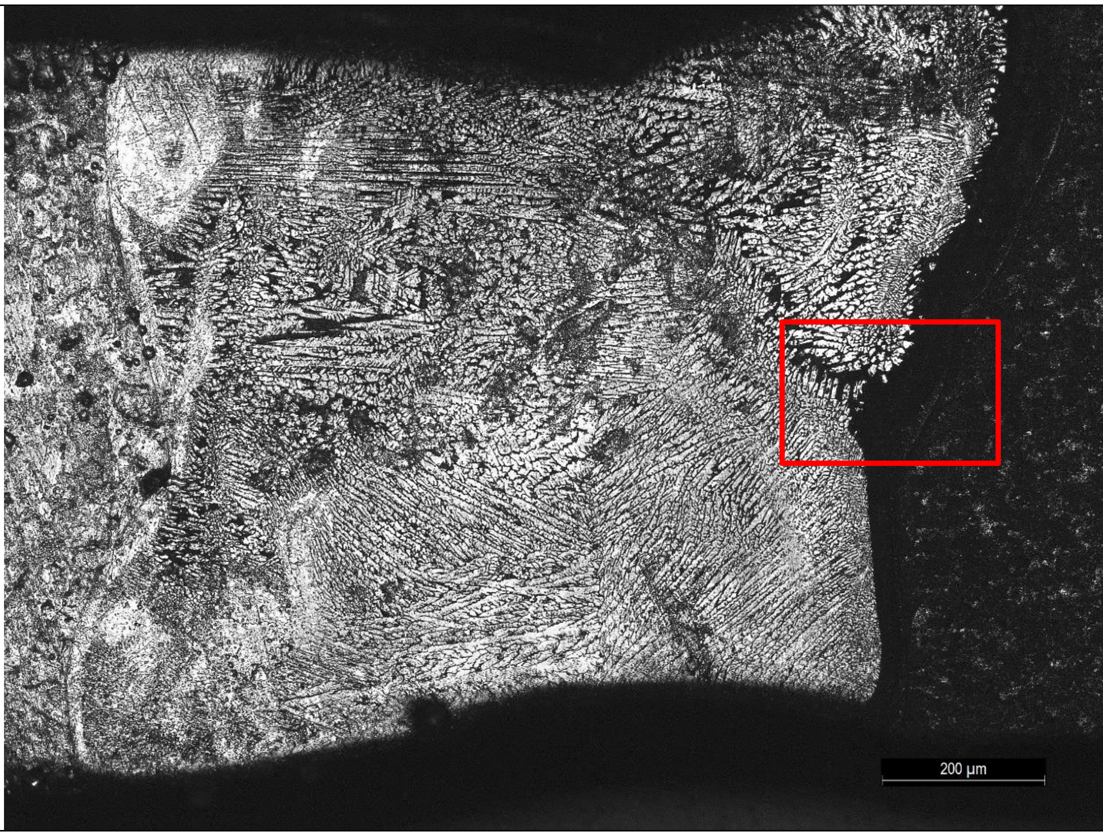

(a) Snapshot of the fusion zone

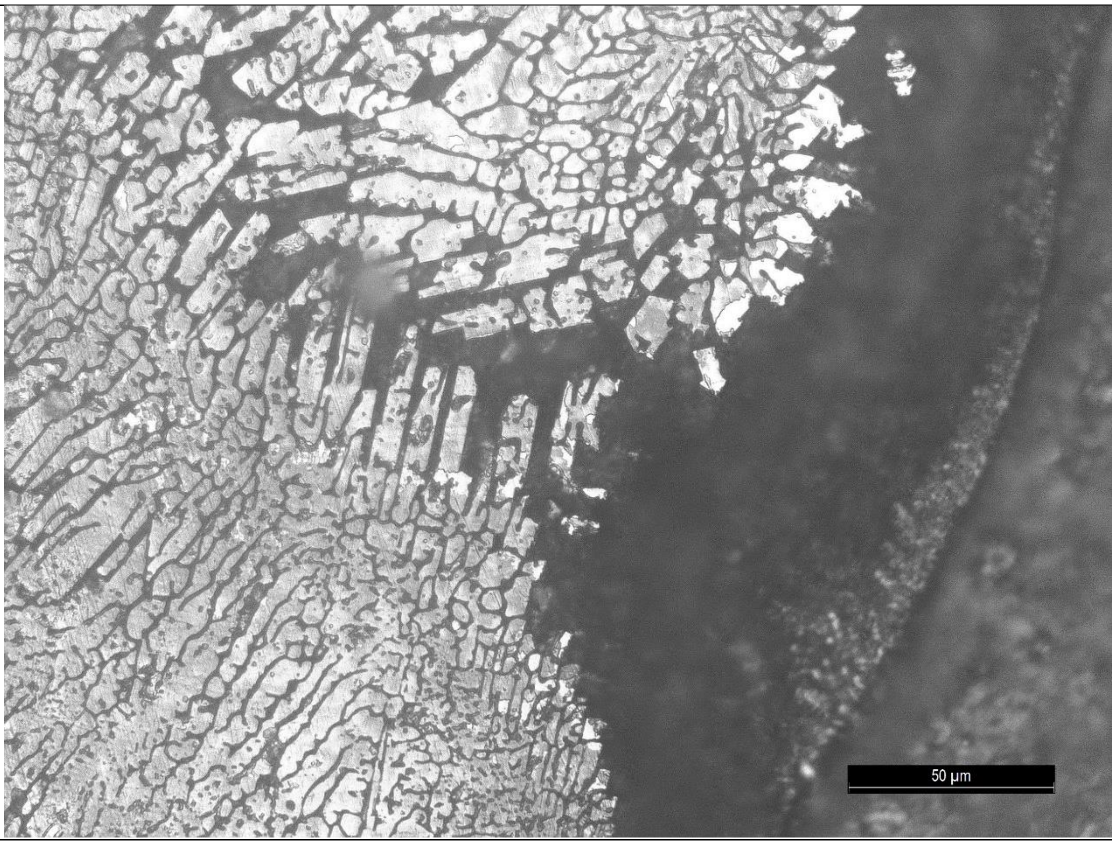

(b) Snapshot of the indicated region in (a)

Fig. 6.6 Cross section of NiTi-Ni-SS joint (sample no: R8090)

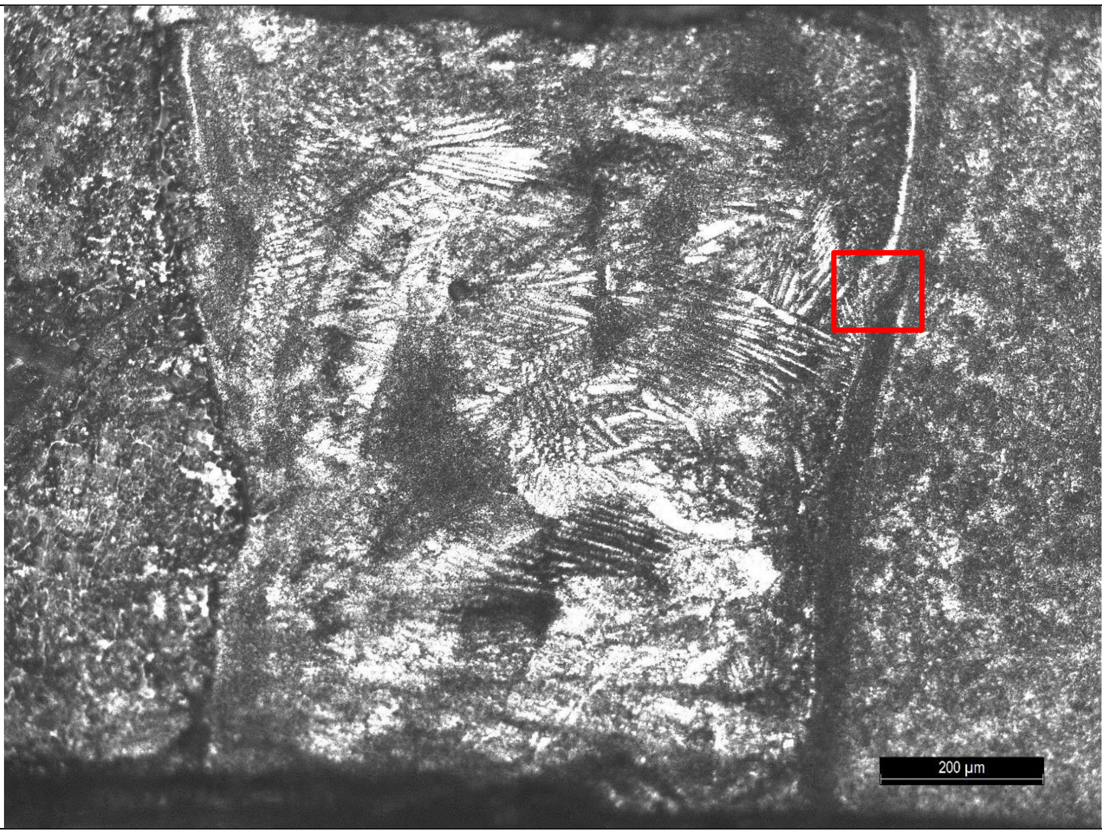

(a) Snapshot of the fusion zone

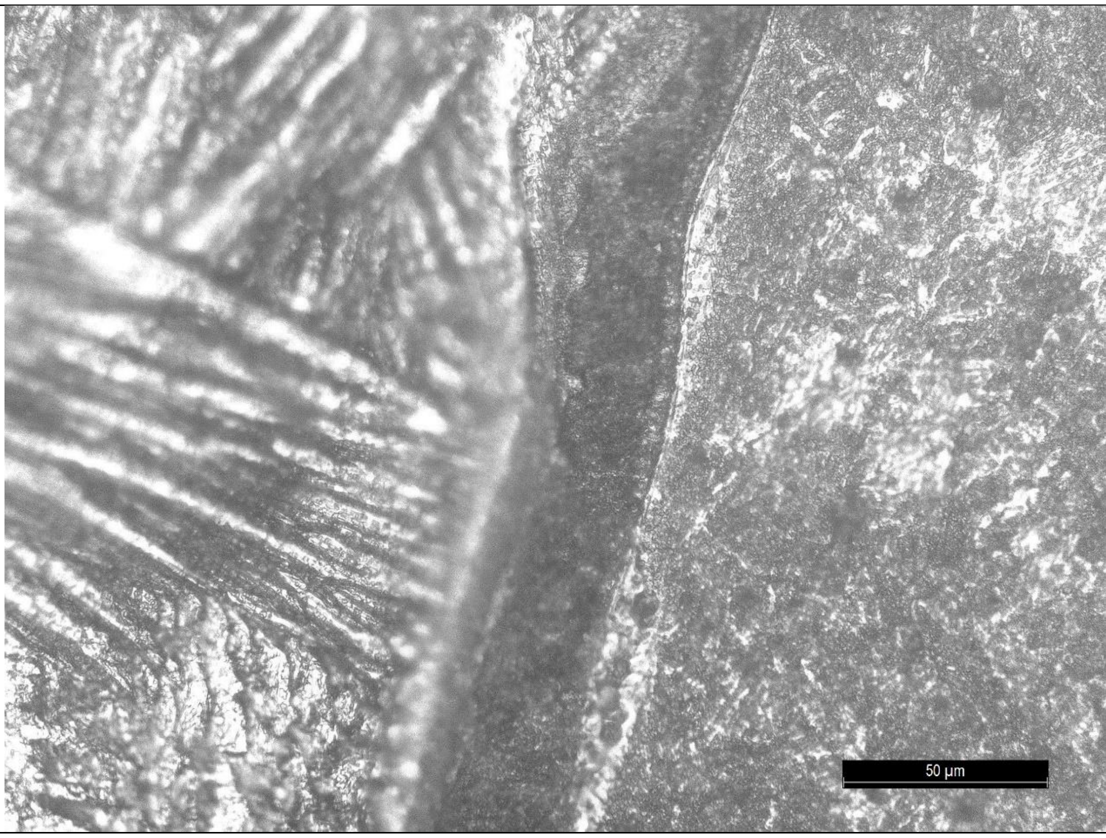

(b) Snapshot of the indicated region in (a)

Fig. 6.7 Cross section of NiTi-Ni-SS joint (sample no: R8110)

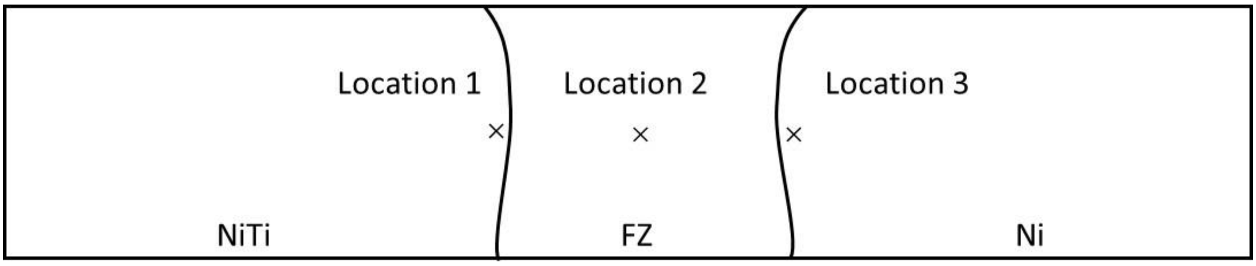

Fig. 6.8 EDX analysis location for region of NiTi and Ni

Table 6.1 Percentages of weight at different spectrums of NiTi-Ni weld joint

	Spectrum 1	Spectrum 2	Spectrum 3
Sample R5110			
Ni (Weight %)	51.82	74.38	98.69
Ti (Weight %)	48.18	25.62	1.31
Possible phases (to be confirmed by XRD and TEM)	NiTi	Ni_3Ti	Ni
Sample R5125			
Ni (Weight %)	51.49	35.38	74.73
Ti (Weight %)	48.51	64.62	25.27
Possible phases (to be confirmed by XRD and TEM)	NiTi	$NiTi_2$	Ni_3Ti
Sample R8090			
Ni (Weight %)	51.34	73.48	96.13
Ti (Weight %)	48.66	26.52	3.87
Possible phases (to be confirmed by XRD and TEM)	NiTi	Ni_3Ti	Ni
Sample R8110			
Ni (Weight %)	51.91	33.90	74.18
Ti (Weight %)	48.09	66.10	25.82
Possible phases (to be confirmed by XRD and TEM)	NiTi	$NiTi_2$	Ni_3Ti

EDX analysis in the region of NiTi-Ni-SS is presented in Fig. 6.8 above. Spectrum 1 is located at the NiTi side, while spectrum 2 is located at the fusion zone and spectrum 3 is located at the fusion interface near the Ni side. The percentages weight of Ni and Ti of different samples are summarized in Table 6.1.

In all the above scans, a significant increase in the Ni content and a possible matching of $NiTi_2$ and Ni_3Ti was found between the NiTi side and the Ni side. In sample R5110, the chemical composition reported in spectrum 2 indicated that the percentage ratio of Ni and Ti weight is about 74.38 wt% and 25.62 wt%, both of which are very close to the composition of the $NiTi_3$ phase in the binary Ni-Ti phase diagram. Therefore, this phase is considered to be the $NiTi_3$ in the fusion zone. In sample R5125, the chemical composition reported by spectrum 2 indicates that the Ni and Ti weight percentage ratio is about 35.38 wt% and 64.62 wt% and thus very close to the composition of the Ti_2Ni phase in the binary Ni-Ti phase diagram. Therefore, this phase is taken as the Ni Ti_2in the fusion zone. $NiTi_3$ is reported in spectrum 3. As a result, both $NiTi_2$ and $NiTi_3$ were found in the fusion zone of the welded joint. Similar phases were found in samples R8090 and R8110. The results indicate that the important factor affecting the joint properties depends on weld compositions, the latter are varied by the laser welding process parameters. This chemical composition variation is the main variable responsible for the deviation of tensile strength and microhardness behavior discussed above in previous sections. Phases of welded samples will be determined and confirmed by XRD and TEM in the latter part of this chapter.

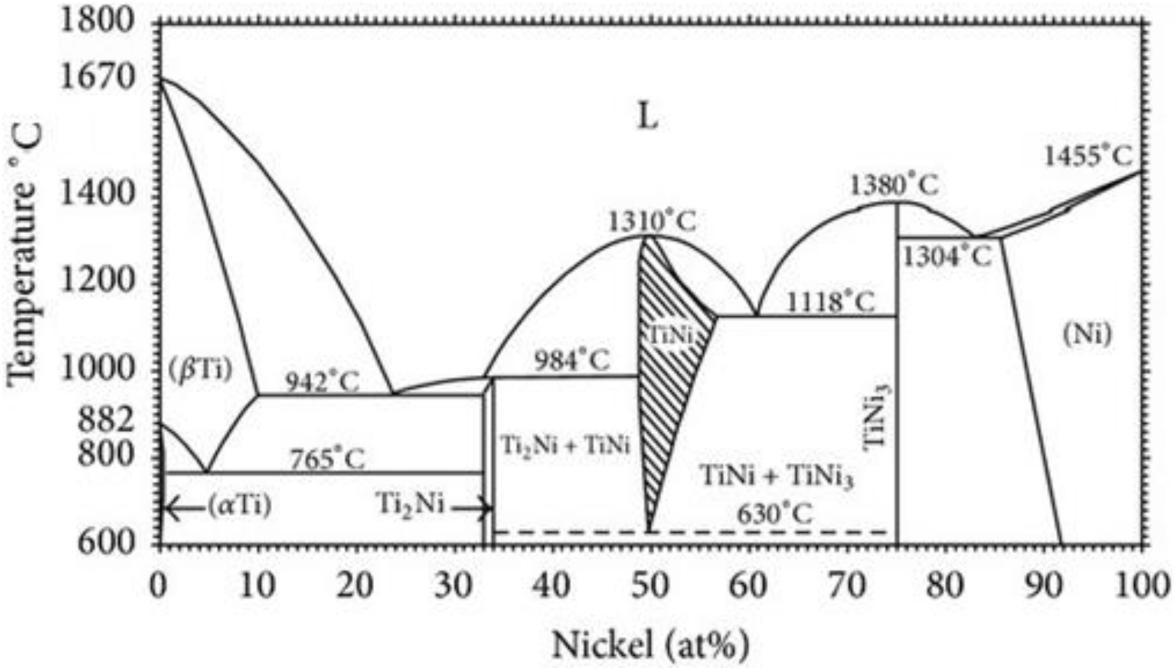

Fig. 6.9 Ni-Ti phase diagram

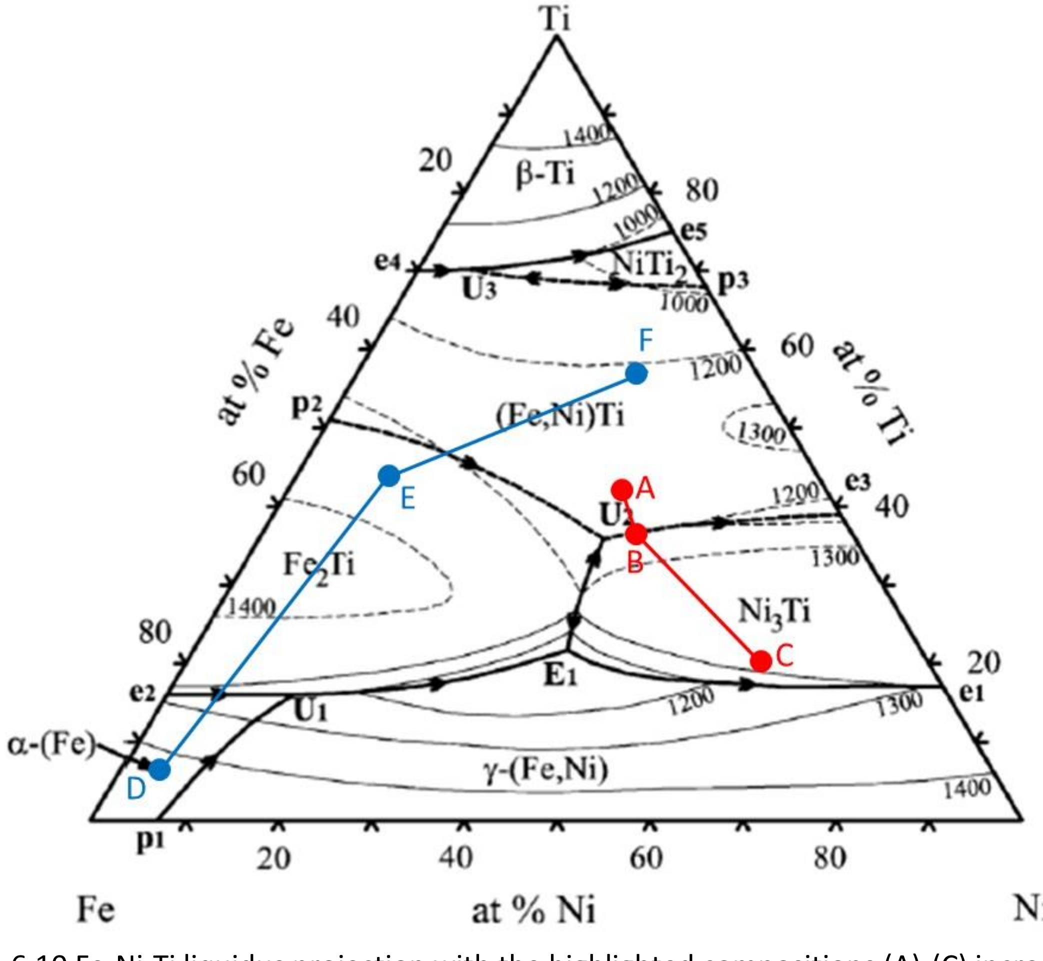

Fig. 6.10 Fe-Ni-Ti liquidus projection with the highlighted compositions (A)-(C) increase of Ni content to Ti (D)-(F) increase of Ni content to Fe

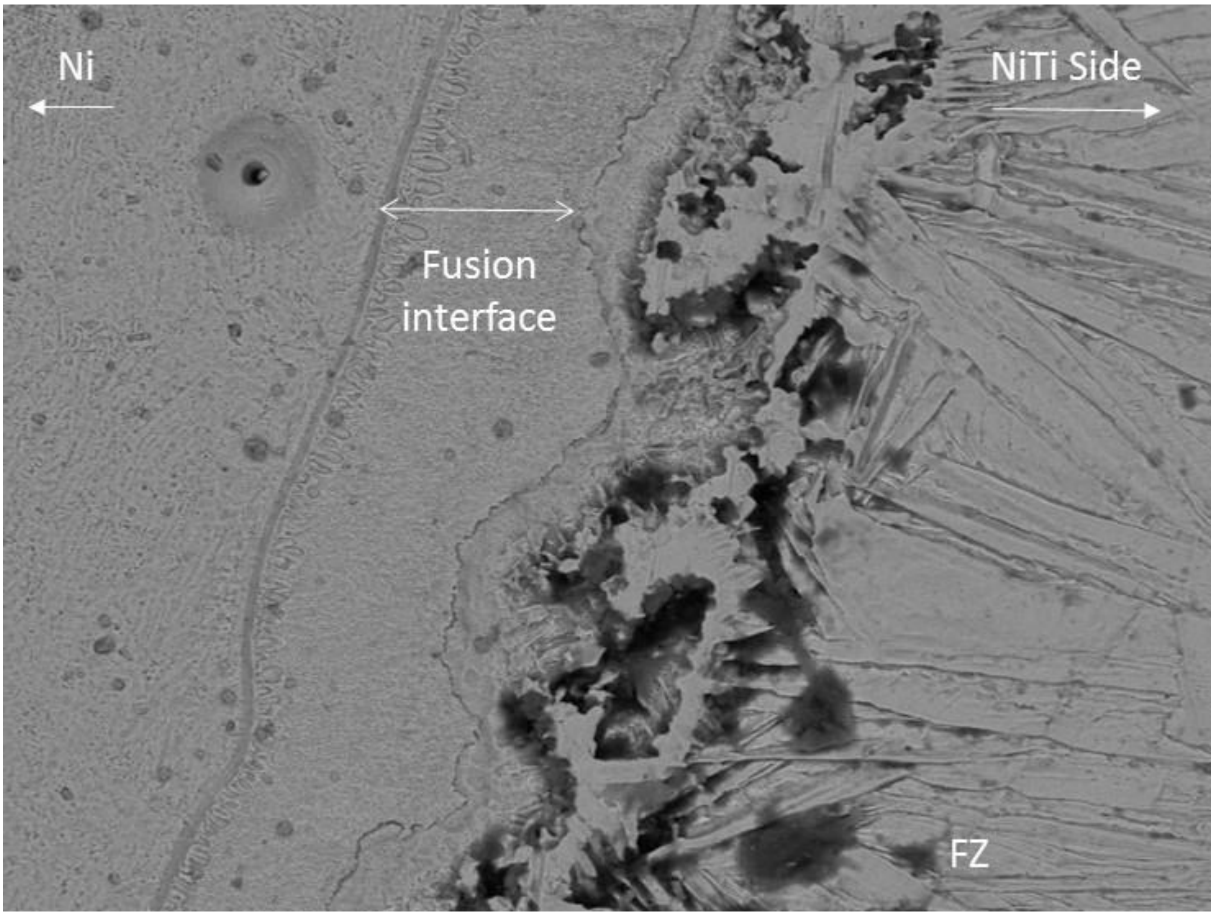

Fig. 6.11 SEM with backscattered electrons (BSE) image from the fusion interface of NiTi and Ni (Sample: R5070)

The relative stability of different phases in the Ni-Ti systems as a composition and temperature function is summarized as shown in Fig. 6.10. In addition to the base material, NiTi, two intermediate phases, which can be form from the liquid: Ni_3Ti and $NiTi_2$, exist in the system. The former is congruently solidifying while the $NiTi_2$ forms via a peritectic reaction involving the liquid and the NiTi phase. The large increase in Ni content can induce the forming of greater quantities of Ni_3Ti based on the Ni-Ti phase diagram and Fe-Ni-Ti liquidus projection as shown in Fig. 6.9 and 6.10. The solubility of nickel in the NiTi phase is restricted at 57% while titanium content in the NiTi phase is limited to a value of below 51% at a particular temperature. By decreasing the temperature, the balance of the phases in the NiTi was affected due to the decrease of the solubility of Ni. In order to freeze the balance of the phases in NiTi at a certain point, a rapid quenching was used to create the metastable material. Therefore, the phase state of NiTi and the formation of Ni_4Ti_3 precipitations were highly dependent on the temperature and aging time (Ke. *et al*., 2012). Since the cooling rate in the FZ and HAZ is slow, the formation of Ni_3Ti and $NiTi_2$ occurs within the fusion interface.

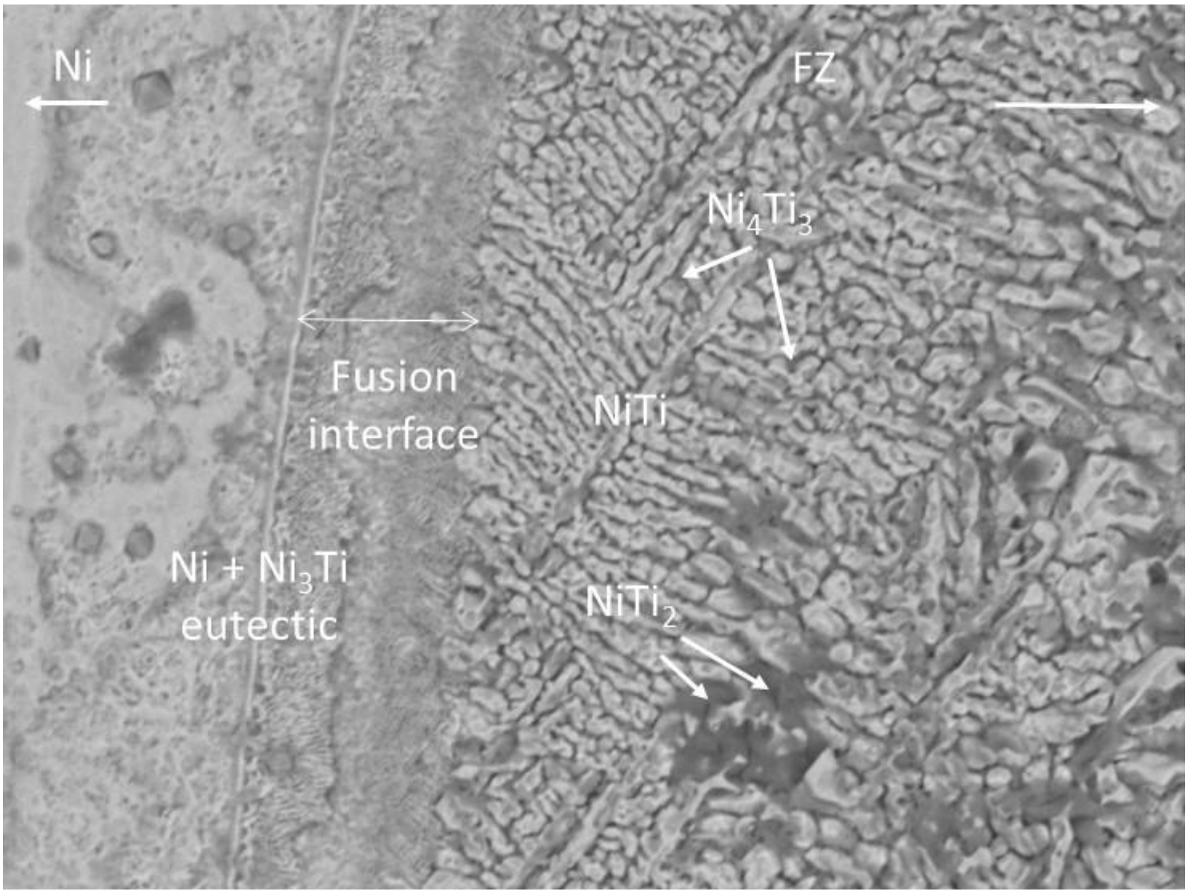

Fig. 6.12 SEM with backscattered electrons (BSE) image of fusion interface of Ni-NiTi joint (Phases identified based on EDX at the pointed location)

A magnified view of the fusion interface between NiTi and Ni is shown in Fig. 6.11. The fusion interface is free of cracks and pores. The fusion zone and fusion interface contain precipitates: $NiTi_2$ and Ni_3Ti phases identified based on the EDX analysis. The microstructure consists mostly of $NiTi_2$ at the fusion interface toward the Ni interlayer. Dendrites observed with a dark grey surrounding phase is $NiTi_2$ based on the EDX analysis, indicating that $NiTi_2$ dendrites in the fusion zone grow toward the Ni interlayer from the NiTi and Ni fusion interface. This forms as a result of a breakdown of the solidification front of the $NiTi_2$ phase and of interest is that this $NiTi_2$ solidification front grows from the weld pool side toward the Ni interlayer, to eventually develop into a dendritic microstructure. Band formation at the fusion interface between NiTi and Ni is illustrated. The microstructure at the fusion interface of Ni-NiTi with Ni_3Ti and Ni_4Ti_3 growing from the weld pool towards the NiTi heat affected zone based on the EDX analysis is shown in Fig. 6.12. The microstructure at the fusion interface of Ni-SS with FeNi, based on the EDX analysis, growing from that fusion towards the weld pool is shown in Fig. 6.13.

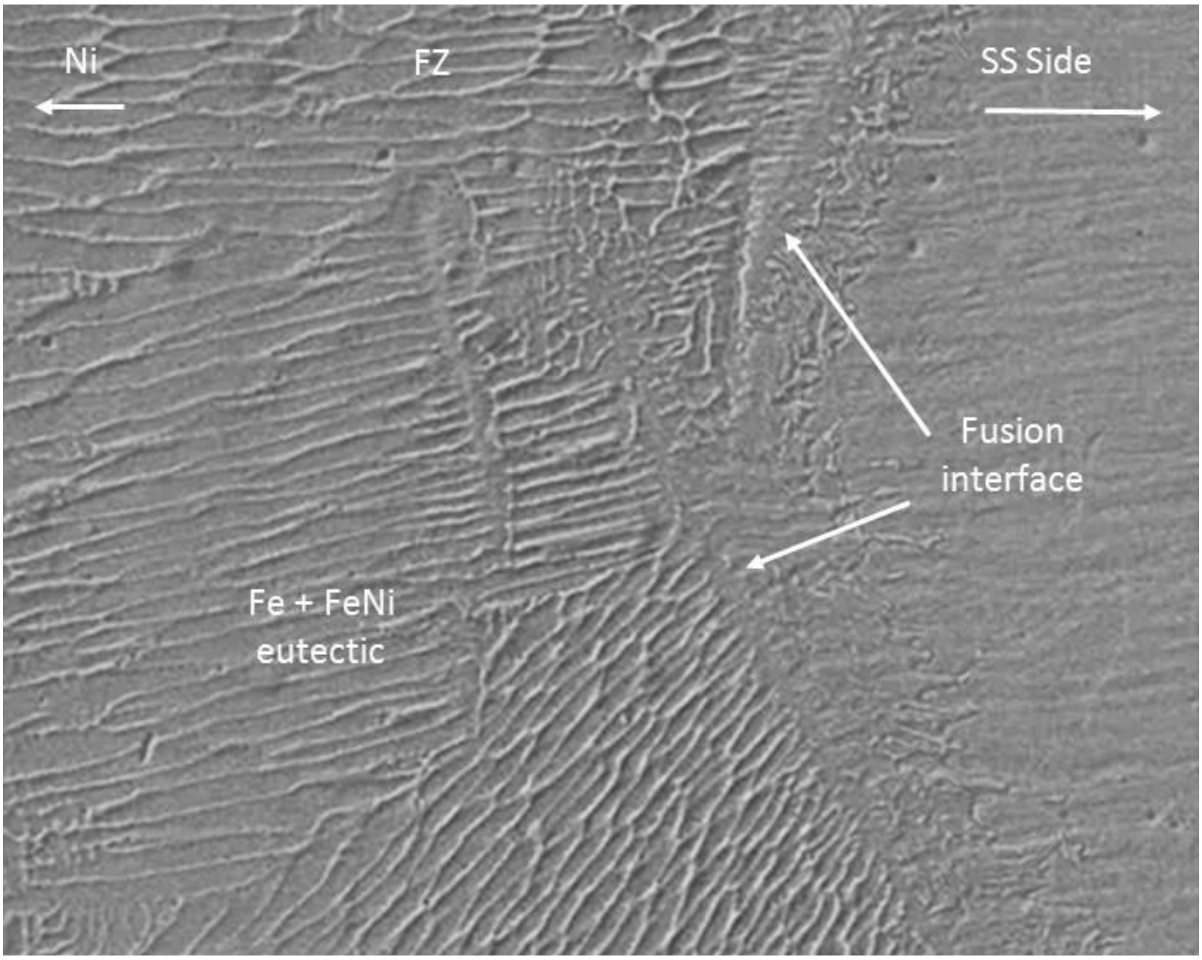

Fig. 6.13 SEM with backscattered electrons (BSE) image of fusion interface of Ni-SS joint

6.2.2 Phase Identification by XRD

XRD was used in the identification of the X-ray interference pattern, scattered by crystals and diffraction and further used to study the structure of matter in the weldments. The XRD pattern of different welding speeds with different interlayer widths were illustrated as shown in Fig. 6.14 to 6.21. XRD patterns of all joints indicated that phases such as $NiTi_2$, Ni_2Ti, Ni_3Ti and Ni_4Ti_3 are presented in the weld joint due to the presence of Ni interlayer causing the increase in Ni-rich compounds in the weld joint, thus inducing the formation of those phases. When NiTi and stainless steel welded with a 5mm interlayer, the increase of the welding speed from 90mm/s to 110mm/s causes a decrease in Ni_3Ti, Ni_4Ti_3 and $NiTi_2$ and an increase in martensite (B19') and R phase as shown in Fig. 6.15 and 6.16. The increase of martensite (B19') and R phase matrix improve the recoverability/superelastic properties of the NiTi (Kainuma, *et al*., 1986). Similar behavior, regarding the effect of welding speed, causes the increase of martensite (B19') and R phase is shown in Fig. 6.18 and 6.19. When comparing Fig. 6.14 to 6.21, the 5mm interlayer with 110mm/s welding speed could produce the smallest amount of Ni_2Ti while more martensite (B19') was added, and hence achieve a higher recoverable bending deflection. In addition, the Ti_2Ni is a FCC structure with a hardness of 700 HV (Chatterjee *et al*., 2008). A decrease of Ni Ti_2 intensity, as shown in Fig. 6.16, causes the microhardness values to decrease and the tensile strength increase within in the welded joint. Peaks near to 41.42 and 46.57 (2θ) indicate the presence of different intensities of $NiTi_2$ and Ni_3Ti in the rectangular shaped interlayer welded samples.

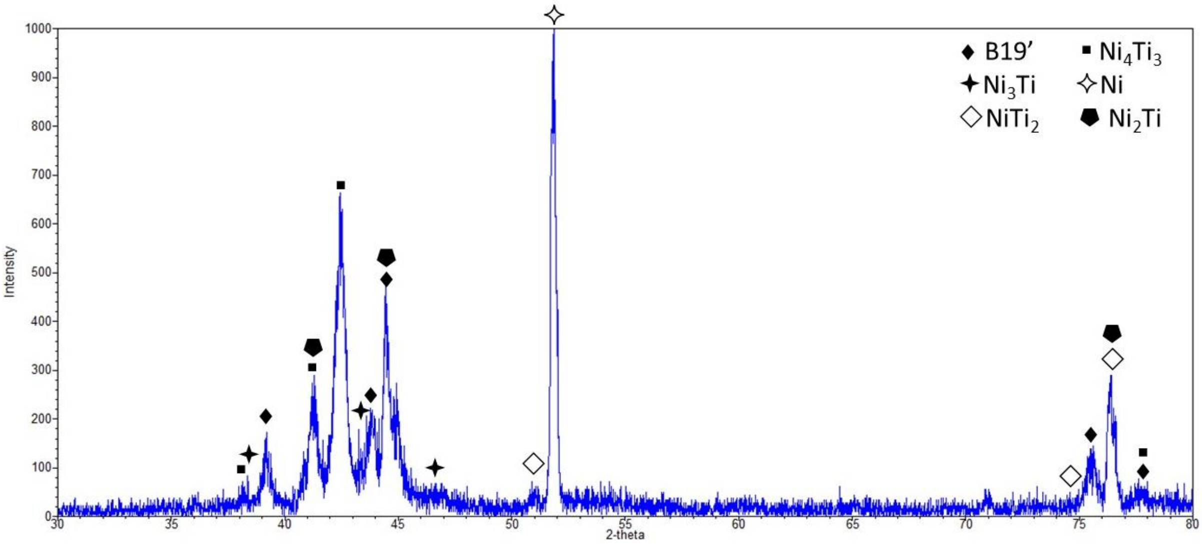

Fig. 6.14 XRD patterns recorded of welded joint with 5mm interlayer (sample no: R5070)

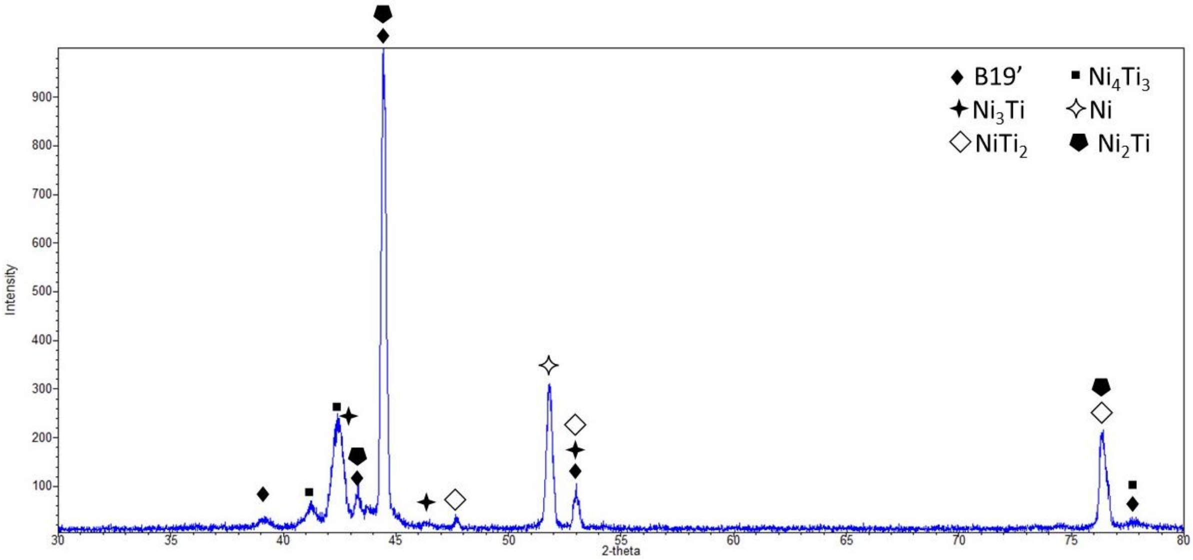

Fig. 6.15 XRD patterns recorded of welded joint with 5mm interlayer (sample no: R5090)

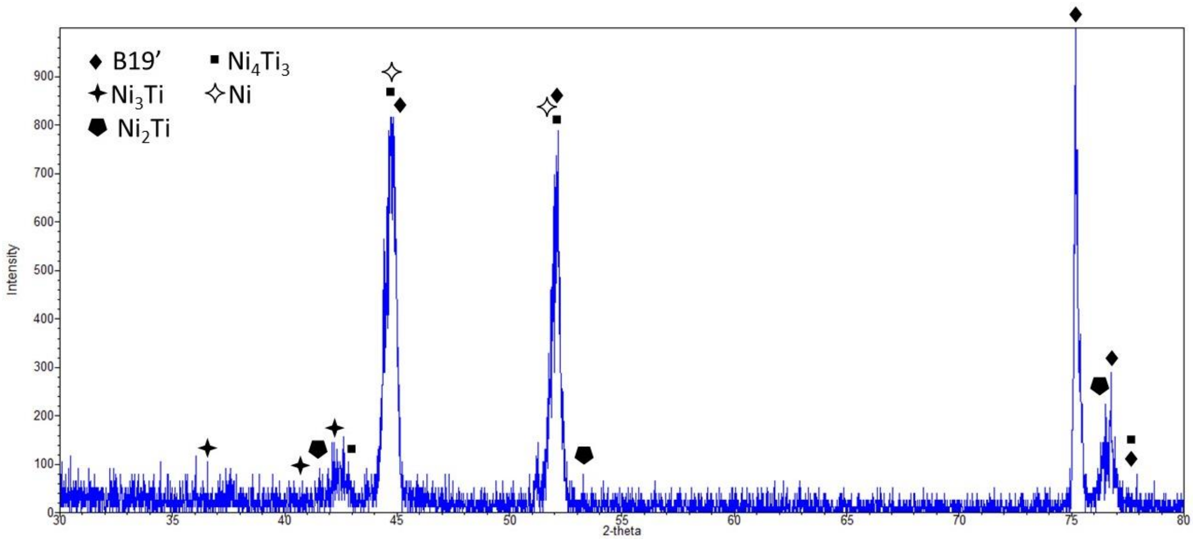

Fig. 6.16 XRD patterns recorded of welded joint with 5mm interlayer (sample no: R5110)

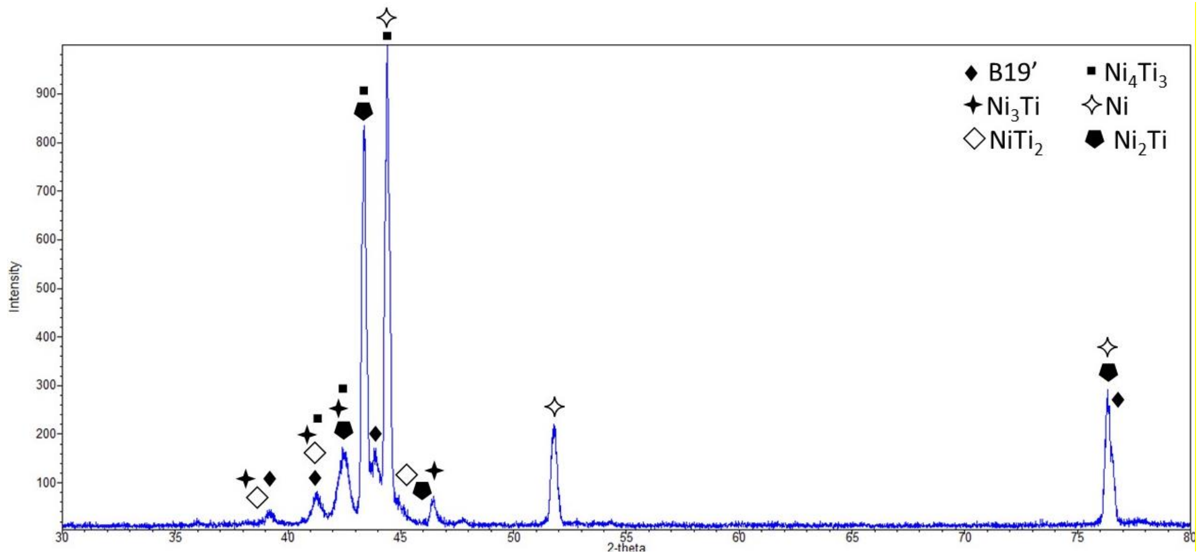

Fig. 6.17 XRD patterns recorded of welded joint with 5mm interlayer (sample no: R5125)

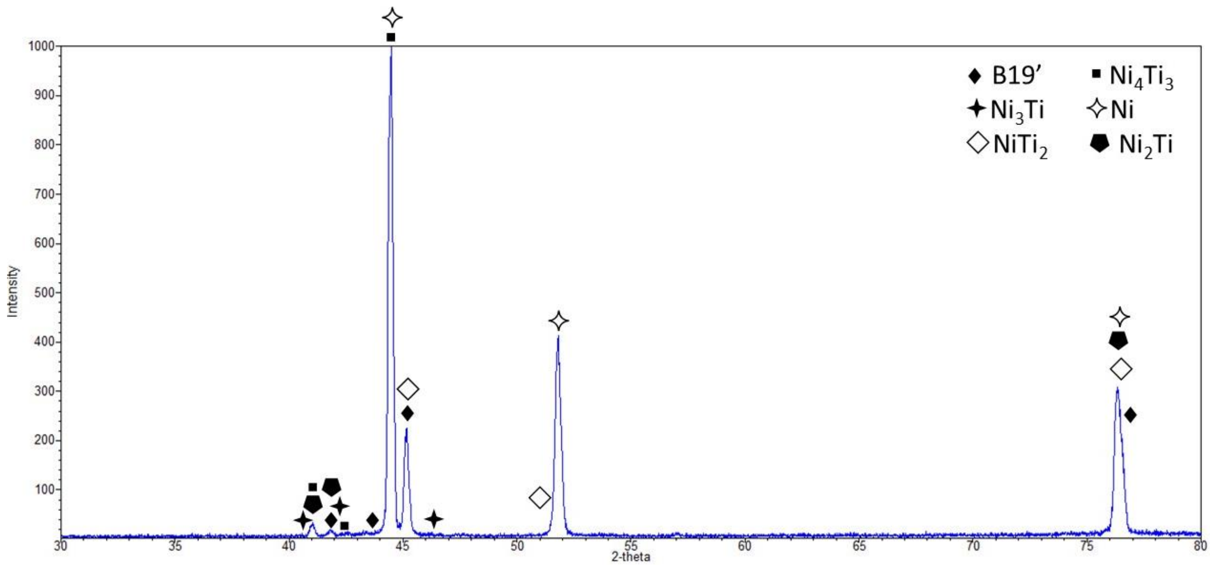

Fig. 6.18 XRD patterns recorded of welded joint with 8mm interlayer (sample no: R8070)

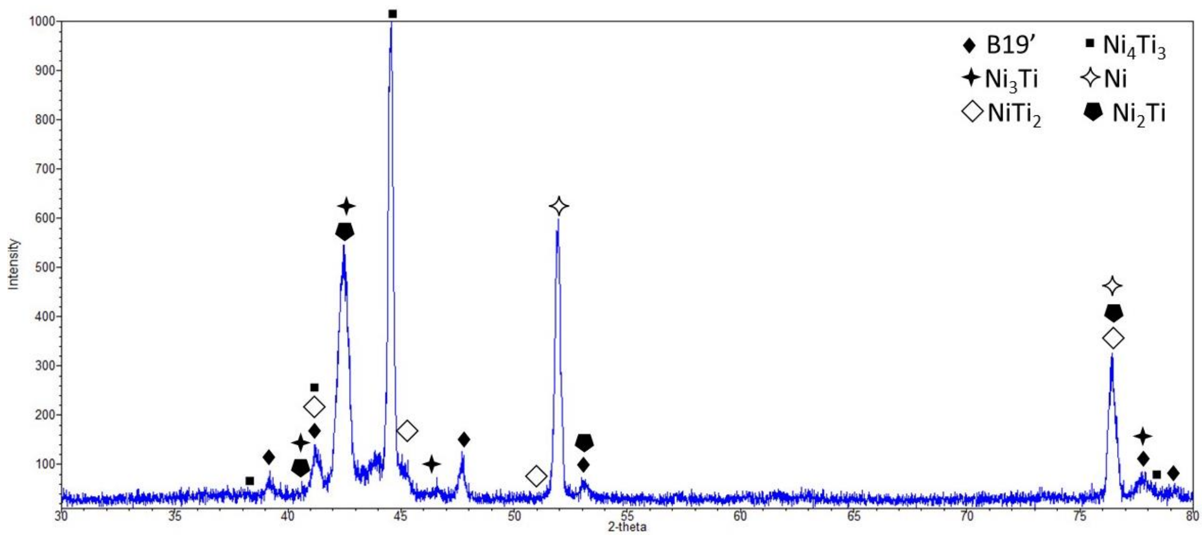

Fig. 6.19 XRD patterns recorded of welded joint with 8mm interlayer (sample no: R8090)

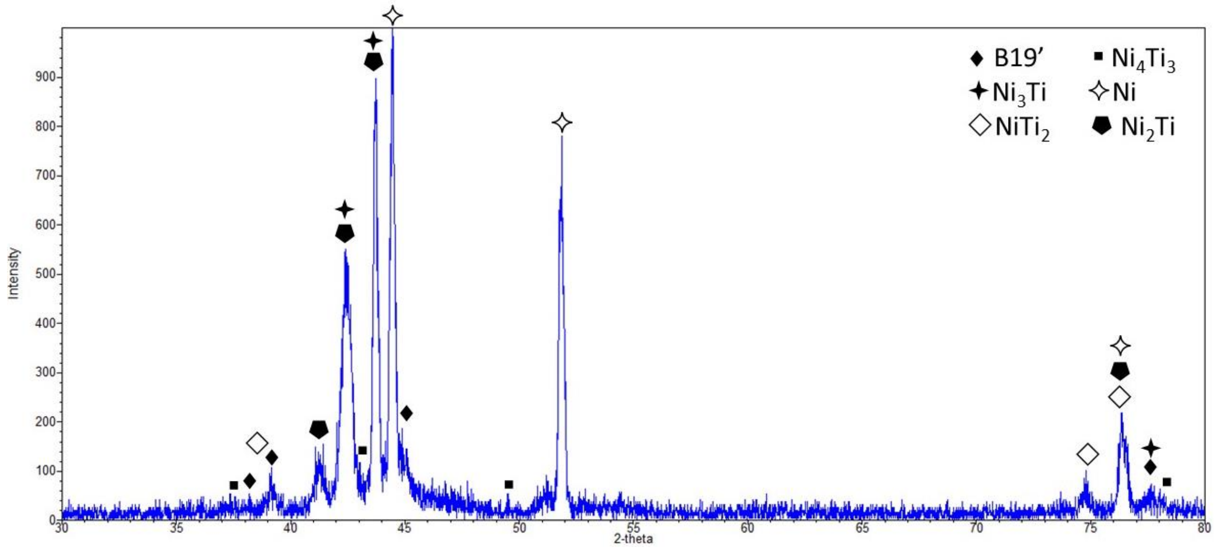

Fig. 6.20 XRD patterns recorded of welded joint with 8mm interlayer (sample no: R8110)

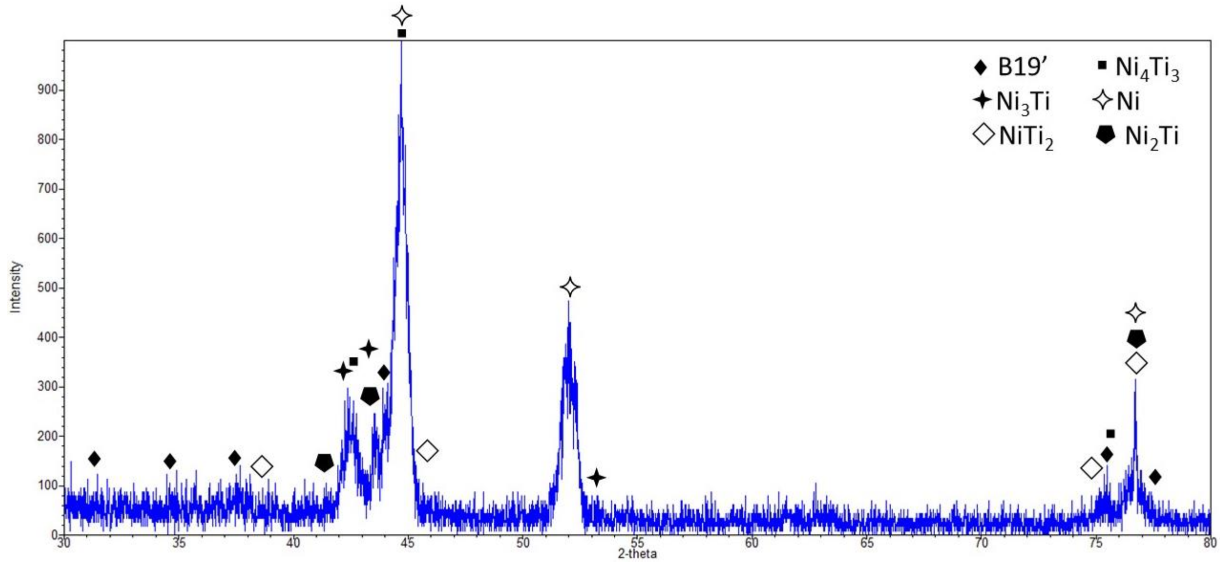

Fig. 6.21 XRD patterns recorded of welded joint with 8mm interlayer (sample no: R8125)

One of the most important aspects of materials science and engineering is the crystal structures because many materials properties depend on the crystal aspect of their structures. A solid consists of crystalline and amorphous. The former is a periodic arrangement of the unit cell into a lattice while the latter is a random arrangement of atoms. A space lattice can be defined as a three dimensional array of points. The space lattice points in a crystal are occupied by atoms. The three unit vectors, a, b, c are called lattice parameters and define the three dimensions generating the crystal structure. Based on their length and orientation, a total of 7 crystal systems can be defined: cubic, tetragonal, orthorhombic, monoclinic, rhombohedral, hexagonal and triclinic. Table 6.2 lists the crystal systems with respect to the phases of the weldment.

Table 6.2 Crystal systems of possible phases in the welding joint of NiTi and Ni

Crystal structure	**Axis system**	**Phases in the weldment**	**Space group**	**Lattice parameters**	**Reference**
Cubic	a=b=c	Ni $NiTi_2$	Fmm Fd3m	a=3.54 a=11.28	Hull, 1921 Yurko *et al.*, 1959
Tetragonal	a=b≠c	/	/	/	/
Orthorhombic	a≠b≠c	Ni_3Ti_2	Bbmm I4/mmm	a= 4.458, b=4.348, c=13.374, α=90, β=90, γ=90 a= 3.108, b=3.108, c=13.436, α=90, β=90, γ=90	Hara *et al.*, 1997
Monoclinic	a≠b≠c	NiTi (B19')	$P2_1/m$	a=2.89, b=4.11, c=4.66, β=98.10	Michal & Sinclair, 1981
Rhombohedral	a=b=c	Ni_4Ti_3	R3	a=11.24, c=5.08	Saburi *et al.*, 1986
Hexagonal	a=b≠c	Ni_3Ti NiTi (R) Ni_2Ti	$P6_3/mmc$ P3 R-3m:H	a=5.11, c=8.30 a=7.3472, c=5.2837 a=2.549, c=43.648	Laves *et al.*, 1939 Schryvers and Potapar, 2002 Bhan, 1971
Triclinic	a≠b≠c	/	/	/	/

Table 6.3 summarizes the fusion zone chemical composition of different weldment of 5 mm interlayer width. The phase constituting the weld of all samples consisted of cubic nickel phase, cubic $NiTi_2$ phase, hexagonal Ni_2Ti and Ni_3Ti and rhombohedral Ni_4Ti_3 phase. When NiTi-Ni welded with 70 mm/s welding speed, monoclinic B19' martensite, hexagonal R phase were found. However, the increase of welding speed caused a decreased amount of formation of monoclinic B19' martensite, cubic Ni and $NiTi_2$ phases. When the welding speed

further increased, an increased amount of monoclinic B19’ martensite, hexagonal R phase and cubic was formed. The formation of cubic Ni_2Ti, hexagonal Ni_3Ti and rhombohedral Ni_4Ti_3, however, were found to have decreased a small amount, while cubic $NiTi_2$ was found to have decreased, very little in weld. If the welding speed was further increased, cubic Ni_2Ti, hexagonal Ni_3Ti and rhombohedral Ni_4Ti_3 were increased while monoclinic B19’ martensite, cubic Ni and hexagonal R phase decreased. However, the increase of cubic $NiTi_2$ causes the reduction of tensile strength.

Table 6.3 Chemical composition of the NiTi-Ni (5mm) fusion zone of different welding speed

	Sample no. (5mm)	R5125	R5110	R5090	R5070
	Welding speed (mm/s)	125	110	90	70
Phase	**Lattice structure**	Quantity (%)			
Ni	Cubic	27.00%	13.40%	6.20%	7.80%
NiTi	Monoclinic (B19’)	12.20%	43.40%	18.90%	31.00%
	Hexagonal (R)	10.70%	16.80%	31.20%	22.40%
$NiTi_2$	Cubic	2.50%	0.00%	5.60%	6.60%
Ni_2Ti	Hexagonal	12.00%	7.40%	10.60%	11.60%
Ni_3Ti	Hexagonal	8.70%	9.30%	12.20%	12.30%
Ni_4Ti_3	Rhombohedral	26.90%	9.70%	15.30%	8.30%

Table 6.4 presents a summary of the chemical composition of the fusion zone with reference to different welding speeds of 8mm interlayer widths. The phase constituting the weld of all samples was similar to those chemical composition of welds of 5mm interlayer widths except the amount of different phases. When NiTi-Ni was welded with a 125 mm/s welding speed,

monoclinic B19’ martensite, hexagonal R phases were found. The decrease of welding speed, however, caused an increase of monoclinic B19’ martensite, hexagonal R phase and cubic Ni. Further decrease of welding speed resulted in an increased monoclinic B19’ martensite, hexagonal R phase and cubic Ni formation. Additionally, the formation of all NiTi phases were found to have decreased almost in line with any further welding speed decrease.

Table 6.4 Chemical composition of the NiTi-Ni (8mm) fusion zone of different welding speed

	Sample no. (8mm)	R8125	R8110	R8090	R8070
	Welding speed (mm/s)	125	110	90	70
Phase	**Lattice structure**	Quantity (%)			
Ni	Cubic	10.50%	32.90%	33.40%	72.50%
NiTi	Monoclinic (B19’)	34.30%	12.30%	13.60%	11.10%
	Hexagonal (R)	12.70%	17.30%	23.90%	3.10%
$NiTi_2$	Cubic	7.70%	6.90%	3.60%	2.80%
Ni_2Ti	Hexagonal	10.60%	6.30%	6.90%	4.80%
Ni_3Ti	Hexagonal	8.00%	14.10%	9.00%	1.20%
Ni_4Ti_3	Rhombohedral	16.20%	10.20%	9.60%	4.50%

A comparison of the chemical composition of R5110 and R8090 revealed , the tensile strength of the R5110 joint highly relied on the monoclinic B19’ and hexagonal R phase, whereas, the cubic Ni and hexagonal R phase improved the tensile strength of R8090. Both the transformation of austenite to R phase and austenite to martensite are martensitic and are easily reversed by heating. Both introduce very small volume changes and can be self-related variants. Twin boundaries in both martensite and the R phase are highly mobile but it is substantially easier to move twins in the R phase than in that of the martensite. Thus, the higher the amount of martensite could possibly enable the welded joint to have greater tensile strength.

6.3 Effect of Phases on Transformation Behavior

Transformation temperatures of the thermally affected regions in the weld joints of NiTi-Ni-SS304, despite their small dimensions, can be determined by differential scanning calorimetry (Lin *et al*., 1994). Referring to the solubility range on the Ti-rich side of the Ni-Ti phase diagram, the dependence of the transformation temperatures on the composition of precipitates located in the thermal affected zone for Ni-rich compounds is more significant. When comparing the heat affected zone and the fusion zone with the base material, the addition of Ni interlayer may bring significant differences in the presence of precipitates and the transformation characteristics.

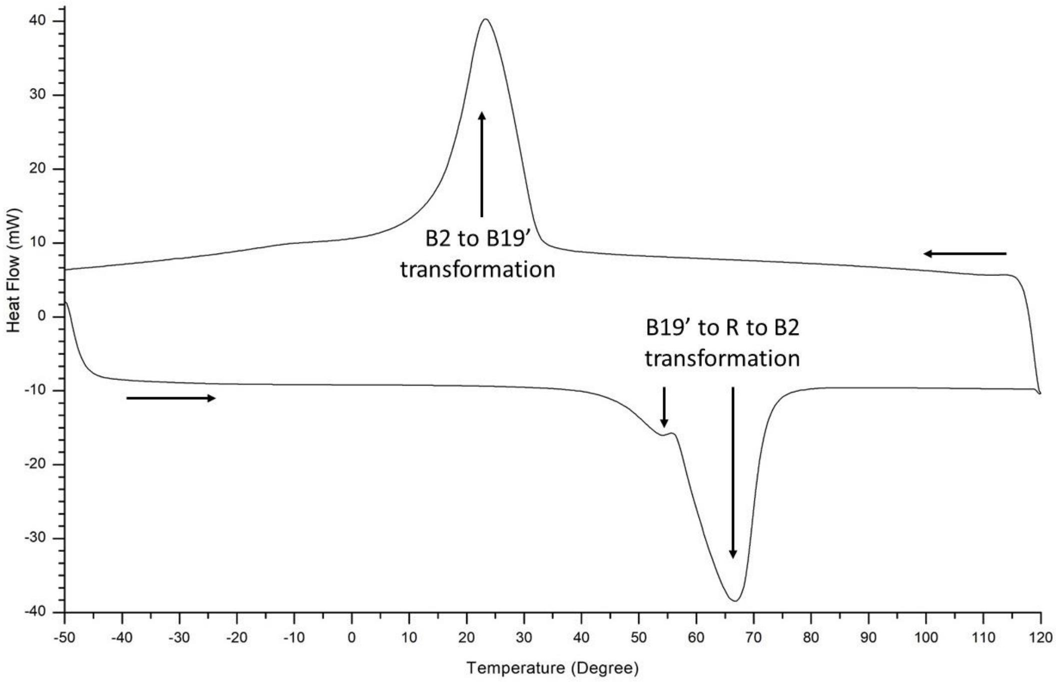

Fig. 6.22 DSC curve for base material of NiTi as received

Fig. 6.22 shows the NiTi material as received DSC curve and shows a 2-stage transformation (B19’-R-B2) during the heating cycle and a 1 stage transformation (B2 to B19’) during cooling cycle. The existence of two endothermic peaks indicates a 2-step transformation from austenite to R-phase and later to a one stage exothermic peak indicates a 1 stage martensite transformation. During the heating, the B19’ martensite transforms to R-phase at 44.81°C. At 56.40°C, the material begins to transform to austenitic and is fully austenitic at 73.23 °C. A hysteresis in the phase transformation temperatures, when transforming from martensite to austenite, as opposed to, from austenite to martensite results from internal friction and defects in the crystal structure. The reason why there is a phase transformation from B19’ to R phase then to B2 phase (two-stage transformation) is that fine precipitates have less resistance to transformation with less strain like B2 to R phase while have strong resistance to transformation with large strain like B2 to B19’. B19’ is the ground state of martensite at low temperature and R phase is another martensite candidate of the Ni-Ti phase diagram. Therefore, the phase transformation behavior and the occurrence of the R phase transformation of NiTi influenced by the presence of Ni_4Ti_3 precipitates.

Because the different welding process parameters affected the chemical composition of fusion zone, the transformation behaviors of the welded samples: R5125, R5110, R8110 and R8125 were illustrated by Fig 6.23 to 6.26 respectively. It can be found from the figures that R8110 and R5110 show a one-stage phase transformation from B2 austenite to B19’ martensite when cooling and from B19’ martensite to B2 austenite when heating. However, R5125 and R8125 show different phase transformation behavior when heating. R5125 shows two–stage phase transformation from B19’ to R phase then to B2 phase during heating while R8125 seems to show two-stage phase transformation from B19’ to R phase but the transformation to B2 phase starts without waiting the completion of transformation of transformation too R phase.

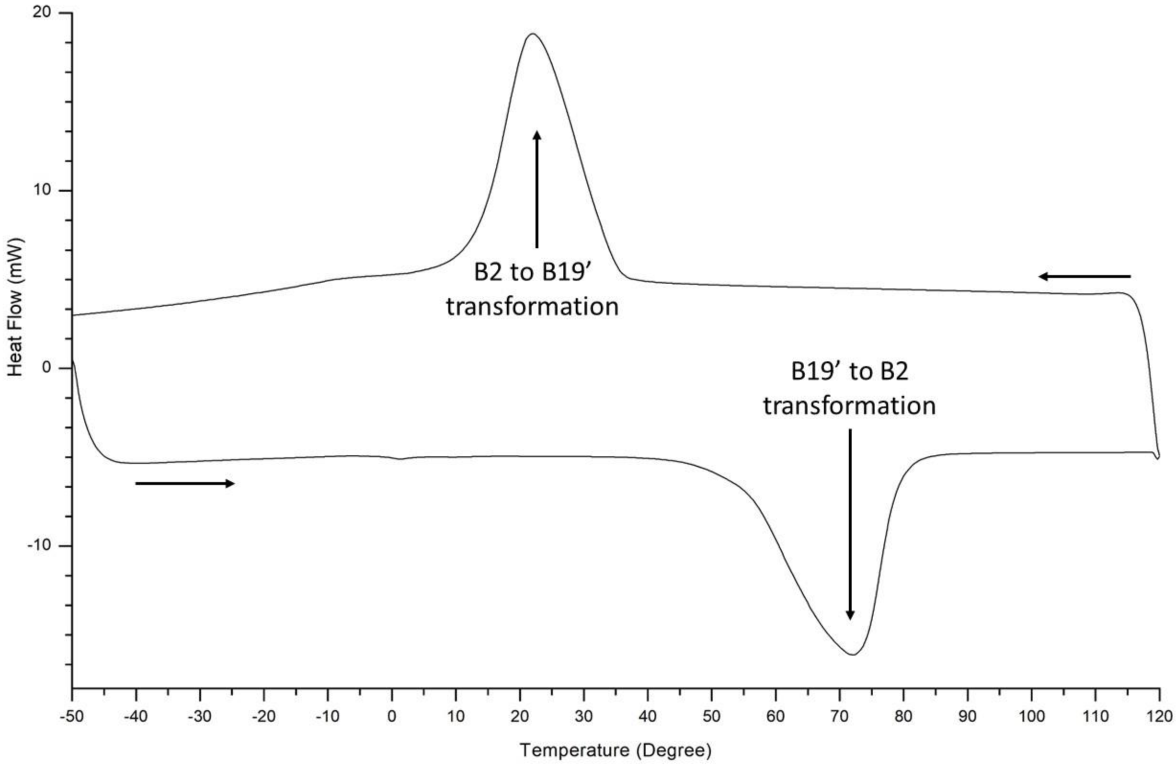

Fig. 6.23 DSC curve for fusion zone of R5110

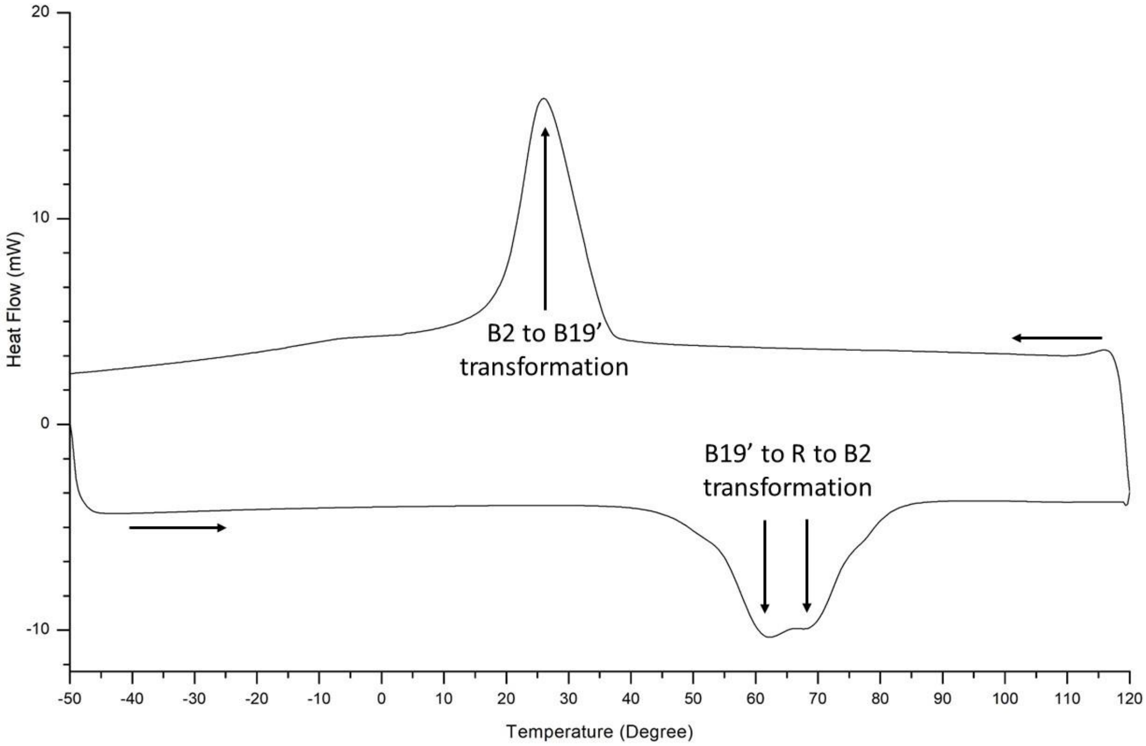

Fig. 6.24 DSC curve for fusion zone of R5125

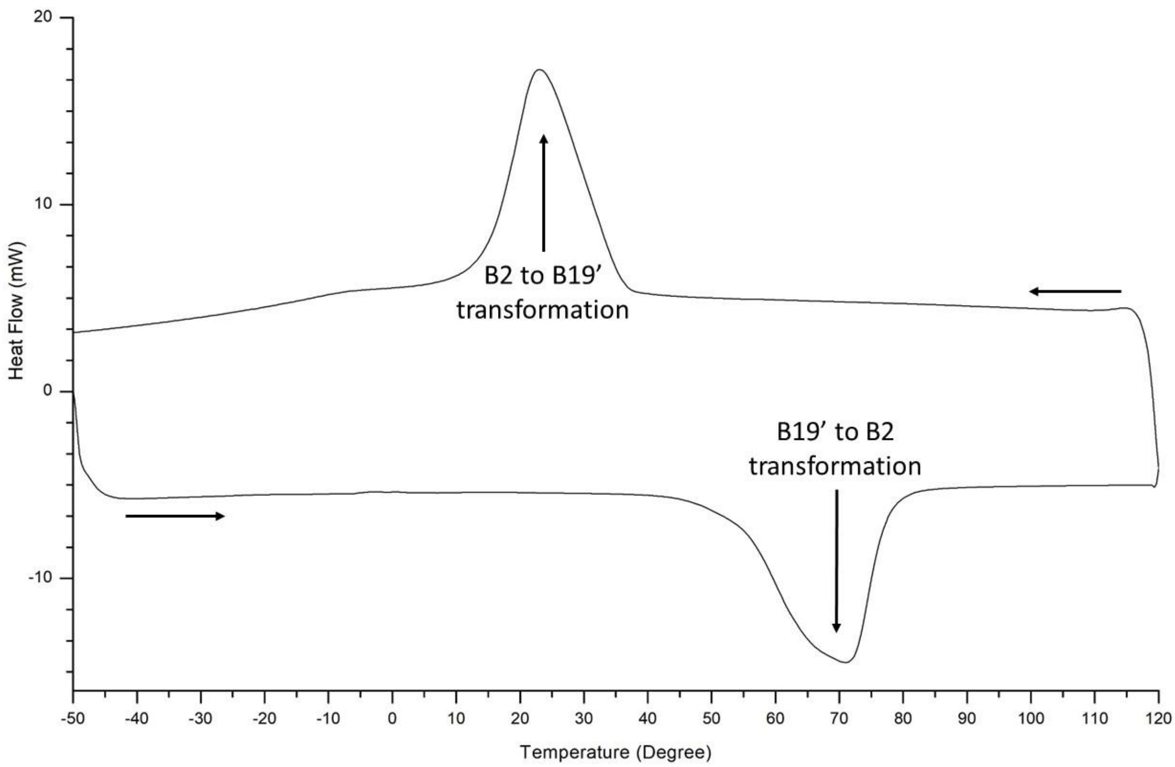

Fig. 6.25 DSC curve for fusion zone of R8110

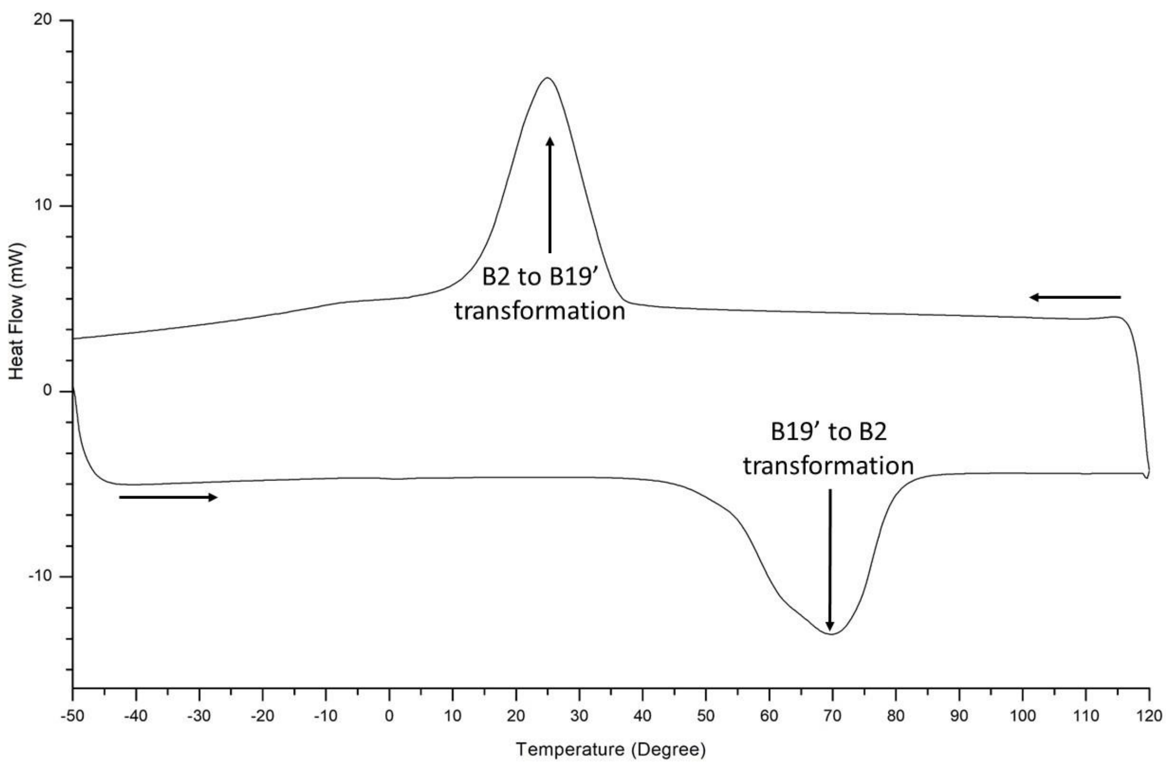

Fig. 6.26 DSC curve for fusion zone of R8125

As the transformation of B2 austenite to R phase and B2 austenite to B19’ martensite are thermoelastic, they both individually follow the Clausius-Clapeyron equation:

$$\frac{d\sigma}{dT} = \frac{\Delta L}{T\varepsilon_t}$$

Where $\frac{d\sigma}{dT}$ is the stress rate, ΔL is the change of latent heat and ε_t is the change of strain. As the latent transformation heats for the two transformations are similar, the change of strain for the transformation of the R phase to B2 austenite is smaller, and the stress rate far greater. Additionally, the R phase and B19’ martensite can reversibly transform between themselves. In this study, although the R phase form first, kinetic barriers are eventually overcome with further heating and the increased thermodynamic preference for B19' martensite enables the B19' martensite to finally replace the R phase.

Hysteresis is largely affected by composition and the specific transformation behavior is dependent on how Ni_4Ti_3 particles are distributed between grain boundary and grain interior (Hamilton *et al.*, 2004). According to the theory of phase transformation kinetics (Christian, 2002), nucleation rate (R_n, the number of stable nuclei formed in the assembly in unit time) can be expressed as

$$R_n \propto \exp(-\frac{\Delta G_c}{kT})$$

where ΔG_c is the critical free energy to form a nucleus (i.e., nucleation barrier); k is the Boltzmann constant; T is transformation temperature. This equation shows that nucleation rate is determined by nucleation barrier ΔG_c.

Given by Russell (1969), the nucleation barrier ΔG_c for coherent nuclei is given as

$$\Delta G_c = 16\pi\sigma^3/[3(\Delta G_v + \varepsilon)^2$$

where ΔG_v is the chemical free energy change associated with the precipitation reaction, ε is the strain energy per unit volume associated with the formation of a nucleus, σ is the interfacial energy associated with the formation of the new interface.

The ΔG_v is the driving force for the formation of new phase. To enable the precipitation to happen, ΔG_v must be negative which require a supersaturated solid solution. That means the solute concentration must beyond its solubility limit in the solid solution which is produced by rapid cooling of more concentrated solid solution from higher temperature as being the case of the laser welding of NiTi and Ni. The larger the degree of supersaturation (i.e., the excess solute concentration beyond solubility limit) the more negative is the driving force ΔG_v for precipitation.

When Ni content is low (the Ni content of NiTi as received), the nucleation rate is very small and thus precipitation of Ni_4Ti_3 is very sensitive to the presence of grain boundary. Nucleation rate at grain interior is much smaller than at grain boundary in this case. As a result, precipitation mainly occurs at grain boundary with less precipitate at grain interior. When Ni content is increased, similar nucleation rate between the grain interior and boundary make precipitation occurs homogeneously. As a result, a homogeneous distribution of precipitates is developed by high Ni content. With Ni as interlayer during the welding of NiTi and stainless steel, the supersaturation is high which makes not much difference in nucleation rate between grain boundary and grain interior. As a result, a homogeneous distribution of precipitates without being affected by grain boundary is obtained.

The nucleation rate in the grain interior region is smaller than that in the grain boundary region based on the kinetics theory of phase transformation, therefore, Ni_4Ti_3 precipitates preferentially grow and nucleate in the grain boundary region. As Ni_4Ti_3 precipitates, then, merge another Ni_4Ti_3 precipitates from the melt and grow increasingly larger, coherency of Ni_4Ti_3 precipitates with the NiTi matrix is lost when Ni_4Ti_3 precipitates reaching a certain value. Therefore, the establishment of the inhomogeneous distribution of Ni_4Ti_3 is indicated in the TEM result as shown in Fig. 6.27.

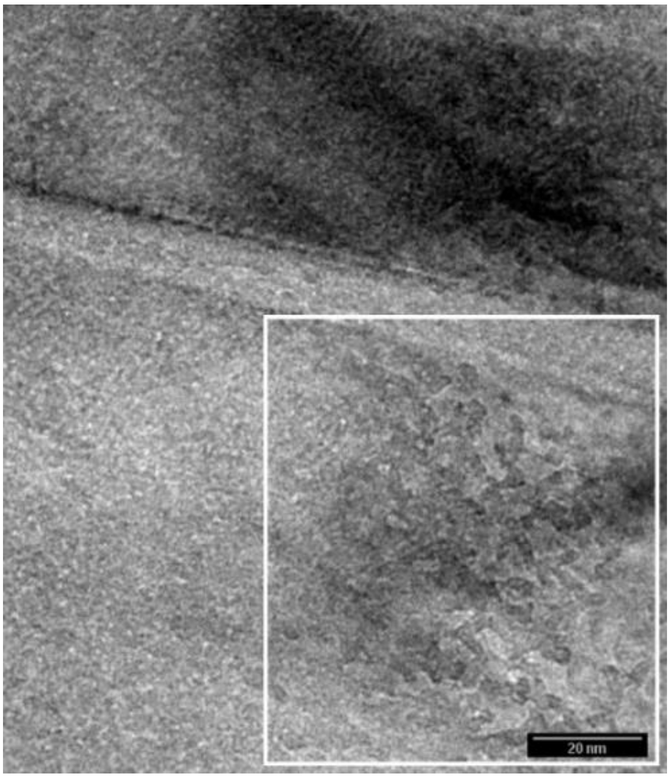

Fig. 6.27 TEM image of weld zone with inhomogeneous distribution of Ni_4Ti_3

Table 6.5 DSC measurements on the base metal and welded zone of different samples

	Temperature (°C)						Quantity of phase (%)
	Mf	Ms	As	Af	Mf - Ms	As - Af	Ni_4Ti_3
NiTi as received	14.78	32.43	56.44	73.38	17.65	16.94	-
R8125	13.84	36.21	52.14	79.79	22.37	27.65	16.2
R8110	14.92	36.09	53.44	77.43	21.17	23.99	10.2
R5110	13.60	35.42	54.01	79.53	21.82	25.52	9.7
R5125	18.99	36.57	52.18	78.26	17.58	26.08	26.9

Experimentally it is known that both martensitic and austenitic transformation temperature is strongly dependent on composition as shown in Table 6.5. The amount of Ni_4Ti_3 increased when the welding speed was increased to 125mm/s in both 5 mm and 8 mm thickness of the interlayer. When the amount of Ni_4Ti_3 increased to 16.2%, two-stage phase transformation from B19' to R phase seems to be appeared. When the amount of Ni_4Ti_3 increased to 26.9%, two-stage phase transformation was occurred when heating. When the amount of Ni_4Ti_3 was below 10.2%, only one-stage phase transformation was occurred when heating. By decreasing the welding speed (equal to increasing the applied laser volume energy density), sufficient thermal energy was presented to accelerate the coarsening and decomposition of the Ni_4Ti_3 precipitate. It appears to act as a heterogeneous nucleation site for the Ni_3Ti phase. The Ni_4Ti_3 phases appears to decompose to Ni_3Ti_2 and finally decompose to the thermodynamically stable phase of Ni_3Ti.

6.4 Effect of Phases on Bending and Recovery Behavior

The results discussed in the previous chapters stated that a successful joining NiTi and stainless steel with rectangular shape Ni interlayer could achieve good tensile strength and corrosion performance while the bending performance of those samples were evaluated by guided bend with no die test and the results are discussed in this section. The test aims to deform the welded sample at a point near the weld line at the NiTi-Ni side to measure the maximum displacement at break and bending stress at a predefined displacement. After that, the bended samples would be heated up to the Austenitic finish temperature and the recoverable bending deflection would be recorded for comparison.

Table 6.6 Results obtained from bending test

Sample No	Welding speed (mm/s)	Interlayer width (mm)	Maximum displacement at break (mm)	Bending stress with 1.98mm displacement (kPa)	Recoverable bending deflection (mm)
A1	70	5	3.50	5,113.6	2.60
A2	90	5	3.50	4,959.1	2.60
A3	110	5	6.80	2,907.8	5.00
A4	125	5	5.60	3,373.6	3.90
B1	70	8	1.98	5,786.4	1.50
B2	90	8	2.83	3,430.9	2.00
B3	110	8	2.20	4,677.5	1.70
B4	125	8	1.98	5,318.2	1.50

Bending test and shape recovery test were performed for the samples welded with different welding speed and interlayer width at a predefined laser power. The results of maximum displacement at break, bending stress at a predefined bending deflection and recoverable bending deflection were obtained and are summarized in the Table 6.6.

The result shows that for a particular bending deflection, the bending stress of sample A1 and sample B1 are the highest while sample A3 and sample B2 are the least for interlayer width of 5mm and 8mm respectively. Their deflection deviated from linearity owning to the non-linearity in the behavior of pseudoelasticity. Regarding the maximum displacement at break, for all samples, there is an improvement of bending deflection to a maximum value when the welding speed is increased, then there is a reduction of bending deflection when further increase the welding speed. Similar behavior regarding the recoverable bending deflection is shown. When comparing sample A3 and B2, the former, interlayer width of 5mm with welding speed of 110mm/s, could not achieve the higher tensile strength than sample B2, but it could produce a more ductile joint to achieve a maximum displacement at break of 6.80mm and recoverable bending deflection of 5.00mm as shown in Fig. 6.28. The original position of the welded specimen was completely recovered after 18s.

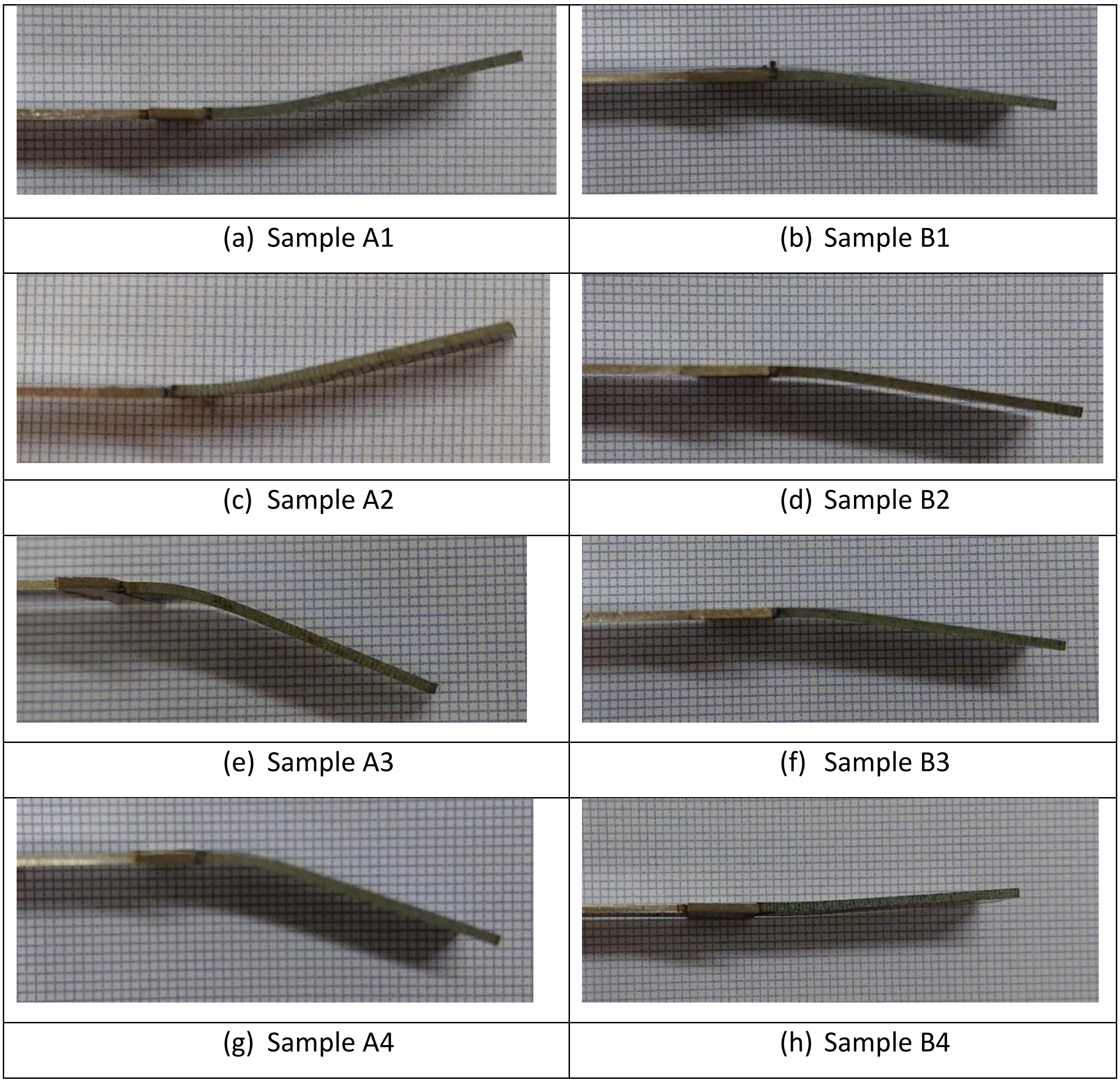

(a) Sample A1
(b) Sample B1
(c) Sample A2
(d) Sample B2
(e) Sample A3
(f) Sample B3
(g) Sample A4
(h) Sample B4

Fig. 6.28 Snapshot of welded samples at maximum recoverable bending deflection

Experiments show that the addition of Ni, interlayer, is beneficial for decreasing the brittle intermetallic compounds. 5mm interlayer width seems to be the appropriate width of interlayer for improving both tensile strength and hardness so as to produce a maximum recoverable bending deflection.

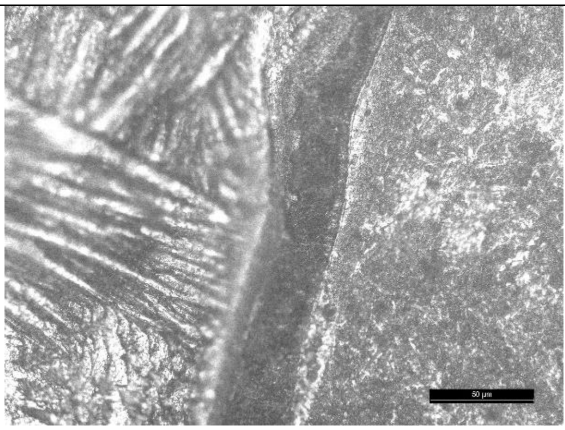	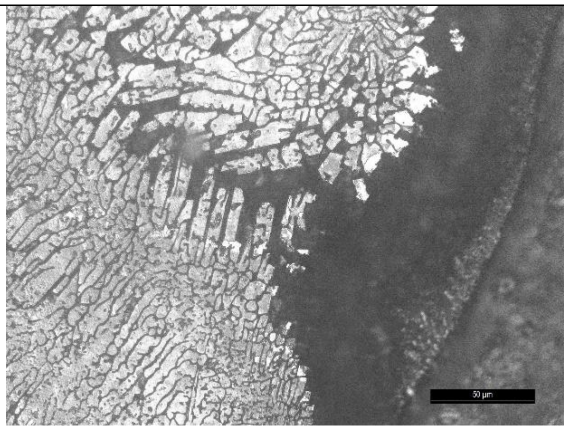
(a) Enlarged region A of sample R8110	(b) Enlarged region B of sample R8090
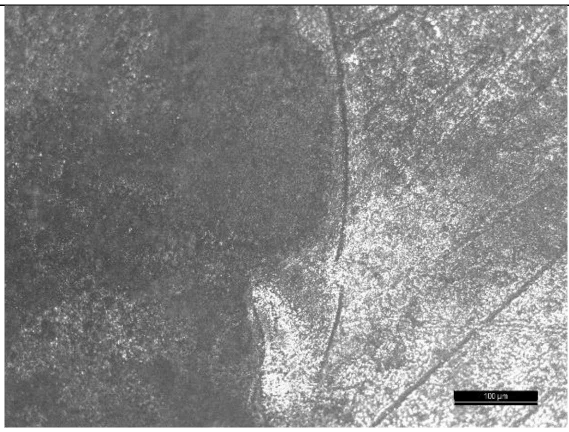	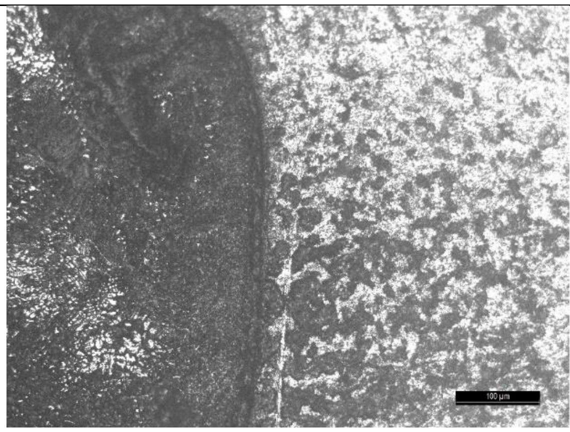
(c) Enlarged region C of sample R5110	(d) Enlarged region D of sample R5125

Fig. 6.29 Size of fusion interface with different welding speed and interlayer width

Results indicated that the welding of NiTi and stainless steel with 5mm interlayer could give a thinner fusion interface between the NiTi and Ni as shown in Fig. 6.29. The thickness of the fusion interface would be increased if the interlayer width increased to 8mm. When compare the sum of amount of Ni, B19' and R phase of the fusion zone as shown in Table 6.7, sample R5125 and R8110 has the lower total amount of Ni, B19' and R phase than the others. The lower amount of those phases may be one of possible causes of reducing the bending displacement at break and recoverable bending deflection. When comparing sample R5110 and R8090, both joints have similar amount of Ni_4Ti_3 which strengthens the B19' matrix and improves the recoverability/superelastic properties of the NiTi (Kainuma. et al., 1986). Also, R5110 has higher amount of B19', therefore, the recoverable bending deflection of R5110 is higher when comparing to that of R8090 as it has lower amount of B19'.

Table 6.7 Amount of phases in the fusion zone of different welded joints

	Sample no. **Welding speed (mm/s)**	R5125 125	R5110 110	R8110 110	R8090 90
Ni	Cubic	27.00%	13.40%	32.90%	33.40%
NiTi	Monoclinic (B19')	12.20%	43.40%	12.30%	13.60%
	Hexagonal (R)	10.70%	16.80%	17.30%	23.90%
Ni_4Ti_3	Rhombohedral	26.90%	9.70%	10.20%	9.60%
$NiTi_2$	Cubic	2.50%	0.00%	6.90%	3.60%
Ni_2Ti	Hexagonal	12.00%	7.40%	6.30%	6.90%
Ni_3Ti	Hexagonal	8.70%	9.30%	14.10%	9.00%

The change of the welding speed will alter the creation of different phases in the fusion zone. Besides, the increase of welding speed to a certain value causes the percentage amount of B19' martensite, R phase and Ni increase to a value that make a little decrease of Ni_2Ti, Ni_3Ti and Ni_4Ti_3 while large decrease of $NiTi_2$. The decrease of $NiTi_2$ makes the highest of tensile strength and recoverable bending deflection. Further increase of welding speed, however, would increase the percentage weight of Ni_2Ti, Ni_3Ti and Ni_4Ti_3 while the percentage weight of B19’ martensite, R phase and Ni decreased causes the tensile strength and recoverable bending deflection decreased.

6.5 Effect of Phases Orientation on Mechanical Performance

The recoverability/superelastic properties of NiTi is mainly contributed by monoclinic B19’ and Ni_4Ti_3 while $NiTi_2$ greatly deteriorates the joint strength. Bragg’s Law and TEM analysis with SAD patterns were applied to investigate the phase orientation of B19’, Ni_4Ti_3 and $NiTi_2$. To calculate unit cell lattice parameters from the diffraction peak positions, the width of the bands can be determined by the interplanar spacing, d_{hkl}. With the plane spacing equation of different crystal geometry and Bragg’s Law, the phase orientation could be defined.Given Bragg’s Law is defined as:

$$d_{\mathrm{hkl}} = \frac{\lambda}{2Sin\theta}$$

where λ is the wavelength of the incident electron beam and θ_{hkl} is the Bragg angle.

With reference to literature, Ni_4Ti_3 has a crystal structure based on the rhombohedral crystal geometry and the rhombohedral unit cell is characterized by lattice parameters a and α. The plane spacing equation for the rhombohedral structure is

$$\frac{1}{d^2} = \frac{(h^2 + k^2 + l^2)\, sin^2\,\alpha + 2(hk + kl + hl)(cos^2\alpha - \cos\alpha)}{a^2\,(1 - 3cos^2\alpha + 2cos^3\alpha)}$$

By substitution of the Bragg’s Law equation to the above equation, the phase orientation of Ni_4Ti_3 is defined as:

$$sin^2\theta = \frac{\lambda^2\,[(h^2 + k^2 + l^2)\, sin^2\,\alpha + 2(hk + kl + hl)(cos^2\alpha - cos\,\alpha)]}{4a^2\,(1 - 3cos^2\alpha + 2cos^3\alpha)}$$

$NiTi_2$ has a cubic crystal structure which is characterized by lattice parameter a. The plane spacing equation for the cubic structure is

$$\frac{1}{d^2} = \left(\frac{h^2 + k^2 + l^2}{a^2}\right)$$

By substitution of the Bragg's Law equation to the above equation, the phase orientation of $NiTi_2$ is defined as:

$$sin^2\theta = \frac{\lambda^2 \, (h^2 + k^2 + l^2)}{4a^2}$$

B19' phase has a crystal structure based on the monoclinic crystal geometry and the monoclinic unit cell is characterized by lattice parameters a, b, c and β. The plane spacing equation for the monoclinic structure is

$$\frac{1}{d^2} = \frac{1}{\sin^2\beta}\left(\frac{h^2}{a^2} + \frac{k^2 \sin^2\beta}{b^2} + \frac{l^2}{c^2} - \frac{2hl\cos\beta}{ac}\right)$$

By substitution of the Bragg's Law equation to the above equation, the phase orientation of B19' is defined as:

$$sin^2\theta = \frac{\lambda^2}{4\sin^2\beta}\left(\frac{h^2}{a^2} + \frac{k^2 \sin^2\beta}{b^2} + \frac{l^2}{c^2} - \frac{2hl\cos\beta}{ac}\right)$$

Based on the XRD result and the calculations results from the above equations, the phase orientation of 3 phases of different samples are summarized as shown in Table 6.8. Table 6.9 stated the intensity of the plane orientation of B19' of three different samples. The B19' with plane (0 2 0), (1-1 1), (0 0 2) and (1 1 1) mainly contribute the increase of recoverable bending deflection and the tensile strength. The present of $NiTi_2$ in sample R5125 and R8090 deteriorated the recoverable bending deflection. The plane (5 1 1) of $NiTi_2$ were found in both sample R5125 and R8090 while three more $NiTi_2$ plane: (4 2 2), (4 4 0) and (6 6 0), were also found in sample R8090. As the amount of Ni_4Ti_3 precipitate would guarantee the pseudoelasticity of the matrix to some degree, the intensity of the plane orientation of Ni_4Ti_3

of three different samples is stated as shown in Table 6.10 and the plane (3-1-2) and (2 1-1) dominated in the phase of Ni_4Ti_3.

Table 6.8 Values of h, k, l with respect to B19', Ni_4Ti_3 and $NiTi_2$

	R5110			R5125			R8090		
Quantity (%)	43.40	9.70	0	12.20	26.90	2.50	13.60	9.60	3.60
Phase	B19'	Ni_4Ti_3	$NiTi_2$	B19'	Ni_4Ti_3	$NiTi_2$	B19'	Ni_4Ti_3	$NiTi_2$
hkl	1 0 0	2 -1 0	-	1 0 0	2 -1 0	-	1 0 0	2 -1 0	4 2 2
	1 -1 0	-	-	1 -1 0	2 -1 -2	5 1 1	1 -1 0	2 -1 -2	5 1 1
	-	2 0 0	-	1 0 1	2 0 0	-	1 0 1	2 0 0	4 4 0
	0 2 0	-	-	0 2 0	3 -1 -1	-	0 2 0	3 -1 -1	6 6 0
	1 -1 1	3 -1 -2	-	1 -1 1	3 -1 -2	-	1 -1 1	3 -1 -2	-
	0 0 2	2 1 -1	-	0 0 2	2 1 -1	-	0 0 2	2 1 -1	-
	1 1 1	3 -2 0	-	1 1 1	3 -2 0	-	1 1 1	3 -2 0	-
	0 2 1	3 0 -1	-	0 2 1	3 0 -1	-	0 2 1	3 0 -1	-
	-	3 -1 -3	-	1 -2 1	3 -1 -3	-	1 -2 1	3 -1 -3	-
	0 2 2	4 -3 0	-	0 2 2	4 -3 0	-	0 2 2	4 -3 0	-
	1 3 0	-	-	1 3 0	4 0 -2	-	1 3 0	4 0 -2	-
	-	-	-	1 -1 3	5 -1 -4	-	1 -1 3	5 -1 -4	-
	-	-	-	-	5 0 -3	-	-	5 0 -3	-

Table 6.9 Intensity of plane orientation of B19'

	R5110		R5125		R8090	
Phase	B19'	Intensity	B19'	Intensity	B19'	Intensity
hkl	1 0 0	7.4	1 0 0	2.3	1 0 0	3.3
	1 -1 0	43.2	1 -1 0	13.6	1 -1 0	19.3
	-	-	1 0 1	10.1	1 0 1	14.3
	0 2 0	150.6	0 2 0	47.4	0 2 0	67.4
	1 -1 1	279.3	1 -1 1	88	1 -1 1	124.9
	0 0 2	153.3	0 0 2	48.3	0 0 2	68.6
	1 1 1	269.7	1 1 1	84.9	1 1 1	120.7
	0 2 1	78.9	0 2 1	24.9	0 2 1	35.3

	-	-	1 -2 1	9.4	1 -2 1	13.4
	0 2 2	70.6	0 2 2	22.2	0 2 2	31.6
	1 3 0	11.3	1 3 0	3.6	1 3 0	12.7
	-	-	1 -1 3	9.3	1 -1 3	13.2

Table 6.10 Intensity of plane orientation of Ni_4Ti_3

	R5110		R5125		R8090	
Phase	Ni_4Ti_3	Intensity	Ni_4Ti_3	Intensity	Ni_4Ti_3	Intensity
hkl	2 -1 0	6.9	2 -1 0	21.3	2 -1 0	9.7
	-	-	2 -1 -2	29.8	2 -1 -2	13.6
	2 0 0	5.9	2 0 0	18.3	2 0 0	8.3
	-	-	3 -1 -1	12.0	3 -1 -1	5.5
	3 -1 -2	98.3	3 -1 -2	305.6	3 -1 -2	138.9
	2 1 -1	92.2	2 1 -1	286.7	2 1 -1	130.3
	3 -2 0	9.8	3 -2 0	30.6	3 -2 0	13.9
	3 0 -1	4.8	3 0 -1	14.8	3 0 -1	6.7
	3 -1 -3	3.7	3 -1 -3	11.6	3 -1 -3	5.3
	4 -3 0	3.6	4 -3 0	11.2	4 -3 0	5.1
	-	-	4 0 -2	64.5	4 0 -2	29.3
	-	-	5 -1 -4	23.7	5 -1 -4	10.8
		-	5 0 -3	45.6	5 0 -3	20.7

Detailed understanding of the interfacial microstructure is an important issue since the properties depend on the microstructure. To identify the phase formation at the fusion zone and to predict the mechanism of the formation, TEM analysis of the fusion zone is important. The SADP images (as shown in Fig. 6.30) show the different phases formation in the fusion zone between the NiTi and Ni of sample R5110, R5125 and R8090. Experiments show that the fusion zone of all samples consists of a mixture of B19’ with R phase, Ni_2Ti, Ni_3Ti and Ni_4Ti_3 phases while $NiTi_2$ was not found in the sample R5110. Fig. 6.31 shows the TEM and SADP images of different phases found in the fusion zone. It was found that the grains with stripe-like structure were of the Ni3Ti phase, and the one devoid of any internal structure was $NiTi_2$. The grain with dotted-spot was B19’ phase. The columnar morphology of the grains also suggests the occurrence of directional growth during the joining process. It is interesting to note, however, that there is no observable orientation-dependence between the columnar grains within the joint and either of the base materials.

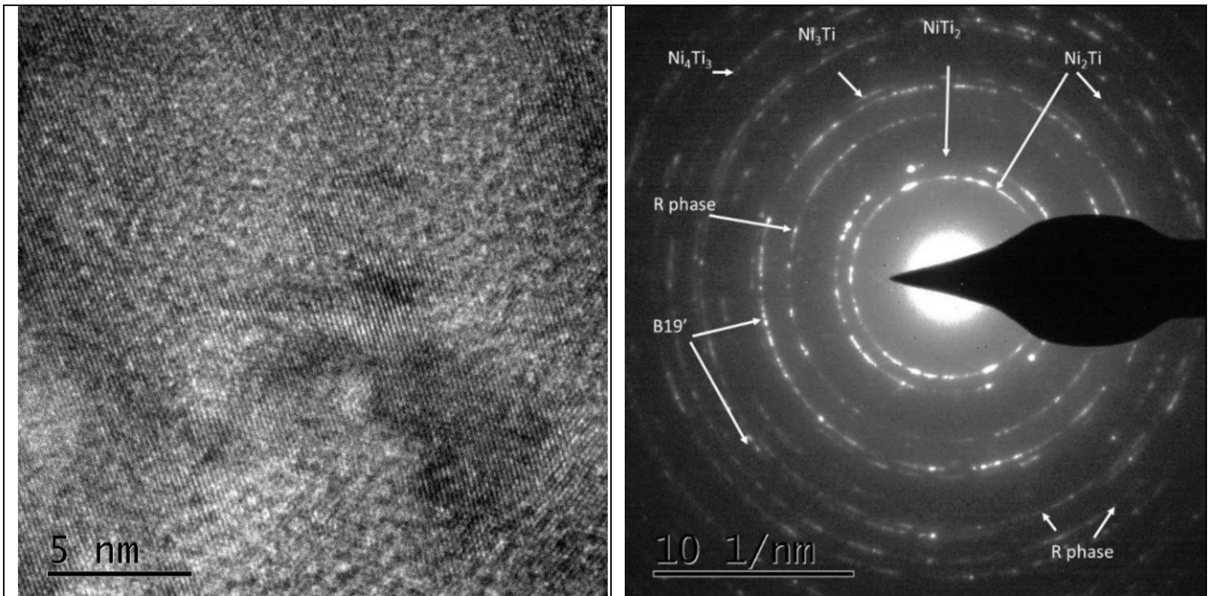

(a)	(d)

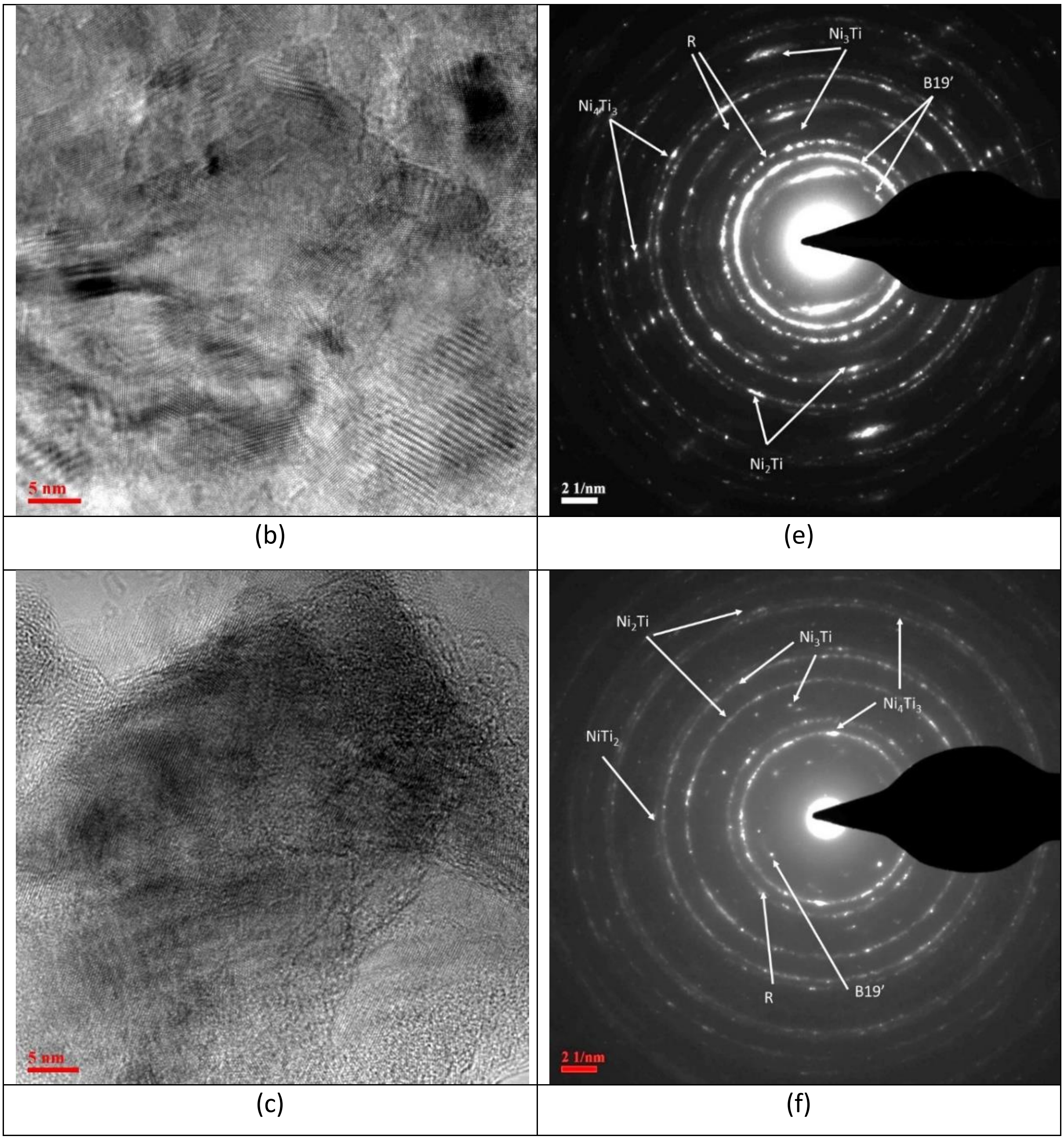

Fig. 6.30 SADP images of sample (a) R5125, (b) R5110 and (c) R8090, (d)-(f) with phases indicated

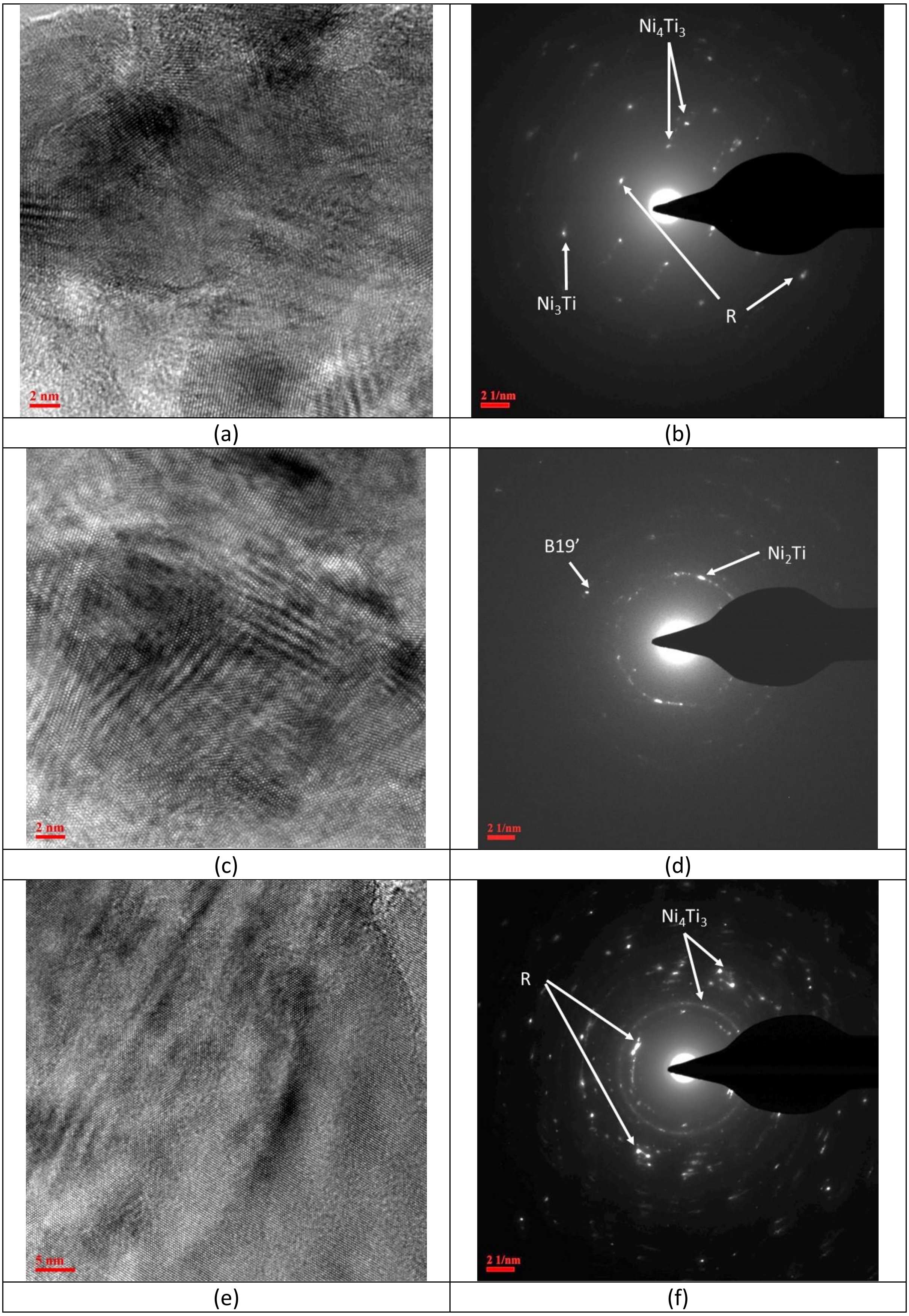

Fig. 6.31 TEM with SADP images of (a)-(b) mixture of R phase, Ni_3Ti and Ni_4Ti_3, (c)-(d) mixture of B19’ and Ni_2Ti, (e)-(f) mixture of R phase and Ni_4Ti_3

TEM and HADDF were conducted on sample R5110 extracted by FIB from specific zones of the weld microstructure in order to confirm the observations made in the previous TEM result. The present bright field TEM images, diffraction patterns and chemical analysis show the weld zone between NiTi and Ni interlayer.

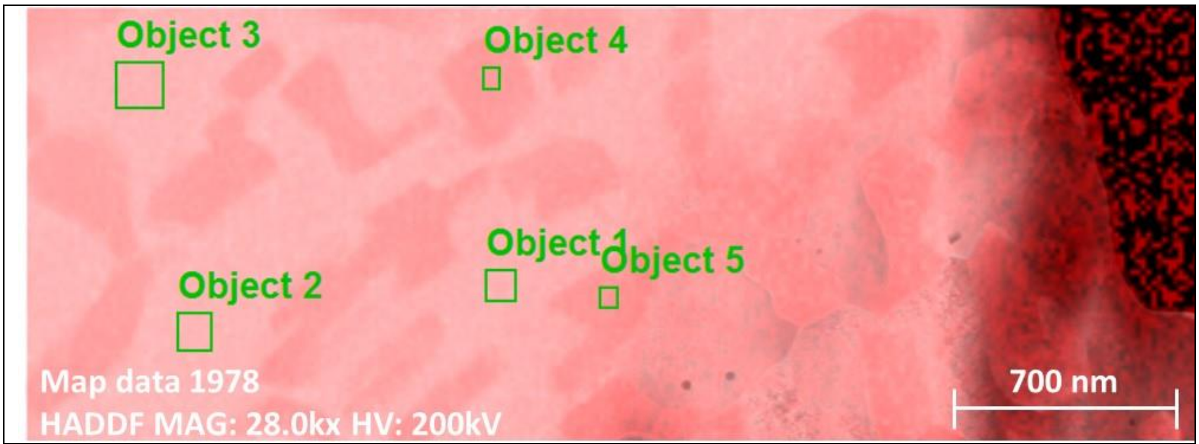

Atomic-% (norm.)	HAADF	Ni	Ti	Ni-Ti ratio (Round up)
Object 1	59587	54.93	41.35	Ni_4Ti_3
Object 2	62879	54.75	43.25	Ni_4Ti_3
Object 3	62242	56.46	41.87	Ni_4Ti_3
Object 4	53661	72.91	24.93	Ni_3Ti
Object 5	47937	71.41	24.65	Ni_3Ti

Fig. 6.32 HAADF Snapshot of fusion zone

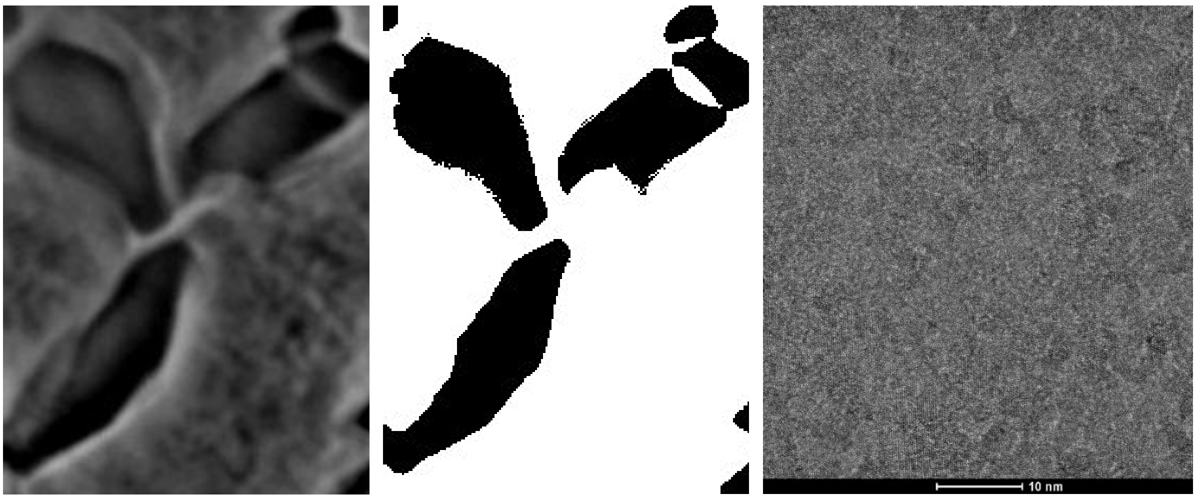

Fig. 6.33 TEM Snapshot of (a) $TiNi_3$, (b) threshold of the snapshot of (a), (c) Ni_4Ti_3

Fig. 6.32 indicated HADDF image of the microstructure of the central area of the fusion zone. Object 1-3 consisted of 54.75 – 56.46 atomic% of Ni and 41.35 – 43.25 atomic% of Ti which is very close to the composition of Ni_4Ti_3 phase in the binary Ni-Ti phase diagram. Object 4-5 consisted of 71.41 – 72.91 atomic% of Ni and 24.65 – 24.93 atomic% of Ti which is very close to the composition of $TiNi_3$ as shown in Fig. 6.33. It indicated $TiNi_3$ and Ni_4Ti_3 precipitate arise.

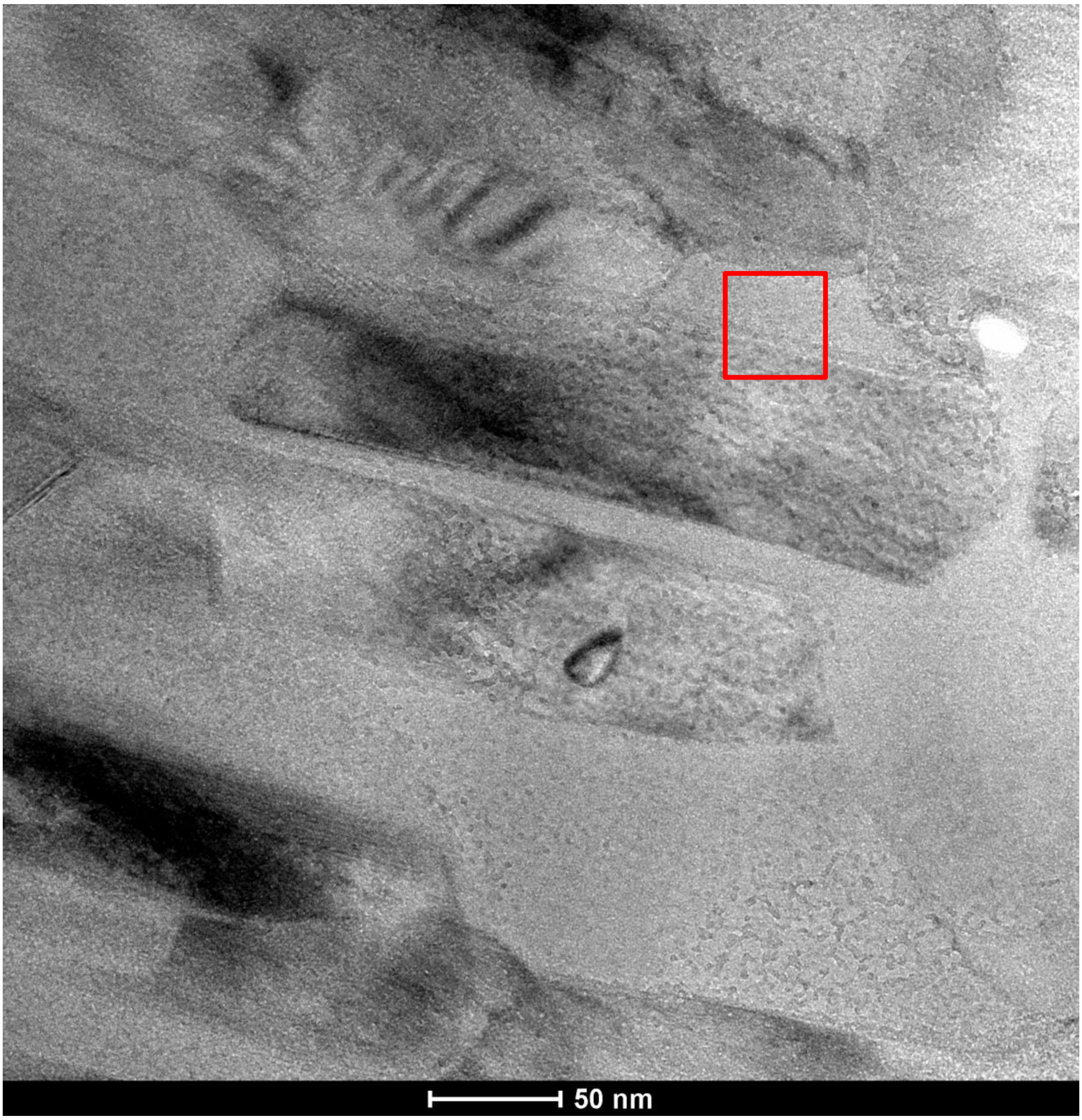

Fig. 6.34 TEM image fusion zone with stripe-like structure

The TEM image (as shown in Fig. 6.34) indicates that stripe-like structure was presented in the fusion zone. Stripe-like structure seems to be Ni_3Ti while the surrounding seems to be Ni_4Ti_3 based on the findings from the HAADF analysis as shown in Fig. 6.32. Zoom in analysis on the edge of the stripe-like structure was conducted. The TEM and SADP image (as shown in Fig. 6.35) of the weld zone indicates that inhomogeneous distribution of phases was established. Coherency with the B19' and R phase was lose.

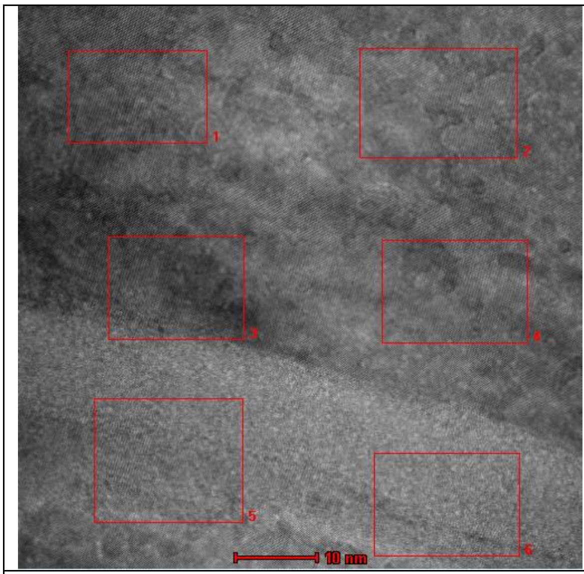

(a)

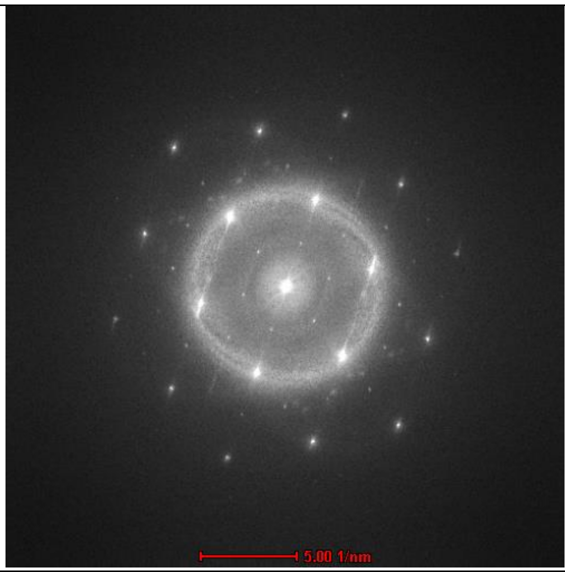

(b)

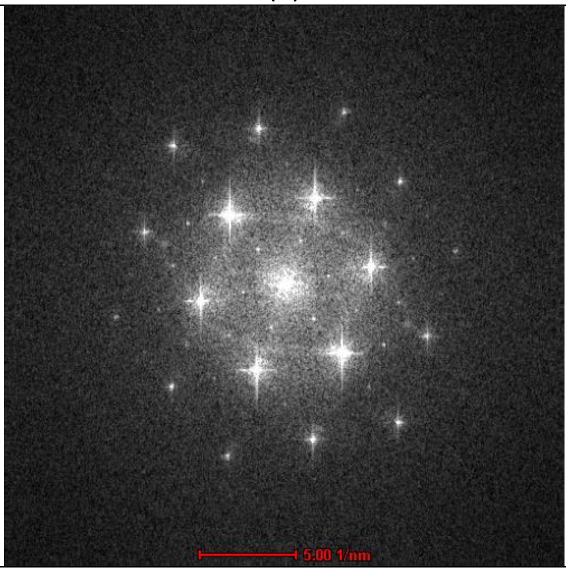

(c)

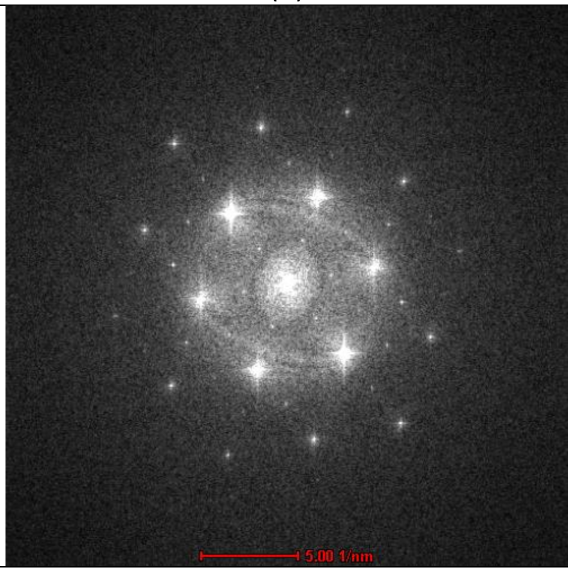

(d)

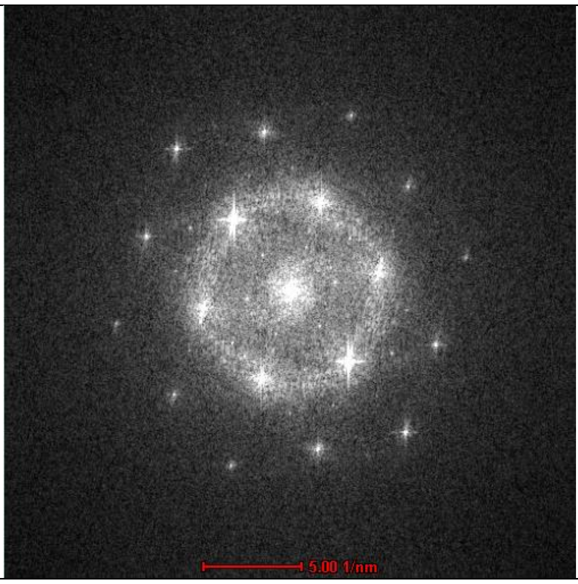

(e)

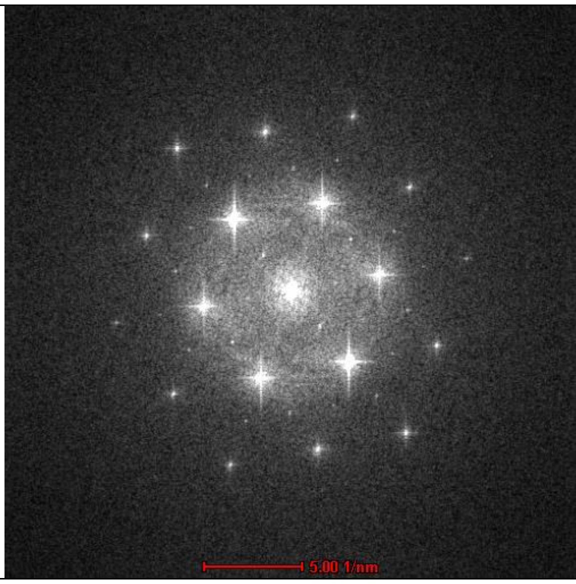

(f)

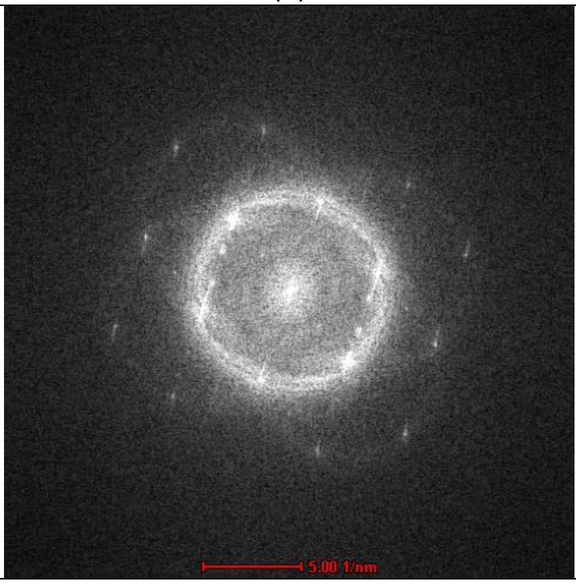

(g)

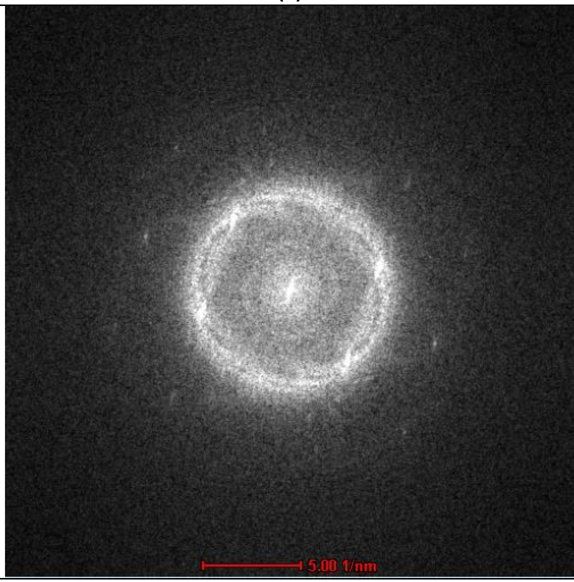

(h)

Fig. 6.35 TEM and SADP images of (a) – (b) weld zone and selected region (c) – (h)

Fig. 6.35 and 6.36 show TEM image of the fusion zone of NiTi and Ni, three observable regions of mixtures were observed. The SAPD of each region indicates that the phase in region 1 is Ni_2Ti with Ni_4Ti_3, region 2 is B19’ with Ni_2Ti and region 3 is R phases with Ni_2Ti, Ni_3Ti and Ni_4Ti_3. Region 1 indicated that the solubility of Ni_4Ti_3 in Ni_2Ti was larger than that of B19’ or in R phase. Large grains were observed in the region 1 as shown in Fig. 6.36(b), which was on the right side of the fusion zone. It consisted of two major phases, Ni_2Ti and Ni_4Ti_3. The Ni_4Ti_3

presented in between the Ni_2Ti phase. Region 2 as shown in Fig. 6.36(c) indicated small grains, which mainly contained B19' and Ni_2Ti phases with amorphous phase between region 1 and 3. Thus it could be concluded that material recrystallizes to B19' phase and this recrystallized grains do not have preferred direction of growth. Overall, it was observed that the different phases in the fusion zone form in layers parallel to the original interface. The location of each phase was observed to follow the trend predicted with increasing Ni content by the Ni-Ti phase diagram going from the NiTi base material through the joint to the Ni interlayer.

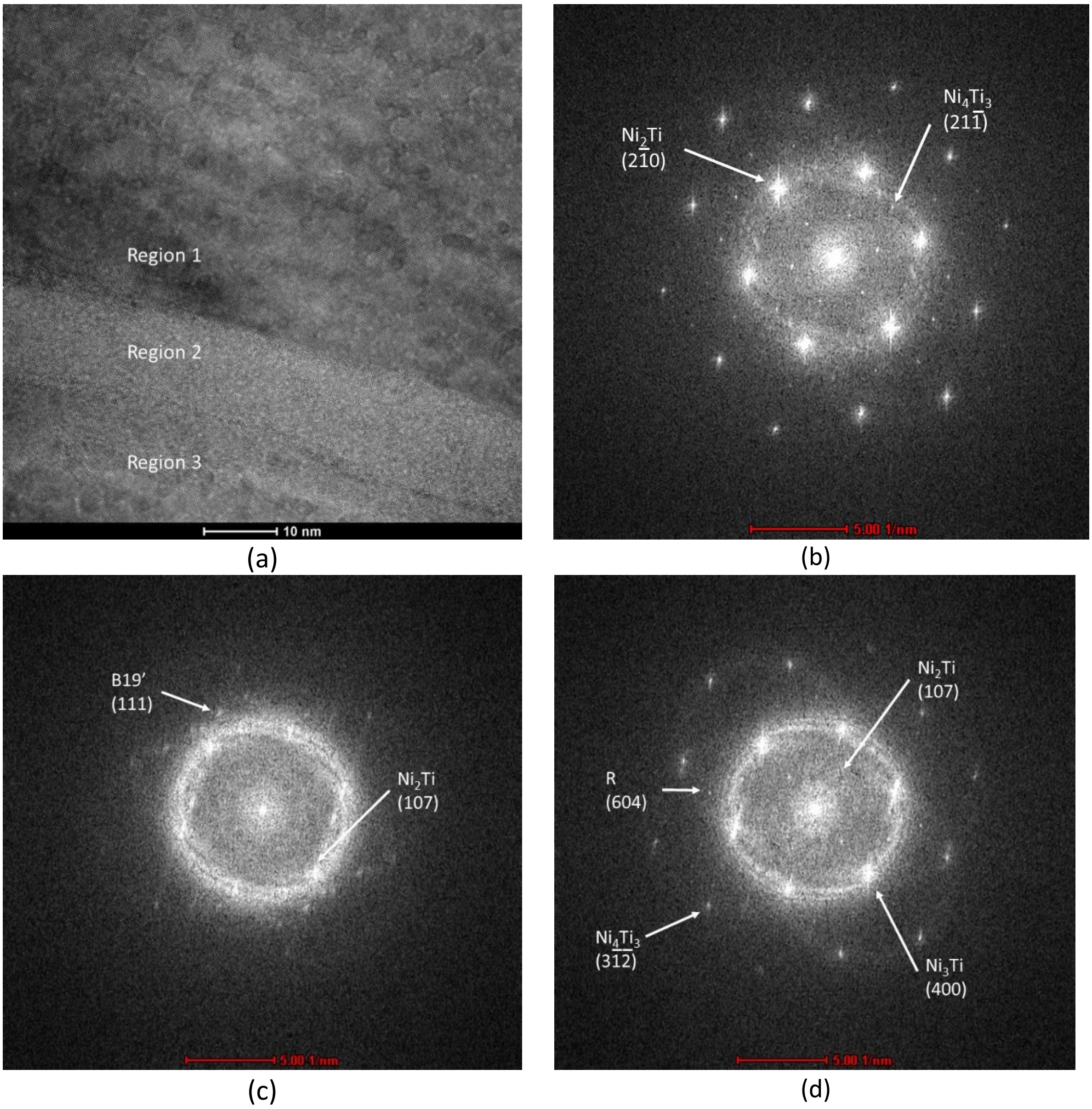

Fig. 6.36 (a) TEM image of weld zone with three regions, (b) SADP patterns of region 1, (c) SADP patterns of region 2 and (d) SADP patterns of region 3

SADP images as shown in Fig. 6.36 show that the fusion zone consists of a mixture of B19' with a strong preferred orientation of (111) planes in region 2 and R phase with a strong preferred orientation of (604) planes in region 3. A NiTi mixture of Ni_2Ti and Ni_4Ti_3 were observed to form in succession across the joint. The region 1 as shown in Fig. 6.36(b) indicated loss of shape memory properties and was not expected to exhibit shape memory properties. Fracture of joint due to tensile stress and bending stress was expected to be occurred in this region.

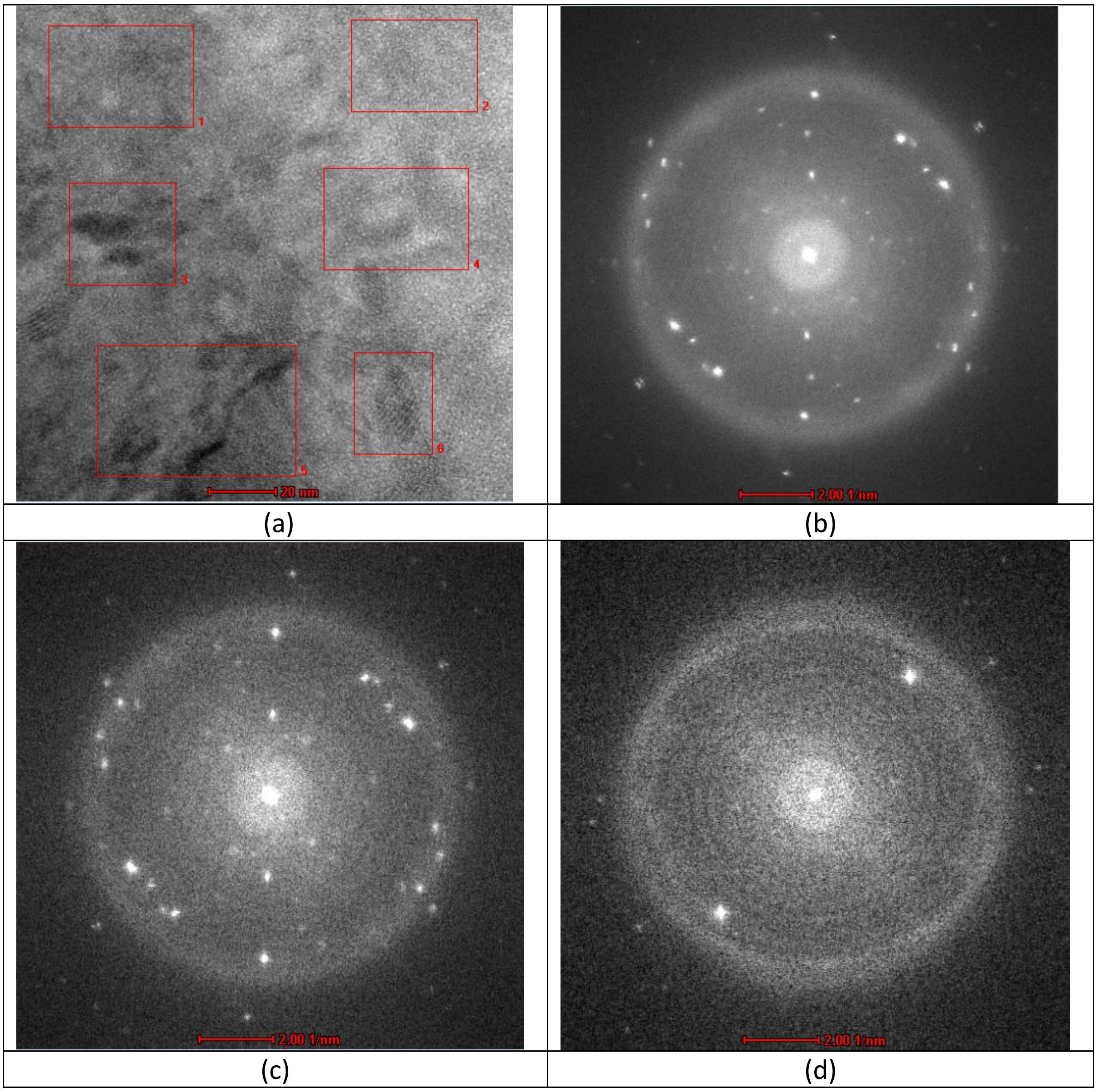

Fig. 6.37 (a) – (b) TEM and SADP image of fusion zone near Ni side, (c) SADP image of region 3 and (d) SADP image of region 4

SADP images as shown in Fig. 6.37 and 6.38 show that the inner region of stripe-like structure consists of a mixture of B19' with strong preferred orientation of (142) planes and R phase with a strong preferred orientation of (604) planes. Besides, Ni_3Ti, Ni_2Ti and Ni_4Ti_3 were also observed. B19' and R phase were mainly presented in the region 3 while Ni_3Ti was mainly presented in the region 4.

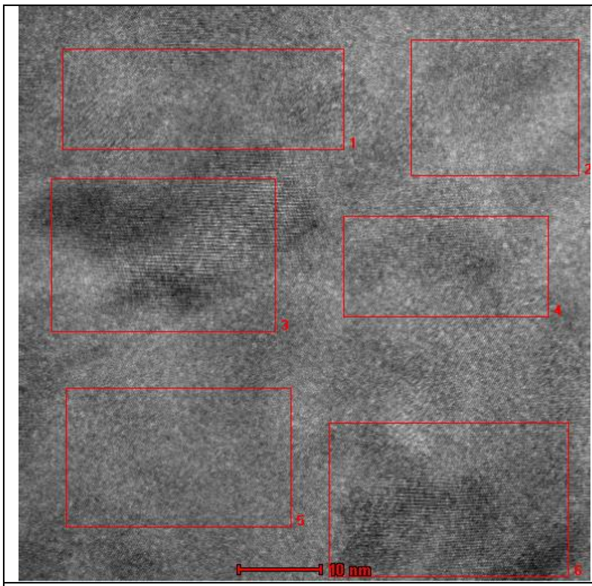

(a)

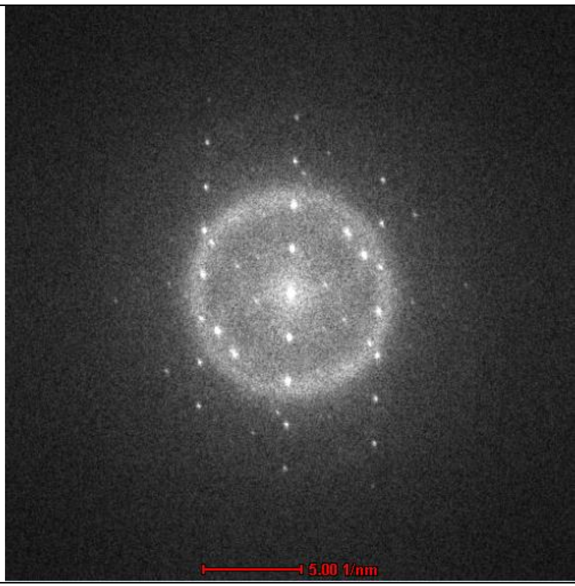

(b) Region 3 of (a)

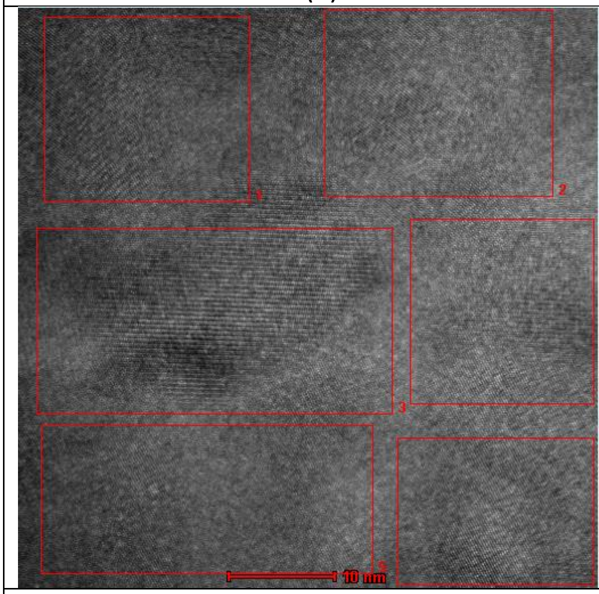

(c)

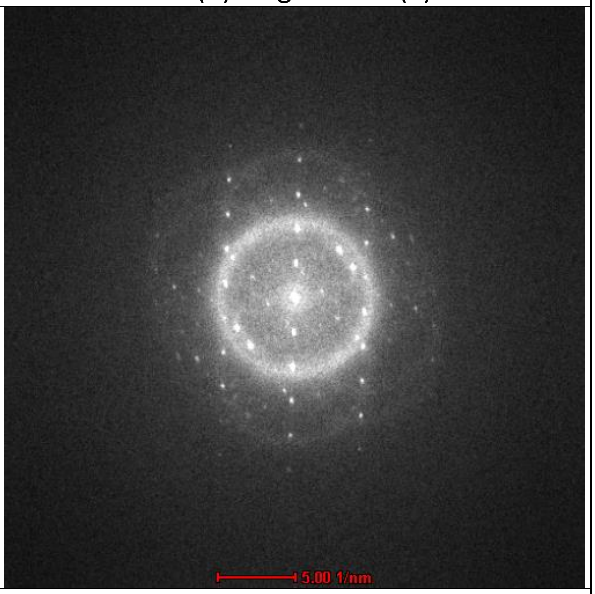

(d) Region 3 of (c)

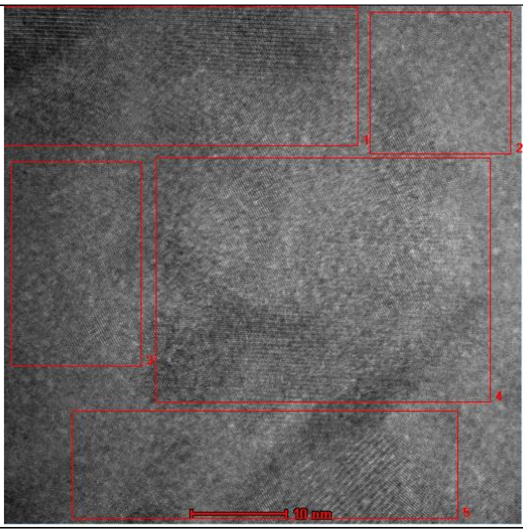	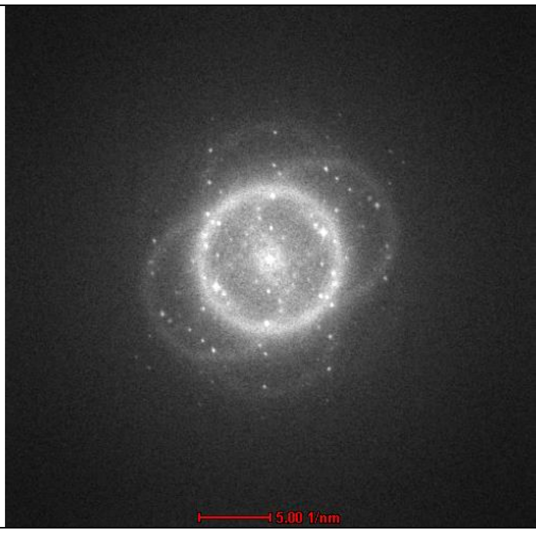
(e)	(f) Region 4 of (e)
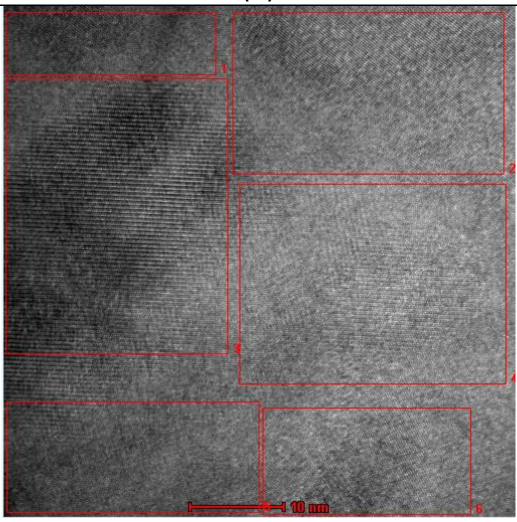	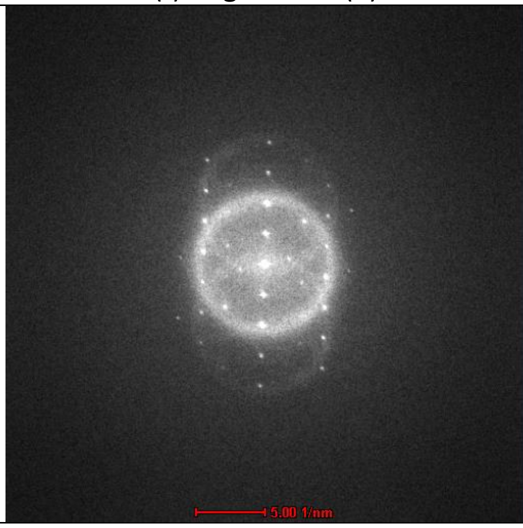
(g)	(h) Region3 of (g)

Fig. 6.38 TEM and SADP images of region 3 and 4 of Fig. 6.31

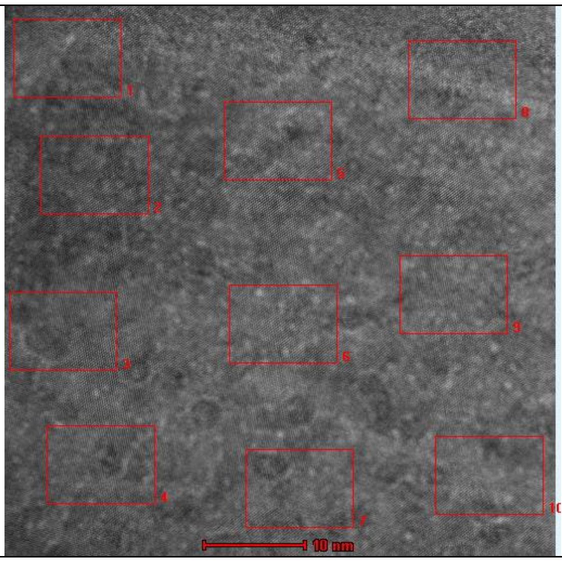	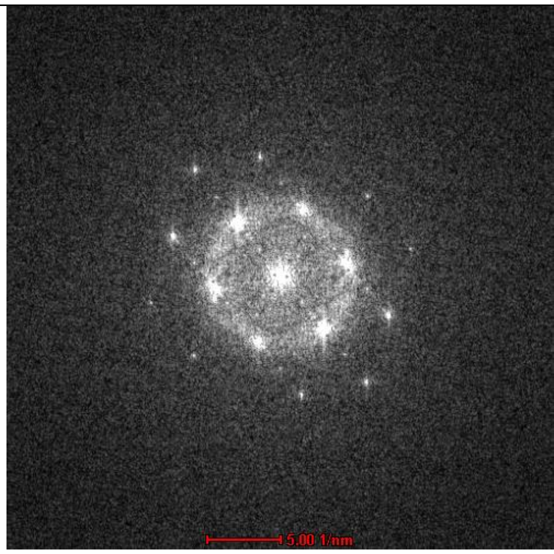
(a)	(b)

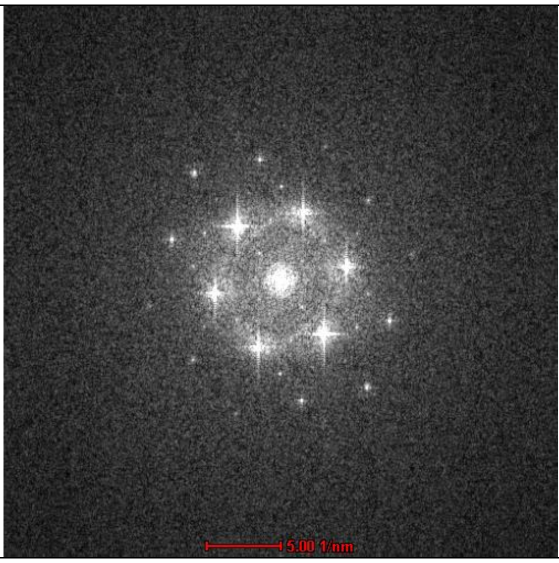

(c)

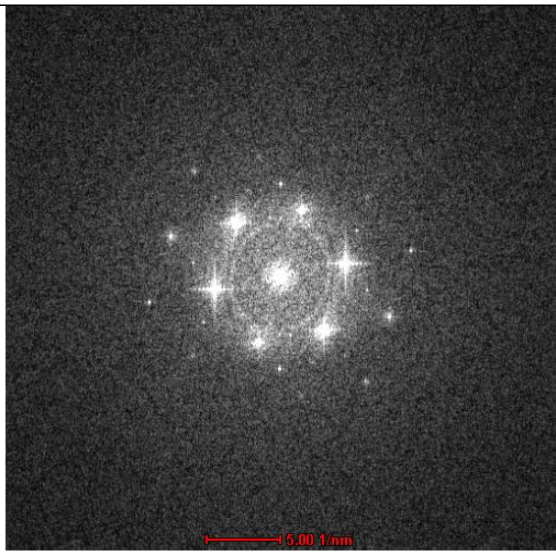

(d)

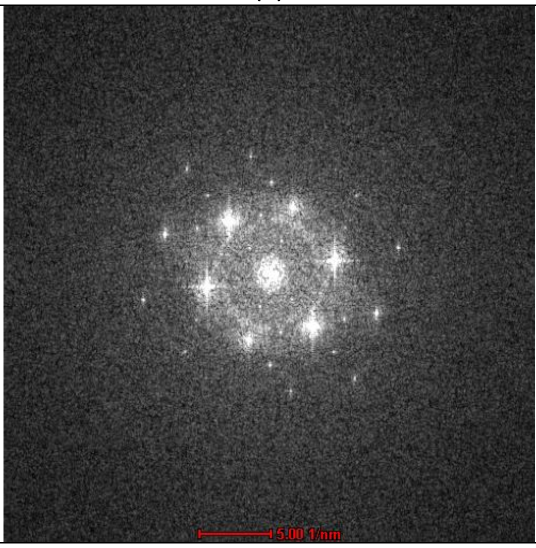

(e)

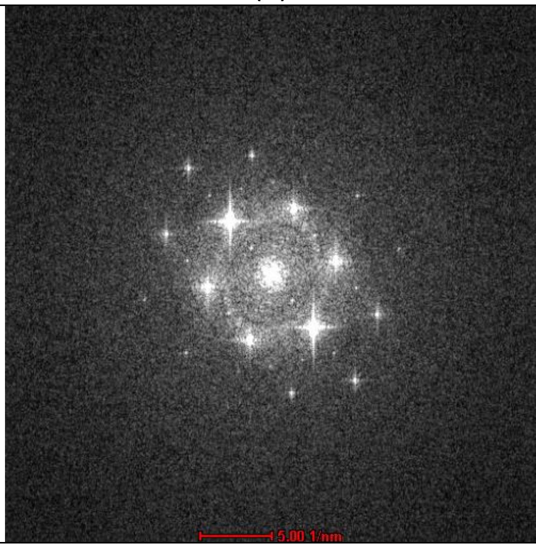

(f)

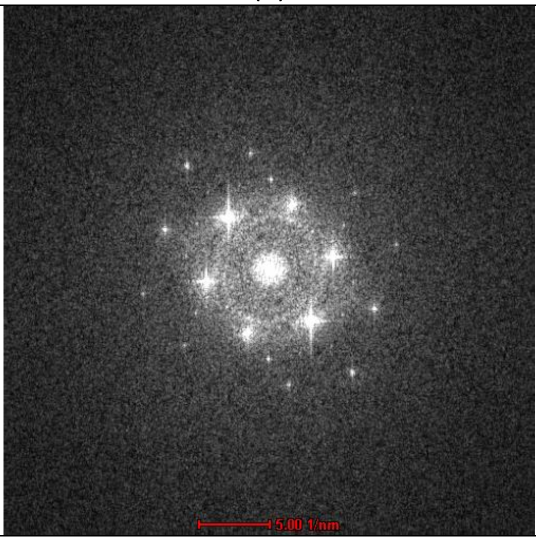

(g)

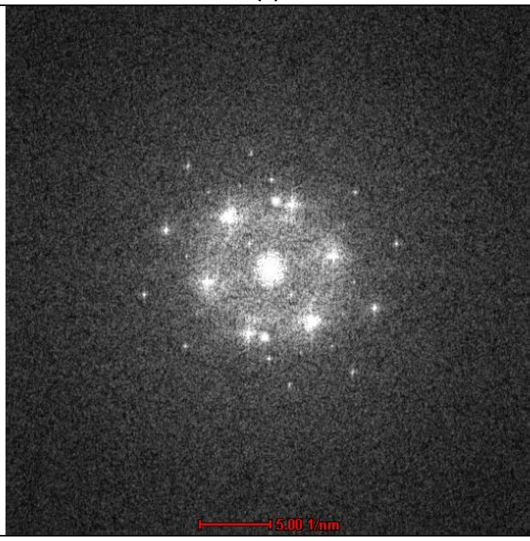

(h)

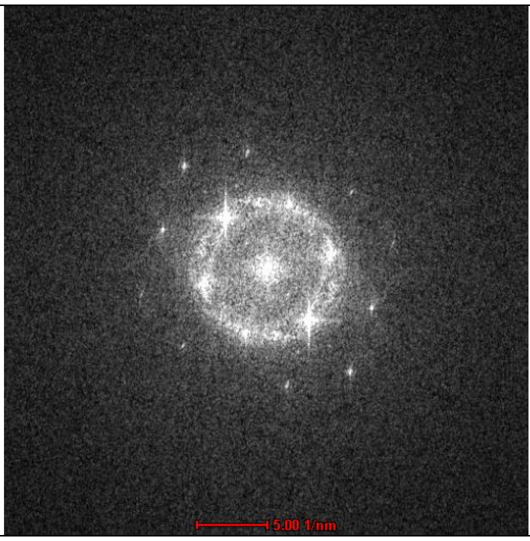

(i)

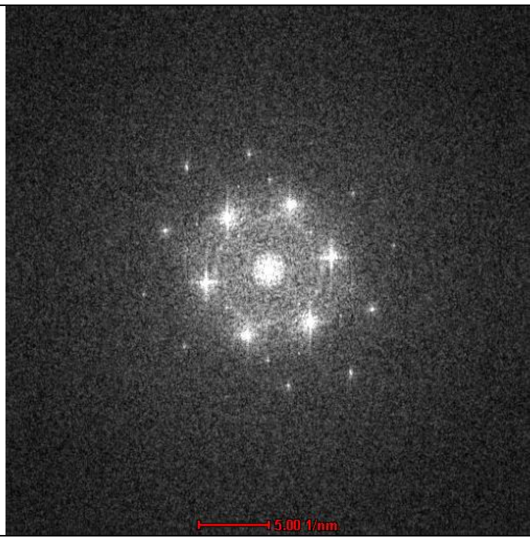

(j)

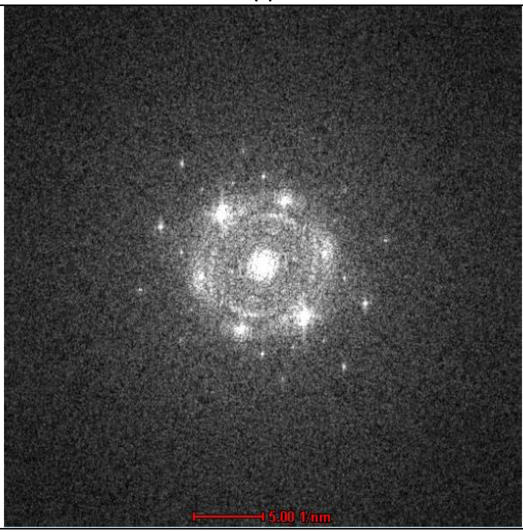

(k)

Fig. 6.39 (a) TEM image of weld zone in region 3, (b) – (k) SADP patterns of the selected regions showing the distribution of Ni_4Ti_3 in different regions

Fig. 6.39 shows TEM image and the corresponding selected area diffraction pattern (SADP) of the microstructure of the location below region 3. It can be seen that Ni_4Ti_3 precipitates arise. The Ni_4Ti_3 precipitate phase are homogeneously dispersed in the grain boundary and grain interior. Ni_4Ti_3 precipitates could establish coherency with the B19' and R phase matrix.

In recent years, EBSD has become an important tool in reconstructing orientation image maps and the grain size distribution. The results of EBSD show the area of the welded joint of NiTi and stainless steel with a 5mm Ni interlayer as shown in Fig. 6.40. Results of EDX scan show that the amount of Ti decreased from the left side to the right side of the NiTi-Ni zone while the amount of Fe decreased to zero from the right side to the left side of the Ni-SS zone as shown in Fig. 6.41. It indicated that undesirable phase such as FeTi/$TiFe_2$ was not formed as the interlayer has successfully blocked the Fe element, which was not found in the NiTi-Ni zone, to react with Ti.

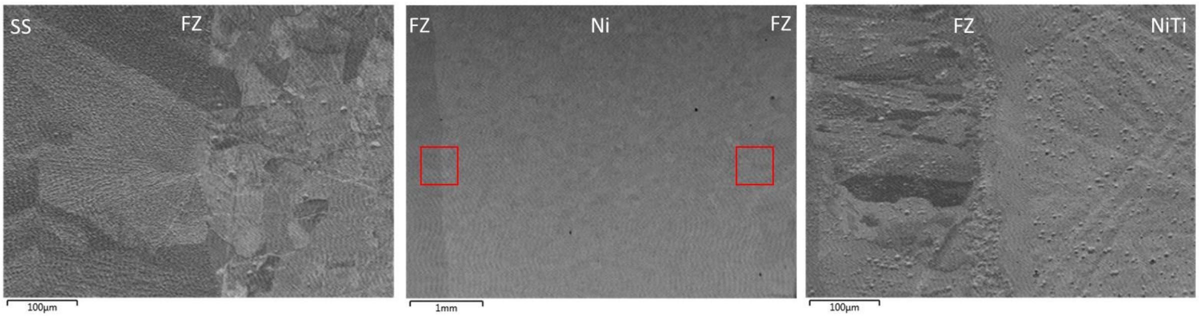

(a) (b) (c)

Fig. 6.40 Microstructure of (a) left fusion zone, (b) the Ni interlayer and (c) right fusion zone of the welded joint

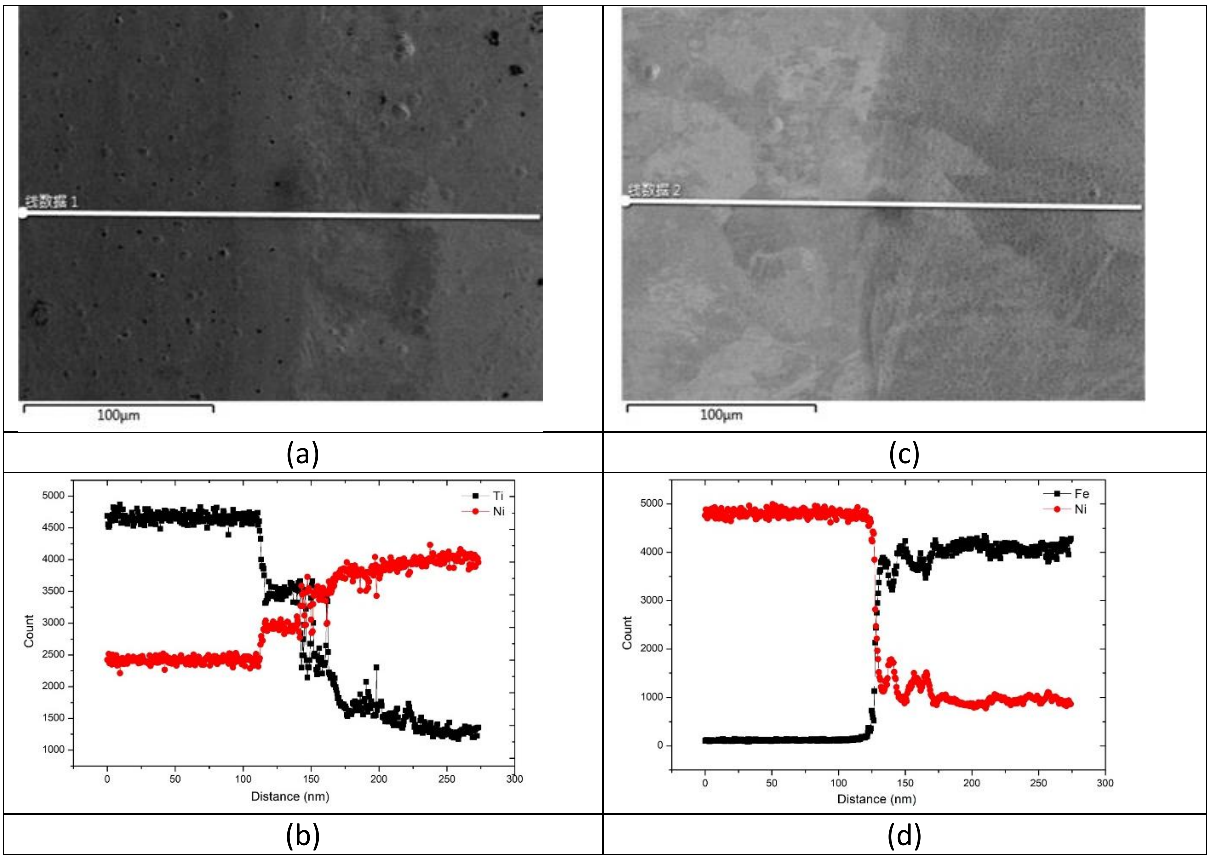

Fig. 6.41 Microstructure of (a) NiTi-Ni side with (b) the change of Ti and Ni along the scan line and (c) Ni-SS304 side with (d) the change of Fe and Ni along the scan line

The results of EBSD show the grain size distribution and orientation map observed at the surface of the NiTi-Ni fusion zone with the attached triangle presents color code of orientation map for NiTi and Ni as shown in Fig. 6.42. The orientation map illustrated a smaller area is formed from larger columnar grain spread along the right side of the fusion zone. Besides, the pole figure calculated of NiTi form the EBSD for the fusion area confirmed that the fine grains are oriented along the {100} while the axes of the grains were tilted of about 5° against the ribbon normal as shown in Fig. 6.43.

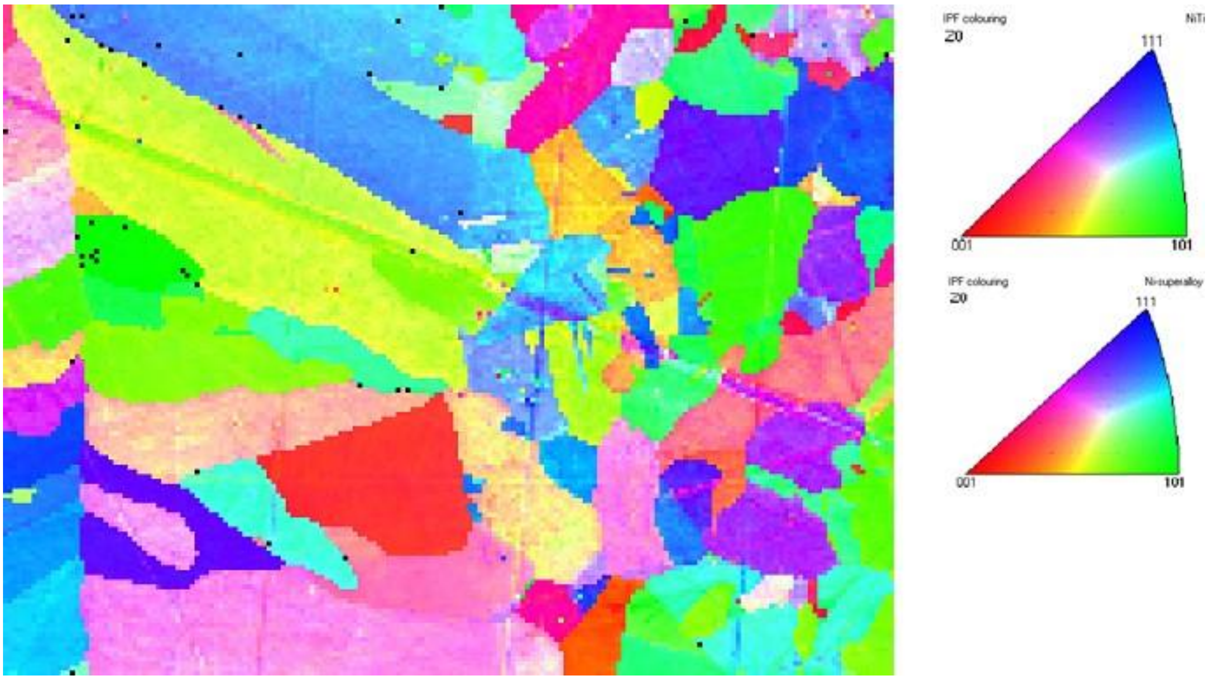

Fig. 6.42 Crystal orientation map of left fusion zone of the welded joint

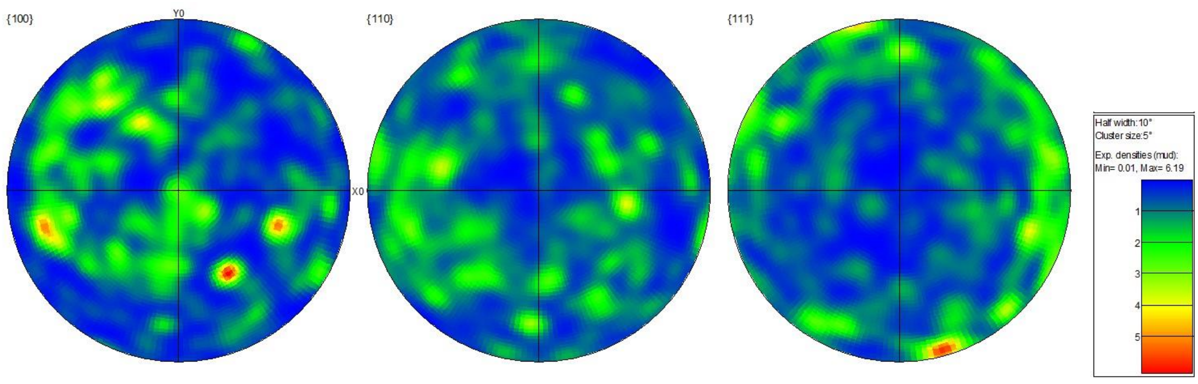

Fig. 6.43 The pole figure calculated of NiTi from EBSD

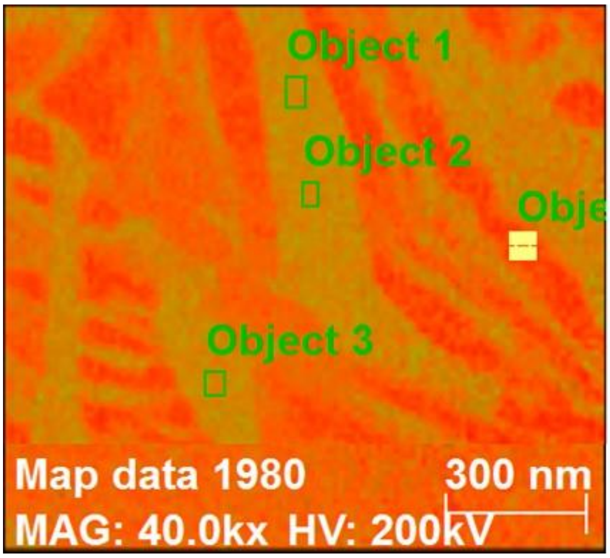

Atomic-% (norm.)	HAADF	Ni	Ti	Ni-Ti ratio (Round up)
Object 1	59640	59.67	37.13	Ni_3Ti_2
Object 2	59342	60.03	36.85	Ni_3Ti_2
Object 3	56585	60.60	36.69	Ni_3Ti_2
Object 4	36272	63.22	31.63	Ni_3Ti

Fig. 6.44 HAADF Snapshot of fusion zone with the present of Ni_3Ti_2

HAADF was conducted to determine the composition in the fusion. Fig. 6.44 indicated HADDF image of the microstructure of the central area of the fusion zone. Object 1-3 consisted of 59.67-60.60 atomic% of Ni and 37.13-36.85 atomic% of Ti which is very close to the composition of Ni_3Ti_2. In consideration of slow cooling time induced by heat accumulation during laser welding, the NiTi matrix and Ni_4Ti_3 precipitates would get coarsened which would restricts the occurrence of stress-induced martensitic phase transformation (Bimber *et al.*, 2016). Slow cooling time would enable the Ni_4Ti_3 to decompose to Ni_3Ti_2 and further decompose to Ni_3Ti ($Ni_4Ti_3 \rightarrow Ni_3Ti_2 \rightarrow Ni_3Ti$). As Ni_4Ti_3 precipitates in NiTi can effectively strengthen the matrix (Jiang *et al.*, 2013), the decomposition of Ni_4Ti_3 to Ni_3Ti is one of the reasons why the recoverable bending deflection would be decreased if the welding speed was decreased and the layer width was increased.

6.6 Chapter Summary

The effect of phase compositions in the NiTi-Ni-SS joint on mechanical performance, transformation behavior, and bending and recovery behavior were investigated. The major observations are summarized as follow:

(i) Seven phases included Ni and $NiTi_2$ (cubic), B19' (monoclinic), R phase, Ni_2Ti and Ni_3Ti (hexagonal) and rhombohedral Ni_4Ti_3 were determined in the fusion zone of the NiTi-Ni-SS joint by XRD and TEM. The chemical composition of the NiTi-Ni fusion zone varied by energy delivered to any specific point, which is achieved by the change of welding speed at a fixed laser power.

(i) The tensile strength of the welded joint of NiTi-Ni-SS is highly relied on the monoclinic B19' and hexagonal R phase while the higher recoverable bending deflection is relied on the higher amount of B19'. The undesirable phase of $NiTi_2$ plays vital role in brittleness and reduction of joint strength.

(ii) The present of Ni_4Ti_3 strengthens the B19' matrix and improves the recoverability of the NiTi (Kainuma, *et al.*, 1986), two-stage phase transformation was occurred if the amount of Ni_4Ti_3 increased. 26.9% Ni_4Ti_3 in the fusion zone induced two-stage transformation in this experiment.

(iii) The power density of 6.37 X 10^6 W/cm^2 with interaction time of 1.82ms could produce a ductile NiTi-Ni-SS joint with a recoverable bending deflection of 5.00mm. Further bending of the welded specimen to 6.80 mm would, however, break the weld. The original position of the welded specimen cannot be completely recovered if the bending distance exceeds 5.10mm. The fusion zone of that joint consists of a mixture of B19’ with a strong preferred orientation of (111) planes and (142) planes.

7 Results and Discussion IV - Constitutive Model for the Recoverable Bending Deflection

7.1 Introduction

In this chapter, a mathematical model based on the quassi equation to define the variability in chemical composition to evaluate the properties of the butt joint that offers a more formidable output is presented and discussed.

7.2 Constitutive Model

The basis of the model developed is to capture the correlation that exists between the chemical composition, laser power and the welding speed. The implication is that the dynamics contained in the variant chemical composition would be able to reflect the strength needed for welding speed and laser power used. To illustrate the underlying principle, the weight fraction is captured based on the variant compounds that are vested for the respective metallic alloys. The weight fraction of NiTi, Ni, Ni_3Ti, Ni_4Ti_3, Ni_2Ti and $NiTi_2$ would be different in different welding conditions.

As a result, the level of laser power required to affect a composition weld may be connotatively higher. Additionally, the metallic alloys may demand a lower laser power due to the different lattice structure formed. The implication is that though the level of the required laser power may initially have been constructed to be at a minimal, however, a relatively higher laser power level may be needed for the formation of the appropriated chemical composition. It is imperative that the set underlying correlation be determined to establish the coherent correct applicable value. In addition, the rate of the welding speed is equally of sporadic essence in establishing the set level of connotative weight fraction. A higher level of welding speed may be essential to ensure a light welding butt joint with a lower joint strength. This will occasionally arise if the anticipated weight fraction level is an easier chemical composition to enable a joint weld. Other chemical compositions, however, will equally demand a declined welding speed. This is coherently captured under fractional atomic lattices that are often more rigid. In such a case, a joint with a higher level of laser power accompanied by slower welding speed is necessary. Dependent on the chemical composition, both the laser power and welding speed are the core defining factors in the final setup.

The percentage weight of Ni will alter the creation of Ni_3Ti, Ni_4Ti_3, Ni_2Ti and $NiTi_2$. The increase of welding speed to a certain value causes the percentage weight of B19' martensite, R phase and Ni to increase to an optimum value that makes a small decrease of Ni_2Ti, Ni_3Ti and Ni_4Ti_3 but a large decrease of $NiTi_2$, giving the highest tensile strength and recoverable bending deflection. Further increase of welding speed, however, would increase the percentage weight of Ni_2Ti, $NiTi_2$ and Ni_4Ti_3 while the percentage weight of B19' martensite, R phase and Ni decreased, hence causing the tensile strength and recoverable bending deflection to decrease.

Rozzoni (2013) simulated the thermo-mechanical behavior of the NiTi in bending and recorded the findings based on the percentage recovery in relation to the heat supplied and the welding speed involved. The temperature of the weld joint is mainly affected by the conduction of the NiTi-Ni and Ni-SS interfaces. If both NiTi and Ni were laser melted, the location of solid-liquid interface at the time for NiTi-Ni and Ni-SS reaching melting point could be defined by an equation.

Five major assumptions are made for a three-dimensional numerical model developed for heat transfer and fluid flow for continuous laser welding of dissimilar metals. The following assumptions are used to formulate the mathematical model.

(a) The density change as a result of temperature variations is accounted for by using the Boussinesq approximation which means that the flow of the liquid metal follows the Newtonian, laminar and incompressible law;
(b) At the region where the temperature making the metal is in between been solid and liquid, the medium is assumed to be porous, which is called the mushy zone;
(c) Gaussian distribution is assumed to be where the position of the laser heat flux at the top surface of the welded sample;
(d) Thermal contact resistance between the metals been joined is not taken into consideration in the mathematical modelling;
(e) Both physical and thermal properties of the molten pool of both metals are assumed to be related to temperature and vary directly with temperature.

On the assumptions derived from a series of models, energy, momentum-transport, thermal energy and aspects of solute transport are key. The following equations reflect the heat and mass transfer of welded NiTi and Ni.

For mass conservation, it can be defined as:

$$\frac{\partial \rho}{\partial t} + \frac{\partial \rho u_i}{\partial x_i} = 0 \dots\dots\dots\dots\dots\dots (1)$$

For mass conservation of momentum-transport, it can be defined as:

$$\frac{\partial \rho}{\partial t} + \frac{\partial (\rho u_i u_j)}{\partial x_j} = \frac{\partial}{\partial x_j}\left(\mu \frac{\partial \rho u_i}{\partial x_j}\right) + \frac{\partial}{\partial x_i}\left(\mu \frac{\partial \rho u_i}{\partial x_i}\right) - \frac{\partial p}{\partial x_i} + \rho g \beta_T (T - T_{ref}) + F_d \quad \dots\dots\dots(2)$$

Where ρ and μ which represents density and viscosity of the fluid respectively. β_T and T_{ref} which are properties which are temperature volumetric expansion factor and the reference temperature respectively. Velocity vector is represented by u_i and pressure is represented by P. Frictional dissipation of momentum in the mushy zone is represented by F_d as in accordance with Carman-Kozeny equation. F_d is derived as in equation below;

$$F_d = \frac{(1-f_l)^2}{f_l^3+\varepsilon_m} K_m u_i \qquad \ldots\ldots\ldots\ldots\ldots (2.1)$$

On conservation of thermal energy, it can be defined as:

$$\frac{\partial(\rho c_p T)}{\partial t} + \frac{\partial\left(u_i \rho c_p T\right)}{\partial x_i} = \frac{\partial}{\partial x_i}\left(K \frac{\partial T}{\partial x_i}\right) - \frac{\partial(\rho \Delta H)}{\partial t} - \frac{\partial(\rho \mu_i \Delta H)}{\partial x_i} \ldots\ldots\ldots\ldots\ldots (3)$$

Where c_p is the specific heat and K is the thermal conductivity, H is the latent enthalpy content of the fusion.

The equations represent five elements namely; B19', R phase, Ni_2Ti, Ni_3Ti and Ni_4Ti_3. The transport solution equation is defined by;

$$\frac{\partial(\rho C)}{\partial t} + \frac{\partial(\rho u_i C)}{\partial x_i} = \frac{\partial}{\partial x_i}\left(\rho D \frac{\partial C}{\partial x_i}\right) + Sc \ldots\ldots\ldots\ldots\ldots\ldots\ldots (4)$$

The source term form of equations is defined by;

$$S_{ui} = -\frac{\partial \rho}{\partial x_i} + \frac{\partial}{\partial x_j}\left(\mu \frac{\partial u_j}{\partial x_i}\right) - K_o\left(\frac{1-f_1}{f_1^3+B}\right) u_i + \rho g_i \beta_T\left(T - T_{ref}\right)$$

$$+ \rho g_i \beta_C\left(C - C_{ref}\right) \ldots\ldots (5)$$

$$S_T = -\frac{\partial(\rho \nabla H)}{\partial t} - \frac{\partial(\rho u_i \nabla H)}{\partial x_i} \ldots\ldots\ldots\ldots\ldots\ldots (6)$$

$$S_C = -\frac{\partial \rho}{\partial x_i}(\rho D\left(\frac{\partial(C_1 - C)}{\partial x_i}\right) - \frac{\partial \rho}{\partial x_i}(\rho f_s (C_1 - C_s) u_i) \ldots\ldots\ldots\ldots\ldots (7)$$

In this, the nonlinear heat equation in the nonstationary distribution of temperature in this method is described in equation below;

$$c\rho\left(\frac{\partial T}{\partial t}+v\frac{\partial T}{\partial y}\right)=\frac{\partial}{\partial t}\lambda\frac{\partial T}{\partial x}+\frac{\partial}{\partial y}\lambda\frac{\partial T}{\partial y}+\frac{\partial}{\partial z}\lambda\frac{\partial T}{\partial z}\ldots\ldots\ldots\ldots\ldots\ldots(8)$$

Where c(T) is the heat capacity of the material, in which the phase transitions are taken into account. Density of the material is expressed by $\rho(T)$ and $\lambda(T)$ is the effective value of the thermal conductivity.

From equation 3, the change in latent heat ∇H and L denotes the latent heat of fusion is defined by;

$$\nabla H = Lf_l \ldots\ldots\ldots\ldots\ldots\ldots\ldots\ldots\ldots (9)$$

The weight fraction f_1 is defined by;

$$f_1=\frac{T-T_s}{T_1-T_s}\begin{cases} & if\ T>T_i \\ if\ T_s\le T\le T_1 & \\ & if\ T<T_s\end{cases} \ldots\ldots\ldots\ldots\ldots\ldots\ldots\ldots\ldots (10\ )$$

A change in temperatures resulted in changes in the melting point of NiTi mix presented within a series of equations.

$$C = f_c C_1 + f_1 C_1 \ldots\ldots\ldots\ldots\ldots\ldots\ldots\ldots (11)$$

The solid states of the experiment defined by;

$$C_s = k_p C_1 \ldots\ldots\ldots\ldots\ldots (12)$$

The heat capacity density, thermal conductivity, mass diffusion coefficients defined by;

$$c_p = f_s C_s + f_1 C_1 \ldots\ldots\ldots\ldots\ldots\ldots\ldots\ldots (12)$$

$$\rho = f_s\rho_s + f_1\rho_1 \ldots\ldots\ldots\ldots\ldots\ldots\ldots\ldots (13)$$

$$k-\left(\frac{g_s}{k_s}+\frac{g_1}{k_1}\right)^{-1}\ldots\ldots\ldots\ldots (14)$$

$$D = f_1 D_1 \ldots\ldots\ldots\ldots\ldots\ldots (15)$$

In the mathematical models, the initial and boundary conditions used in solving the thermal problem for the respective models are defined. Energy and pressure conditions are considered in the boundary conditions of the free surface. The energy balance of the laser heat flux and the heat dissipation by the way of convection and radiation is expressed from equation 16 to 18. At the initial time when t= 0, body temperature was taken as $T = T_0$. This temperature is when the laser action has not taken place. The laser heat flux at liquid or gas interface is expressed as;

$$\frac{KdT}{dZ} = q_{laser} - q_{conv} - q_{rad} \;\ldots\ldots\ldots\ldots\ldots\ldots (16)$$

$$q_{ener} = \frac{2Q_e}{\pi r_b^2}\exp\left(\frac{-2r^2}{r_b^2}\right) - h_c(T - T_0) - \sigma_b\varepsilon(T^4 - T_0^4) \quad \ldots\ldots\ldots (16.1)$$

Where, the input heat follow a Gaussian distribution defined by;

$$q_{laser} = \frac{aQn}{\pi r_{b^2}}\exp\frac{-a(x^2 + y^2)}{r_{r_{b^2}}} \ldots\ldots\ldots\ldots\ldots\ldots\ldots\ldots\ldots\ldots (16.2)$$

The heat loss, which is through convectional and radiational is defined by the equation;

$$q_{loss} = h_c(T - T_a) + \sigma_b\varepsilon(T^4 - T_a^4) \ldots\ldots\ldots\ldots\ldots\ldots (16.3)$$

On the series of equations, alloy vaporization is negligible hence the weld pool temperature below the boiling point. The top surface of the alloy is defined by the equation;

$$\frac{KdT}{dZ} = q_{laser} - q_{loss} \ldots\ldots\ldots\ldots\ldots\ldots\ldots\ldots (17)$$

If the normal law of power density distribution of laser radiation is adopted;

$$F_{\frac{L}{G}} = \sigma\boldsymbol{n}^*k - \nabla_s T\frac{d\sigma}{dT} \qquad (18)$$

Where;

$$q_0 = \frac{AP}{\pi r_{0^2}}W/m^2 \;\ldots\ldots\ldots (18.1)$$

$A = (1 - R)$ which represents absoptivity

R is reflection coefficient, P is the total power of the laser radiation and r_0 is the radius of the focusing spot in meters.

The natural convention is defined by the marangoni-driven flow at the surface realized by the equations;

$$\mu \frac{du}{dz} = f_1 \left(\frac{\partial \sigma_{sur}}{\partial T}\right) \left(\frac{\partial T}{\partial x}\right) + \frac{f_1(\partial \sigma_{sur})}{\partial C} \left(\frac{\partial C}{\partial x}\right) \dots \dots \dots \dots \dots \dots . . (19)$$

$$\mu \frac{du}{dz} = f_1 \left(\frac{\partial \sigma_{sur}}{\partial T}\right) \left(\frac{\partial T}{\partial y}\right) + \frac{f_1(\partial \sigma_{sur})}{\partial C} \left(\frac{\partial C}{\partial y}\right) \dots \dots \dots \dots \dots \dots . . (20)$$

All the above equations are of great importance in the determination heat and mass transfer of the mix. For the sake of shape recovery for bending, the system of equations is applied in modelling. On each of the phases of the bending fractions, the following conditions hold.

$$\xi_s + \xi_m + \xi_a = 1, \xi_{s\,,}\xi_m, \xi_a \in [0,1] \dots \dots \dots \dots \dots \dots (21)$$

In the bending process, conversions from multivariate martensite to single variant austenite occur. Each process is comprised of kinetic equations with a series of phase fractions involved. Bending then occurs within the bar, defined by the conditions below.

$$T < M_F, \sigma_S \leq |\sigma| \leq \sigma_F, |\dot{\overline{\sigma}}| \geq 0, \dot{T} = 0 \dots \dots \dots \dots \dots \dots . (22)$$

The dot on top of time indicates time differentiation. Whenever $|\sigma| \leq \sigma_F$ experiences an increase from σ_S to σ_F, the different quantities of the alloy volumes change , with the first condition equivalent to 0 with the second condition equivalent to 1.

$$\xi_s = \frac{|\sigma| - \sigma_S}{\sigma_F - \sigma_S} \dots \dots \dots \dots \dots \dots \dots . . (23)$$

$$\xi_m = \frac{\sigma_F - |\sigma|}{\sigma_F - \sigma_S} \dots \dots \dots \dots \dots \dots \dots \dots (24)$$

After the heating process, both the single and multi-variant materials from nickel and NiTi are converted to their respective alloys, through the SMA process defined by the conditions below.

$$T \geq A_s, |\dot{\overline{\sigma}}| - C_A\dot{T} \leq 0, \ldots \ldots \ldots \ldots \ldots .. (25)$$

0,

$$C_A(T - A_F) \leq |\sigma| \leq C_A(T - A_S) \ldots \ldots \ldots \ldots \ldots \ldots \ldots \ldots \ldots (26)$$

From equation (7), whenever $C_A > 0$ defined as a material component with relation to the latent heat per unit mass during the martensitic phase transforms. As T widens, the volume fractions change from the conditions set of;

$\xi_s + \xi_m + \xi_a = 1, \xi_a = 0$, the set of equations;

$$\xi_s = \xi_{s0} + \xi_{s0} \frac{|\sigma| - C_A T + C_A A_S}{C_A A_F - A_S} \ldots \ldots \ldots \ldots \ldots \ldots \ldots \ldots \ldots . (27)$$

$$\xi_m = \xi_{m0} + \xi_{m0} \frac{|\sigma| - C_A T + C_A A_S}{C_A A_F - A_S} \ldots \ldots \ldots \ldots \ldots \ldots \ldots \ldots \ldots . (28)$$

$$\xi_a = \frac{(-|\sigma| - C_A T + C_A A_S}{C_A A_F - A_S} \ldots \ldots \ldots \ldots \ldots \ldots \ldots \ldots \ldots . (29)$$

7.3 Chapter Summary

The proposed model connotatively states that as both the temperature rises due to the increase laser power, the welding speed will equally do so, as the curvature of deflection. Such an incremented level in the values will lead to a rise in the thermodynamic changes of mixture composition. Coherently a more stable outcome will be noted and measure for the respective data combination. Since B19’ and R phase %wt increases with increase in welding speed which makes the tensile stress and recoverable bending deflection increases rather than decreases. However, a further welding speed increase would decrease the %wt of B19’ and R phase. This forms a non-linear relationship correlation output. The set of variability will cordially be dependent on the level of both the laser power and the welding speed. This implies that elemental compounds of either the B19’ and R phases need an appropriated welding speed to attain a successful welded joint. A strong positive correlation exists between the weight fraction of the phases and the welding speed during laser welding. The successful welding of a butt joint must ascertain the level of weight fraction of B19’ and R phase.

8 Conclusions

Dissimilar metal welding has consistently drawn the attention of industry as it can effectively reduce material costs and weight, increase design flexibility and complexity and improve functionality. However, directly joining dissimilar metals can cause serious problems due to the formation of intermetallic compounds. Based on the literature review, laser welding experiments with both pulsed laser and continuous laser were conducted by the Taguchi method followed by ANOVA to increase the welding efficiency. In addition to the laser welding parameters, such as mode of laser, laser power, welding speed and focus position, cobalt and nickel interlayer were investigated. Ni interlayer was found to be the appropriate interlayer in joining NiTi and stainless steel, the shape and size of Ni interlayer influences the chemical composition of the fusion zone were also investigated.

Experimental works involved the determination of the chemical composition of fusion zone, tensile strength, hardness, corrosion, bending and recovery properties resulting from welding of NiTi and stainless steel with Ni interlayer were conducted.

The best welded couples were obtained with the highest tensile strength by applying the Taguchi method and ANOVA. A trend to increase the power density to 6.37x10-6 W/cm^{r} has been clearly observed in the experiments in order to reach higher tensile strength. Afterwards, a restricted number of parameters were investigated over narrower ranges to identify the effect of welding speed on the chemical composition of the welded joint with rectangular shape Ni interlayer. Both 5mm and 8mm interlayer width with different welding speed showed the presence of intermetallic phases in the welded areas and a visible fusion interface layer between the NiTi and Ni. Nevertheless, the best sample with high tensile strength overpassed significantly the tensile strength of directly welded NiTi and stainless steel joint.

The best laser weld condition was defined as a reference condition to produce sound joined couples between NiTi and stainless steel.

It was found that a suitable welding speed and power density results to improvement in tensile strength and hardness so as to enable recoverable bending deflection of the welded joint of NiTi and stainless steel. Thus, it enables a piece of stainless steel with a recoverable deformation region of NiTi up to 5.00mm. The addition of Ni interlayer has an obvious effect on the tensile strength, hardness and ductility of the NiTi and stainless steel joint. It is beneficial for decreasing brittle intermetallic compounds. Ni_3Ti is more ductile while $NiTi_2$ is detrimental for the corrosion behavior, by varying the welding speed, the ratio of amount of Ni_3Ti and Ni_2Ti were controlled to improve the mechanical and corrosion properties of the welded joint.

The weld condition can be summarized as follows:

- The laser power density has to be set to 4.46 x 10^6 W/cm^2 in order to produce sufficient energy to avoid an unwelded part remains near the center of the contact interface which reduces the fusion zone.
- The energy delivered to any specific point has set to 3.64J with power density of 6.37x10^6 W/cm^2 for welding NiTi- SS with rectangular shape interlayer width of 5mm.

Microanalysis revealed that Ni_4Ti_3 were presented in different welding condition, contribute the shape memory characteristics, and strengthen the matrix to increase the yield strength of the welded joint. However, the increase of Ni_4Ti_3 to over 20% of the matrix would increase the Ms, Mf and Af. As the same time, two-stage phase transformation was occurred on heating arises when the amount of Ni_4Ti_3 increased to around 26 % in this project. The B19' with a strong preferred orientation of (111) planes and Ni_4Ti_3 with a preferred orientation of

(3-1-2) and (2 1-1) planes were found in the fusion zone, which contribute the improvement of the tensile strength and recoverable bending deflection. A model outline the correlation existing under various phases and recoverable bending deflection was presented.

The values of this research are outlined as follows:

(i) The welding parameters of fiber laser to produce a stainless steel sheet with a portion of NiTi, which has a recoverable region with improvement of tensile strength, are determined and has been reported.

(ii) The corrosion resistances in Hank's solution of the weldment are found to be improved by decreasing the amount of $NiTi_2$, which is controlled by the welding speed and interlayer width at a power density of $6.37x10^6$ W/cm^2. It contributes to obtain more opportunity to the application in medical devices/implant..

(iii) To better understanding of the crucial factors that could affect the chemical composition of the laser welded NiTi – Ni –SS joint. The quantity of phases formed and their orientations that could affect the tensile strength and recoverable bending deflection of welded joint and the transformation behavior of the fusion zone were reported.

9 Recommendations for Further Works

Although this research study produces interesting acceptable results, improvements are likely to be made, either by further developments of recommendations presented in this thesis. Firstly, the application of thermocouple to monitor the weld pool during laser welding could make a more accurate representation in term of the solidification and cooling rates. The measured temperature change could enable a control of appropriated amount of energy supplied and appropriate cooling rates to the weld pool. Furthermore, investigations of surface treatments and different types of joints could be made to evaluate the degree of further influence and how necessary the treatments were when making a sound weld. Besides, it would be of interest to further investigate the effect of post welded heat treatment to reconstruct the microstructure of the fusion zone with favorable phases. An improved investigation is the study of fatigue strength together with further shifting of the laser to the Ni side to reduce the amount of energy absorb by NiTi and the formation of favorable phases could be further investigated. Last but not least, an improved focus of the data related to stainless steel and nickel interaction during laser welding could be studied to further investigate the potential effect to NiTi and the Ni joint.

Bibliography

A. Falvo, F.M. Furgiuele, C. Maletta. (2008). Functional behaviour of a NiTi-welded joint: Two-way shape memory effect, Materials Science and Engineering A. 481–482, pp.647–650.

Abderrazak K., Salem W. B., Mhiri H., Lepalec G., Autric M. (2008). Modelling of CO2 laser welding of magnesium alloy. Journal of Optics & Laser Technology. 40, pp. 581-588.

Allmen, Von M., Blatter A. (1995). Laser-beam interactions with materials: physical principles and applications. Springer.

American Welding Society.(2014). http://www.aws.org/w/a/about/index.html?id=RhsoxULQ (accessed 8 April 2014).

Arthur L. (1968). Introductory welding metallurgy: instructor's manual: American Welding Society.

ASTM F2129. (2004). Standard reference test method for conducting cyclic potentiodynamic polarization measurements to determine the corrosion susceptibility of small implant devices. ASTM International, West Conshohocken, PA.

ASTM G5. (2014). Standard reference test method for making potentiodynamic anodic polarization measurements. ASTM International, West Conshohocken, PA.

Auricchio F., Fugazza, D., Desroches, R. (2008). Rate-dependent thermo-mechanical modelling of superelastic shape-memory alloys for seismic applications. J. Intell. Mater. Syst. Struct. 19(1), pp. 47–61.

Auricchio F., Lubliner J. (1997). An uniaxial model for shape-memory alloys. Int. J. Solids Struct. 34(27), pp. 3601–3618.

Auricchio F., Sacco E. (1997). A superelastic shape memory alloy beam model. J. Intell. Mater. Syst. Struct. 8 (6), pp. 489–501.

Auricchio F., Taylor R. L., Lubliner J. (1997). Shape-memory alloys: macromodelling and numerical simulations of the superelastic behavior, Comput. Methods Appl. Mech. Eng. 146, pp. 281–312.

Baker, D., Koehler, D. C., Fleckenstein, W. O., Roden, C. E. (1971). Physical design of electronic systems vol. 3 .Integrated device and connection technology. Prentice-Hall, Inc., Englewood Cliffs, NJ.

Balasubramanian K. R., Shanmugam N. S., Buvanashekaran G., Sankaranarayanasamy K. (2008). Numerical and experimental investigation of laser beam welding of AISI 304 stainless steel. Advanced in production engineering and management 3. 2, pp. 93 -105.

Bandyopadhyay D., Sharma R. C., Chakraborti N. (2000). The Ti-Co-C system (titanium-cobalt-carbon). Journal of Phase Equilibria and Diffusion 21. (2), pp. 179-185.

Benat, K. (2007). Shape memory bahavior of ultrafine grained NiTi and TiNiPd shape memory alloys. Texas A&M University. https://repository.tamu.edu/bitstream/handle/1969.1/ETD-TAMU-2543/KOCKAR-DISSERTATION.pdf?sequence=1(accessed 8 April 2014).

Berretta J. R., et al. (2007). Pulsed Nd:YAG laser welding of AISI 304 to AISI 420 stainless steels. Optics and Lasers in Engineering. vol. 45, pp. 960-966.

Beyer, E. (1995). Schweissenmit Laser. Springer.

Beyer, J., Hiensch, E.J.M. and Besselink, P.A. (1989). Resistance welding of TiNi-shape memory alloys. The Martensitic Transformation in Science and Technology. pp.199–206.

Bhagyaraj, J., Ramaiah, K.V., Saikrishna, C.N., Bhaumik, S.K., Gouthama. (2013). Behavior and effect of Ti2Ni phase during pocessing of NiTi shape memory alloy wire from cast ingot. J Alloys Compd. 581, pp.344-351.

Bhan, S. (1971). Structure of high temperature Ti (Ti.11 Ni.89)3 phase. Journal of the Less-Common Metals. Vol. 25, pp.215-220.

Bimber B.A., Hamilton R., Keist J., Palmer T.A. (2016). Anisotropic microstructure and superelasticity of additive manufactured NiTi alloy bulk builds using laser directed energy deposition. Mater. Sci. Eng. A. 674 pp. 125–134.

Borrisutthekul, R., Tachi, T., Miyashita, Y., and Mutoh, Y. (2007). Suppression of intermatallicreaction layer formation by controlling heat flow in dissimilar joining of steel and alniniium alloy. Material Science Engineering A. 467, pp.108-113.

Brandal, G., Satoh, G., Yao, Y., Naveed, S. (2013). Beneficial interface geometry for laser joining of NiTi to stainless steel wires.

Cacciamani, G., Keyzer, J.De, Ferro, R., Klotz, U.E., Lacaze, J., Wollants, P. (2006). Critical evaluation of the Fe-Ni, Fe-Ti and Fe-Ni-Ti alloy systems. Intermetallics. 14(10-11), pp.1312–1325.

Cacciamani, G., Keyzer, J., Ferro, R., Klotz, U., Lacaze, J. and Wollants, P. (2006). Critical evaluation of the FeeNi, FeeTi and FeeNieTi alloy systems. Intermetallics. 14, pp.1312–1325.

Calkins, F., Butler, G. and Mabe, J. (2006). Variable geometry chevrons for jet noise reduction. AIAA-2006-2546, 12th AIAA/CEAS Aeroacoustics Conference, Cambridge MA.

Campanile, L.F. and Sachau, D. (2000). The belt-rib concept: A structronic approach to variable camber. Journal of Intelligent Material Systems and Structures. 11, pp.215–224.

Canning J. (2006). Fiber Lasers and related technologies. Journal of Optics and Lasers Engineering. 44, pp. 647-676.

Casper van der Eijk, Hans, F., Zuhair, K.S., Odd, M.A. (2003). Plasma welding of NiTi to NiTi, stainless steel and Hastelloy c276. Conference Proceedings ASM Materials Solutions. pp.393-399.

Chan C.W., Chan S.H.J., Man H.C., Ji P. (2012). 1-D constitutive model for evolution of stress-induced R-phase and localized Lüders-like stress-induced martensitic transformation of super-elastic NiTi wires. Int J Plast. 32–33, pp.85–105.

Chan C.W., Chan S.H.J., Man H.C., Ji P. (2012). Constitutive model for localized Lüders-like stress-induced martensitic transformation and super-elastic behaviors of laser-welded NiTi wires. Comput Mater Sci. 63, pp.197–206.

Chan C.W., Hussain I., Waugh D.G., Lawrence J., Man H.C. (2013). In vitro mesenchymal stem cell responses on laser-welded NiTi alloy. Mater Sci Eng C. 33, pp.1344–54.

Chan C.W., Man H.C. (2013). Reduction of environmentally induced cracking of laser-welded shape memory NiTi wires via post-weld heat-treatment. Mater Sci Eng A. 588, pp.388–94.

Chan C.W., Man H.C.(2011) Laser welding of thin foil nickel–titanium shape memory alloy. Opt Lasers Eng. 49, pp.121–126.

Chan C.W., Man H.C., Cheng F.T. (2013). Fatigue behavior of laser-welded NiTi wires in small-strain cyclic bending. Mater Sci Eng A. 559, pp.407–415.

Chan C.W., Man H.C., Yue T.M. (2011). Effects of process parameters upon the shape memory and pseudo-elastic behaviors of laser-welded NiTi thin foil. Metall. Mater Trans A Phys Metall. 42:22, pp.64–70.

Chan C.W., Man H.C., Yue T.M. (2012). Effect of postweld heat treatment on the microstructure and cyclic deformation behavior of laser-welded NiTi-shape memory wires. Metall Mater Trans A. 43, pp.1956–65.

Chan C.W., Man H.C., Yue T.M. (2012). Effect of post-weld heat-treatment on the oxide film and corrosion behaviour of laser-welded shape memory NiTi wires. Corros Sci. 56, pp.158–67.

Chan C.W., Man H.C., Yue T.M. (2012). Susceptibility to environmentally induced cracking of laser-welded NiTi wires in Hanks' solution at open-circuit potential. Mater Sci Eng A. 544, pp.38–47.

Chan C.W., Man H.C., Yue T.M. (2012). Susceptibility to stress corrosion cracking of NiTi laser weldment in Hanks' solution. Corros Sci. 57, pp.260–9.

Chatterjee S., Abinandanan T., Chattopadhyay K. (2008). Phase formation in Ti/Ni dissimilar welds. Materials Science and Engineering A. Vol. 490 (1-2), pp.7-15.

Chen H., Pinkerton A. J., Li L. (2008). Single mode Fiber Laser welding of dissimilar aerospace alloys. PICALEO 2008 Conference Proceedings. paper 107.

Chou, D.S., Pan, L.K. and Chang, B.D. (2001). Optimization for solidification of low-level-radioactive resin using Taguchi analyses. Waste Management. 21, pp.762–72.

Christian J.W. (2002). The theory of transformations in metals and alloys. Oxford: Pergamon, Part I. p. 422.

Cieslak, M.J. (1993). ASM Handbook: volume 6: welding, brazing, and soldering. ASM International.

Civjan, S., Huget, E.F. and Desimon, L.B. (1975). Potential applications of certain Nickel–Titanium (Nitinol) alloys. Journal of Dental Research. 54, pp.89–96.

Clark, J.B. (1963). Conventions for plotting the diffusion paths in multiphase ternary diffusion couples on the isothermal section of ternary phase diagram. Trans MetallSoc AIME. 227, pp.1251–1252.

Dahotre N. B., Harimkar S. P. (2008). Laser Fabrication and Machining of Materials: Springer US.

Dantzig, J.A. and Rappaz, M. (2009). Solidification. CRC Press.

Darren, J., Hartl, J. and Mooney, T., and Dimitris, C. (2008). Experimentally validated numerical analysis of aerostructures incorporating shape memory alloys. The Boeing Company, Seattle, WA, U.S.A.

Dietmar, M. (1987). Method of bonding titanium or titanium alloy to an iron-nickel alloy. US Patent 4674675A.

Dilibal, D., Murat Tabanli, R. and Dikicioglu, A. (2004). Development of shape memory actuated ITU robot hand and its mine clearance compatibility. J. Mater. Process. Technol. 105/106, pp.1390-1394.

Domnita, F. and Cristian, C. (2011). Application of Taguchi method to selection of optimal lubrication and cutting conditions in face milling of AlMg3. Journal of Cleaner Production. 19, pp. 640-645.

Dudkina, L.P. and Kornilov, I.I. (1967). Investigation of the equilibrium diagram of the TiNi-TiFe system. Russian Metallurgy. 4, pp.98–101.

Duerig,T., Pelton, A. and Stockel, D. (1999). An overview of nitinol medical applications. Materials Science and Engineering A. 273-275, pp.149–160.

Fan G., Chen W., Yang S., Zhu J., Ren X., Otsuka K. (2004). Acta Material. 52, pp. 4351.

Favez, D. (2009). Soudage laser or-acier: métallurgieetprocédé. Ph.D. thesis, EcolePolytechniqueFédérale de Lausanne.

Favez, D., Wagnie`re, J. and Rappaz, M. (2008). ICALEO 2008 – 27th International Congress on Applications of Lasers and Electro-optics. pp. 327–331.

Fellman A., Salminen A., (2007) Study of the phenomena of Fiber laser-MAG hybrid welding. ICALEO ® 2007 Congress Proceeding, paper 1604.

Fernandes, J., Peres, V., Mendes, M. And Elias, N. (2011). Understanding the Shape-Memory Alloys Used in Orthodontics. ISRN Dentistry. http://www.hindawi.com/journals/isrn/2011/132408/(accessed 8 April 2014).

Foster, W.T. (2000). Basic Taguchi design of experiments. National Association of Industrial Technology Conference, Pittsburgh.

Fox, G., Hahnlen, R. AndDapino, M.J. (2012). Fusion welding of nickel–titanium and 304 stainless steel tubes: Part II:tungsten inert gas welding. Journal of Intelligent Material Systems and Structures. pp. 1–11.

Fukumoto, S., Inoue, T., Mizuno, S., Okita, K., Tomita, T. and Yamamoto, A. (2010). Friction welding of TiNi alloy to stainless steel using Ni interlayer. Science and Technology of Welding and Joining. 15. pp.124–30.

Fukumoto, S., Matsuo, T., Tsubakino, H. and Yamamoto A. (2007). Resistance Microwelding of SUS304 stainless steel fine wires. Materials Transactions. 48 (4), pp.813-820.

Ghaini F. M., et al. (2007). Weld metal microstructural characteristics in pulsed Nd:YAG laser welding. Scripta Materialia. vol. 56, pp. 955-958.

Gisario, A., Mehrpouya, M., Pizzi, E. (2017). Dissimilar joining of transparent Poly (ethy-lene terephthalate) to aluminum 7075 sheets using a diode laser. J Laser Appl. 29(2), pp.418.

Gobel G., Brenner B., Beyer E. (2007). New Application Possibilities for Fiber Laser Welding ICALEO ® Congress Proceedings. paper 209.

Goldak J.A., Akhlaghi M. (2005). Computational Welding Mechanics. Springer. New York.

Gopinath, T., Sukumar, K., Brajendra, M., Subrata, C. (2013). Effect of Bonding Time on Interfacial Reaction and Mechanical Properties of Diffusion-Bonded Joint Between Ti-6Al-4V and 304 Stainless Steel Using Nickel as an Intermediate Material. Metallurgical and Materials Transactions A. 45 (4), pp.2078-2090.

Guber A.E., Giordano N., Schussler A., Baldinus O., Loser M., Wieneke P. (1996). Nitinol-based microinstruments for endoscopic neurosurgery. In: Proceedings actuator 96 – 5th int conf new actuators, p. 375–8.

Gugel, H., Schuermann, A., Teisen, W. (2008). Laser welding of NiTi wires. Materials Science and Engineering A. 481–482, pp.668–671.

Gupta, K.P. (1990). Phase diagrams of ternary nickel alloys. part 1. The Indian Institute of Metals.

H. HIRAG A. and TINOU E. (2012). Effects of the shielding gas and laser wavelength in laser welding magnesium alloy sheets, Welding International. 16, 6, pp.442-450.

Hall, P.C. (2004). Method of welding titanium and titanium based alloys to ferrous metals. US Patent 6875949B2.

Hall, P.C. (2000). Resistance welding Ti-rich Nitinol wire. SMST-2000: The International Conference on Shape Memory and SuperelasticTechnologies. pp.67-75.

Hall, P.C. (2004). Laser welding nitinol to stainless steel. Proceedings of the International Conference on Shape Memory and Superelastic Technologies (SMST-2003). California. 5–8, pp.219–228.

Hall, P.C. (2005). Method of welding titanium and titanium based alloys to ferrous metals. US Patent 6875949.

Hamilton, R.F., Sehitoglu, H., Chumlyakov, Y., Maier, H.J. (2004). Stress dependence of the hysteresis in single crystal NiTi alloys. Acta Materialia. 52 (11) pp. 3383-3402.

Han G. M., et al. (2007). Dynamic simulation of the temperature field of stainless steel laser welding. Materials & Design. vol. 28, pp. 240-245.

Hand, H.M., Arah, C.O., McNamara, D.K., Mecklenburg, M.F. (1991). Effects of environmental exposure on adhesively bonded joints. International Journal of Adhesion and Adhesives. 11(1), pp.15–23.

Hara, T., Ohba, T., Otsuka, K., Nishida, M. (1997). Materials Transcations, JIM. Phase transformation and crystal structures of Ti2ni3 precipitates in Ti-Ni alloys. Vol. 38, pp.277-284.

Hartl, D.J., Mooney, J.T., Lagoudas, D.C. (2008). Experimentally validated numerical analysis of aerostructures incorporating shape memory alloys. The Boeing Company.

He Gang, (2018) Numerical and Experimental Investigations of Solidification Parameters and Mechanical Property during Laser Dissimilar Welding. Growth rate and microstructure of metallic compounds pp. 74-88.

Hinotani, S. (1990). Microstructure and growth of reaction phases in the diffusion bonding of Ti to Fe, Ni and Cu. Sumitomo Met. 42(4), pp. 241–246.

Hirose, A., Uchihara, M., Araki, T., Honda, K., Kondoh, M. (1990). Laser welding of Ti-Ni type shape memory alloy. Nippon Kinzoku Gakkai-si. 54(3), pp. 262–269.

Hodgson, D., Russell, S. (2000). Nitinol melting, manufacture and fabrication. Minimally Invasive Therapy and Allied Technologies. vol. 9(2), 61-66.

Holm, R. (1976). Electric contacts, theory and applications. Berlin, Springer-Verlag.

Hora, J. (2004). Laser microwelding of Ti and Ni-Ti shape memory alloys. MSc Thesis. Cranfield University, Bedfordshire, UK.

Howse, M. (2001). Rolls-Royce. Derby. Presentation given at the Paris Air Show, Paris.

Hsu, Y. T., Wang, Y. R., Wu, S. K., Chen, C. (2001). Effect of CO2 laser welding on the shape-memory and corrosion characteristics of TiNi alloys. Metallurgical and Materials Transactions A: Physical Metallurgy and Materials Science. 32(3), pp.569–576.

Hull A.W. (1921). X-ray crystal analysis of thirteen common metals. Phys. Rev. B, 17, pp. 571–588.

Jani J.M., Leary M., Subic A., Gibson M.A. (2014). A review of shape memory alloy research, applications and opportunities. Materials and Design. 56, pp.1078–1113.

Jiang, S.Y., Shu, Y., Zhao, Y.N., Zhang, Y.Q., Hu, L., Liang, Y.L. (2013). Effect of solution treatment and aging on microstructural evolution and mechanical behavior of NiTi shape memory alloy. Transaction of Nonferrous Metals society of China. Volume 23, Issue 12, December 2013, pp. 3658-3667.

Jiang, S.Y., Yu, J.B. and Zhang, Y.Q. (2017). Investigation on deformation mechanisms of NiTi shape memory alloy tube under radial loading. Metals. Vol. 7, pp.268-277.

Jurczyk, M. (2018). Handbook of Nanomaterials for Hydrogen Storage. Pan Standford Publishing Pte. Ltd. pp149-177.

Jyotsna, D.M. and Indranil, M. (2013). Laser-Assisted Fabrication of Materials. Springer.

Kainuma, et al. (1986). The mechanism of the all-round shape memory effects in a Ni-rich TiNi Alloy. ICOMAT-86, JIM Nara Japan. Pp.717-722.

Kaiser, J. G., Dunn, G. J. and Eagar, T . W. (1982). The effect of electrical resistance on nugget formation during spot welding. Welding Research Supplement. pp.167-174.

Kar, A. and Langlais, M.D. (1995). Optical and Quantum Electronics. 27, pp.1165-80.

Kauffman, G. B. and Mayo, I. (1997). The story of Nitinol: The serendipitous discovery of the memory metal and its applications. The Chemical Educator. 2(2), pp.1-21.

Ke Chang Bo, Cao Shan Shan, MA Xiao, Zhang Xin-Ping. (2012). Modeling of Ni4Ti3 precipitation during stress-free and stress-assisted aging of bi-crystalline NiTi shape memory alloys, Transactions of Nonferrous Metals Society of China. October 2012. Vol.22(10), pp.2578-2585.

Kell J., Tyrer J., Higginson R., Thomson R., Jones J., Noden S. (2006). Holographic diffractive optical elements allow improvements in conduction laser welding of steels ICALEO ® 2006 Congress Proceedings. paper 102.

Khan, M. I. (2007). Spot welding of advanced high strength steels. MASc. thesis. University of waterloo, Waterloo, Ontario, Canada.

Kim J. D., (1991). Parametric evaluation of CO2 laser beam welding. ASME publication PED, welding and Joining Processes. Vol. 51, pp. 195-201.

Kirindi T., Sari U., Dikici M. (2009). The effects of pretrain recovery temperature and bending deformation on shape memory effect in an Fe–Mn–Si–Cr–Ni alloy. J. Alloy. Compd. 475(1–2), pp. 145–150.

Kirkaldy, J.S. and Brown, L.C. (1963). Diffusion behaviour in ternary. multiphase systems. Canadian Metallurgical Quarterly. 2(1), pp.89–117.

Ko W.S., Grabowski B., Neugebauer J. (2015). Development and application of a Ni-Ti interatomic potential with high predictive accuracy of the martensitic phase transition. Phys. Rev. B 92, 134107, pp. 1-22.

Krishen K. (2008). New technology innovations with potential for space applications. Acta Astronautica. 63, pp. 324-333.

Kundu, S. and Chatterjee, S. (2008). Characterization of diffusion bonded joint between titanium and 304 stainless steel using a Ni interlayer. Material Characterization. 59, pp.631 – 637.

Lagoudas, D.C. (2010). Shape memory alloys: modeling and engineering applications. 1st ed. New York: Springer. pp.6-11.

Laves F., Wallbaum H.J., Die Kristallstruktur von. (1939). Ni3Ti und Si2Ti (zwei neue Typen). Z. Kristallogr. Cryst. Material. 101, pp. 78–93.

Lee, J.Y., Ko, S.H., Farson, D.F. and Yoo, C.D. (2002). Mechanism of keyhole formation and stability in stationary laser welding. Journal of Physics D: Applied Physics. 35(13), pp.1570–1576.

Lee, M.K., Lee, J.G., Choi, Y.H., Kim, D.W., Rhee, C.K., Lee, Y.B., Hong, S.J. (2013). Interlayer engineering for dissimilar bonding of titanium to stainless steel. Materials Letters. 64, pp.1105 -1108.

Li H., Sun D., Gu X., Dong P., Lv Z. (2013). Effects of the thickness of Cu filler metal on the microstructure and properties of laser-welded TiNi alloy and stainless steel joint. Mater De 50, pp.342–50.

LI, B.F. (2004). Study on the weldability of titanium and steel and titanium clad steel plate. Development and Application of Materials. 19(1). pp.4144.

Li, D. Y. and Chen, L. Q. (1997). Selective variant growth of coherent Ti11Ni14 precipitate in a TiNi alloy under applied stresses. ActaMaterialia. 45, pp.471-479.

Li, H.M, Sun, D.Q., Cai, C.L., Dong, P. and Gu, X.Y. (2013). Laser welding of TiNi shape memory alloy and stainless steel using Co filler metal. Optics and Laser Technology. 45, pp.453-460.

Li, H.M., Sun, D.Q., Cai, X.L., Dong, P. and Wang, W.Q. (2012). Laser welding of TiNi shape memory alloy and stainless steel using Ni interlayer. Materials and Design. 39, pp.285–293.

Li, M.G., Sun, D.Q., Qiu, X.M. Liu, J.B., Miao, K. and Wu, W.C. (2007). Effects of silver based filler metals on microstructure and properties of laser brazed joints between TiNi shape memory alloy and stainless steel. Science and Technology of Welding and Joining. 12 (2), pp. 183.

Li, M.G., Sun, D.Q., Qiu, X.M., and Yin, S.Q. (2006). Corrosion behaviour of the laser-brazed joint of TiNi shape memory alloy and stainless steel in artificial saliva. Materials Science and Engineering A. 441, pp.271-277.

Li, M.G., Sun, D.Q., Qiu, X.M., Sun, D.X. and Yin, S.Q. (2005). Microstructures and properties of capacitor discharge welded joint of TiNi shape memory alloy and stainless steel. China Welding. 14, pp. 95–100.

Lin, P.H., Tobushi, H., Tanaka, K., Hattori, T., Makita, M. (1994). Pseudoelastic behaviour of TiNi shape memory alloy subjected to strain variations. J Intell Mater Syst Struct. 5, pp.694–701.

Lison, R., Lugscheider, E. and Klohn, K. (1979). Strength of high temperature brazed joints – influence of brazing parameters. Welding Journal. 59(10), pp.296-300.

London, B., Fino, J., Pelton, A.R. and Mahoney, M. (2005). Friction stir processing of Nitinol. In Friction Stir Welding and Processing III.

Luisa, Q. and Rosa M, M. (2012). Welding Shape Memory Alloys with NdYAG lasers. Soldag. Insp. São Paulo. 17 (3), pp.210-217.

Mabe, J.H., Ruggeri, R.T., Rosenzweig, E., and Yu, C.J. (2004). NiTinol performance characterization and rotary actuator design. Boeing Phantom Works.

Martukanitz R. P. (2005). A critical review of laser beam welding," Proceedings of the SPIE - The International Society for Optical Engineering. vol. 5706, pp. 11-24.

Massalski, T.B. (1990). Binary Alloy Phase Diagrams. ASM International. Metal Park (OH).

Mehrpouya M., Emamian S. (2017). Recent advantages in laser fabrication of micro-channel heat exchangers. Materialwissenschaft und Werkstofftechnik 48(1), pp.1–5.

Michal G.M., Sinclair R. (1981). The structure of TiNi martensite. Acta Crystallogr. B, 37, pp. 1803–1807.

Mirshekari GR, Saatchi A., Kermanpur A., Sadrnezhaad SK. (2013). Laser welding of NiTi shape memory alloy: comparison of the similar and dissimilar joints to AISI 304 stainless steel. Opt Laser Technol. 54, pp.151–8.

Miyazaki, S. and Otsuka, K. (1986). Deformation and transformation behavior associated with the rphase in Ti-Ni alloys. Metallurgical Transactions. A17A, pp.53-63.

Miyazawa, S., Loh, N.H. and Tam, S.C. (1993). Application of experimental design in ball burnishing. International Journal of Machine Tools & Manufacturer. 33(6), pp.841–52.

Montgomery D. C., Runger G. C., Hubele N. F. (2007). Engineering Statistics. Fourth edition, John Wiley & Sons, Inc.

Montgomery, D.C. (1984). Design and analysis of experiments. 2nd ed. New York: Wiley.

Morgan, N B. (2004). Medical shape memory alloy applications – the market and its products. Mater. Sci. Engineering. A378, pp.16-23.

Mubashar A., Ashcroft, I.A., Critchlow, G. W., and Crocombe, A.D. (2011). Strength prediction of adhesive joints after cyclic moisture conditioning using a cohesive zone model. Engineering Fracture Mechanics. 78(16), pp.2746–2760.

Nakata Y, Tadaki T, Shimizu K. (1998). In: Inoue K, Mukherjee K, Otsuka K, Chen H (eds) Displacive phase transformations and their applications in materials engineering. TMS, Warrendale, pp. 187.

Nishikawa, M., Tanaka, H., Kohda, M., Nagaura, T., Watanabe, K. (1982). Behaviour of welded part of Ti-Ni shape memory alloy. In Journal de Physique (Paris). Volume 43 of ICOMAT-82: International Conference on Martensitic Transformations.

Otsuka, K. and Ren, X. (2005). Physical Metallurgy of Ti-Ni-based shape memory alloys. Progress in Materials Science. 50, pp.511-678.

Otsuka, K. and Wayman, C.M. (1998). Shape memory materials. Cambridge University Press, Cambridge.

Otsuka, K., Ren, X. (2005). Physical metallurgy of Ti−Ni-based shape memory alloys. Prog Mater Sci. 50, pp.511−678.

P'ng, Danny, Molian Pal. (2008). Q-switch Nd: YAG laser welding of AISI 304 stainless steels foils. Journal of Materials Science & Engineering A. 486, pp. 680-685.

Padmanaban, G. and Balasubramanian, V. (2010). Optimization of laser beam welding process parameters to attain maximum tensile strength in AZ31B magnesium alloy. Optics and Laser in Engineering. 42(8), pp.1253-1260.

Paine, J.S.N., Jones, W.M. and Rogers, C.A. (1992). Nitinol actuator to host composite interfacial adhesion in adaptive hybrid composites. Proc. 33rd Structural Dynamics and Materials Conference. AIAA. pp.556-565.

Pan, L.K., Wang, C.C., Hsiao, Y.C. and Ho, K.C. (2005). Optimization of Nd:YAG laser welding onto magnesium alloy via Taguchi analysis. Optics and Laser Technology. 37(1), pp.:33–42.

Patankar S.V. (1980). Numerical Heat Transfer and Fluid Flow. McGraw-Hill, New York.

Pouquet et al. (2012). Dissimilar laser welding NiTi to stainless steel. The international journal of advanced manufacturing technology. Vol. 61, pp.205-212.

Predki, W., Kl¨onne, M., and Knopik, A. (2006). Cyclic torsional loading of pseudoelastic NiTi shape memory alloys: Damping and fatigue failure. Materials Science and Engineering: A 417 (1-2), pp.182–189.

Qiu, X.M., Sun, D.Q., Li, M.G. and Liu, W.H. (2004). Microstructures and properties of welded joint of TiNi shape memory alloy and stainless steel. Transactions of the Nonferrous Metals Society of China. 14, pp.475–459.

Quintino L., Costa A., Miranda R., Yapp D., Kumar V., Kong C. J. (2007). Welding with high power fiber Lasers - A preliminary study, Journal of Materials and Design, 28, pp. 1231-1237.

Quintino, L., et al. (2007). Welding with high power fiber lasers - A preliminary study, Materials & Design. vol. 28, pp. 1231-1237.

Rao, R.S., Kumar, C. G., Prakasham, R. S. and Hobbs, P. J. (2008). The Taguchi methodology as a statistical tool for biotechnological applications: A critical appraisal. Biotechnology Journal. 3 (4), pp.510–523.

Rizzoni Raffaella. (2017). Shape recovery behaviour of NiTi strips in bending:experiments and modelling. pp. 207-227.

Roh, J., Kim, K., and Lee, I. (2009).Shape adaptive airfoil actuated by a shape memory alloy and its aerodynamic characteristics. Mechanics of Advanced Materials and Structures. 16 (3), pp.260-274.

Rong Liang. (2016). A study on keyhole evolution and weld ripple formation in dissimilar welding under pulsed laser. Science and Technology of welding and joining. pp. 587-594.

Rossi, S., Deflorian, F., Pegoretti, A., D'Orazio, D. and Gialanella, S. (2008). Chemical and mechanical treatments to improve the surface properties of shape memory alloy wires. Surf. Coat. Technol. 202, pp.2214-2222.

Rudolf Steiner. (2006). New Laser technology and future applications. Journal of Medical Laser

Application. 21, pp. 131-140.

Russell KC. (1969). Phase transformations. Ohio: ASM, pp. 219.

Saburi T., Nenno S., Fukuda T. (1986). Crystal structure and morphology of the metastable X phase in shape memory Ti-Ni alloys. J. Less-Common Met. 125, pp. 157–166.

Saggere, L. and Kota, S. (1999). Static shape control of smart structures using compliant mechanisms. AIAA journal. 37(5), pp.572–578.

Salminen A., Fellman A. (2007). The effect of laser and welding parameters on keyhole and melt pool behavior during Fiber Laser welding. ICALEO ® 2007 Congress Proceedings. paper 806.

Satoh, G and Yao, Y. (2011). Strength and Microstructure of Laser Fusion Welded Ti-SS Dissimilar Material Pair. Proceedings of NAMRI/SME. 39.

Satoh, G. (2013). Modification and integration of shape memory alloys through thermal treatments and dissimilar metal joining. Columbia University.

Schryvers, D. and Potapar, P.L. (2002). Ti-Ni SMAs-R-phase structure refinement using electron diffraction data. Material Transition, JIM. Vol. 43, pp.774-779.

Seki, M., Yamamoto, H., Nojiri, M., Uenishi, K. and Kobayashi, K.F. (2000). Brazing of Ti-Ni shape memory alloy with stainless steel. Journal of the Japan Institute of Metals. 64. pp.632–640.

Sevilla, P., Martorell, F., Libenson, C., Planell, J.A. and Gil, F.J. (2008). Laser welding of NiTi orthodontic archwires for selective force application. Journal of Materials Science: Materials in Medicine. 19(2), pp.525–529.

Shinoda, T., Tsuchiya, T. and Takahashi, H. (1991). Functional characteristics of friction welded near-equiatomicTiNi shape memory alloy. Trans. Jap. Weld. Soc. 22, pp.30-36.

Shi-xiong LÜ, Zhong-lin YANG, Hong-gang DONG. (2013). Welding of shape memory alloy to stainless steel for medical occlude, Transactions of Nonferrous metals society of China. 23, pp. 156-160.

Sibillano T., Ancona A., Berardi V., Schingaro E., Basile G., Lugara P. M. (2006). A study of the shielding gas influence on the laser beam welding of AA5083 aluminuim alloys by in-process spectroscopic investigation. Journal of Optics and Lasers in Engineering. 44, pp. 1039-1051.

Siekmeyer G., Schrader B., Hegel A., Steegmüller R., Strobel M., Schuessler A. (2005). Novel micro-joining techniques to improve stent radiopacity: a comparison of welding and riveting processes. Adv Mater Process. 163, pp.72.

Song, G., Ma, N. and Li, H.N. (2006). Applications of shape memory alloys in civil structures. Engineering Structures. 28, pp.1266-1274.

Steegmüller R., Strobel M., Flaxmeier E., Schüßler A. (2004) Micro-welding for improved radiopacity of nitinol-stents. Proc Int Conf Shape Mem Superelastic Technology. pp.591–6.

Steen W. M. (2003). Laser material processing - an overview. Journal of Optics A Pure and Applied Optics. vol. 5, pp. S3-S7.

Stephen Wayne. (2018). A Review on Melt-Pool Characteristics in Laser Welding of Metals, Advances in material science and engineering. pp.799-800.

Sun Z., Ion J. C. (1995). Laser-welding of dissimilar metal combinations. Journal of Materials Science. vol. 30, pp. 4205-4214.

Sun, Z., Karppi, R.J. (1996). Material Process. Technol. 59. pp.257.

Taguchi, G., Konishi, S. (1987). Taguchi Methods, orthogonal arrays and linear graphs, tools for quality American supplier institute. American Supplier Institute. pp.8-35.

Thomas, W.M., Nicholas, E.D., Needham, J.C., Murch, M.G., Temple-Smith, P., Dawes, C.J. (1991). Friction-stir butt welding. GB Patent No. 9125978.8. International Patent Application No. PCT/GB92/02203.

Tosun, N. (2006). Determination of optimum parameters for multi performance characteristics in drilling by using grey relational analysis. International Journal of Advanced Manufacturing Technology. 28, pp.:450–455.

Trease, B.P., Lu, K.J. and Kota, S. (2003). Biomemetic compliant system for smart actuator-driven aquatic propulsion: Preliminary results. In Proc. of IMECEŠ03, pp.1–10.

Triantafyllidis D., Schmidt M. J. J., Li L. (2003). Comparison of high power diode laser and Nd: YAG Laser microwelding of K-type thermocouples. Journal of Materials Processing Technology. 138, pp.102-108.

Tsoi K.A., Stalmans R., Schrooten J. (2002). Transformational behaviour of constrained shape memory alloys. Acta Materialia. 50 (14), pp. 3535–3544.

Tsukamoto S. (2003). laser welding. Journal of the Japan welding society welding international. 17, (10), pp. 767-774.

Uenishi, K., Seki, M., Kunimasa, T., Takatsugu, M., Kobayashi, K., Ikeda, T. (2002). YAG laser micro welding of stainless steel and shape memory alloy. Proceedings of SPIE – the International Society for Optical Engineering. 4830, pp.57–62.

Ujjwal Singla. (2017). Fiber Laser Welding Benefits and Industrial Applications, International Journal of Progressive Sciences and Technologies (IJPSAT) Vol. 5 No. 1 June 2017, pp. 07-10.

UPM. (2019). 304/304L Data Sheet. Retrieved from https://www.upmet.com/products/stainless-steel/304304l.

Valasek, J. (2012). Morphing aerospace vehicles and structures. John Wiley & Sons.

Vogel, R. and Wallbaum, H.S. (1938). Das System Eisen-Nickel-Nickeltitanid Ni3Ti-Eisentitanid Fe2Ti. Archiv fur das Eisenhuttenwesen. 12, pp.299–304.

Vollertsen F. (2005). Developments and trends in laser welding of sheet metal. Advanced Materials Research. vol. 6-8, pp. 59-70.

Vollertsen F., Thomy C. (2005). Welding with Fiber Lasers From 200 To 17000W. ICALEO ® 2005 Congress Proceedings. paper 506.

Vollertsen F., Thomy C. (2005). Welding with fiber lasers from 200 to 17000 W. in ICALEO 2005 - 24th International Congress on Applications of Laser and Electro-Optics. Miami, FL, USA, pp. 254-263.

Vollertsen, F. and Grupp, M. (2005). Laser beam joining of dissimilar thin sheet materials. Steel

Research International. 76(2), pp.240-244.

Wang, G. (1997). Welding of nitinol to stainless steel. Proceedings of the Second International Conference on Shape Memory and Superelastic Technologies. pp.131–136.

Wang, Y.L., Li, H., Li, Z. X. and Feng, J. C. (2008). Research on transient liquid phase diffusion bonding process of TiNi shape memory alloy to stainless steel. Journal of Materials Engineering. 9, pp.48–55.

Watanabe E., Stigall G., Elshahawy W., Watanabe I. (2012). Deflection load characteristics of laser-welded orthodontic wires. Angle Orthod. 82, pp.698–702.

Wei, et al. (2014). Effect of laser welding parameters on formation of NiTi shape memory alloy welds. Advances in Materials Science and Engineering. V. pp.4.

Winzek, B., Sterzl, T., Quandt, E. (2001). Bistable thin film composites with TiHfNi shape memory alloys. Proceedings of the International Conference Transducers ’01/Eurosensors XV München, Germany, vol. 1, pp. 706–709.

Wu, M.H. (2001). Fabrication of Nitinol materials and components. Proceedings of the International Conference on Shape Memory and Superelastic Technologies. pp. 258-292.

Xu Z. W., Ngan A. H. W. (2004). TEM study of electron beam-induced crystallization of amorphous GeSi films. Philosophical Magazine Letters. 84 (11), pp. 719-728.

Yan X, Ge Y. (2014). Influence of post-weld annealing on transformation behavior and mechanical properties of laser-welded NiTi alloy wires. J Mater Eng Perform 23, pp.3474–9.

Yan X.J.J., Yang D.Z.Z., Liu X.P.P. (2007). Influence of heat treatment on the fatigue life of a laser-welded NiTi alloy wire. Mater Charact 58, pp.262–6.

Yaowu Hu. (2012). Heat and mass transfer in laser dissimilar in welding of stainless steel and nickel. Journal of applied surface science. pp. 5914-5922.

Ye X. H., Chen X. (2002). Three-dimensional modelling of heat transfer and fluid flow in laser full-penetration welding. Journal of Physics D-Applied Physics. vol. 35, pp. 1049-1056.

Yen, Y.W., Su, J.W., Huang, D.P. (2008). Phase equilibria of the Fe-Cr-Ni ternary systems and interfacial reactions in Fe-Cr alloys with Ni substrate. J Alloys Compd. 457(1-2), pp.270–278.

Yeung, K. W. K., Cheung, K. M. C., Lu, W. W., Chung, C. Y. (2004). Optimization of thermal treatment parameters to alter austenitic phase transition temperature of NiTi alloy for medical implant. Materials Science and Engineering:A. 383, pp.213-218.

Yurko G.A., Barton J.W., Parr J.G. (1959). The crystal structure of Ti2Ni. Acta Crystallogr., 12, pp. 909–911.

Zhou, G., Lloyd, P. (2009). Design, manufacture and evaluation of bending behavior of composite beams embedded with SMA wires. Compos. Sci. Technol. 69(13), pp. 2034–2041.

Zhou, Y. (2008). Microjoining and nanojoining. Woodhead Publishing Ltd., Cambridge, England.

Zhou, Y., Zhang, J., Fan, G., Ding, X., Sun, J., Ren, X. and Otsuka, K. (2005). Origin of 2-stage R-phase transformation in low temperature aged Ni-rich Ti-Ni alloys. Journal of Acta Materialia. Vol. 53(20), pp. 5365-5377.

Zhu J., Li L., Liu Z. (2005). CO2 and diode laser welding of AZ31 magnesium alloy. Applied Surface Science. 247, pp. 300-306.

Zotov Nikolay, Marzynkevitsch, Vladimir Mittemeijer, Eric J. (2014). Evaluation of kinetic equations describing the martensite–austenite phase transformation in NiTi shape memory alloys. Journal of Alloys and Compounds. 15 December 2014, Vol.616, pp.385-393.

Zuhailawati, H., Saeed, A. M., Ismail, A. B., Samad, Z. and Ariga, T. (2010). Spot resistance welding of a titanium/nickel joint with filler metal. Welding Journal. pp101-104.